Dissertation

submitted to the
Combined Faculties for the Natural Sciences and for Mathematics
of the Ruperto-Carola University of Heidelberg, Germany
for the degree of
Doctor of Natural Sciences

presented by
Diplom-Physiker Sebastian E. Egner
born in Wertingen

Oral examination: 22nd November 2006

Multi-Conjugate Adaptive Optics for LINC-NIRVANA

Laboratory tests of a Ground-Layer Adaptive Optics System and Vertical Turbulence Measurements at Mt. Graham

Referees: Prof. Dr. Hans-Walter Rix
Prof. Dr. Andreas Quirrenbach

ABSTRACT

Turbulence in Earth's atmosphere severely limits the image quality of ground-based telescopes. With the technique of Adaptive Optics, the induced distortions of the light can be measured and corrected in real-time, regaining nearly diffraction-limited performance. Unfortunately, when using a single guide star to measure the distortions, the correction is only useful within a small angular area centered on the guide star.

The first part of this thesis presents a laboratory setup, which uses four guide stars to measure the turbulence-induced distortions and one deformable mirror to correct the most turbulent layer. With such a Layer-Oriented Ground-Layer Adaptive Optics (GLAO) system, the area of useful correction is significantly increased. The system is characterized in static and dynamic operation, and the influence of non-conjugated turbulent layers, the effect of brightness variations of the guide-stars and the impact of misalignments are studied. Furthermore, calibration strategies and the performance of the Kalman control algorithm are examined.

The second part of this thesis focuses on SCIDAR measurements of the atmospheric turbulence above Mt. Graham. This dataset provides for the first time a statistical and thorough analysis of the vertical turbulence structure above the LBT site. Based on 16 nights of measurements, spread over one year, Mt. Graham appears to be an excellent site for an astronomical observatory. By extending an analytical model, describing the filtering of the turbulence-induced distortions by an AO system, we calculate performance expectations of the LINC-NIRVANA instrument. In particular, the optimal conjugation heights of the deformable mirrors are studied. Furthermore, we present a new method to measure the atmospheric turbulence near the ground with 40 times increased vertical resolution, compared to standard SCIDAR. First on-sky results demonstrate the power of this technique.

ZUSAMMENFASSUNG

Turbulenzen in der Erdatmosphäere beeinträchtigen erheblich die Bildqualität von bodengebundenen Teleskopen. Mit der Hilfe der Adaptiven Optik können diese Störungen gemessen und in Echtzeit korrigiert werden, wodurch wieder eine nahezu beugungsbegrenzte Auflösung ermöglicht wird. Benutzt man nur einen Leitstern um die Störungen zu vermessen, ist die Korrektur leider auf einen nur sehr kleinen Winkelbereich um den Leitstern herum begrenzt.

Im ersten Teil dieser Doktorarbeit wird ein Laboraufbau präsentiert, der vier Leitsterne und einen deformierbaren Spiegel benuzt, um die Störungen aufgrund der Turbulenzen zu vermessen und die stärkste turbulente Schicht zu korrigieren. Mit einem solchen "schichten-orientierten Ground-Layer Adaptiven Optik" (GLAO) System kann eine erhebliche Vergrößerung des korrigierten Bereichs erreicht werden. Dieses System wird im statischen und dynamischen Betrieb charakterisiert, der Einfluß von nicht-konjugierten turbulenten Schichten und unterschiedlichen Helligkeiten der Leitstern, sowie die Auswirkungen von Ungenauigkeiten in der Justierung werden untersucht. Desweiteren werden Strategien für die Kalibration des Systems und die Verbesserung der erreichbare Korrektur mit Hilfe des Kalman Filters aufgezeigt.

Der zweite Teil der Arbeit konzentriert sich auf SCIDAR Messungen der atmosphärischen Turbulenzen über Mt. Graham. Dieser Datensatz ermöglicht zum ersten Mal eine statistische und tiefgehende Analyse der vertikalen Struktur der Turbulenzen über dem Ort des LBT. Basierend auf Messungen während 16 Nächten, verteilt über ein Jahr, scheint es, als sei Mt. Graham exzellent für astronomische Beobachtungen geeignet. Durch die Erweiterung eines analytischen Modells, das die Filterung der Turbulenzeffekte durch die Adaptive Optik beschreibt, können die Auswirkungen der atmosphärischne Turbulenz auf die erreichbare Abbildungsqualität von LINC-NIRVANA, insbesondere die optimale konjugierte Höhe der deformierbaren Spiegel bestimmt werden. Desweiteren wurde ein neue Methode entwickelt, zur Vermessung der atmosphärischen Turbulenz in den ersten Kilometern über dem Boden mit einer 40-fach höheren vertikalen Auflösung, verglichen mit SCIDAR in Standard-Konfiguration. Die theoretischen Konzepte dieser Methode, sowie erste Ergebnisse am Himmel werden gezeigt.

Contents

1 Introduction **1**

1.1 Optical Imaging through the Atmosphere 1

1.2 Why Adaptive Optics? 2

1.3 Goals of this work 3

2 Turbulence and Adaptive Optics **5**

2.1 Overview 5

2.2 Atmospheric Turbulence 5

2.2.1 Turbulence Models 6

2.2.2 Structure Function 7

2.2.3 Temporal Aspects 8

2.2.4 Effects on Astronomical Imaging 9

2.2.5 Scintillation 12

2.2.6 Zernike modes 13

2.3 SCIDAR Technique 17

2.3.1 SCIDAR principle 17

2.3.2 Theoretical Background 19

2.4 Adaptive Optics Technique 23

2.4.1 Wavefront Sensors 23

2.4.2 Deformable Mirrors 25

2.4.3 Wavefront Errors 26

2.5 Multi-Conjugate Adaptive Optics 30

2.5.1 Layer-Oriented MCAO 31

2.5.2 Star-Oriented MCAO 32

2.5.3 Ground-Layer Adaptive Optics 32

2.6 The LBT & LINC-NIRVANA 34

2.6.1 The LBT 34

2.6.2 LINC-NIRVANA 36

3 MCAO – Theoretical Considerations **39**
3.1 Introduction . . . 39
3.2 Filtering of C_N^2-profiles . . . 40
3.2.1 Layer-transfer functions . . . 40
3.2.2 Modal Covariance Matrix . . . 41
3.2.3 Total filter functions . . . 43
3.3 Optimal conjugation height . . . 45
3.3.1 Calculation principle . . . 45
3.3.2 Influence of AO Performance . . . 47
3.4 Off-axis MCAO performance estimation . . . 48
3.5 Conclusion . . . 50

4 Kalman Control Theory **51**
4.1 Introduction . . . 51
4.2 Calibration of AO Systems . . . 51
4.3 Least-Squares Reconstruction . . . 52
4.4 Condition number . . . 53
4.5 The Kalman Filter for Adaptive Optics Systems . . . 53
4.5.1 Theoretical Background . . . 54
4.5.2 The required atmospheric and system parameters . . . 56
4.6 The Kalman Filter with Vibrations . . . 57
4.6.1 Theoretical Background . . . 57
4.6.2 The required atmospheric and system parameters . . . 58
4.6.3 Numerical Verifications . . . 59
4.7 Conclusions . . . 59

5 Characterizing an MCAO prototype for LINC-NIRVANA **61**
5.1 Introduction . . . 61
5.2 System Description . . . 62
5.2.1 The Light Source . . . 62
5.2.2 MAPS . . . 62
5.2.3 The Telescope Simulator . . . 66
5.2.4 The Deformable Mirror . . . 68
5.2.5 Wavefront Sensor Unit . . . 69
5.2.6 CARMA – Control Software . . . 71
5.3 Calibration Issues . . . 72
5.3.1 Alignment accuracy . . . 72
5.3.2 Injection Matrix . . . 73
5.3.3 Linear range and optimal calibration amplitude . . . 74

5.4 Static Verification . . . 76
5.5 Dynamic Measurements . . . 81
5.6 Ground-Layer AO Measurements . . . 82
  5.6.1 Filtering of non-conjugated heights . . . 82
  5.6.2 Modal Covariance Matrix . . . 83
  5.6.3 Off-axis PSF structure . . . 85
  5.6.4 Different Brightness . . . 87
5.7 Kalman filter for AO . . . 88
  5.7.1 Kalman filter for classical AO . . . 88
  5.7.2 Kalman filter for GLAO . . . 88
  5.7.3 Kalman filter with vibrations . . . 90
5.8 Conclusion & Outlook . . . 91
  5.8.1 Calibration Issues . . . 92
  5.8.2 Ground-Layer AO . . . 92
  5.8.3 Kalman filter . . . 93
  5.8.4 Outlook . . . 93

6 Site-characterization for LINC-NIRVANA **95**
6.1 Introduction . . . 95
6.2 The VATT-SCIDAR . . . 96
  6.2.1 Description of the Instrument . . . 96
  6.2.2 The Vatican Advanced Technology Telescope . . . 97
6.3 The Data-Reduction Pipeline . . . 98
  6.3.1 Principle of Data-Reduction . . . 98
  6.3.2 Verification of the Pipeline . . . 101
6.4 Observing parameters . . . 104
6.5 Turbulence Profiles . . . 106
  6.5.1 Vertical Turbulence Structure . . . 106
  6.5.2 Contribution by the Ground-Layer . . . 107
  6.5.3 Average discretized C_N^2 profile . . . 108
  6.5.4 Wind Speed Profiles . . . 111
6.6 Astro-climatic Parameters . . . 111
  6.6.1 Dome-seeing . . . 112
  6.6.2 Seeing . . . 114
  6.6.3 Wavefront Coherence Time . . . 117
  6.6.4 Isoplanatic Angle . . . 119
  6.6.5 Isopistonic Angle . . . 119
  6.6.6 Temporal Correlations . . . 121
  6.6.7 Vertical Correlations . . . 122

6.6.8 Comparison to other sites 123
6.7 High-Resolution C_N^2 profiles 123
6.7.1 High vertical resolution method (HVR-GS) 125
6.7.2 HVR-GS on-sky validation 126
6.7.3 Results of HVR-GS and Discussion 127
6.8 Impact on LINC-NIRVANA MCAO Performance 130
6.8.1 Optimal conjugated heights of the DMs 130
6.8.2 Loop-frequency and number of modes 136
6.9 Conclusion & Outlook 139
6.9.1 Site-characterization 139
6.9.2 High-vertical resolution SCIDAR 140
6.9.3 Impact on LINC-NIRVANA 140
6.9.4 Outlook 141

A The C_N^2-Profiles **143**

B The Wind-Profiles **159**

C Acronyms **163**

D Bibliography **165**

CHAPTER 1

Introduction

Cuz I'm a 21st century digital boy,
I don't know how to live,
But I've got a lot of toys

Bad Religion, "21st century digital boy"

1.1 OPTICAL IMAGING THROUGH THE ATMOSPHERE

It's a frustrating fact that photons coming from an astronomical object are severely disturbed by turbulence in Earth's atmosphere in the last few kilometers on their way to the observer after an essentially undisturbed journey of up to several billion light-years. When observed with a telescope, the image of this object is not sharp, but rather it is dissociated into many small bright spots, so-called *speckles*. These speckles evolve rapidly, resulting in a smeared image with a typical diameter of 1 arcsec, as soon as the exposure time is longer than a few milli-seconds (fig. 1.1). The size of this so-called *seeing-disk* is the limit for the angular resolution, which can be achieved with a telescope from the ground. By contrast, without the atmosphere, the angular resolution of a telescope would be limited by diffraction and increases linearly with the diameter D_{tel} of the telescope. This means that without clever techniques, even the largest ground-based telescopes, with diameters of up to 10 m, cannot produce sharper images than those of a backyard astronomer's.

Besides the limited angular resolution, the signal-to-noise ratio of the images is also significantly lower than without the atmosphere, because the light is spread over a much larger area. In order to detect faint sources and to lift their signal above the noise of the detector or the background, much longer integration times are necessary in the presence of atmospheric turbulence. Without the atmosphere, the SNR of a point-source grows with D_{tel}^2, while in seeing-limited operation it grows only with D_{tel} (Hardy, 1998, chapter 2).

There are several options to overcome these limitations. The most rigorous is to build a satellite telescope and go to space. This also avoids the problem of limited transparency of the atmosphere, both temporal by clouds and in certain wavelength regions. The downside is that this approach is extremely laborious, expensive and hard to upgrade. Another method is to take many short-exposure images and perform a statistical analysis of the speckle pattern (Dainty, 1976, see chapter 7). For a binary star, the speckle pattern is very similar for both stars: the

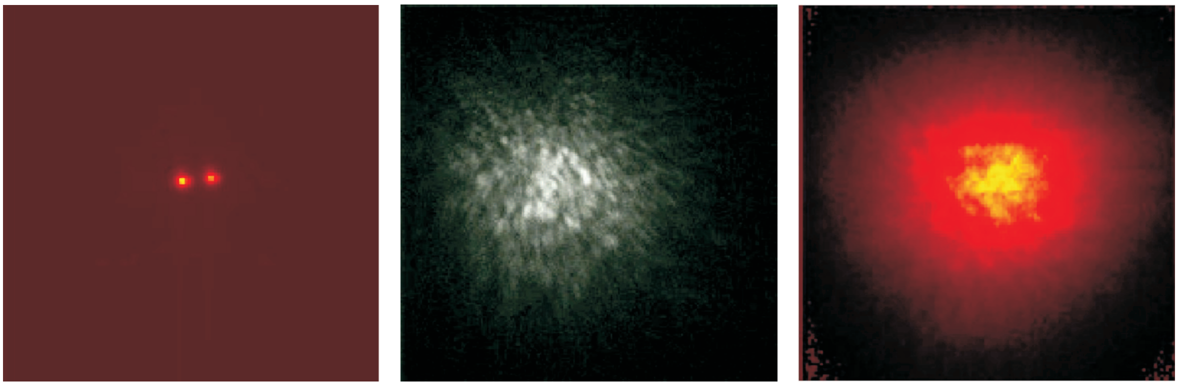

FIGURE 1.1: Illustrative comparison of the angular resolution of a telescope with a diffraction-limited image (**left**) and a short (**middle**) and long exposure image (**right**) in the presence of atmospheric turbulence. This turbulence significantly degrades the image and limits the achievable angular resolution to ≈1 arcsec. The two components of a close binary, as in this example, can thus no longer be studied individually. (D. Watson, University of Rochester)

two patterns are only slightly shifted with respect to each other in the image. By calculating the auto-correlation and thus looking for similar patterns in the image, the characteristics of the binary can be retrieved. However, since it is very difficult to obtain images with this technique, called speckle-interferometry, it is limited to only a few scientific applications. Another method is to take many images with short exposure times and select only the "sharpest" few percent. When combining only these few images, diffraction-limited resolution and a significantly increased SNR can be achieved (Tubbs, 2003; Law et al., 2006). Unfortunately, this lucky-imaging method is limited to rather small telescopes up to ≈2 m and wavelengths longer than ≈0.8 μm and has only very low efficiency.

A somewhat different approach is to correct the induced distortions of the light before imaging it with a detector. The idea of Adaptive Optics (AO) is to use a guide star to measure the distortions of the star-light with a wavefront sensor (WFS) and to compensate them with a Deformable Mirror (DM). This has to be done in real-time, and the shape of the DM has to be adjusted several hundred times per second to follow the rapid evolution of the atmosphere. In the case that a suitable guide star is located close to the interesting science-object, AO systems can currently deliver nearly diffraction-limited images at large optical telescopes for wavelengths longer than ≈1 μm at a very high observing efficiency.

1.2 WHY ADAPTIVE OPTICS?

The idea of Adaptive Optics was first proposed in the 1950s by Babcock, but it was not until the early 1990s that technology was advanced enough to actually build an AO system for astronomy. Since then, rapid progress has been accomplished in this field, making it a mature and established technique today. Currently, there is an AO system in operation at almost every telescope larger than 4 m. By rivaling the angular resolution and sensitivity of space-based telescopes in the near infrared, AO systems affect almost every aspect of observational astrophysics, like the research on the center of the milky way (Genzel et al., 2005) and nearby galaxies

(Haering-Neumayer et al., 2006), star formation and stellar disks (Menard, 2005), exo-planets (Neuhaeuser et al., 2005), solar system objects like Titan (Hartung et al., 2004), and even observations of the solar surface (Keller, 2005). All of these would have been impossible from the ground without AO.

All currently operational AO systems are classical ones, which means that they use one single guide star to measure the distortions of the light. A major problem of these systems is that the science object has to be very close to the guide star, because the correction performance drops rapidly with angular separation. Since the number of suitable guide stars is limited, only a tiny fraction of the complete sky can be observed with classical AO systems. To overcome these limitations, a number of new concepts have been proposed and are currently being implemented.

One method is to create an artificial guide star close to the science object by projecting a powerful laser onto the sky (Foy and Labeyrie, 1985). But even for this technique, a natural guide star is required, which, however, can be fainter and farther away from the science object. Furthermore, since lasers with the specific wavelength and required power are expensive and difficult to operate, such systems are currently in routine operation only at two observatories.

Another method to increase the area of useful correction is Multi-Conjugated Adaptive Optics (MCAO), as proposed by Beckers (1988) and Rigaut et al. (2000). Such systems use multiple guide stars to measure the distortions induced by the individual turbulent atmospheric layers. By placing multiple DMs optically to the same altitude as these layers, the distortions induced by entire layers can be corrected, and not only in the direction of the single guide stars. The performance is not as good as for a classical AO system on-axis, but the diameter of the area with useful correction can be increased by a factor of up to 10. Similarly, the observable fraction of the sky can be increased to almost 100%. MCAO systems are currently under development for a number of observatories, such as the VLT (Marchetti et al., 2006), the LBT (Gaessler et al., 2005) and Gemini South (Ellerbroek et al., 2003).

In a slightly different direction, eXtreme AO (XAO) systems are under development. These systems are designed to achieve the highest possible performance on-axis within a rather small field-of-view (FoV) (Fusco et al., 2006). For example, the direct imaging of exo-planets near a bright star is only possible for performance very close to the diffraction limit, and is only required in a very small FoV around the star.

The development of hardware components for AO systems of future giant telescopes with diameters of between 30 and 100 m is another active field of research. This involves both new concepts for WFS (e.g. Kellner, 2005), but also the design of new types of DMs, such as deformable secondary mirrors (e.g. Riccardi et al., 2004) or micro-DMs (MOEMS) (e.g. Morzinski et al., 2006).

1.3 GOALS OF THIS WORK

This thesis consists of two major parts and was conducted within the framework of LINC-NIRVANA, which is a Fizeau Interferometer for the Large Binocular Telescope (LBT). One part is the characterization of the vertical structure of the atmospheric turbulence above Mt. Graham, the site of the LBT. From this study, performance expectations for the Adaptive Optics system and all the instruments at the LBT can be derived, since this crucially depends on the strength and vertical distribution of the atmospheric turbulence. Concerning especially LINC-NIRVANA, this study will moreover help to optimize the opto-mechanical design, the operational modes and the control architecture of the MCAO system.

The second part focuses on dynamically testing a layer-oriented Ground-Layer AO system with optical co-addition in the lab, which serves as a prototype for the MCAO system of LINC-NIRVANA. With such a lab experiment, the design concepts can be verified, and the actual performance can be compared to numerical simulations. Furthermore, experience with the alignment, calibration and operation of an AO system with multiple guide-stars can be aquired and the performance of novel control algorithms can be experimentally evaluated.

This chapter has provided a general introduction to the problem, chapter 2 presents a more quantitative introduction of the concepts and equations of Adaptive Optics. This includes an overview of atmospheric turbulence and its impact on the achievable image quality for ground-based astronomical telescopes, techniques to measure the vertical turbulence structure, and concepts and devices for Adaptive Optics. Chapter 2 will conclude with a brief summary of the LBT and the LINC-NIRVANA instrument.

Chapter 3 will give some more theoretical background on the connection between the vertical turbulence profiles and the correction by an MCAO system. An extension of a semi-analytical model is presented on how to estimate the performance of an MCAO system for a given turbulence profile, and to determine the optimal conjugation height of the DMs for different criteria.

An overview of calibration concepts and control algorithms of AO systems is presented in chapter 4. The theory of the Kalman filter is shown by a summary of the literature, along with the modifications required to adapt it to the MCAO system of LINC-NIRVANA.

Chapters 5 and 6 form the core of this thesis, presenting the main results acquired. In chapter 5 the tests of the laboratory setup of a Ground-Layer Adaptive Optics (GLAO) system are shown and chapter 6 presents the results of Generalized SCIDAR measurements of the vertical structure of the atmospheric turbulence above Mt. Graham. Also included in chapter 6 is the description and first results obtained with the new High Vertical Resolution Generalized SCIDAR (HVR-GS) technique. Finally, plots of all the measured turbulence profiles appear in appendix A.

CHAPTER 2

Turbulence and Adaptive Optics

Coz it's easy once you know how it's done,
you can't stop now, it's already begun,
you feel it running through your bones

Caesars, "Jerk it out"

2.1 OVERVIEW

This chapter provides a more detailed and quantitative introduction to the concepts of Adaptive Optics. This starts with a statistical description of the induced distortions of the light by atmospheric turbulence, techniques to measure the related parameters and the basics of Adaptive Optics. An overview of the LBT and the LINC-NIRVANA instrument will conclude this chapter.

2.2 ATMOSPHERIC TURBULENCE

The wavelength λ_n of light in a medium with refractive index n is $\lambda_n = \lambda_0/n$, for a given wavelength in vacuum λ_0. Since the refractive index of air, n_{air}, itself depends on the temperature T and the pressure P via (Cox, 2000)

$$n_{\mathrm{air}}(P\,[\mathrm{mbar}],\, T\,[\mathrm{K}],\, \lambda_0\,[\mu\mathrm{m}]) \;=\; 1 \;+\; 7.76\cdot 10^{-5}\left(1 \;+\; 7.52\cdot 10^{-3}\,\frac{1}{\lambda^2}\right)\cdot\frac{P}{T}\,, \qquad (2.1)$$

the wavelength and thus also the number of waves fitting into a certain propagation length depends on n_{air}. After having travelled through an inhomogeneous medium with varying n, the individual phases of parallel light rays are thus shifted with respect to each other. A common concept to describe this effect is the wavefront, which is the imaginary plane of the same phase for parallel light rays. This plane is initially flat for the light coming from the star, but gets distorted due to variations of n in the atmosphere.

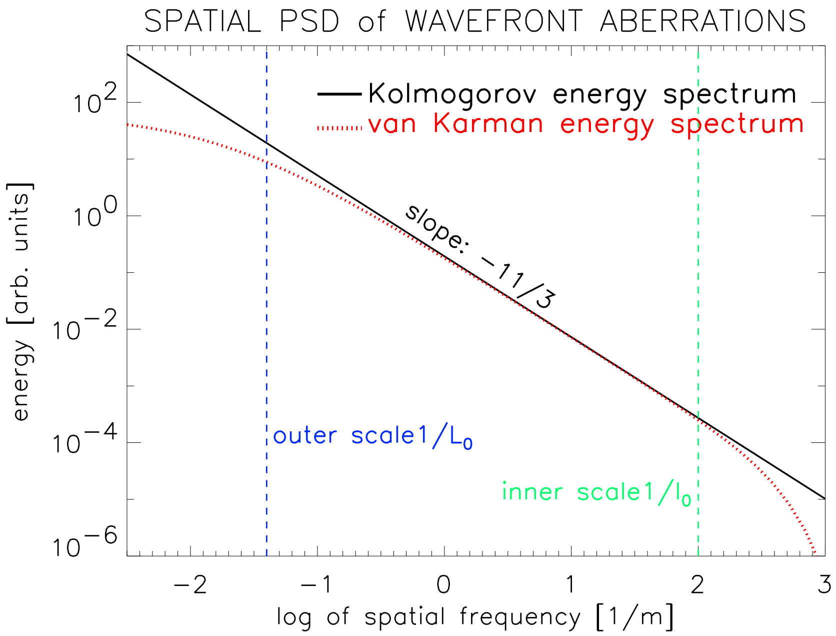

FIGURE 2.1: The power-spectral density (PSD) of the wavefront aberrations for the Kolmogorov and von Karman turbulence model. The typical size of the inner (1 cm) and the outer scale (25 m) are indicated by the two vertical, dashed lines.

2.2.1 TURBULENCE MODELS

A statistical model of the wavefront aberrations induced by the turbulent atmosphere was proposed by Kolmogorov (Tatarski, 1961). This model is based on the idea that energy is fed into the system at large scales and propagates down to smaller structures, where it eventually dissipates into heat.

To describe the statistics of the wavefront aberrations, the power-spectral density (PSD) $\Psi(\kappa)$ is defined. This is a measure of the relative contribution of aberrations with spatial frequency κ to the total wavefront distortion. For the Kolmogorov model, it is given by (Noll, 1976):

$$\Psi(\kappa) \;=\; 0.033\, C_N^2\, \kappa^{-11/3}\;. \tag{2.2}$$

The scaling to different atmospheric conditions is accomplished with the refractive index structure function C_N^2. However, the Kolmogorov model is only useful between the largest (the outer scale L_0), and the smallest structures (the inner scale l_0) of the turbulence. For a better description of this truncation, usually the von Karman model is used:

$$\Psi(\boldsymbol{\kappa}) \;=\; \left(\kappa^2+\kappa_0^2\right)^{-11/6} \exp\left[-\frac{\kappa^2}{\kappa_i^2}\right] C_N^2\;, \tag{2.3}$$

with $\kappa_0 = 2\pi/L_0$ and $\kappa_i = 5.92/l_0$. The power spectral densities $\Psi(\boldsymbol{\kappa})$ for both models are shown in figure 2.1.

At the ground, l_0 is typically less than 10 mm (Livingston, 1972; Eaton and Nastrom, 1998), whereas L_0 is of the order of a few tens of meters (Conan et al., 2002). The outer scale L_0 limits the contribution of low spatial frequencies to the wavefront aberrations. Since these spatial frequencies dominate the overall wavefront distortions, L_0 has a significant influence on the achievable performance and image

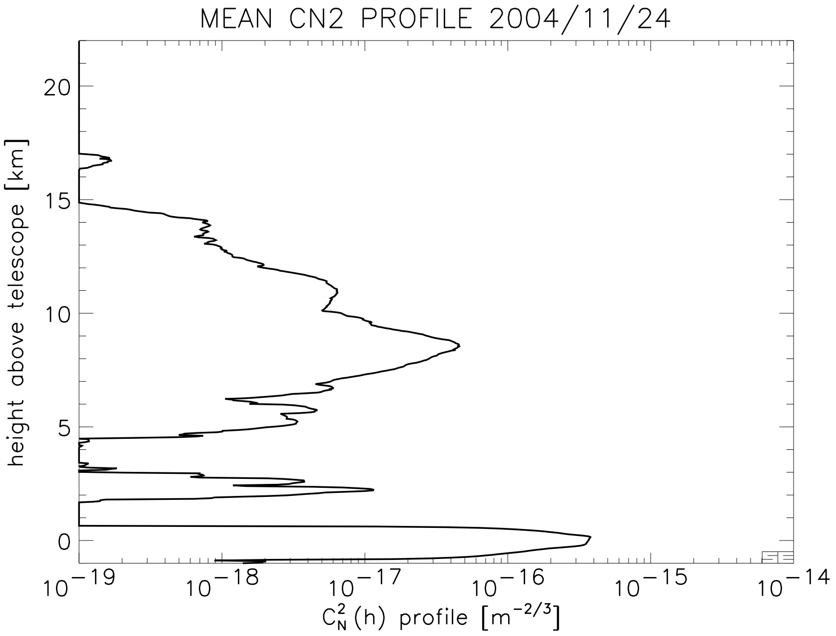

FIGURE 2.2: A typical $C_N^2(h)$ profile measured with a SCIDAR instrument at Mt. Graham (see chapter 6 for details). Usually $C_N^2(h)$ is plotted with the height h above the telescope along the y-axis, and the strength of the turbulence along the x-axis in logarithmic scale. In this specific case, there is a very strong layer just above the ground, a weaker layer at ≈3 and a weak, but vertically extended layer at ≈9 km above the telescope (6 and 12 km above sea-level).

quality of future giant telescope (ELTs) or ground-based interferometers (Quirrenbach, 2006).

2.2.2 STRUCTURE FUNCTION

Another way to describe the phase statistics of an incident wavefront $\Phi(\mathbf{r})$ at the ground is the phase structure function $D_\Phi(\mathbf{r})$. For the Kolmogorov turbulence model, $D_\Phi(\mathbf{r})$ is given by (e.g. Hardy, 1998)

$$D_\Phi(\mathbf{r}) = \left\langle \left| \Phi(\mathbf{r}') - \Phi(\mathbf{r}' + \mathbf{r}) \right|^2 \right\rangle \Big|_{\mathbf{r}'} \tag{2.4a}$$

$$= 2.91 \left(\frac{2\pi}{\lambda} \right)^2 \sec\zeta \; r^{5/3} \int_0^\infty C_N^2(h)\, dh \; , \tag{2.4b}$$

which includes all wavefront aberrations induced in the total atmosphere above the ground and depends on the zenith angle ζ. To describe the vertical distribution of the atmospheric turbulence strength, the vertical profile of the refractive index structure function $C_N^2(h)$ is used. This function is defined as the variance of the index of refraction n as a function of the distance $\mathbf{r}$ (Hardy, 1998)

$$C_N^2(h) \cdot \mathbf{r}^{2/3} = \left\langle \left| n(h, \mathbf{r}') - n(h, \mathbf{r}' + \mathbf{r}) \right|^2 \right\rangle \Big|_{\mathbf{r}'} \; . \tag{2.5}$$

A typical C_N^2-profile is plotted in figure 2.2. Usually, there is a strong layer at the ground where the interaction of the wind with the local surface structure creates turbulent mixing of air with different temperatures. This results in variations of the index of refraction and thus in significant wavefront distortions. Another strong layer is usually located at the height of the jet-stream at ≈10 to 15 km above sea-level. The very high wind-speeds in this layer again cause rapidly evolving optically active turbulence.

2.2.3 TEMPORAL ASPECTS

Of course, the wavefront distortions not only change in space, but also in time.

TEMPORAL STRUCTURE FUNCTION

Similar to equation 2.4 above, a temporal structure function $D_\Phi(\delta t)$ can be defined:

$$D_\Phi(\delta t) \;=\; \left\langle |\Phi(\mathbf{r},\,t) \,-\, \Phi(\mathbf{r},\,t+\delta t)|^2 \right\rangle\Big|_{t,\,\mathbf{r}} \;. \tag{2.6}$$

Under the simplifying assumption that the wavefront aberrations are fixed, and only the layer is moving with the wind speed $\mathbf{v}$ over the telescope, the temporal structure function depends in this *frozen-flow* model essentially on the wind-speed $\mathbf{v}(h)$ (Conan et al., 1995) and the spatial frequency κ:

$$D_\Phi(\mathbf{v},\,\kappa) \;\propto\; \int_0^\infty \frac{1}{\mathbf{v}(h)} \left(\frac{\kappa}{\mathbf{v}(h)}\right)^{-8/3} C_N^2(h)\,dh \tag{2.7}$$

GREENWOOD FREQUENCY AND WAVEFRONT COHERENCE TIME

To describe the characteristic time-scales for the changes in the wavefront aberrations, the wavefront coherence time τ_0 is defined. It describes the time, after which the variance of the change in the wavefront amounts to 1 rad^2.

$$\tau_0 \;=\; 0.057\,\lambda^{6/5} \left(\sec\zeta \int C_N^2(h)\cdot v_W(h)^{5/3}\,dh\right)^{-3/5} \;. \tag{2.8}$$

For good astronomical sites, τ_0 is of the order of a few milli-seconds at visible wavelengths (λ =0.5 μm).

Usually the inverse of τ_0, the Greenwood-frequency f_G (Greenwood, 1977) is used in the context of AO systems, because f_G is a measure of the bandwidth needed for an AO control system to compensate the wavefront distortions effectively. For a wind-speed profile $v_W(h)$ and the Kolmogorov model, f_G is given by (Hardy, 1998):

$$f_G \;=\; \left[0.102\left(\frac{2\pi}{\lambda}\right)^2 \sec\zeta \int C_N^2(h)\cdot v_W(h)^{5/3}\,dh\right]^{3/5} \;. \tag{2.9}$$

Typical values for f_G in the visible are a few hundred Hertz.

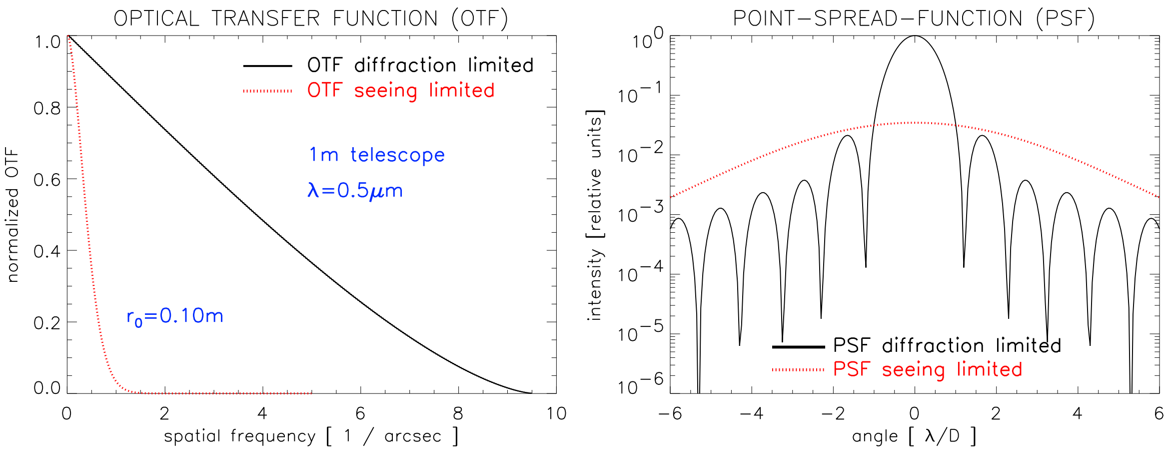

FIGURE 2.3: The optical transfer function (OTF) (**left**) and the point-spread function (PSF) (**right**) for diffraction-limited imaging (solid line) and atmospheric turbulence degraded imaging (dotted line). High spatial frequencies are completely suppressed in the later case, resulting in an “unsharp” image. This can also be seen in the PSF, which shows that the light is spread over a much larger area in the turbulence degraded image and thus smearing any fine details. The curves for the diffraction-limited case are evaluated for a circular aperture with no central obstruction and D_{tel}/r_0 =10.

2.2.4 EFFECTS ON ASTRONOMICAL IMAGING

Naturally, the question arises of what happens to the image of the science object, when such a distorted wavefront is imaged with a telescope.

OTF AND PSF

Two good measures to describe the image quality of an optical system are the Optical-Transfer-Function (OTF) and the Point-Spread-Function (PSF). The OTF describes how effectively spatial frequencies in the object space are transfered to the image space through the optical system, while the PSF is the resulting image of a point-source. The image of an arbitrary object can then be determined from a convolution of the projected object with the PSF of the optical system.

The perfect PSF is defined as the absolute value of the Fourier-transform of the aperture function $\Theta(\mathbf{r})$, with possible wavefront aberrations $A(\mathbf{r})$ being included as a complex weighting function:

$$\mathbf{PSF}(\mathbf{r}) = \left|\mathbf{FT}\left\{\Theta(\mathbf{r}) \cdot \exp[2\pi i\, A(\mathbf{r})]\right\}\right|^2 . \tag{2.10}$$

For a circular aperture with no central obstruction, $\Theta(\mathbf{r})$ is given by:

$$\Theta(\mathbf{r}) = \begin{cases} 1 & \text{for} \quad |r| \leq 1 \\ 0 & \text{else} \end{cases} . \tag{2.11}$$

The OTF is related to the PSF via

$$\mathbf{OTF}(\boldsymbol{\kappa}) \overset{\mathbf{FT}}{\Longleftrightarrow} \mathbf{PSF}(\mathbf{r}) . \tag{2.12}$$

The PSF and OTF are plotted in figure 2.3 for a perfect optical system with circular aperture and for one limited by the atmospheric turbulence.

SEEING AND FRIED PARAMETER

A resolution criterion for optical systems can be derived using the PSF. According to Rayleigh, two sources of equal brightness can still be separated, if the maximum of the first PSF coincides with the first minimum of the second one. For circular apertures with no central obstruction, this minimum angular separation α_{res} is given by

$$\alpha_{\mathrm{res}} = 1.22\,\frac{\lambda}{D_{\mathrm{tel}}}\,. \tag{2.13}$$

From this equation, it is apparent that the radius of the central peak of the PSF, also called Airy-disk, decreases with the diameter D_{tel} of the telescope and increases with the observing wavelength λ.

In the seeing-limited case, the time-average (long-exposure) OTF is given by

$$\mathbf{OTF}(f) = \mathbf{exp}\left[-\frac{1}{2}D_{\Phi}(\lambda\cdot\kappa_{\alpha})\right]\,, \tag{2.14}$$

with the angular spatial frequency κ_{α} and the phase-structure function $D_{\Phi}(\mathbf{r})$ as defined in equation 2.4. Transforming this equation into the space domain and calculating the FWHM of the corresponding PSF, gives the size ϵ_{FWHM} of the seeing-disk and thus the achievable angular resolution for turbulence degraded imaging (Fried, 1965). With the zenith angle ζ and the observing wavelength λ, ϵ_{FWHM} can be determined via

$$\epsilon_{\mathrm{FWHM}} = \left[0.409\cdot\frac{(2\pi)^2}{\lambda^{1/3}}\sec\zeta\int C_N^2(h)\,dh\right]^{3/5}\,. \tag{2.15}$$

For good astronomical sites, ϵ_{FWHM} in the visible is $\approx$0.7 arcsec (chapter 6). Even for moderate size telescopes, the angular resolution is therefore dramatically worse in the seeing-limited case.

The seeing is a positive random variable and it was shown at various sites to obey the log-normal distribution $f_{\text{log-n}}(x)$ (e.g. Vernin and Munoz-Tunon, 1998; Tokovinin and Travouillon, 2006; Subaru Telescope, 2006; Sarazin, 2006):

$$f_{\text{log-n}}(x) = A\,\exp\left[-\frac{(\log x - x_0)^2}{2\sigma^2}\right]\,. \tag{2.16}$$

In this equation, A is a simple scaling parameter, x_0 is the mean value of the distribution, and σ is the width of the distribution.

To describe the characteristic spatial extent of the wavefront aberrations, the Fried Parameter r_0 can be used, which can be calculated via (Fried, 1965)

$$r_0 = \left[0.423\,\left(\frac{2\pi}{\lambda}\right)^2\sec\zeta\int C_N^2(h)\,dh\right]^{-3/5}\,. \tag{2.17}$$

With this definition, r_0 is roughly the diameter of an area within which the variance σ_{wf}^2 of the wavefront aberrations is 1 rad^2 (Noll, 1976):

$$\sigma_{\mathrm{wf}}^2 = 1.030\,\left(\frac{D}{r_0}\right)^{5/3}\,. \tag{2.18}$$

Typical values for r_0 are 0.1 m in the visible and 0.6 m in the K-band. For an 8 m telescope, the typical rms σ_{wf} of the wavefront aberrations is thus $\sigma_{\mathrm{wf}} \approx 3.0\,\mu$m.

Using equations 2.15 and 2.17, a relation between the seeing ϵ_{FWHM} and the Fried Parameter r_0 can be found:

$$\epsilon_{\text{FWHM}} = 0.98\,\frac{\lambda}{r_0}\ . \tag{2.19}$$

STREHL RATIO

Another measure of the image quality of an optical system is the Strehl ratio SR. It describes which fraction of the light is concentrated in the diffraction-limited core and which fraction is spread into the seeing-limited halo. For higher SR, the light is concentrated more into the core, resulting in “sharper” images. The Strehl ratio is defined (Strehl, 1902) as the ratio of the observed PSF peak-intensity I_{obs} divided by the theoretical maximum intensity of the diffraction-limited PSF I_{diff}:

$$SR = \frac{\max\left(I_{\text{obs}}\right)}{\max\left(I_{\text{diff}}\right)}\ . \tag{2.20}$$

If the wavefront aberrations are not exactly known, but the overall wavefront variance σ_p^2 is smaller than $\approx 2\,\text{rad}^2$ (thus Strehl ratio being higher than $\approx$15%), the Strehl ratio can be approximated by (Marechal, Born et al., 1999)

$$SR \approx e^{-\sigma_p^2}\ . \tag{2.21}$$

In the K-band (λ =2.0 - 2.4 μm), the Strehl ratio of astronomical images is typically less than one percent under seeing-limited conditions and can be increased up to $\approx$70% with the use of an Adaptive Optics system.

TEMPORAL CORRELATION

To describe the typical time-scales of the temporal evolution for the seeing ϵ_{FWHM} or the wavefront coherence time τ_0, two methods are generally used. These timescales do not describe the change of the wavefront itself (that timescale is τ_0) but of its statistical properties and therefore the change of the long-exposure image quality.

The first method is the temporal auto-correlation $\mathbf{TA}[f(t)](\Delta t)$ (Racine, 1996; Munoz-Tunon et al., 1997; Tokovinin et al., 2003; Avila et al., 2004). For a given function $f(t)$ and a temporal separation Δt, $\mathbf{TA}[f(t)](\Delta t)$ it is defined as:

$$\mathbf{TA}[f(t)](\Delta t) = \frac{\left\langle \Big(f(t) - \langle f(t)\rangle\Big)\cdot\Big(f(t+\Delta t) - \langle f(t)\rangle\Big)\right\rangle_t}{\left\langle \left|f(t) - \langle f(t)\rangle\right|^2\right\rangle_t}\ . \tag{2.22}$$

The average temporal auto-correlation $\langle\mathbf{TA}[f(t)]\rangle(\Delta t)$ for N_s sequences $f_i(t)$ of respective lengths N_i is given by

$$\langle\mathbf{TA}[f(t)]\rangle(\Delta t) = \frac{\sum_i \mathbf{TA}[f_i(t)](\Delta t)\cdot N_i}{N_s\cdot\sum_i N_i}\ . \tag{2.23}$$

From equation 2.22 it follows that $\mathbf{TA}[f(t)](0) = 1.0$. For large temporal separations Δt, the values for a random variable $f(t)$ are uncorrelated, which means

$$\lim_{\Delta t\to\infty}\mathbf{TA}[f(t)](\Delta t) = 0.0\ . \tag{2.24}$$

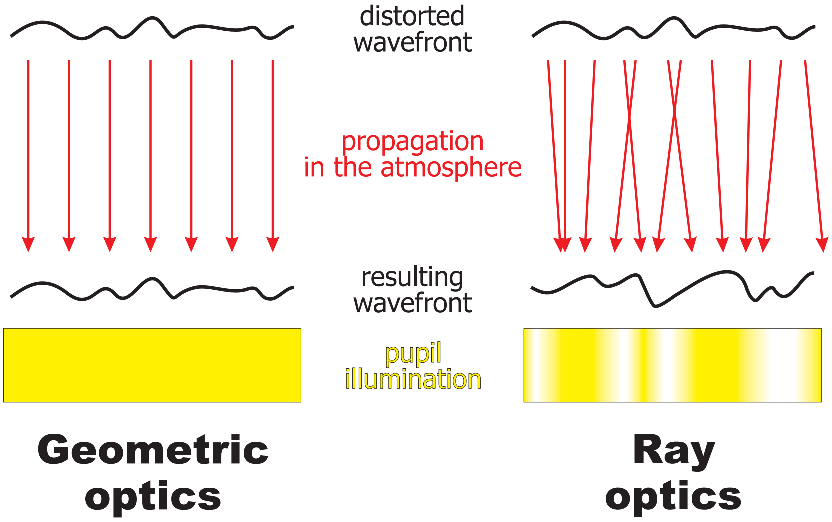

FIGURE 2.4: A sketch to illustrate the concept of geometric optics and the origin of scintillation with ray optics.

Another way to describe the correlation of two values of a function $f(t)$ separated by an interval Δt, is the normalized structure function $\mathbf{SF}[f(t)](\Delta t)$, defined as

$$\mathbf{SF}[f(t)](\Delta t) \;=\; \frac{\left\langle \left| f(t) - f(t+\Delta t) \right|^2 \right\rangle_t}{\left\langle \left| f(t) - \langle f(t) \rangle \right|^2 \right\rangle_t} \,. \tag{2.25}$$

For N_s sequences $f_i(t)$ of respective lengths N_i, the average normalized structure function $\langle \mathbf{SF}[f(t)] \rangle(\Delta t)$ is given by

$$\langle \mathbf{SF}[f(t)] \rangle(\Delta t) \;=\; \frac{\sum_i \mathbf{SF}_i[f_i(t)](\Delta t) \cdot N_i}{N_s \cdot \sum_i N_i} \,. \tag{2.26}$$

From equation 2.25 it can be seen that $\mathbf{SF}[f(t)](0) \;=\; 0.0$ and since the structure function $\mathbf{SF}(\Delta t)$ is normalized to the variance, the limit for large Δt is given for a random variable $f(t)$ by

$$\lim_{\Delta t \to \infty} \mathbf{SF}[f(t)](\Delta t) \;=\; 1.0 \,. \tag{2.27}$$

The typical time-scale τ_{TA} and τ_{SF}, are usually defined as the time for which the temporal auto-correlation $\mathbf{TA}(\Delta t)$ has dropped to 0.5, or the normalized temporal structure function $\mathbf{SF}(\Delta t)$ has reached 0.5.

2.2.5 SCINTILLATION

In Adaptive Optics, the geometrical approximation is usually used for the propagation of light. In this case, it is assumed that the distortion of the wavefront remains exactly the same all along the propagation path (see fig. 2.4, left). To find the valid range for this approximation, we assume a tilt of 1 rad of the wavefront over one turbulence cell (with a diameter of the Fried Parameter r_0). For $r_0 = 10$ cm and $\lambda = 0.5\,\mu$m, the deflection angle of the rays is then ≈ 1 arcsec (fig. 2.4, right).

The geometric optics approach can be used as long as the deflected light rays from the single turbulent cells do not overlap on the ground. This is fullfilled when the height h of the turbulent layer is less than the critical height h_{crit} (Hardy, 1998)

$$h_{\mathrm{crit}} = \frac{r_0^2}{\lambda} . \tag{2.28}$$

Under good seeing conditions, h_{crit} is ≈20 km in the visible ($\lambda = 0.5\,\mu$m). The turbulence above this altitude is usually negligible (chapter 6), justifying the usage of the geometric approximation for AO.

Since most of the turbulence is in the first few kilometers, the deflection of the individual rays is of the order of a few centimeters on the ground (see also fig. 2.9). The resulting intensity variations caused by scintillation are thus averaged out by the collecting area of large telescopes (two orders of magnitude larger than the scintillation pattern) and are therefore usually negligible for imaging purposes at modern astronomical telescopes. However, for smaller apertures, like the human eye, scintillation plays an important role and causes for example the twinkling of stars apparent to naked eye observes. A nice, concise summary of scintillation can be found in the three articles by Dravins et al. (1997a,b, 1998).

2.2.6 ZERNIKE MODES

In principle, there are two ways to describe an instantaneous distorted wavefront in the spatial domain. The first is to define a regular grid over the telescope pupil and describe the distorted wavefront as deviations from the mean value at these discrete points. This method is called the zonal approach and is described by e.g. Fried (1977); Hunt (1979); Southwell (1980).

However and especially for AO systems, the so-called modal approach is usually used (Southwell, 1980; Herrmann, 1981; Roggemann, 1992). In this case, the wavefront $W(x, y)$ is described as a superposition of suitable basis functions $Z_i(x, y)$, weighted with coefficients c_i:

$$W(x, y) = \sum c_i \cdot Z_i(x, y) \tag{2.29}$$

The modal approach has some advantages for practical implementation. It is superior in terms of error propagation (Wang and Markey, 1978; Southwell, 1980; Roggemann, 1992; Dai, 1996, 1995) and it is computationally easier and faster. Since the wavefront aberrations caused by the atmosphere are concentrated in the low spatial frequencies (fig. 2.1), good performance can already be achieved when correcting only a few modes. Furthermore, the mapping of the subapertures of the WFS to the actuators of the DM is not critical and their number does not have to be equal. With the modal approach it is thus possible to adapt the number of subapertures and corrected modes to the SNR to achieve optimal performance.

In order to efficiently describe the wavefront aberrations, it is essential to choose appropriate basis functions for the modal approach. For the description of the atmospheric turbulence, the Zernike functions are usually used. They are easy to handle and similar to the aberrations encountered in optical engineering.

MATHEMATICAL DESCRIPTION

In cylindrical coordinates (ρ, ϑ) on the unit circle, the Zernike functions $Z_i(\rho, \vartheta)$ are defined as (Noll, 1976):

$$\begin{aligned} Z_{i_{\text{even}}}(\rho, \vartheta) &= \sqrt{j+1}\, R_j^m(\rho)\, \sqrt{2}\cos(m\vartheta) && \text{for} \quad m \neq 0 \\ Z_{i_{\text{odd}}}(\rho, \vartheta) &= \sqrt{j+1}\, R_j^m(\rho)\, \sqrt{2}\sin(m\vartheta) && \text{for} \quad m \neq 0 \;, \\ Z_i(\rho, \vartheta) &= \sqrt{j+1}\, R_j^0(\rho) && \text{for} \quad m = 0 \end{aligned} \tag{2.30}$$

with the common function $R_n^m(\rho)$:

$$R_j^m(\rho) = \sum_{s=0}^{\frac{j-m}{2}} \frac{(-1)^s\,(j-s)!}{s!\cdot\left(\frac{j+m}{2}-s\right)!\,\left(\frac{j-m}{2}-s\right)!}\,\rho^{j-2s}\;. \tag{2.31}$$

The values of the radial j and the azimuthal order m must satisfy the conditions $m \leq j$ and $j - m =$ even. This means that there are $j+1$ modes with radial order j and a total number of n

$$n = \frac{(j+1)\cdot(j+2)}{2} \tag{2.32}$$

modes (including piston) with a radial order of up to j. A surface plot of the first 36 Zernike modes appears in figure 2.5.

MODAL COVARIANCE MATRIX

The Zernike modes are orthonormal on the unit circle:

$$\int\limits_{|\mathbf{r}|<1} \Theta(\mathbf{r})\; Z_i(\mathbf{r})\cdot Z_j(\mathbf{r}) = \delta_{ij}\;, \tag{2.33}$$

with δ_{ij} being the Kronecker-Delta, and the aperture function $\Theta(\mathbf{r})$ as defined in equation 2.11. With this normalization, the variance σ_Φ^2 of the wavefront is given as the sum of the square of the modal coefficients c_i:

$$\sigma_\Phi^2 = \sum_{i=0}^{\infty} c_i^2\;. \tag{2.34}$$

The average (temporal or spatial) of the modal coefficients c_i^2 is the modal covariance matrix $\mathbf{C}_\Phi$. For Zernike modes and the Kolmogorov model, $\mathbf{C}_\Phi$ can be calculated for the radial order n and azimuthal order m via (Noll, 1976):

$$\begin{aligned} \mathbf{C}_{\Phi,j,j'} = &\frac{0.046}{\pi^2}\left(\frac{D}{2r_0}\right)^{5/3} \\ &\times\sqrt{(n+1)(n'+1)}\;(-1)^{(n+n'-2n)/2}\,\delta_{m,m'} \\ &\times\int k^{-8/3}\,\frac{J_{n+1}(2\pi\,k)\,J_{n'+1}(2\pi\,k)}{k^2}\,d\mathbf{k}\;. \end{aligned} \tag{2.35}$$

$\mathbf{C}_\Phi$ is given for the first few modes in table 2.2.6. For an optimal description of the wavefront aberrations under given atmospheric turbulence statistics, $\mathbf{C}_\Phi$ has to be

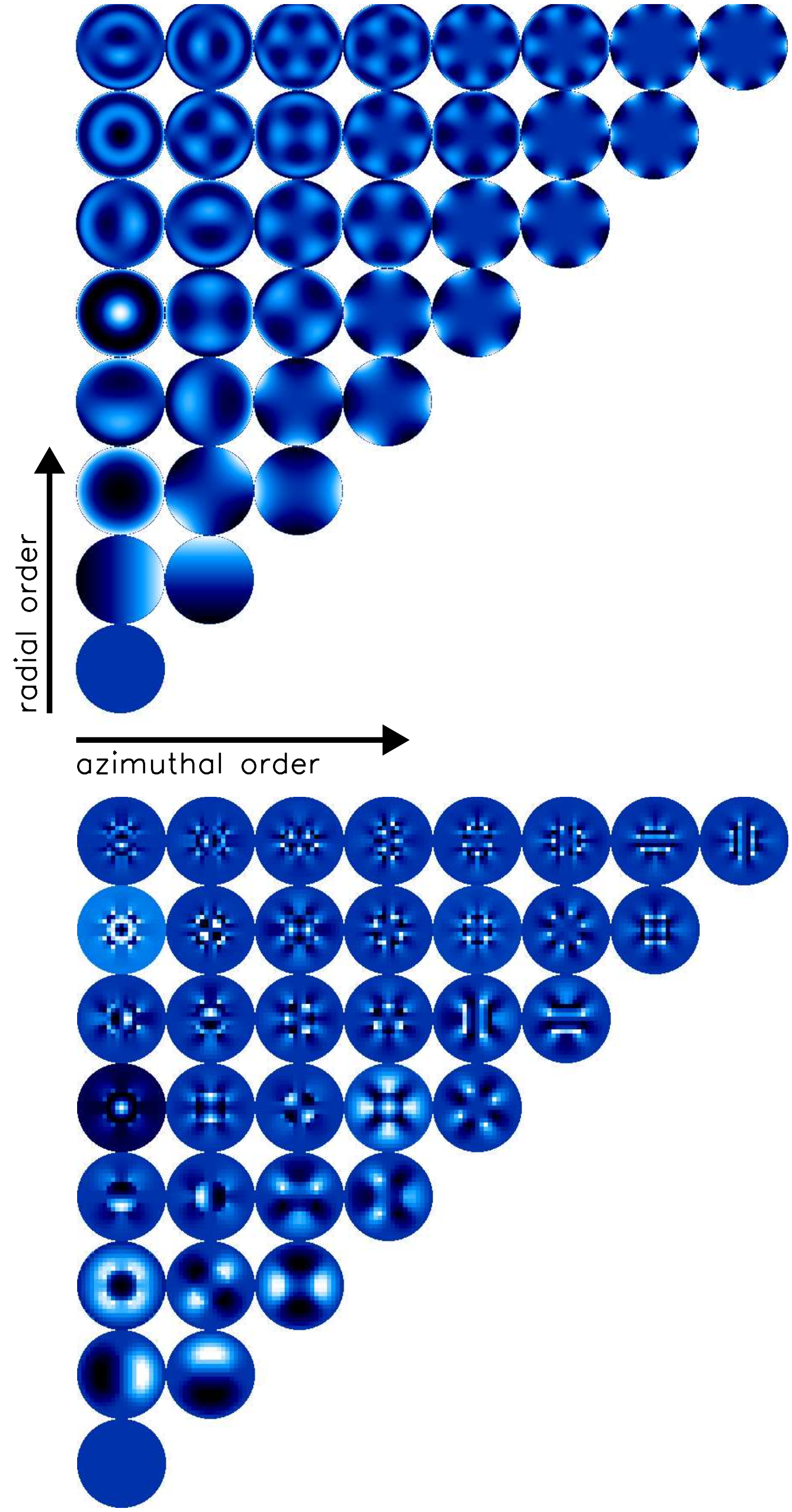

Figure 2.5: Surface plots of theoretical (**top**) and oversized (**bottom**) Zernike modes. The radial order j goes from bottom to top, the azimuthal order m from left to right. The oversized modes are for the actual used actuators of the DM of LINC-NIRVANA, used in the MANU-CHAO setup (see section 5.3.2 for more details).

$$
\mathbf{C}_{\Phi} = \begin{pmatrix}
0.4482 & 0 & 0 & 0 & 0 & 0 & -0.0141 & 0 & 0 & 0 & 0 \\
0 & 0.4482 & 0 & 0 & 0 & -0.0141 & 0 & 0 & 0 & 0 & 0 \\
0 & 0 & 0.0232 & 0 & 0 & 0 & 0 & 0 & 0 & -0.0039 & 0 \\
0 & 0 & 0 & 0.0232 & 0 & 0 & 0 & 0 & 0 & 0 & 0 \\
0 & 0 & 0 & 0 & 0.0232 & 0 & 0 & 0 & 0 & 0 & -0.0039 \\
0 & -0.0141 & 0 & 0 & 0 & 0.0062 & 0 & 0 & 0 & 0 & 0 \\
-0.0141 & 0 & 0 & 0 & 0 & 0 & 0.0062 & 0 & 0 & 0 & 0 \\
0 & 0 & 0 & 0 & 0 & 0 & 0 & 0.0062 & 0 & 0 & 0 \\
0 & 0 & 0 & 0 & 0 & 0 & 0 & 0 & 0.0062 & 0 & 0 \\
0 & 0 & -0.0039 & 0 & 0 & 0 & 0 & 0 & 0 & 0.0024 & 0 \\
0 & 0 & 0 & 0 & -0.0039 & 0 & 0 & 0 & 0 & 0 & 0.0024
\end{pmatrix}
$$

TABLE 2.1: The Modal covariance matrix of the Zernike modes and the Kolmogorov model of the atmospheric turbulence. The values are scaled to $(D_{\text{tel}}/r_0)^{5/3} = 1$.

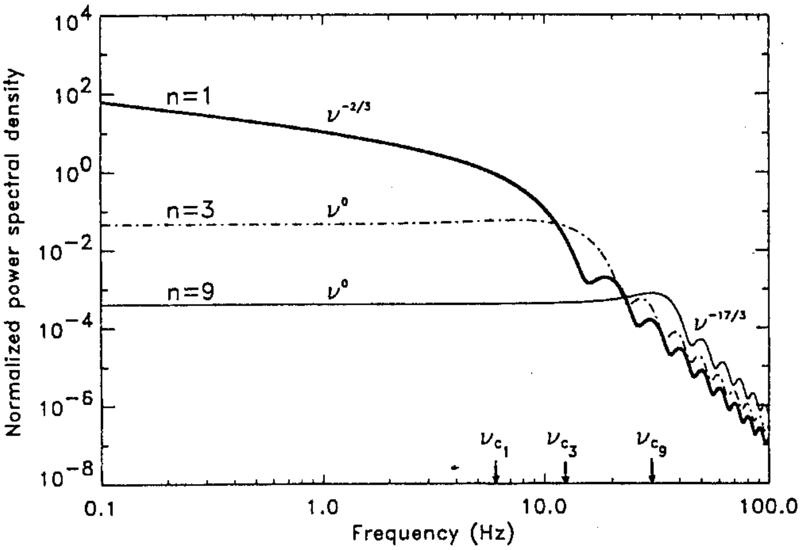

FIGURE 2.6: The temporal power spectral density (PSD) for the individual radial orders of Zernike modes.

purely diagonal and concentrate the variance in as few modes as possible. Zernike modes are not optimal for Kolmogorov statistics, and therefore have some, albeit very small, off-diagonal elements. Nevertheless, most of the wavefront variance is concentrated in the low-order modes.

ZERNIKE TEMPORAL POWER-SPECTRUM

In addition to the average variance of each Zernike mode, the characteristic time-scales are also important. These can be described by a temporal power spectral density (PSD). As shown in figure 2.6, the PSD depends only on the radial order n of the Zernike modes (Conan et al., 1995). With the exception of $n = 1$, the power-spectral density is constant below a cut-off spatial frequency ν_c, and then drops with $\nu^{-17/3}$. This cut-off frequency ν_c is higher for higher radial orders, meaning that for effective correction of high-order Zernike modes, not only does the spatial sampling of the WFS / DM combination has to be higher, but also the bandwidth of the AO control-loop must be increased.

2.3 SCIDAR TECHNIQUE

In section 2.2.4 the astro-climatic parameters seeing ϵ_{FWHM} and wavefront coherence time τ_0 were defined as a function of the atmospheric turbulence profile represented by $C_N^2(h)$. One, out of many methods to measure this profile is the SCIDAR technique. A recent overview of other techniques can be found in Eaton (2005).

2.3.1 SCIDAR PRINCIPLE

The SCIntillation Detection And Ranging (SCIDAR) technique was introduced by Rocca et al. (1974) and Vernin and Azouit (1983). It relies on the analysis of scintillation images produced by a binary star in the pupil plane of the telescope. Let us assume for the moment that there is only one turbulent layer at an altitude h_{layer} above the telescope. Each component of the binary star, with separation ϕ, produces a scintillation pattern. These patterns overlap in the pupil plane (fig. 2.7). Since the pupil footprints of the two stars on the turbulent layer are for the most part identical, the two scintillation patterns are very similar, and are shifted by Δx_{height} pixel in the pupil image along the direction of the binary star:

$$\Delta x_{\text{height}}[\text{pixel}] \;=\; \frac{n_{\text{pupil}}}{D_{\text{tel}}} \cdot \sin\phi \cdot h_{\text{layer}} \cdot \cos z \; . \qquad (2.36)$$

Where n_{pupil} is the number of pixels across the image of the pupil on the detector, D_{tel} the diameter of the telescope and z the zenith angle.

Calculating the auto-correlation **AC** of the combined scintillation pattern reveals the similarities and the shift of the two patterns in the pupil image. From the separation of the **AC** peaks, the height of the layers can be determined via equation 2.36, and the strength of the turbulence from the value of the **AC** peak. The integration time for the scintillation images has to be shorter than τ_0 (eqn. 2.8) to exclude any change in the scintillation pattern during the integration, and thus a smearing in the **AC**. Usually an integration time of $\approx$1 ms is used. This limits the technique to bright stars and $D_{\text{tel}} \gtrapprox 2\,\text{m}$.

As the **AC** function is symmetric, it produces two identical peaks for each layer, on different sides of the origin, but at the same distance. For typical atmospheric conditions, there are multiple turbulent layers, resulting in multiple peaks in the auto-correlation image at various positions along the axis of the binary (fig. 2.8).

In order to determine the wind-speed profile with a SCIDAR, the temporal cross-correlation **CC** can be calculated. In this case, the correlation between two scintillation images, separated by a short ($\approx$40 msec) time interval ΔT_{cc} is determined. Under the assumption of frozen flow, the scintillation pattern caused by the single turbulent layers is the same in the two pupil images, but shifted by Δx_{wind} pixel in the direction of the respective wind-speeds $\mathbf{v}$:

$$\Delta \mathbf{x}_{\text{wind}} \;=\; \Delta T_{cc} \cdot \mathbf{v} \cdot \frac{n_{\text{pupil}}}{D_{\text{tel}}} \cdot \cos z \; . \qquad (2.37)$$

Each turbulent layer produces a triplet in the **CC** images, similar to the **AC** images, with two lateral peaks at a distance Δx_{height} from the central peak. But the triplet is not located at the origin. Rather it is shifted by $\Delta \mathbf{x}_{\text{wind}}$ due to the wind-speed. A typical **CC** image appears in figure 2.8.

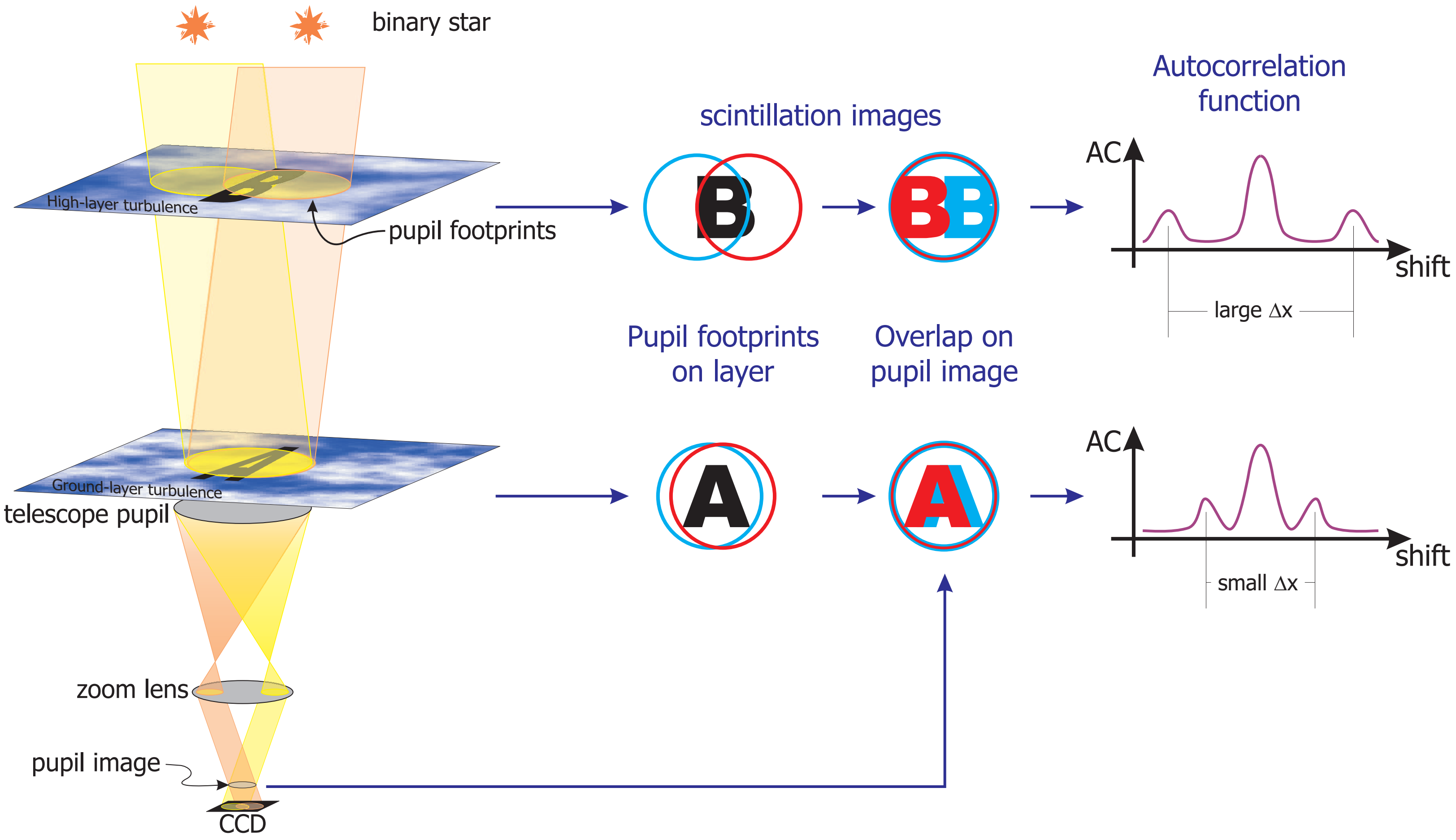

FIGURE 2.7: The principle of the SCIDAR technique. When observing a close binary, the footprints of the pupil of the two stars on a turbulent layer will be slightly different. A wavefront aberration pattern (“A” and “B”) in this layer will thus produce two similar, albeit slightly shifted scintillation patterns in the pupil plane. When calculating the auto-correlation of the pupil image, the separation of the two patterns can be retrieved, thus giving the height of the turbulent layer. For the Generalized SCIDAR, the detector is conjugated to an altitude below the ground in order to measure the turbulence in the ground-layer.

A problem of classical SCIDAR with the detector in the pupil plane is that it cannot measure the turbulence at the ground, because the scintillation needs some distance to develop (see sect. 2.2.5). Furthermore, at the origin of the **AC** image, the peak associated with the ground-layer turbulence overlaps with the peak caused by the correlation of the complete image with itself. The value of the **AC** peak of the ground-layer can thus not be determined. To overcome this limitation, Fuchs et al. (1998) proposed the concept of the "Generalized SCIDAR" (G-SCIDAR), where the detector is conjugated to an altitude h_{GS} below the ground, usually $h_{\mathrm{GS}} \approx -3$ to $-4\,\mathrm{km}$. The scintillation images of the two stars then no longer overlap on the detector, but are slightly separated. A typical such scintillation image is shown in figure 2.9. For the analysis of the scintillation images nothing changes, except that the height h_{layer} of the individual layers is then given above the conjugation plane of the detector. From equation 2.36 it thus follows:

$$h_{\mathrm{layer}} = \Delta x_{\mathrm{height}} \cdot \frac{D_{\mathrm{tel}}}{n_{\mathrm{pupil}} \cdot \sin\phi \cdot \cos z} - h_{\mathrm{GS}} \,. \tag{2.38}$$

With the G-SCIDAR, it is thus possible to reliably measure the vertical turbulence profile of the complete atmosphere. For this reason, this method is currently implemented in a number of instruments at different telescopes, and extensive site-testing campaigns have been carried out with G-SCIDAR instrument at various astronomical sites (see sect. 6.6.8 for an overview).

2.3.2 THEORETICAL BACKGROUND

As described above, the C_N^2-profile is extracted from the scintillation images with the **AC**-function. The auto-correlation $\mathbf{AC}\big[f(\mathbf{x}')\big](\mathbf{x})$ of a two-dimensional function $f(\mathbf{x}')$ is defined as

$$\mathbf{AC}\big[f(\mathbf{x}')\big](\mathbf{x}) = \frac{\Big\langle \big(f(\mathbf{x}') - \langle f(\mathbf{x}')\rangle\big) \cdot \big(f(\mathbf{x}) - \langle f(\mathbf{x}')\rangle\big) \Big\rangle\Big|_{\mathbf{x}'}}{\big\langle \, |f(\mathbf{x}') - \langle f(\mathbf{x}')\rangle|^2 \, \big\rangle\big|_{\mathbf{x}'}} \,. \tag{2.39}$$

Similarly, the cross-correlation $\mathbf{CC}\big[f(\mathbf{x}'), g(\mathbf{x}')\big](\mathbf{x})$ of two functions $f(\mathbf{x}')$ and $g(\mathbf{x}')$ is given by

$$\mathbf{CC}\big[f(\mathbf{x}'), g(\mathbf{x}')\big](\mathbf{x}) = \frac{\Big\langle \big(f(\mathbf{x}') - \langle f(\mathbf{x}')\rangle\big) \cdot \big(g(\mathbf{x}) - \langle g(\mathbf{x}')\rangle\big) \Big\rangle\Big|_{\mathbf{x}'}}{\sqrt{\big\langle \, |f(\mathbf{x}') - \langle f(\mathbf{x}')\rangle|^2 \, \big\rangle\big|_{\mathbf{x}'} \cdot \big\langle \, |g(\mathbf{x}') - \langle g(\mathbf{x}')\rangle|^2 \, \big\rangle\big|_{\mathbf{x}'}}} \,. \tag{2.40}$$

For the SCIDAR technique, the first step is to calculate the mean-normalized scintillation images $\mathbf{I}_i^*(\mathbf{x})$ from the measured scintillation images $\mathbf{I}_i(\mathbf{x})$ via

$$\mathbf{I}_i^*(x,y) = \frac{\mathbf{I}_i(\mathbf{x}) - \langle \mathbf{I}_i(\mathbf{x})\rangle|_{\mathbf{x}}}{\langle \mathbf{I}_i(\mathbf{x})\rangle|_{\mathbf{x}}} \,. \tag{2.41}$$

Using these images, the average and normalized **AC** images $\mathbf{SA}^*(\mathbf{x})$

$$\mathbf{SA}^*(\mathbf{x}) = \frac{\langle \mathbf{AC}\big[\mathbf{I}_i^*(\mathbf{x}')\big](\mathbf{x})\rangle\big|_i}{\mathbf{AC}\big[\, \langle \mathbf{I}_i^*(\mathbf{x}')\rangle\big|_i \,\big](\mathbf{x})} \tag{2.42}$$

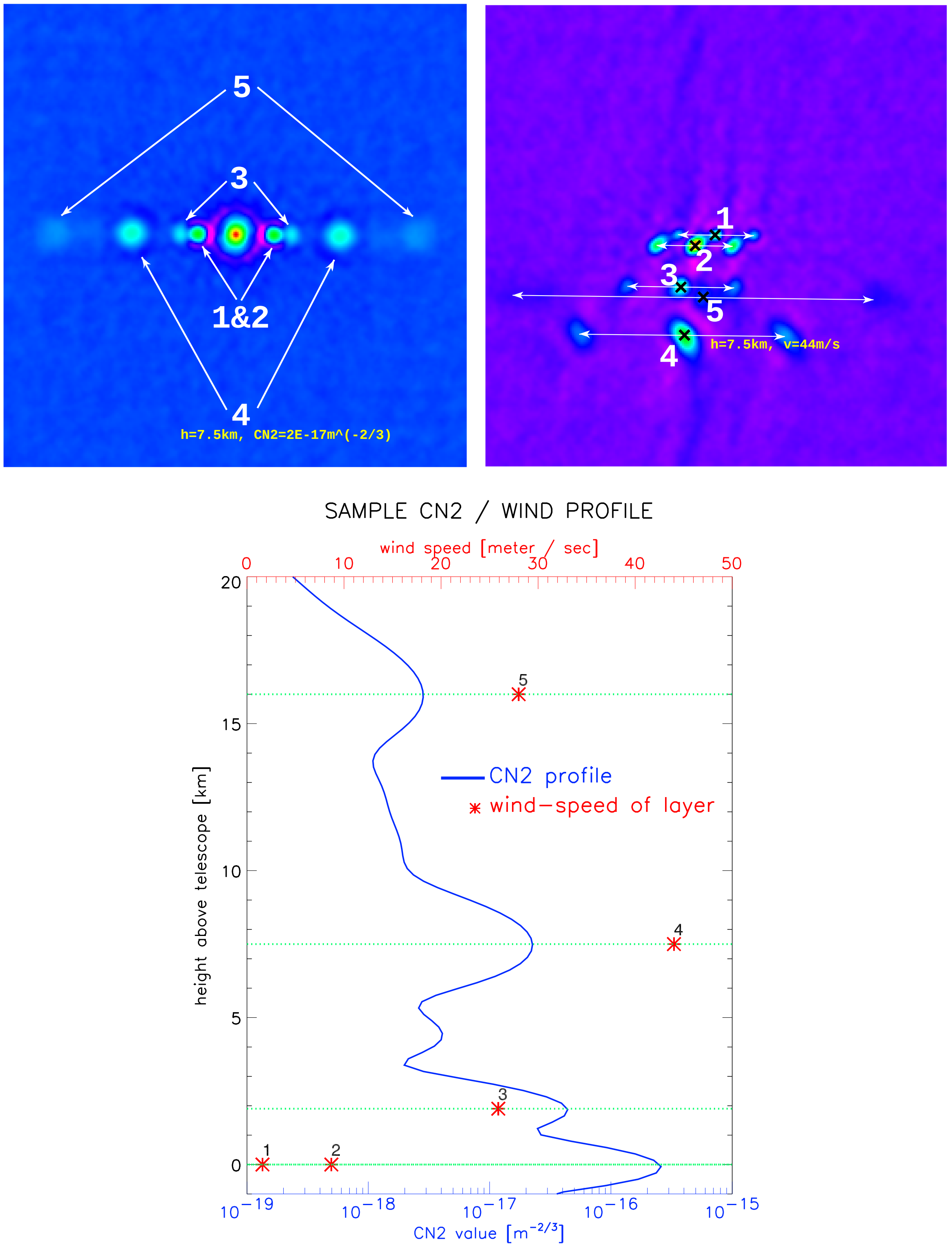

FIGURE 2.8: An example of measured auto- (**AC**, **top left**) and cross-correlation (**CC**, **top right**) images and the retrieved C_N^2- and wind-speed profiles. The detected correlation triplets in the **AC** and **CC** images are marked and for one triplet the height, C_N^2-value (from **AC** image) and wind-speed (from **CC** image) are indicated. The determined respective height and wind-speeds for all triplets are over-plotted on the calculated C_N^2-profile (**bottom**). As can be seen, the two layers at the ground are too close in altitude to separate them in the auto-correlation image. But since they have different wind-speeds, they can be resolved in the cross-correlation image.

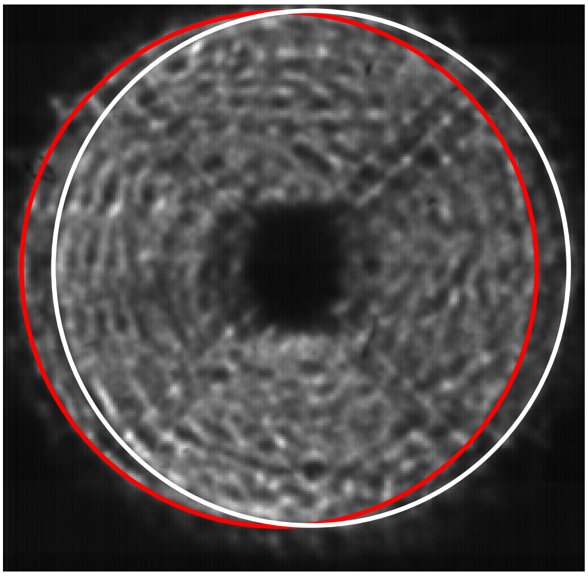

FIGURE 2.9: A typical scintillation image with 1 ms integration time as measured with the Generalized SCIDAR at the VATT. The pupil footprints of the two stars are marked by red and white circles, respectively. The central obstruction and the spiders of the telescope can be clearly seen. With a diameter of the telescope of 1.75 m as a scale, the typical size of the scintillation pattern is a few centimeters.

are calculated for a set of ≈500 to 5 000 scintillation images to achieve a good SNR. A similar calculation can be done for the normalized temporal **CC** images $\mathbf{SC}^*(\mathbf{x})$.

A slice $\mathbf{SA}^*(r)$ through the **AC** image along the axis of the binary star is then given by (Vernin and Roddier, 1973)

$$\mathbf{SA}^*(r) = \frac{1+\alpha^2}{(1+\alpha)^2}\,\mathbf{SA}_0^*(r) + \frac{\alpha}{(1+\alpha)^2}\,\mathbf{SA}_I^*(r)\,, \tag{2.43}$$

where α corrects for the difference in brightness Δm between the binary components:

$$\alpha = 10^{-0.4\Delta m}\,. \tag{2.44}$$

The slice $\mathbf{SA}^*(r)$ consists of a central peak $\mathbf{SA}_0^*(r)$, produced by the correlation of the scintillation image with itself and the noise in the image. This peak contains no information about the height and the strength of the turbulence. The second component $\mathbf{SA}_I^*(r)$ is the interesting part, because it consists of the correlation peaks, produced by the individual turbulent layers.

From $\mathbf{SA}^*(r)$, the log amplitude covariance $\mathbf{SA}_\chi^*(r)$ of the scintillation fluctuations

$$\mathbf{SA}_\chi^*(r) = \frac{\log\left[\mathbf{SA}_I^*(\mathbf{r}) + 1\right]}{4} \tag{2.45}$$

is calculated. And finally, using Rytov approximation and Kolmogorov statistics, a connection between $\mathbf{SA}_\chi^*(r)$ and the C_N^2-profile is found to be (Tyler, 1992)

$$\mathbf{SA}_\chi^*(r) = \frac{8.16}{2\lambda}\int_0^\infty C_N^2(h)\,h^{5/6}\,T(Q)\,dh\,, \tag{2.46}$$

for the observing wavelength λ and a kernel function $T(Q)$

$$T(Q) \;=\; \int_0^\infty P^{-8/3}\, J_0(Q\,P)\,\left[1 \;-\; \cos\left(P^2\right)\right]dP \tag{2.47a}$$

$$Q \;=\; \left(\frac{2\pi}{\lambda\,h\,\sec(z)}\right)^{1/2} \left|r \;-\; \phi\,h\,\sec(z)\right| . \tag{2.47b}$$

Equation 2.46 is a so-called inverse problem – more specifically a Fredholm integral equation of the first kind – which is usually ill-conditioned and numerically hard to invert. Later, in section 6.3, an implementation and a comparison between different inversion algorithms will be presented.

In discretized form, with n_{pupil} pixels across the pupil image on the detector, equation 2.46 can be conveniently written in matrix form with the vectors $\mathbf{SA}^*_\chi(r)$ and $C_N^2(h)$ of length $n_{\text{pupil}}/2$ and a matrix $\mathbf{T}(\mathbf{Q})$ with dimension $n_{\text{pupil}}/2 \times n_{\text{pupil}}/2$.

The vertical resolution of the SCIDAR depends on the height h of the turbulent layer above the telescope and is given by (Vernin and Azouit, 1983)

$$\Delta h_{\text{GS}} \;=\; \frac{0.5}{\sin\phi\,\cdot\,\cos z}\sqrt{\lambda\,\left(h \;-\; |h_{\text{GS}}|\right)} . \tag{2.48}$$

As can be seen e.g. in figure 2.8, the correlation peak associated with one single, thin turbulent layer has a certain size, which corresponds to a vertical extent of Δh_{GS} in the atmosphere as given in equation 2.48. If the vertical separation of two layers is smaller than Δh_{GS}, their respective correlation peaks overlap and can no longer be separated. In such a case, it will appear as there is one strong layer instead of two weaker ones. The limited vertical resolution of the G-SCIDAR is thus due to the inherent characteristics of the scintillation and cannot be resolved, even when using a detector with high sampling of the pupil or larger telescope size.

On the other hand, the vertical size Δh_p corresponding to one pixel on the detector in the **AC** image and along the axis of the binary can be calculated from geometry and is given by

$$\Delta h_p \;=\; \frac{D_{\text{tel}}}{n_{\text{pupil}}\,\cdot\,\sin\phi\,\cdot\,\cos z} . \tag{2.49}$$

This means that for correlation peaks at the edge of the **AC** images, the maximum achievable height h_{max} above the conjugation height for a SCIDAR is given by

$$h_{\text{max}} \;=\; \frac{D_{\text{tel}}}{2\sin\phi\,\cdot\,\cos z} . \tag{2.50}$$

If the turbulent layer is located at an altitude above h_{max}, the pupil footprints of the two stars on this layer no longer overlap. The scintillation pattern in the pupil image no longer shows any self-similar patterns, and therefore no correlation peak appears in the **AC** image. To achieve a good vertical resolution (small Δh_{GS}) and to cover the complete atmosphere ($h_{\text{max}} > 20\,\text{km}$), a large telescope ($D_{\text{tel}} \gtrapprox 2\,\text{m}$) and a bright (V<5 mag) binary star with a separation of ≈10 arcsec is required. See section 6.4 for a detailed discussion on the optimal characteristics of the binary.

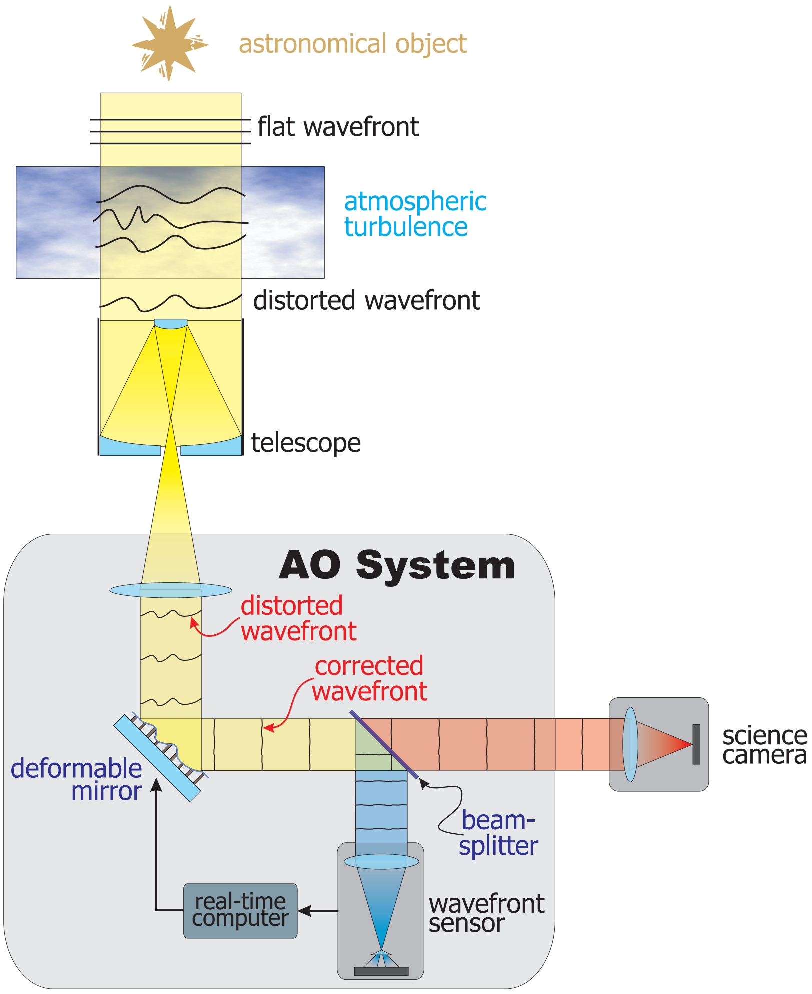

FIGURE 2.10: A sketch to illustrate the principle of Adaptive Optics. A wavefront sensor measures the distortions of the incoming light and sends correction signals to the deformable mirror, which corrects the distorted wavefront. Some part of the reflected light goes into the science camera, while usually the visible light is reflected by a beam-splitter into the wavefront sensor.

2.4 ADAPTIVE OPTICS TECHNIQUE

As mentioned in the introduction, one possibility to overcome the limitations in image quality imposed by atmospheric turbulence is the Adaptive Optics technique. The principle of an AO system is illustrated in figure 2.10 and consists of two major functions: one is to measure the wavefront distortions and the other is to correct them. The first is achieved with a so-called wavefront sensor (WFS), while for the latter, usually a so-called deformable mirror (DM) is used.

2.4.1 WAVEFRONT SENSORS

Over the last few decades a number of devices to measure the wavefront aberrations have been developed. These include the Shack-Hartmann Sensor (SHS) (Shack and Platt, 1971), the curvature sensor (Roddier, 1988) and the pyramid sensor (Ragazzoni, 1996). For this work, only the pyramid WFS is of relevance, and is therefore discussed in more detail in this section.

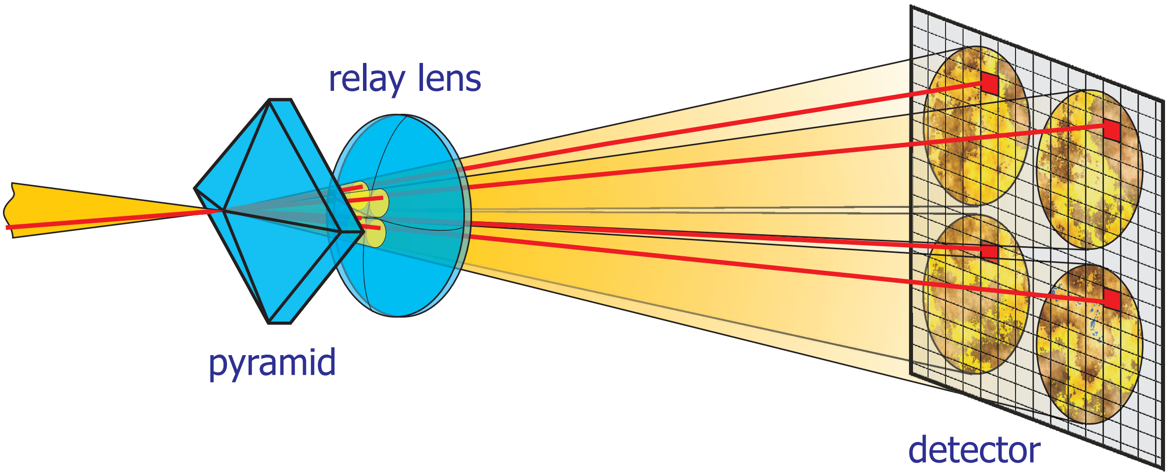

FIGURE 2.11: The principle of the pyramid wavefront sensor. Light coming from the left is focused onto the tip of the pyramid and split into four beams. The four pupils are then imaged with a relay lens onto the detector. The path of one sample light-ray is indicated by the solid red line. In the presence of wavefront aberrations, the intensity in the individual four light-rays is different, but the total amounts remains the same. The light missing from one pupil image is refracted into the other three. From the intensity distributions in the corresponding four pixels, the local tilt of the wavefront can be calculated.

In a pyramid sensor, the light of the guide star is focused onto the tip of a glass pyramid (Ragazzoni, 1996). The four facets of the pyramid split the light into four beams, which are then imaged onto a detector with a relay lens (fig. 2.11 and 2.12). The principle of the pyramid WFS is thus similar to the Foucault knife edge test.

If the wavefront is flat, then the light is split into four beams with equal amounts of light. In the presence wavefront aberrations, however, the shape of the PSF on the tip of the pyramid is changed (eqn. 2.10), and thus the distribution of the light into the four beams changes. In the simple case of a pure tilt, the focus of the light is shifted onto one facet of the pyramid, yielding one bright and three darker pupil images on the detector.

The average slopes $d/dx\ W(x,y)$ and $d/dy\ W(x,y)$ of the wavefront over the sub-aperture at position (x,y) can then be calculated from the intensity distribution $I_i(x,y)$ in the corresponding pixels in the four pupil images (fig. 2.12):

$$\frac{d}{dx}W(x,y) = c \cdot \frac{[I_1(x,y)+I_2(x,y)]-[I_3(x,y)+I_4(x,y)]}{\sum_i I_i(x,y)} \tag{2.51a}$$

$$\frac{d}{dy}W(x,y) = c \cdot \frac{[I_1(x,y)+I_3(x,y)]-[I_2(x,y)+I_4(x,y)]}{\sum_i I_i(x,y)} . \tag{2.51b}$$

In contrast to other WFS, the spatial sampling of the pyramid can be adjusted relatively easily by binning the detector, or by changing the focal length of the re-imaging lens. On the other hand, the dynamic and linear range of a pyramid WFS is rather small. As soon as the focused spot leaves the tip of the pyramid, only one facet is illuminated. Since only one pupil image is bright, while the other three are completely dark under these circumstances, it is no longer possible to retrieve the exact amount of tilt. The linear range can thus be estimated to be

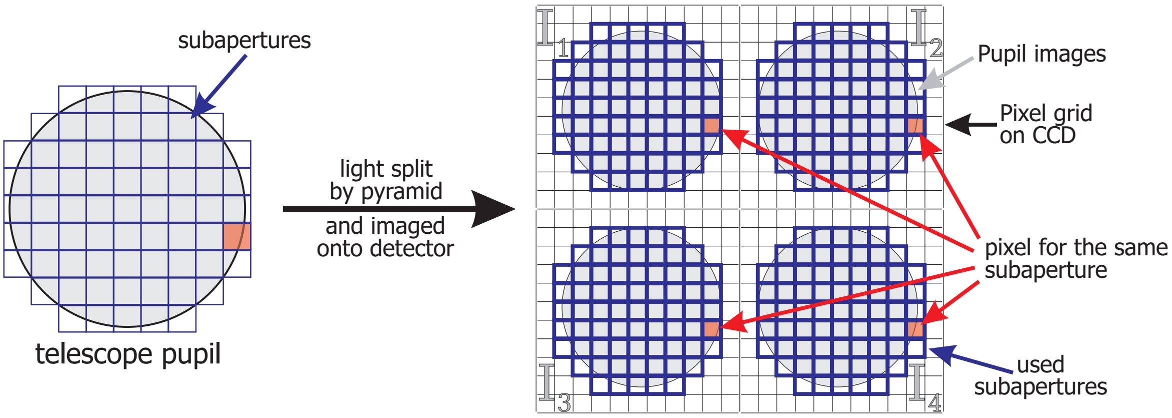

FIGURE 2.12: A sketch to illustrate the matching of the four pupil images I_1 to I_4 produced by the pyramids and the pixel on the CCD. The highlighted red pixels correspond to the same subaperture on the telescope pupil and are used to calculate the local slope of the wavefront over this subaperture. However, when the distance of the pupil images is not an integer multiply of the pixel size, the pixel in the four pupils map to different regions on the telescope pupil. This effect causes aliasing, limiting the performance of the pyramid for high-order modes. There is no possibility to correct for this effect once the system is assembled, thus placing tight requirements on the vertex angles of the pyramid and the focal length of the relay lens.

$\approx 0.5\lambda$ rms, which in the visible is much smaller than the atmospheric aberrations (see sect. 2.2.4). A technique to overcome this limitation is to modulate the beam on the tip of the pyramid along e.g. a circle (Ragazzoni, 1996). If the modulation frequency is an integer multiple of the frame-rate of the CCD and its amplitude is large enough, then during some fraction of the integration time, the PSF will also lie on the other facets. The relative amount of light in the four pupil images is then proportional to the overall amount of tilt of the wavefront.

Another problem for the un-modulated pyramid is that the tip of a real pyramid cannot be made infinitesimal small. Due to diffraction at an extended tip of the pyramid, more than half of the light is scattered out of the pupil images (Costa, 2005), limiting the performance and the required minimum brightness of the guide star. To minimize this effect, the size of the PSF on the tip of the pyramid has to be at least 10 times larger than the size of the tip itself, which can be accomplished by making the f-ratio of the beam very large, typically ≈f/300.

Usually the pyramid is used in transmission, but recently it was proposed to coat the pyramid and use it in reflection (Feldt et al., 2006). In this case the optical characteristics of the substrate material are not important. One can therefore choose a material which can be more easily machined to achieve sharper edges. This in turn reduces the required f-ratio of the beam on the tip of the pyramid, making the whole system more compact.

2.4.2 DEFORMABLE MIRRORS

Once the wavefront aberrations are measured with a wavefront sensor, they have to be somehow corrected. A mirror, whose surface can be locally bent, a so-called deformable mirror (DM), is usually used for this purpose.

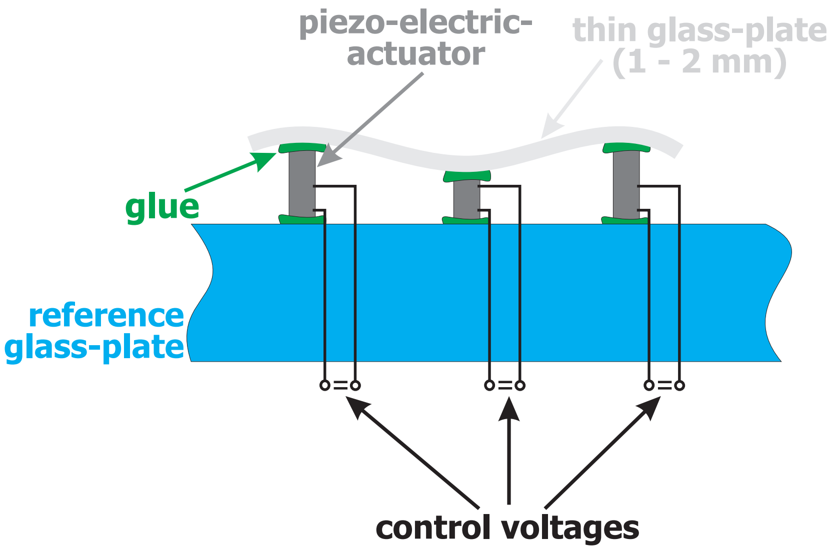

FIGURE 2.13: Illustration of the principle of the piezo Deformable Mirror technology.

One technique to realize a DM is to make use of the piezo-electric effect. When applying a voltage (up to ≈150 V) to a piezo-ceramic element, it expands by a tiny amount. For a piezo DM many (up to several hundred) of these piezo-elements are glued to a reference plate (see fig. 2.13), and a thin, coated glass plate is glued on top of them. The typical stroke of the single actuators is a few microns, which usually is too small to compensate tip and tilt (atmospheric or induced by the telescope). Therefore a separate fast tip-tilt mirror is additionally required. Piezo-DMs are quite common in AO systems, for the GLAO system presented later in chapter 5 of this thesis, also this kind of DM was used.

2.4.3 WAVEFRONT ERRORS

However, an AO system can never completely compensate the wavefront distortions induced by the atmosphere: there will be always some residual aberrations. The remaining wavefront variance σ^2_{res} can be divided into several components, according to their respective origin:

$$\sigma^2_{\mathrm{res}} = \sigma^2_{\mathrm{fit}} + \sigma^2_{\mathrm{temp}} + \sigma^2_{\mathrm{rec}} + \sigma^2_{\mathrm{alias}} + \sigma^2_{\mathrm{aniso}} \, . \tag{2.52}$$

FITTING ERROR

The first component of the residual wavefront error is caused by the limited number N of corrected (Zernike) modes. All higher order modes are left uncorrected and thus also uncorrected are the high spatial frequencies they represent. This so-called fitting error σ^2_{fit} can be determined from the modal covariance matrix $\mathbf{C}_\Phi$ (eqn. 2.35) by summing up the average variances of all uncorrected modes (Hardy, 1998):

$$\sigma^2_{\mathrm{fit}} = \left(\frac{D_{\mathrm{tel}}}{r_0}\right)^{5/3} \cdot \sum_{i=N+1}^{\infty} \mathbf{C}_{\Phi,i,i} \, . \tag{2.53}$$

TEMPORAL ERROR

An AO system is not infinitely fast. It takes some time to integrate and read the CCD, perform the required calculations, and apply the correction signals to the DM. During this time, the wavefront aberrations have already evolved. The AO system is thus actually not correcting the current wavefront distortions, but rather those of one or two loop steps ago. With the Greenwood frequency f_G (eqn. 2.9) and the loop frequency f_{loop}, the resulting temporal error σ^2_{temp} can be estimated by (Hardy, 1998)

$$\sigma^2_{\text{temp}} = \kappa_{\text{loop}} \cdot \left(\frac{f_G}{f_{\text{loop}}} \right)^{5/3} . \tag{2.54}$$

The factor κ_{loop} is a constant (between 0.2 and 1.0) and describes the frequency response of the control system.

RECONSTRUCTION ERROR

Since the integration times for the single frames of the WFS have to be as short as possible to reduce σ^2_{temp}, the number of available photons to determine the wavefront in each frame is very limited. The result is that the measured intensities in the single pixels of the pupil images in a pyramid WFS are corrupted by Poisson statistics and read-out noise (RON) of the detector. This leads to an error in the calculation of the local wavefront slopes and thus to an error in the overall reconstructed wavefront. It is difficult to quantify this reconstruction error σ^2_{rec} for the general case, because it depends strongly on the parameters of the particular WFS and the reconstruction algorithm (Kasper, 2000).

ALIASING ERROR

Because of the finite sampling of the pupil with the WFS, high spatial frequencies are projected into the measured low order modes, leading to an error when applying these signals to the DM. This is similar to the effect for Fourier-transformation on a discrete grid, and the resulting error is thus also called aliasing error σ^2_{alias}. This error depends on the modal covariance of the wavefront aberrations $\mathbf{C}_\Phi$ and on the geometry of the wavefront sensor. It is thus relatively difficult to quantify analytically (Kasper, 2000).

ISOPLANATIC ANGLE AND ISOPLANATIC ERROR

Depending on the angle ϑ between the guide star and the science object, the light goes through different parts of the atmosphere, especially for turbulent layers at high altitudes (see fig. 2.14). The correction by the AO system is only efficient in the direction of the guide star and the performance degrades rapidly with ϑ. To characterize the size of the area with useful correction, the isoplanatic angle ϑ_0 is defined (Hardy, 1998):

$$\vartheta_0 = 0.057\, \lambda^{6/5} \left(\sec\zeta \int C_N^2(h) \cdot h^{5/3}\, dh \right)^{-3/5} . \tag{2.55}$$

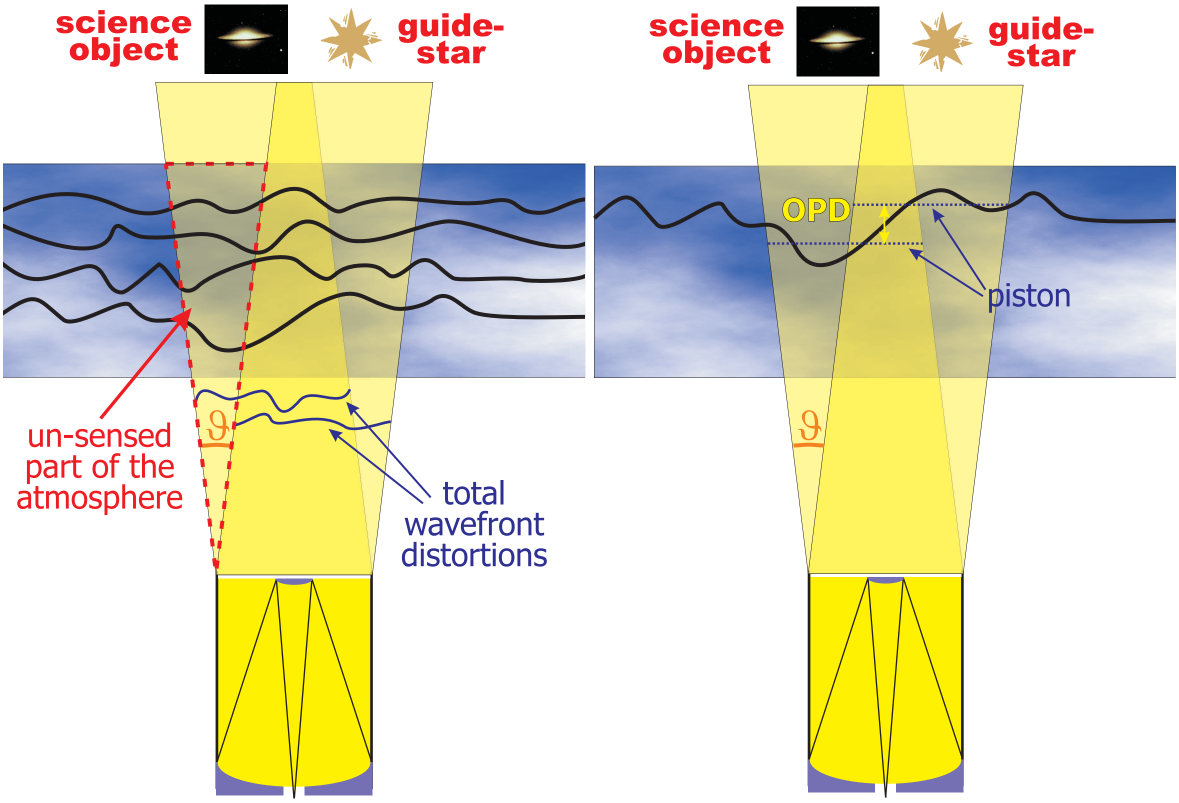

FIGURE 2.14: Illustration of the anisoplanatic (**left**) and anisopistonic (**right**) effect in Adaptive Optics. The distorted wavefronts are illustrated by the thick black lines.

With this definition, ϑ_0 is the angular separation at which the differential variance between the wavefront of the guide star and the science object is $1\,\mathrm{rad}^2$. Typical values for ϑ_0 in the K-Band are ≈20 arcsec.

For a single-star AO system and an off-axis science object, an additional error source due to the finite size of ϑ_0 has thus to be considered. This isoplanatic error $\sigma^2_{\mathrm{aniso}}$ depends on the angle ϑ between the science object and the guide star and on the isoplanatic angle ϑ_0 (eqn. 2.55):

$$\sigma^2_{\mathrm{aniso}} = \left(\frac{\vartheta}{\vartheta_0}\right)^{5/3} . \tag{2.56}$$

Reducing one error source usually increases another. For example, when using a high frame-rate for the WFS, σ^2_{temp} is small, but σ^2_{rec} becomes large. For a given brightness of the guide star and atmospheric conditions like ϵ_{FWHM} and τ_0, the spatial sampling of the WFS, the number of reconstructed modes and the loop frequency f_{loop} have to be chosen to minimize the total residual wavefront variance σ^2_{res} in equation 2.52.

ISOPISTONIC ANGLE AND ISOPISTONIC ERROR

When imaging with a single telescope, a shift of the entire wavefront within the telescope aperture along the propagation direction (so-called piston) is not important, since it does not affect the image. However, for interferometers like LINC-NIRVANA (sect. 2.6.2), which consists of more than one aperture, the optical path-

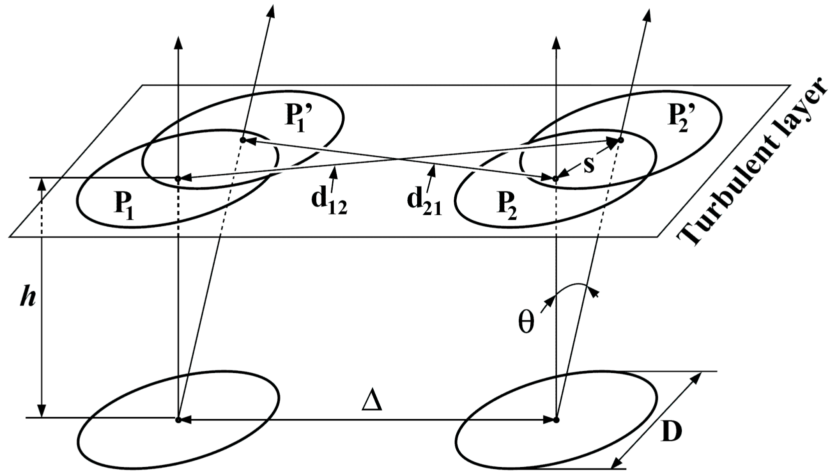

FIGURE 2.15: The required quantities for the calculation of the isopistonic angle. Reproduced from Esposito et al. (2000).

lengths through the different telescopes to the detector have to be exactly the same (to within a tiny fraction of the observing wavelength). Therefore also the piston of the wavefront has to be actively controlled. The Optical Path Difference (OPD) between the beams from the individual telescopes has to be continuously measured with a guide star and corrected with an adjustable delay-line or piston-mirror.

However, as illustrated in figure 2.14, especially turbulent layers at high altitudes can introduce an OPD between the guide star and the science object. The average variance σ_P^2 of the OPD as a function of the distance to the guide star can be derived from the formula in Esposito et al. (2000):

$$
\begin{aligned}
\sigma_p^2 \quad = \quad & 0.155\ \pi^{8/3}\, D_{\text{tel}}^{5/3} \iint C_N^2(h)\, \frac{J_1^2(x)}{x\left[x^2 + \left(\pi\,\dfrac{D_{\text{tel}}}{L_0(h)}\right)^2\right]^{11/6}} \\
& \times \left\{ 2\left[1 - J_0\left(2x\frac{s}{D_{\text{tel}}}\right) - J_0\left(2x\,\frac{\Delta}{D_{\text{tel}}}\right)\right]\right. \\
& \left. + J_0\left(2x\,\frac{d_{12}}{D_{\text{tel}}}\right) + J_0\left(2x\,\frac{d_{21}}{D_{\text{tel}}}\right)\right\} dx\, dh\ .
\end{aligned}
\qquad (2.57)
$$

Here, $J_1(x)$ is the first order Bessel function of the first kind, D_{tel} is the diameter of the single telescope, Δ is the baseline between the telescopes' centers, s, d_{12} and d_{21} are the distances as defined in figure 2.15, and L_0 denotes the outer scale of the turbulent layer. However, the precise value of L_0 is not known. There are many measurements with various techniques, but the results range from a few meters to a few kilometers. Considering the latest publications, it seems that the value for L_0 is converging to $\approx$20 m (Conan et al., 2002), but with large variations over time-scales of a few minutes (Maire et al., 2006).

For typical interferometric imaging, the OPD has to be smaller than $\approx \lambda/10$, the isopistonic angle ϑ_P is thus defined as the angular separation where the $\sigma_P = \lambda/10$. As already noted by Esposito et al. (2000), ϑ_P shows a strong dependence on L_0 and

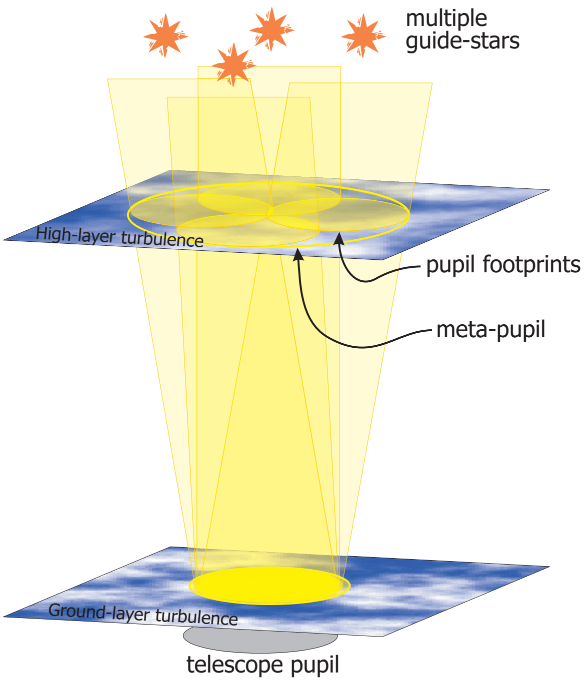

FIGURE 2.16: Illustration of the principle of Multi-Conjugate Adaptive Optics. Using multiple guide stars, the turbulence can be measured in the complete volume above the telescope.

on the position angle with respect to the OPD guide star. The isopistonic angle ϑ_P is slightly smaller in the direction parallel to the baseline than perpendicular to the LBT baseline (fig. 6.25). For the calculations and analysis presented in chapter 6 of this thesis, we used the parameters of the LBT, $L_0 = 25\,\mathrm{m}$ and the direction parallel to the baseline, yielding typical values for ϑ_P in K-band of $\approx$40 arcsec.

2.5 MULTI-CONJUGATE ADAPTIVE OPTICS

Classical AO system use one natural guide star to measure the deformations of the incoming wavefront and one DM to correct them. However, as described in the previous section, the resulting correction is only useful for angular separations from the GS of less than the isoplanatic angle ϑ_0. Since ϑ_0 is small and the number of sufficiently bright guide stars (typically brighter than 14 mag in V) is limited, only a tiny fraction ($\approx$1%) of the complete sky can be observed with classical AO systems.

One possibility to increase the size of the corrected area and thus the sky-coverage is by using several guide stars to measure the turbulence in the complete 3D volume above the telescope (fig. 2.16). In such an Multi-Conjugate Adaptive Optics (MCAO) system, as first proposed by Beckers (1988), the turbulence is then corrected by multiple DMs, which are placed optically at the altitude of the most turbulent layers. The result is that the maximum achievable performance on-axis is not as good as for Classical AO system, because of uncorrected turbulence in between the single corrected layers, but the correction is much more uniform over a significantly increased field-of-view (Rigaut et al., 2000; Fusco et al., 2000; Diolaiti et al., 2001; Louarn, 2002).

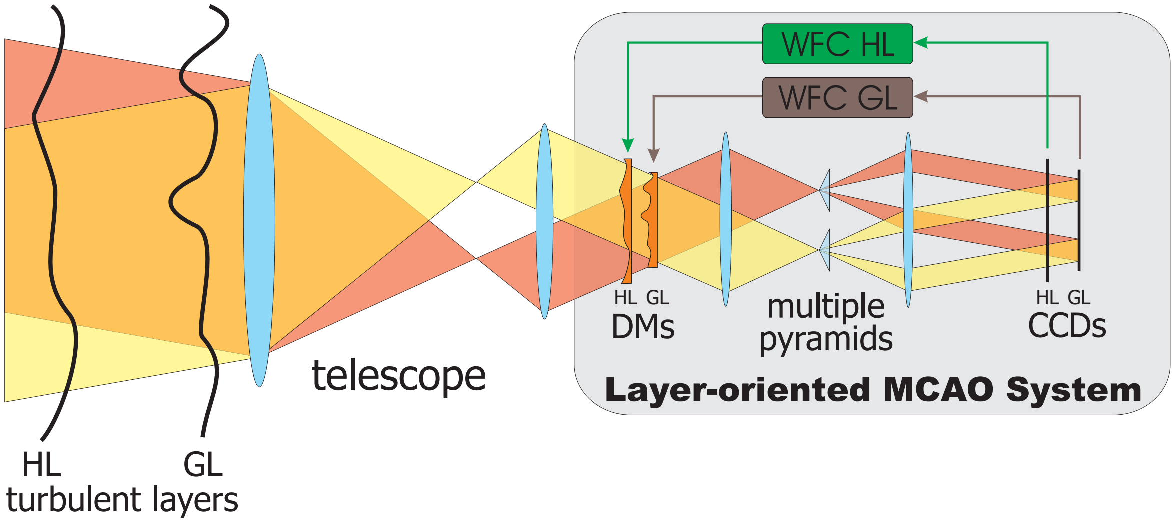

FIGURE 2.17: Illustration of the principle of Layer-Oriented Multi-Conjugate Adaptive Optics with optical co-addition. Multiple pupil-plane wavefront sensors like e.g. pyramids are placed in the focal plane at the position of the guide star images. The split beams of all pyramids are re-imaged with a common optics onto one detector per layer. This detector is focused to a certain turbulent layer and therefore sees only the wavefront aberrations induced by this layer. The correction signals for the DMs, which are conjugated to the same altitudes, are thus relatively easy to calculate.

2.5.1 LAYER-ORIENTED MCAO

One possible implementation of an MCAO system is to focus the WFS at a certain turbulent layer and measure only the wavefront aberrations caused by that layer. The DM is also conjugated to the same altitude as the WFS, in order to correct only that layer. This method requires a pupil plane wavefront sensor such as the pyramid, and one wavefront sensor unit per layer. It was introduced by Ragazzoni (2000), while some more details and various refinements can be found in Ragazzoni et al. (2000a); Diolaiti et al. (2001); Farinato et al. (2004b).

The optical co-addition principle is an elegant implementation of this concept. As illustrated in figure 2.17, the pupils of the individual pyramids are all imaged on the same detector and overlap according to the footprint of the associated guide stars on the corresponding layer. In this way, the light from all guide stars is added up. The individual guide stars can be faint: the important quantity is the total amount of the combined light from all guide stars. A single layer can be corrected as long as the footprints of the guide stars completely cover the metapupil of the field-of-view (fig. 2.16). The number of required guide stars is thus given by the desirable FoV and the maximum altitude of the layer which has to be corrected. Since fainter stars are more abundant than brighter ones, the sky-coverage of such systems is significantly increased as compared to classical AO, not only because of the increased field of correction, but also because of the larger number of suitable guide stars (Arcidiacono, 2004).

One disadvantage of layer-oriented MCAO systems is that if the guide stars have different brightness, the correction is not uniform over the FoV, but rather biased towards the brightest guide star (sect. 5.6.4).

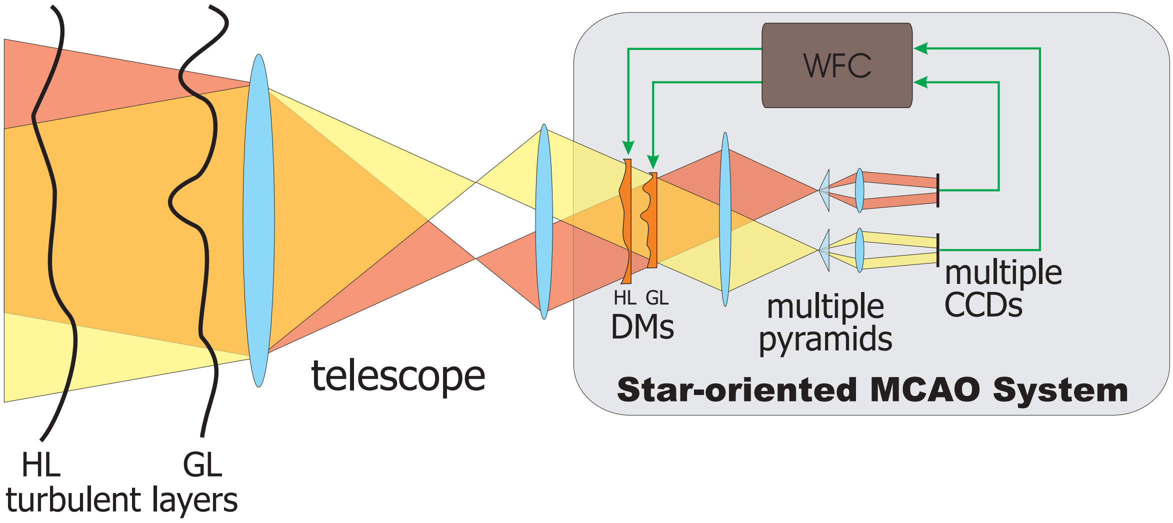

FIGURE 2.18: Illustration of the principle of Star-Oriented Multi-Conjugate Adaptive Optics. For each guide star there is a dedicated wavefront sensor unit with e.g. a pyramid and a CCD. From the signals of all these wavefront sensors the complete vertical structure of the turbulence is reconstructed numerically, and the appropriate signals are then sent to the DMs, which are conjugated to the most turbulent layers.

2.5.2 STAR-ORIENTED MCAO

The other concept for an MCAO system is to measure the wavefront aberrations in the direction of the single guide stars, just as in classical AO system. By combining the information from the single guide stars numerically with the wavefront computer (WFC), the vertical structure of the turbulence can be retrieved and the appropriate commands for controlling the DM determined (fig. 2.18). This approach is thus also called atmospheric tomography. The advantages of this concept is that established WFS techniques can be used, and with the help of sophisticated wavefront reconstruction algorithms, optimal performance in the direction of the science object can be achieved. Within some limits, it is possible to adjust the distribution of the Strehl ratio in the field to the requirements of the specific science case. On the downside, this method requires rather bright guide stars, each of which has be to bright enough to serve as a guide star on its own. The number of sufficiently bright stars is rather small, therefore the achievable sky-coverage of the star-oriented approach is worse than that of the layer-oriented technique. A comparison based on extensive simulations of the achievable performance of the layer-oriented and the star-oriented approach can be found in Bello et al. (2003a,b).

2.5.3 GROUND-LAYER ADAPTIVE OPTICS

Considering the complexity of MCAO, the extension from a Classical AO system to an MCAO system might be too risky to take in a single step. In an MCAO system, there are multiple WFS and DMs, requiring new concepts for the actual hardware implementation and control loop architecture to handle the interaction between the single layers. Furthermore, the costs of such a system are non-negligible, and they still have to prove that they really fullfill the performance expectations derived from numerical simulations.

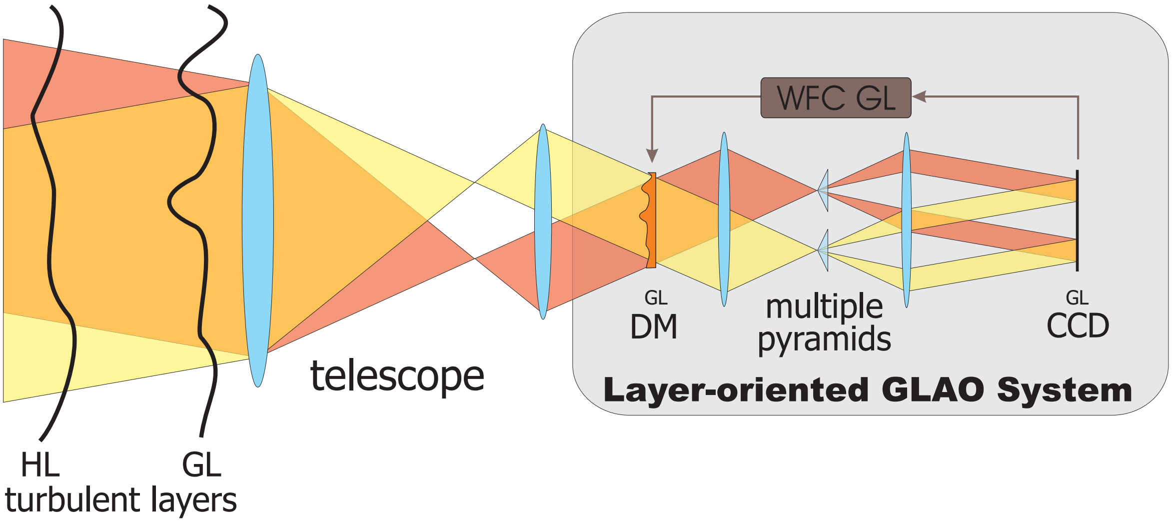

FIGURE 2.19: Illustration of the principle of Layer-Oriented Ground-Layer Adaptive Optics. For this concept, several pupil plane wavefront sensors measure the wavefront aberrations of several guide stars, but the wavefront aberrations of only the most turbulent layer (the ground-layer) are corrected with one DM. Multiple guide stars are necessary to disentangle the wavefront aberrations induced by the different turbulent layers.

For these reasons, Rigaut (2002) proposed an “MCAO-light” system, using multiple guide stars, but correcting only a single turbulent layer. Fortunately, the atmosphere is in favor of such an approach: most of the turbulence is concentrated in only a few layers. By far the most turbulent is located in the first few tens to hundreds of meters above the ground. As shown in chapter 6, this ground-layer contains typically up to 70% of the total turbulence at Mt. Graham. The situation is similar at other sites as shown by SCIDAR observations at e.g. San Pedro Martir (Avila et al., 2004), La Palma (Fuensalida et al., 2004b), Cerro Pachon (Tokovinin and Travouillon, 2006), Cerro Tololo (Tokovinin et al., 2003), La Silla (Sadibekova et al., 2006) and Calar Alto (Weiss et al., 2002b).

If only the turbulence effects of this ground-layer are corrected, then the performance will of course not be as good as for Classical on-axis AO, because at least $\approx$30% of the wavefront aberrations have to be left uncorrected. However, the wavefront aberrations induced by the ground-layer exhibit only a very small dependence on the viewing direction (fig. 2.16): they are almost the same for all objects in the FoV. Therefore, the performance of a GLAO system should be uniform over the FoV and there is no anisoplanatism effect like in Classical AO Systems. Simulations performed for GLAO systems indeed predict only a moderate Strehl ratio, but the FWHM of the PSF in the field is significantly reduced by a factor of $\approx$2 at $\lambda = 0.7\,\mu$m, as compared to seeing-limited observations, even over a wide field of several arcminutes (Tokovinin, 2004; Nicolle et al., 2004; Rutten et al., 2006). Such a GLAO system would be well suited for scientific applications where a diffraction-limited image is not required, but a significant gain is already achieved for an effective improvement of the seeing by a factor of $\approx$2 over a few arcminutes. Multi-object spectroscopy is an obvious example.

There are two possibilities to separate the wavefront aberrations induced by the ground-layer from those of the other high-altitude turbulent layers. One is to create an artifical guide star with a laser at an altitude of only a few kilometers above the telescope, and thus sample only the turbulence below this altitude. This approach is currently being pursued by a number of observatories: at the GMT (Athey et al., 2004), ESO (Hubin et al., 2004), the WHT (Morris et al., 2004), and SOAR (Tokovinin et al., 2004).

The other possibility is to use multiple guide stars and then – similar to a full-fledged MCAO system – to retrieve the wavefront aberrations introduced by the single layers from the correlation of the wavefront aberrations in the different directions. This can be done in the Layer-Oriented or Star-Oriented fashion as introduced above. Figure 2.19 illustrates the principle of a layer-oriented GLAO system as a comparison to figure 2.17, which shows a full MCAO system. This approach is currently being developed for example at the TNG (Egner et al., 2006a).

Open-loop measurements with a SHS already demonstrated the principle of the MCAO concept by comparing the wavefront reconstructed from multiple off-axis guide stars to the measured wavefront of an on-axis star (Ragazzoni et al., 2000b; Velur et al., 2006; Baranec et al., 2006). However, no GLAO or MCAO system is currently operating in closed loop on the night sky. One of the first such systems, the MAD instrument of ESO, achieved first closed loop operation in the Star-Oriented mode in the lab at the end of 2005 (Marchetti et al., 2006). The solar observatories are more advanced in this respect: there are already 2 MCAO systems running on-sky to observe the solar surface (Berkefeld et al., 2005; Rimmele et al., 2006).

2.6 THE LBT & LINC-NIRVANA

Since this thesis is focused on the MCAO system of LINC-NIRVANA, a brief overview of the LBT and the LINC-NIRVANA instrument itself will be given in this section.

2.6.1 THE LBT

The Large Binocular Telescope (LBT) is nearing completion on Mt. Graham in south-western Arizona (Hill and Salinari, 2004). The current status can be seen in figure 2.20, with the telescope being operational, but still with only one instrument mounted to it. According to the current schedule, it will be fully operational with full interferometric capabilities in late 2008 with the first generation of instruments being commissioned. The LBT is being built and operated by a consortium of various astronomical institutes, including the MPIA.

As can be seen in figure 2.20, the LBT will have two primary mirrors with a diameter of 8.4 m each and a center-to-center distance of 14.4 m on one common alt-az mounting. These mirrors are spin-cast and have a honeycomb back-structure to save not only a significant amount of time and money in their manufacturing, but also to guarantee optimal stability and very short latencies for temperature adjustments (Martin et al., 2003). They are supported by an active optics system to keep them in shape, independent of the telescope altitude (Martin et al., 2004), and they have a very short f-ratio of 1.14, allowing for a compact design of the telescope. The Gregorian optical design with a first focus before the secondary mirrors has a big advantage when using deformable secondary mirrors. In such a case, their surface can be made concave, making the manufacturing, polishing, testing and calibration much easier.

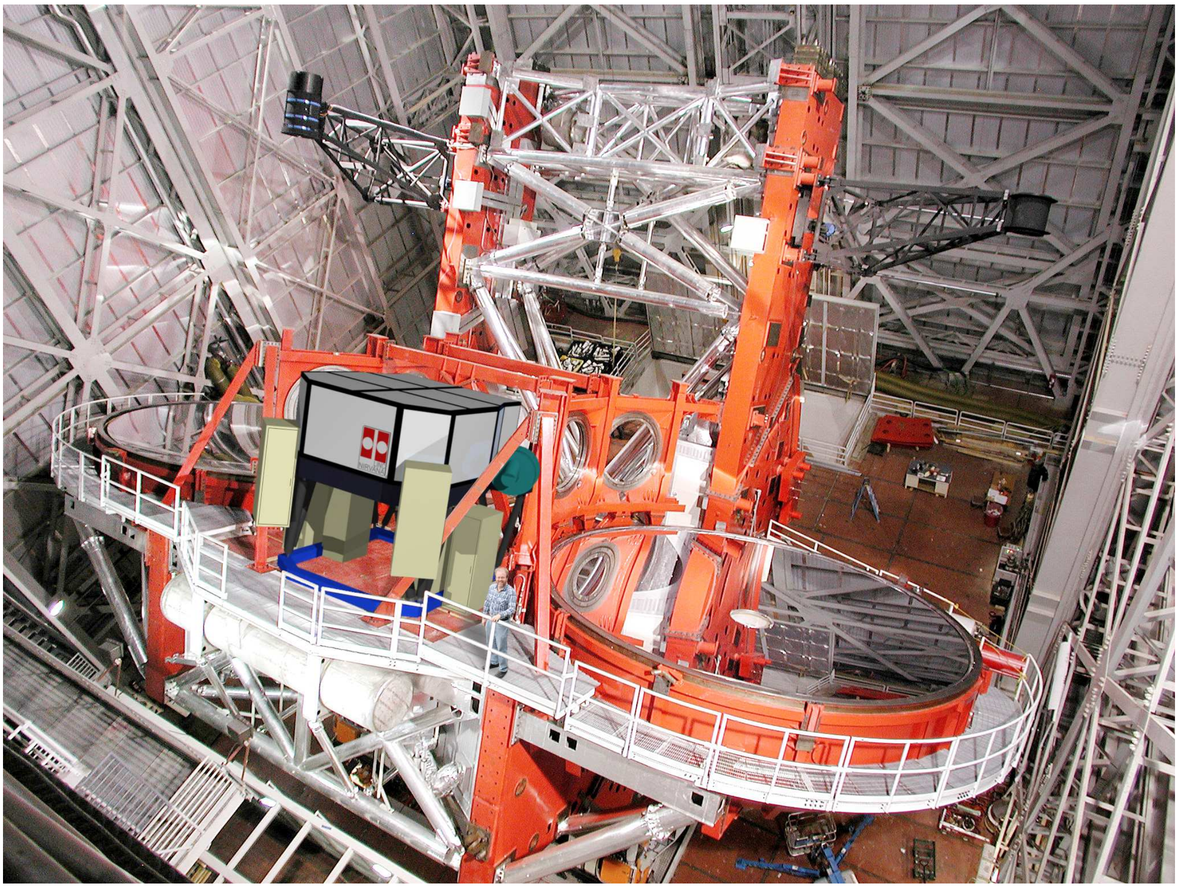

FIGURE 2.20: Picture showing the status of the LBT in mid 2006. The two primary mirrors are installed and aluminized and the LBC blue camera (black can) is mounted above the left primary. Above the right primary one can see the mounting of LBC red. The other instruments (LUCIFER, LBTI and LINC-NIRVANA) will be mounted on the platform between the two primaries. MODS will be mounted in the Cassegrain focus below each of the two primaries and the fiber-fed PEPSI instrument will sit in an optical lab in the pier of the telescope. A CAD model of LINC-NIRVANA was included in this picture to show the size and location of the final instrument. Note the human figure for scale. Photo composition courtesy Tom Herbst.

Several instruments will be mounted permanently to the telescope between the two primary mirrors. A movable flat tertiary mirror reflects the light into the desired instrument. What is also unique with the LBT is that except for the prime focus cameras and MODS, all other instruments will have AO correction available. This can be achieved by a common wavefront sensing unit AGW (Storm et al., 2004) and two deformable secondary mirrors, each with 672 voice-coil actuators (Esposito et al., 2004; Riccardi et al., 2004). In total, there are 12 focal stations where instruments can be attached to the telescope (Wagner, 2004). In the first phase, this will include two visible to NIR wide-field cameras (LBC), a visible to NIR high-resolution spectrograph (PEPSI), two IR imagers and low-resolution, multi-object spectrographs (LUCIFER), two visible multi-object spectrographs with medium resolution (MODS), a nulling interferometer (LBTI) and a Fizeau Interferometer (LINC-NIRVANA). Both of the latter work in the NIR.

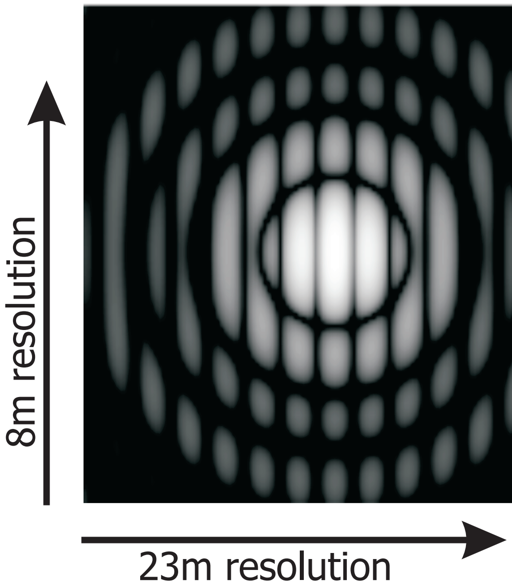

FIGURE 2.21: The ideal theoretical PSF of LINC-NIRVANA in logarithmic scale, with the typical fringe-pattern.

2.6.2 LINC-NIRVANA

LINC-NIRVANA will combine the light from the two primary mirrors coherently in Fizeau mode. In this interferometry type, the light comes together in the focal plane on the detector. The single telescopes thus act like holes in a mask covering a much larger telescope. For such a configuration, true imaging over a wide field-of-view is possible, with an angular resolution corresponding to the maximum edge-to-edge distance in the telescope configuration, i.e. 22.8 m. The kind of exciting new science, which can be done when such a high angular resolution is available is described in Rix and Herbst (1998); Eckart et al. (2006).

However, to achieve this theoretical angular resolution, the telescope and the instrument have to be adjusted very precisely. For example, the length of the light path through the atmosphere, the telescope and the instrument to the detector has to be the same for all light rays to within a fraction of the observing wavelength. Furthermore, any aberrations induced by the atmosphere or the telescope have to be corrected with an sophisticated AO system. If all these conditions are fullfilled, the PSF of a star will look like an 8.4 m Airy disk, crossed by fringes, as shown in figure 2.21.

Due to the geometry of the LBT, the high angular resolution corresponding to a 22.8 m telescope can be achieved only in the direction along the line connecting the two primaries. Perpendicular to this direction, the resolution is that of an 8.4 m telescope. However, since the LBT is mounted alt-az, the projection of the entrance pupil of the LBT onto the sky rotates during the night and thus also the PSF with respect to the science object. By taking several images of the science object at different times of the night and numerically combining the information, the full angular resolution can be retrieved in all directions.

The actual hardware implementation of LINC-NIRVANA is shown in figure 2.22. All opto-mechanical components are mounted on a carbon fiber bench to guarantee optimal stability and good vibration damping (Rohloff et al., 2006). The light in an

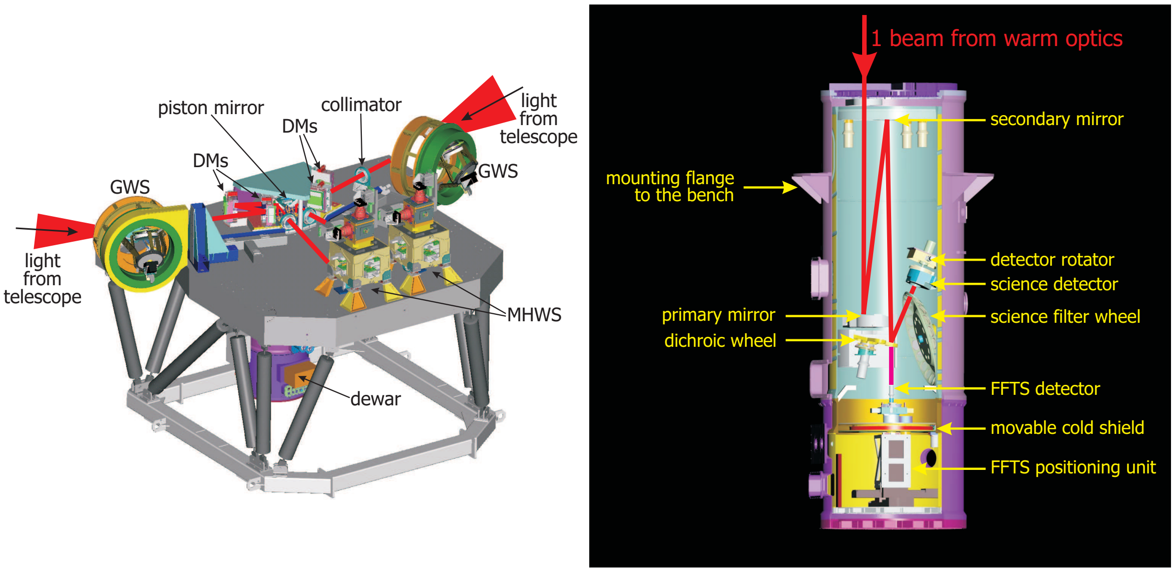

FIGURE 2.22: CAD drawings of the optical bench (**left**) and the inside of the dewar (**right**) of LINC-NIRVANA with the main components.

annulus of 2 to 6 arcmin diameter coming from the telescope is reflected by an annular mirror into the Ground-Layer Wavefront Sensor (GWS). The two GWS units measure the wavefront aberrations caused by the turbulence near the ground in a layer-oriented fashion and send correction signals to the deformable secondary mirrors of the LBT. These mirrors are conjugated to $\approx$100 m above the ground. Each GWS uses up to 12 natural guide stars, whose wavefront aberrations are measured with individual pyramids. These pyramids can be moved with motorized linear stages to the position of the guide stars in the FoV and the beams of all guide stars are collimated with a common optics to image the pupils on a single detector (Farinato et al., 2006; Diolaiti et al., 2005a).

The light from the inner part of the field is collimated by a set of warm optics (Bizenberger et al., 2006) and corrected for wavefront aberrations induced by high-altitude turbulent layers by one (with the option of a second) additional deformable mirror in each arm of LINC-NIRVANA. Depending on the vertical atmospheric turbulence structure, the conjugation altitude of these DMs can be adjusted to between 4 and 15 km above the ground. After the collimator, the light is reflected off the so-called piston-mirror, which is mounted on a fast moving piezo-stage to compensate for the optical path differences between the beams coming from the two telescopes. The infrared part of the light enters the cryostat, while the visible light is reflected by a dichroic mirror into the Mid-High-Layer Wavefront Sensor (MHWS).

The opto-mechanical design of the MHWS is similar to the GWS, it uses up to 8 pyramids to measure the wavefront distortions induced by high-altitude turbulent layers in the atmosphere and sends correction signals to the DMs within LINC-NIRVANA (Farinato et al., 2006; Diolaiti et al., 2005b). Similar to the GWS, the pyramids can be moved in the 2 arcmin FoV and the pupils are imaged onto the WFS cameras with one common optics. When operating only the GWS with the deformable secondary mirror, a layer-oriented GLAO system is realized, when using both the GWS and the MHWS to correct the wavefront aberrations, LINC-NIRVANA will contain a full-fledged layer-oriented MCAO system (Gaessler et al., 2004, 2005).

As mentioned, the infrared part of the light enters the cryostat (Laun et al., 2006), where it is focused with two parabolic mirrors. Part of the light is reflected to the science detector, the other part is used by the Fringe and Flexure Tracking System (FFTS) to measure the optical path difference between the two beams and send correcting signals to the piston mirror (Bertram et al., 2004, 2006b,a). The FFTS can be moved in a 1×1.5 arcmin field, to use a bright source other than the science object for fringe tracking. The cryostat also contains some filter wheels for the science channel and a dichroic wheel to use the science object also for fringe-tracking. For the science detector a Hawaii-II chip with 2048×2048 pixel is used. In order to achieve Nyquist sampling of the diffraction-limited PSF of this effective 22.8 m telescope at $\lambda = 1.1\,\mu$m, the pixel-scale is 5.11 mas / pixel, which results in a FoV of 10×10 arcsec.

CHAPTER 3

MCAO – Theoretical Considerations

> 'the problem is all inside your head', she said to me
> 'the answer is easy if you take it logically'
>
> *Paul Simon, "50 ways to leave your lover"*

3.1 INTRODUCTION

The performance of an GLAO or MCAO system depends critically on the conjugation height h_{conj} of the Deformable Mirrors (DMs). This will be demonstrated explicitly in section 5.6.1. Only if h_{conj} match the vertical turbulence structure, can a large Strehl ratio over a wide field be achieved. In this chapter, we will discuss how the optimal conjugation height h_{opt} can be determined from measured C_N^2-profiles and derive an analytical tool-box to obtain fast performance estimations. This allows optimization of the parameters of an MCAO instrument, even online during on-sky operation, and gives astronomers an idea of what they can expect.

One possibility to determine h_{opt} is full end-to-end simulations. In this case, the propagation of the light from the star through the atmosphere, the telescope and the AO system to the science detector is modelled. To achieve a statistically significant result, a time-sequence of a few seconds is usually simulated. However, such end-to-end simulations are computationally extremely intensive, requiring several hours with current computer hardware to determine the performance of the system for just one set of parameters. The optimal conjugation height can therefore be calculated only for a few selected C_N^2-profiles. A study of the short-term variability of h_{opt} over the course of one night is thus not possible. Another problem of such simulations is that they usually discretize the atmospheric turbulence in a few (5 to 9) infinitely thin layers (Arcidiacono, 2004; Bertram, 2005; Femenia and Devaney, 2003). When this is done, h_{opt} depends critically on where exactely these layers are placed, resulting in a limited significance of the derived results.

Another method to study the optimal conjugation heights h_{opt} of the DMs are semi-analytical models of the interaction of an MCAO system with the vertical turbulence structure of the atmosphere. To determine h_{opt} for maximal isoplanatic angle, such an analytical model was presented by Tokovinin et al. (2000). However, depending on the science case, one might want to adjust h_{conj}, not to achieve a maximum isoplanatic angle, but maximal Strehl-ratio on-axis, or maximal isopistonic angle. In this chapter we therefore present a different analytical model to optimize h_{conj} according to these criteria. This model is an extension of the approach proposed by Owner-Petersen and Gontcharov (2002). After the presentation of the principle of this model, we will then systematically apply this approach to measured C_N^2-profiles to determine h_{opt} for different criteria.

This model takes only a few seconds to calculate h_{opt} for one C_N^2-profile. On the other hand, it has to make certain assumptions and simplifications: it cannot take into account many effects and error-sources of the MCAO system. For example, the position and brightness of the guide stars are fixed and do not represent a real asterism. A map of the Strehl ratio in the field can therefore not be derived with this model. Nevertheless, as will also be shown in this chapter, the main results obtained, especially h_{opt} are independent of such simplifications.

3.2 FILTERING OF C_N^2-PROFILES

The semi-analytical model presented here is based on filtering the measured $C_N^2(h)$ profiles with filter functions $\mathbf{TFF}(h)$, which represents the correction efficiency at an altitude h of the layer-oriented (LO) MCAO system.

In a LO-MCAO system, only the wavefront aberrations caused by the turbulent layer at the conjugation altitude h_{conj} of the wavefront-sensors are seen in focus. Layers above or below are smeared out. Therefore, the correction of a turbulent layer by the DM, which is conjugated to the same altitudes as the WFS, depends on the vertical separation Δh between the altitude of the layer h_{layer} and the WFS h_{conj}. The reduction in the correction efficiency with Δh depends primarily on the field-of-view (FoV) of the WFS and the total correction efficiency of the MCAO system. For a larger FoV, the focal depth of the LO-WFS is smaller, the correction efficiency decreases therefore more rapidly with Δh than for a narrow FoV. The total correction efficiency then depends essentially on the number N_{modes} of corrected modes, the loop frequency f_{loop} and other characteristics of the actual hardware components of the MCAO system.

The $\mathbf{TFF}(h)$ functions include all these effects and are defined in a way that multiplying a measured C_N^2-profile with $\mathbf{TFF}(h)$ gives the fraction of the remaining turbulence at an altitude h after correction by the AO system. This remaining turbulence is left uncorrected, because it can either not be seen with the WFS or it cannot be corrected due to finite spatial and temporal sampling of the AO system. The residual C_N^2-profile can then be used to calculate the residual variance of the wavefront aberrations $\sigma^2_{\mathrm{tot,res}}$, the on-axis residual Fried-Parameter $r_{0,\mathrm{res}}$ or the isoplanatic angle $\vartheta_{0,\mathrm{res}}$ for the given parameters of the MCAO system. Finally, the h_{opt} are found by changing the conjugation heights of the DMs in the calculation of $\mathbf{TFF}(h)$, until $r_{0,\mathrm{res}}$ or $\vartheta_{0,\mathrm{res}}$ are maximal.

3.2.1 LAYER-TRANSFER FUNCTIONS

The first step in the calculation of the total filter functions $\mathbf{TFF}(h)$ is to quantify the smearing of the measured wavefront aberrations of the non-conjugated layers. This smearing is best expressed in Fourier-space as a function of the spatial frequency $\mathbf{k}$. For one DM at a conjugation altitude of h_{conj} and several guide stars

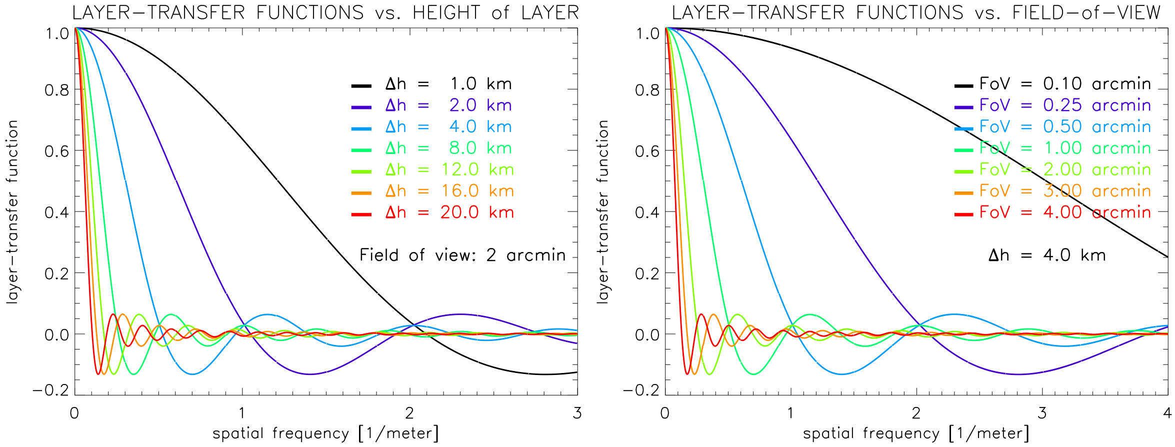

FIGURE 3.1: **Left:** The layer-transfer functions $T(k,\ \Delta h)$ for different distances Δh between the altitude of the turbulent layer and the conjugation height of the layer-oriented wavefront-sensor, as a function of the spatial frequency k. **Right:** The layer-transfer functions $T(k,\ \Delta h)$ for different sizes of the field-of-view.

located at angular separation $\vec{\alpha}$ from the optical axis, the fraction $T(\mathbf{k}, \Delta h)$ of the wavefront aberrations, which is seen by the WFS is given by (Owner-Petersen and Gontcharov, 2002)

$$T(\mathbf{k}, \Delta h) \;=\; \frac{1}{Q} \sum_{q=1}^{Q} \mathbf{exp}\left[2\pi\, i\, \cdot \Delta h \cdot \mathbf{k} \cdot \vec{\alpha}\right] \;, \tag{3.1}$$

with $\Delta h \;=\; (h_{\text{layer}} - h_{\text{conj}})$. For an homogenous distribution of an infinite number of guide stars on a circle with radius α_0, the layer-transfer function $T(k,\ \Delta h)$ can be expressed as

$$T(k,\ \Delta h) \;=\; 2\, \frac{J_1\left[2\pi\ \Delta h\ k\, \alpha_0\right]}{2\pi\ \Delta h\ k\, \alpha_0} \;, \tag{3.2}$$

with $k = \mathbf{abs}(\mathbf{k})$ and $J_1(x)$ the first order Bessel function of the first kind. Figure 3.1 plots $T(k,\ \Delta h)$ for different values of Δh and the FoV. For example, any wavefront aberrations with spatial frequencies larger than $0.3\,\text{m}^{-1}$ are filtered out by more than 90%, when the distance between the h_{layer} and h_{conj} is more than 8 km for a WFS-FoV of 2 arcmin.

3.2.2 MODAL COVARIANCE MATRIX

To describe the filtering on the single Zernike modes as measured by a Layer-Oriented MCAO system, the temporal average variance of their modal coefficients has to be examined. Assuming the Kolmogorov model for the single turbulent layers (eqn. 2.2), the residual power-spectrum $\Psi^*(k)$ for a layer can be calculated:

$$\Psi^*(k) \;=\; 0.033\, C_N^2\, k^{-11/3} \cdot \left|T(\mathbf{k},\, \Delta h)\right|^2 \;. \tag{3.3}$$

Using this equation as a substitute for equation 2.2, the residual wavefront variance σ^2_{res} in the center of the field after correction of all measured wavefront aberrations is given by (Owner-Petersen and Gontcharov, 2002)

$$\sigma^2_{\text{res}}(\Delta h) \;=\; 0.023 \left(\frac{D}{2r_0}\right)^{5/3} \int k^{-8/3} \left[1 - \left(2\,\frac{J_1^2(2\pi\, k)}{2\pi\, k}\right)^2\right] \left|T(\mathbf{k},\, \Delta h)\right|^2 d\mathbf{k} \;. \tag{3.4}$$

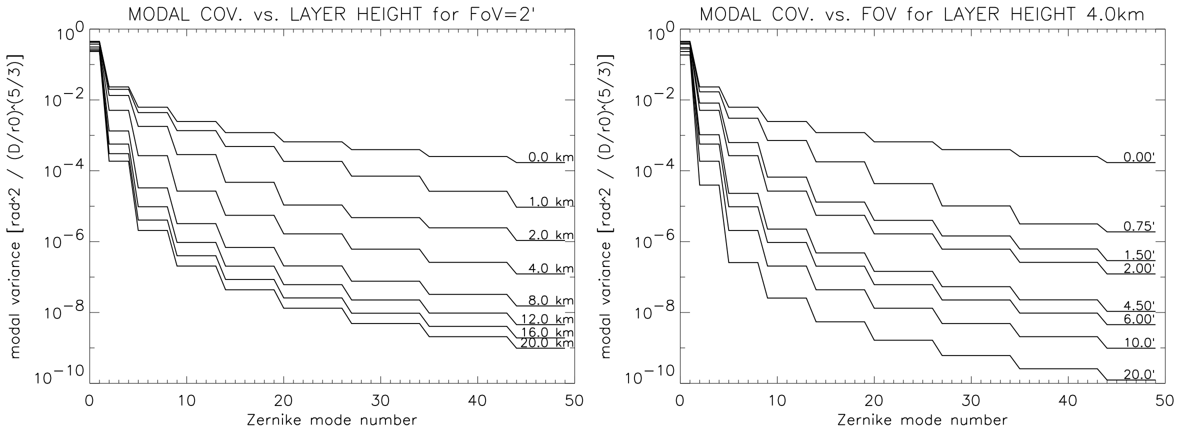

FIGURE 3.2: The diagonal elements of the perceived modal covariance matrix $\mathbf{C}^*_\Phi(\Delta h)$ for one turbulent layer in a LO-MCAO system. **Left:** $\mathbf{C}^*_\Phi(\Delta h)$ for a FoV of 2 arcmin and various vertical separations between the turbulent layer h_{layer} and the conjugation plane h_{conj} of the WFS. **Right:** $\mathbf{C}^*_\Phi(\Delta h)$ for different FoV and a fixed distance of 4 km between h_{layer} and h_{conj}.

Similarly, the residual modal covariance matrix $\mathbf{C}^*_{\Phi,j,j'}(\Delta h)$ of Zernike polynomials can be calculated for a given FoV by modifying equation 2.35 with $T(\mathbf{k}, \Delta H)$:

$$\begin{aligned}\mathbf{C}^*_{\Phi,j,j'}(\Delta h) \;=\; & \frac{0.046}{\pi^2}\left(\frac{D}{2r_0}\right)^{5/3} \\ & \times\sqrt{(n+1)(n'+1)}\;(-1)^{(n+n'-2n)/2}\,\delta_{m,m'} \\ & \times\int k^{-8/3}\,\frac{J_{n+1}(2\pi k)\,J_{n'+1}(2\pi k)}{k^2}\,\left|T(\mathbf{k},\Delta h)\right|^2 d\mathbf{k}\;.\end{aligned} \tag{3.5}$$

In figure 3.2, the diagonal elements of the modal covariance matrix for Zernike modes and Kolmogorov turbulence are plotted for different separations Δh between h_{conj} and h_{layer} and various sizes of the FoV. Since Zernike modes are approximately ordered according to spatial frequencies, and the filtering is more efficient for high-spatial frequencies, high-order Zernike modes are attenuated more than low-order modes. Tip-tilt can be sensed almost independently of Δh. On the other hand, the perceived modal weight of, for example, Zernike mode 25 is suppressed by 2 orders of magnitude for $\Delta h = 8$ km and a FoV of 2 arcmin (fig. 3.2, left).

To calculate the variance of the seen wavefront aberrations, we follow the approach of Noll (1976), but using equation 3.5 instead of 2.35. For N corrected Zernike modes, the perceived residual variance of the wavefront aberrations is:

$$\sigma_N^{2*}(\Delta h, \alpha) \;=\; \langle\Psi(\kappa)\rangle - \sum_{j=0}^{N}\left\langle \mathbf{C}^*_{\Phi,j,j}(\Delta h)\right\rangle\;, \tag{3.6}$$

where $\langle\Psi(\kappa)\rangle$ is the phase power-spectrum for Kolmogorov turbulence (eqn. 2.2). The singularity due to $\langle\Psi(\kappa)\rangle \propto \kappa^{-11/3}$ at low spatial frequencies κ is solely due to the piston term, thus posing no problem for the evaluation of equation 3.6 for $j > 0$. For $\Delta h = 0$, this equation gives the known result of $\sigma_1^2 = 1.030(D/r_0)^{5/3}\,\text{rad}^2$ (eqn. 2.18). The layer-filter functions $\mathbf{LFF}(\Delta h)$ are then defined as the fraction of the perceived and thus maximal correctable wavefront aberrations for a given FoV

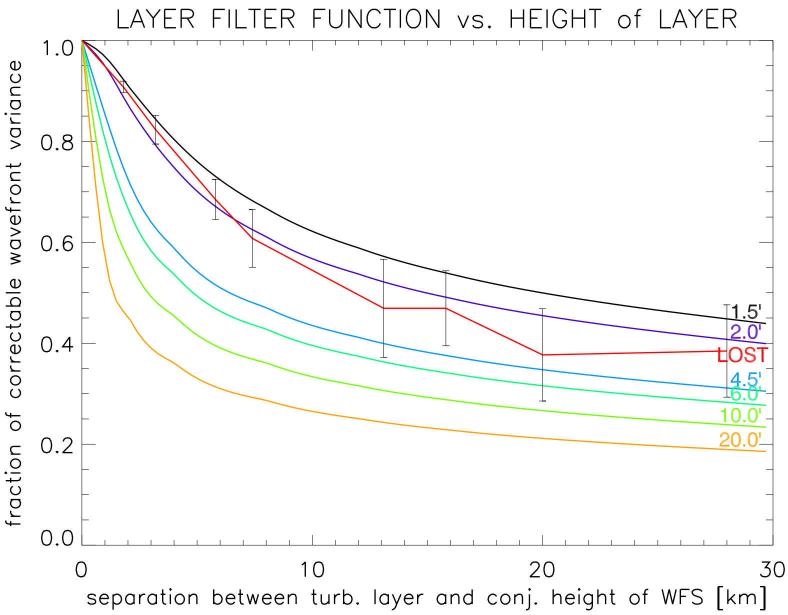

FIGURE 3.3: The layer-filter functions for various sizes of the field-of-view as a function of the distance between the turbulent layer and the conjugation height of the wavefront-sensor. Also shown are the results of numerical simulation with the LOST code using the parameters of LINC-NIRVANA (FoV=2 arcmin).

α and the separation Δh between h_{layer} and h_{conj}:

$$\mathbf{LFF}(\Delta h) \;=\; \frac{\sigma_1^{2*}(\Delta h, \alpha)}{\sigma_1^2} \; . \tag{3.7}$$

The $\mathbf{LFF}(\Delta h)$ are plotted for different field-of-views in figure 3.3. This figure also shows a nice match between these analytic predictions and numerical simulations performed with the LOST code (Arcidiacono, 2004).

3.2.3 TOTAL FILTER FUNCTIONS

The $\mathbf{LFF}(\Delta h)$ as defined in equation 3.7 describe which fraction of the wavefront variance can be seen with the LO-WFS. To describe the fraction of the turbulence, which is seen by the WFS and can be also corrected by, for example, two DMs, the total filter functions $\mathbf{TFF}(h)$ are defined:

$$\begin{aligned}\mathbf{TFF}(h) \;&=\; 1 \;- \\ &\mathbf{max}\Big[\mathbf{min}\big[\mathbf{LFF}(h-h_{\text{conj},GL}),\, c_{\text{max,GL}}\big],\; \mathbf{min}\big[\mathbf{LFF}(h-h_{\text{conj},HL}),\, c_{\text{max,HL}}\big]\Big](h)\;,\end{aligned} \tag{3.8}$$

which can also be readily extended to more DMs. These $\mathbf{TFF}(h)$ therefore describe which fraction of the turbulence is left uncorrected as a function of the altitude h above the ground.

The respective correction efficiency of the DMs are described by the coefficients $c_{\text{max},i}$ $(0 < c_{\text{max},i} < 1)$. For $c_{\text{max}} = 1$, all measured wavefront aberrations are also perfectly corrected by the DMs, while for $c_{\text{max}} = 0$, they are left completely uncorrected. For the Kolmogorov model, c_{max} can be estimated from the fitting error

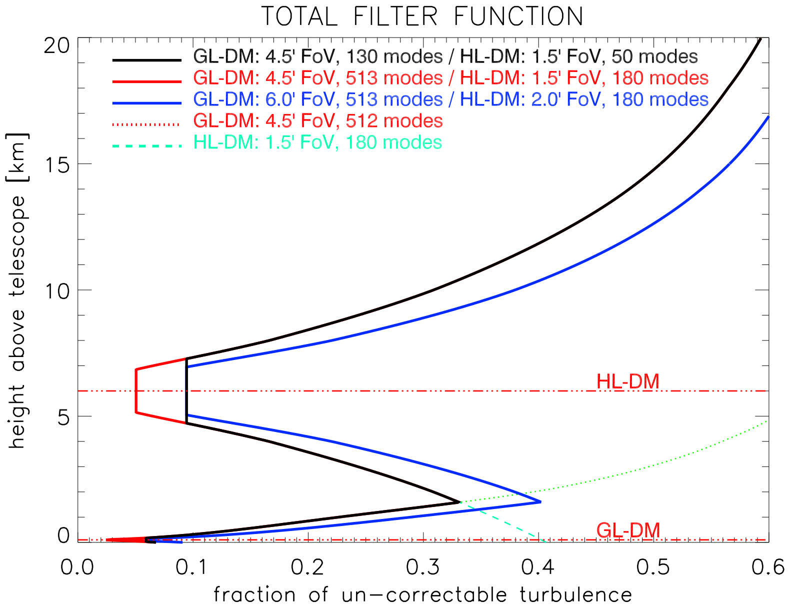

FIGURE 3.4: The total filter functions $\mathbf{TFF}(h)$ for different numbers of corrected modes and sizes of the FoV of a layer-oriented WFS, where the conjugation altitude $h_{\text{conj,i}}$ of the two WFS are indicated by the dashed-dotted lines (0.1 and 6 km). Close to $h_{\text{conj,i}}$ most of the turbulence is seen and can be corrected, and only 5% of the wavefront variance remain for example un-corrected between 5 and 7 km altitude, for 180 corrected modes and 1.5 arcmin WFS-FoV. These remaining wavefront aberrations are either not seen by the WFS because they are defocused, or they consist of too high spatial frequencies, which cannot be corrected with the limited number of modes.

(eqn. 2.53) via the number N_{modes} of corrected modes, by summing up the modal variances $\mathbf{C}_\Phi$ (eqn. 2.35):

$$c_{\max} = 1 - \frac{2}{1.030} \cdot \sum_{n=1}^{N_{\text{modes}}} \mathbf{C}_{\Phi,n,n} \; , \tag{3.9}$$

and assuming a similar value for the temporal error σ^2_{temp}. Figure 3.4 plots the $\mathbf{TFF}(h)$ for 1 and 2 DMs, various fields-of-view and numbers of corrected modes.

The residual $C^2_{N,\text{res}}(h)$ profile after correction by the AO system can be calculated from the measured C_N^2-profile via

$$C^2_{N,\text{res}}(h) = C_N^2(h) \cdot \left(1 - \sqrt{1 - \mathbf{TFF}(h)}\right) . \tag{3.10}$$

For a sample C_N^2-profile, the residual $C^2_{N,\text{res}}(h)$ profile is plotted in figure 3.5 for a GLAO and a MCAO system with 2 DMs. For comparison, the filtering efficiency for a single-star AO system on-axis is independent of the height of the layers. The vertical structure of the residual C_N^2-profile for such a system is the same as the original one. It is only attenuated by the same factor, independent of the height of the layer.

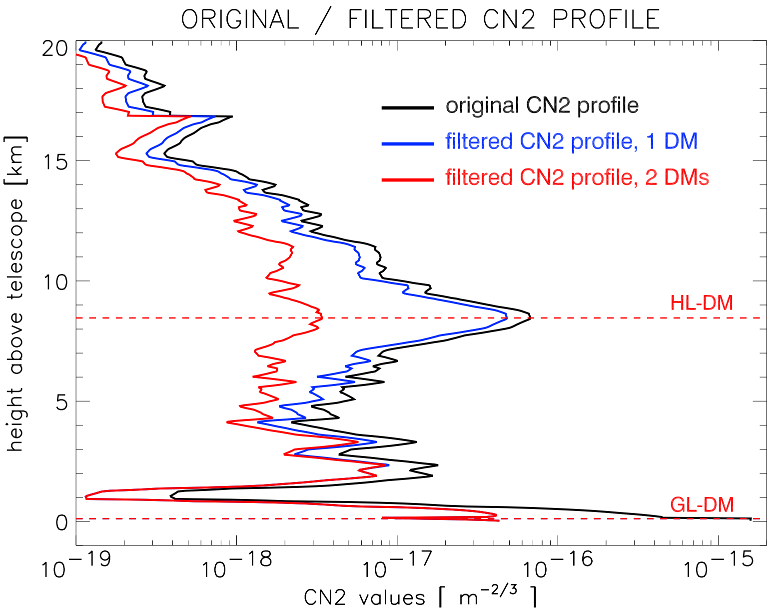

FIGURE 3.5: An original and the residual C_N^2-profile after applying the total filter functions $\mathbf{TFF}(h)$ for one and two DMs. The conjugation altitudes of the two WFS / DMs are indicated by the dashed lines. In this particular case, 80% of the turbulence are corrected by the GLAO system and 90% with the MCAO system having two DMs.

3.3 OPTIMAL CONJUGATION HEIGHT

The residual $C_{N,\text{res}}^2(h)$ profile once determined, can be used to calculate the residual Fried-Parameter $r_{0,\text{res}}$, Isoplanatic Angle $\vartheta_{0,\text{res}}$ and Isopistonic Angle $\vartheta_{P,\text{res}}$. Changing h_conj obviously also changes these values. The conjugation heights $h_\text{conj,i}$ of the DMs when these parameters are optimal are subsequently called the respective optimal conjugation heights $h_\text{opt,i}$. These might be different for the different optimization criteria.

3.3.1 CALCULATION PRINCIPLE

Since the C_N^2-profiles presented in this thesis (chapter 6) were measured at Mt. Graham, we applied the total filter functions $\mathbf{TFF}(h)$ with the parameters of LINC-NIRVANA, which will be installed at the LBT. The relevant parameters for the application of the $\mathbf{TFF}(h)$ are the independent control loop architecture of the two layers (sect. 2.6.2), making it possible to apply sequentially the $\mathbf{TFF}(h)$ for the two DMs to the measured $C_N^2(h)$ profiles. As in the optical path, first the correction by the Ground-Layer (GL) DM is subtracted from the C_N^2-profile and then the contribution of the High-Layer (HL) DM. Using 8 and 12 guide stars, respectively, with the same rough brightness and random distribution in the field, results in a large number of baselines in the Fourier space, rendering the approach of infinite guide stars (eqn. 3.2) applicable. This is important for the homogenous filtering of all spatial frequencies as required for the applied simplified $\mathbf{TFF}(h)$. Nevertheless, since the guide stars in LINC-NIRVANA are randomly distributed all over the FoV, the baselines are biased with respect to shorter ones. For this reason, we used a circular guide star distribution with a diameter of 0.75 of the FoV of the respective WFS for the calculation of the $\mathbf{TFF}(h)$.

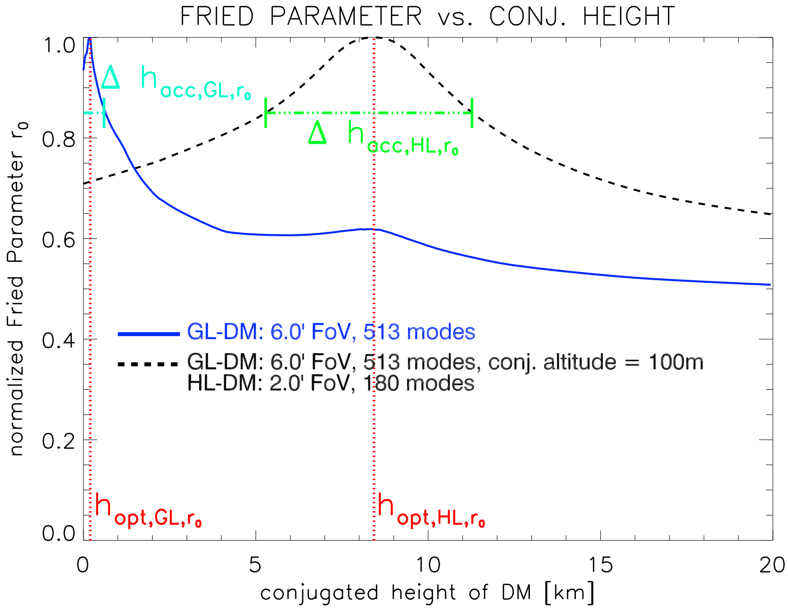

FIGURE 3.6: The residual normalized Fried parameter $r_{0,\mathrm{res}}^N$ versus the conjugated altitude for 1 DM and 2 DMs for the same C_N^2-profile as in figure 3.5. For the 2 DM case, $h_{\mathrm{conj,GL}}$ is fixed at 100 m and only the influence of $h_{\mathrm{conj,HL}}$ is shown. Considering for example a maximum Strehl ratio on-axis (i.e. maximum $r_{0,\mathrm{res}}$), the optimal conjugation height $h_{\mathrm{opt,GL},r_0}$ for the DM in a GLAO system is ≈100 m and the range of mis-conjugation $h_{\mathrm{acc,GL},r_0}$ for a drop in $r_{0,\mathrm{res}}$ by 15% is ≈400 m.

The absolute performance of the MCAO system is not relevant in the context of this chapter. Rather, it will be analyzed in chapter 6. Here, we will use the normalized values of the residual astro-climatic parameters. For a sample C_N^2-profile, the normalized residual Fried-parameter $r_{0,\mathrm{res}}^N$ as a function of the conjugated height $h_{\mathrm{conj,GL}}$ of the GL-DM in a GLAO system is plotted in figure 3.6. Each point on this curve corresponds to an $h_{\mathrm{conj,GL}}$. Its value is calculated by determining $\mathbf{TFF}(h)$ for this $h_{\mathrm{conj,GL}}$, applying $\mathbf{TFF}(h)$ to the measured C_N^2-profile and calculating the Fried Parameter from the resulting, residual $C_{N,\mathrm{res}}^2(h)$ profile. Also shown is $r_{0,\mathrm{res}}^N$ as a function of the conjugation altitude of the HL-DM $h_{\mathrm{conj,HL}}$ for a MCAO system with a fixed $h_{\mathrm{conj,GL}} = 100$ m. The respective optimal conjugation altitudes $h_{\mathrm{opt,GL},r_0}$ and $h_{\mathrm{opt,HL},r_0}$ are indicated for both cases. The same, but for a MCAO system with free adjustment possibilities of both DMs is shown in figure 3.7.

To assess the sensitivity of performance to mis-conjugations, the acceptable conjugation range $\Delta h_{\mathrm{acc,i},r_0}$ is defined. It is given as the maximum distance between the actual conjugation altitude $h_{\mathrm{conj,i}}$ and the optimal conjugation altitude $h_{\mathrm{opt,i},r_0}$ for a relative reduction of $r_{0,\mathrm{res}}$ of less than 15%. For the two cases in figure 3.6, $h_{\mathrm{acc,GL},r_0}$ and $h_{\mathrm{acc,HL},r_0}$ are indicated. It is obvious that $h_{\mathrm{conj,GL}}$ of the GL DM is critical to achieve a good Strehl ratio on-axis (large $r_{0,\mathrm{res}}$) for a GLAO or MCAO system (fig. 3.6 and 3.7). Even a mis-conjugation of a few hundred meters already makes a large difference in the achievable performance. Once $h_{\mathrm{conj,GL}}$ is set, $h_{\mathrm{conj,HL}}$ is much less critical: $h_{\mathrm{acc,HL},r_0}$ is usually a few kilometers (fig. 3.6 and 3.7). Concerning $h_{\mathrm{acc,i},r_0}$, one should keep in mind that the vertical resolution of the measured C_N^2-profiles with a SCIDAR is ≈1 km (eqn. 2.48). $h_{\mathrm{opt,i}}$ can thus be determined with an accuracy of not more than ≈100 to 300 meters.

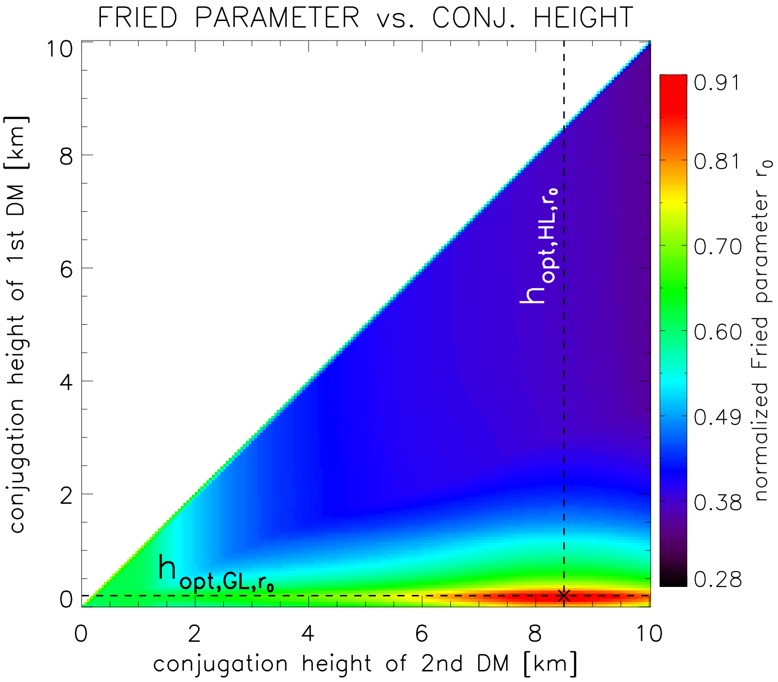

FIGURE 3.7: Color-coded plot of the residual normalized $r^N_{0,\mathrm{res}}(h_{\mathrm{conj,GL}}, h_{\mathrm{conj,HL}})$ versus the conjugated heights $h_{\mathrm{conj,GL}}$ and $h_{\mathrm{conj,HL}}$ of the two DMs for the same C_N^2-profile as in figure 3.5. To achieve a high Strehl ratio on axis (large $r_{0,\mathrm{res}}$), the ground-layer DM should be placed at ≈200 m, and the high-layer DM at ≈8.5 km above the telescope.

The procedure to find the optimal conjugation altitudes $h_{\mathrm{opt,i},\vartheta_0}$ and $h_{\mathrm{opt,i},\vartheta_P}$ for maximum residual isoplanatic angle $\vartheta_{0,\mathrm{res}}$ and isopistonic angle $\vartheta_{0,\mathrm{res}}$ is very similar to the one for the Fried parameter $r_{0\mathrm{res}}$ and thus not shown here. A comparison of the results obtained with this analytical model, relying on the layer filter functions $\mathbf{LFF}(h)$, and the model proposed by Tokovinin et al. (2000) is shown later in section 6.8.1 on page 134 with actual measured C_N^2-profiles.

3.3.2 INFLUENCE OF AO PERFORMANCE

For the determination of the optimal conjugated heights h_{opt} it is important to know the influence of the parameters of the MCAO system. The derived values for h_{opt} only have a general meaning, if the influence of the size of the field-of-view of the WFS and the overall correction efficiency is small.

The first verification step was to examine the influence of the overall correction efficiency of the MCAO system. Lower correction efficiency, due to smaller f_{loop}, fewer N_{modes}, etc. can be described by a smaller c_{max} in the calculation of the total filter function $\mathbf{TFF}(h)$ in equation 3.9. For each of the ≈10 000 measured C_N^2-profiles at Mt. Graham (chapter 6), h_{opt,r_0} was determined for various values of c_{max} and the resulting difference to the case of optimal correction ($c_{\mathrm{max}} = 1.0$) was calculated. As can be seen in figure 3.8, h_{opt,r_0} seems to be slightly larger for worse correction. For comparison, to achieve a Strehl ratio of 40% in the K-band at an 8 m telescope for a seeing of 0.8" in V-band, requires the correction of 98% of the wavefront aberrations. The 3-σ change in $h_{\mathrm{opt,HL},r_0}$ is ≈600 m in this regime, and thus of the order of the vertical resolution Δh_{GS} of the measured C_N^2-profiles. The impact on $h_{\mathrm{opt,GL},r_0}$ is much smaller: the 3-σ change is ≈150 m.

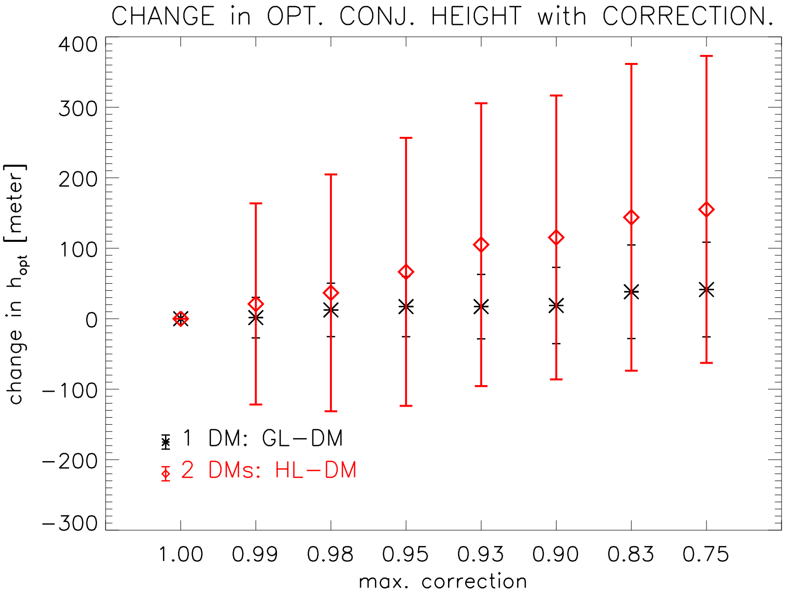

FIGURE 3.8: The mean change of the optimal conjugation altitude $h_{\mathrm{opt,GL},r_0}$ of the GL-DM in a GLAO system and $h_{\mathrm{opt,HL},r_0}$ of the HL-DM in a MCAO system with fixed $h_{\mathrm{conj,GL}}$ for different values of the correction efficiency of the AO system, as compared to theoretical maximal correction efficiency. The symbols are the mean value for all ≈10 000 measured C_N^2-profiles at Mt. Graham, and the error bars indicate their standard deviation.

As mentioned above, the field-of-view of the WFS in an MCAO system is an input parameter for the calculation of the total filter functions $\mathbf{TFF}(h)$. The mean change in h_{opt,r_0} for different sizes of the FoV for each of the measured C_N^2-profiles is shown in figure 3.9 for one DM in a GLAO and for a 2 DM MCAO system with a fixed $h_{\mathrm{conj,GL}} = 100\,\mathrm{m}$. The 3-$\sigma$ change is ≈600 m for $h_{\mathrm{opt,HL},r_0}$, which is of the order of the vertical resolution of the C_N^2-profiles and is thus acceptable for this application. Again, the impact on $h_{\mathrm{opt,GL},r_0}$ is much smaller.

Summarizing these findings, we can conclude that the optimal conjugation heights h_{opt} of the WFS-DMs combinations are mainly a characteristics of the C_N^2-profile and rather independent of the precise parameters of the MCAO system and thus have an universal meaning. Considering the C_N^2-profiles measured at Mt. Graham, changing the parameters of the MCAO system, changes $h_{\mathrm{opt,GL}}$ by ≈100 m and $h_{\mathrm{opt,HL}}$ by a few hundred meters, which both are much smaller than the vertical resolution of the used C_N^2-profiles.

3.4 OFF-AXIS MCAO PERFORMANCE ESTIMATION

The Strehl ratio in the field for an MCAO system depends critically on the distribution of the guide stars. To retrieve a map of the Strehl ratio in the field thus usually requires extensive, numerical end-to-end simulations. Nevertheless, in the case of only one turbulent layer, a simple estimation of the off-axis performance can be given (Fusco et al., 2000). This estimate is based on calculating the fraction of the pupil footprint of the science object which overlaps with the pupil footprint of the guide star on the turbulent layer (see fig. 3.10, left). For a single layer at an height h_{layer}, an angle α between the guide star and the science object and the telescope

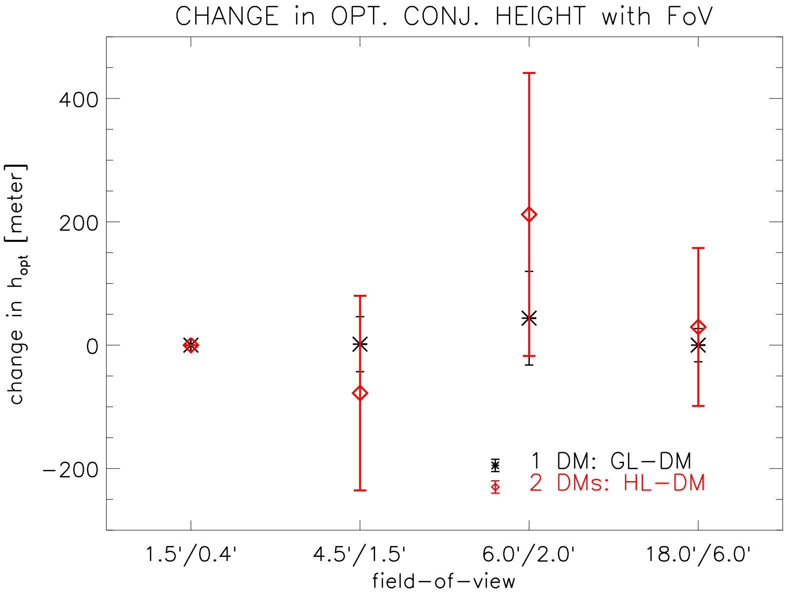

FIGURE 3.9: Dependence of the optimal conjugation altitude h_{opt,r_0} on the field-of-view of the LO-MCAO system. Shown are the results for a GLAO (1 DM) and an MCAO system with 2 DMs, but a fixed $h_{\mathrm{conj,GL}}$. In this case, the reference was a FoV of 1.5 arcmin for the GL-WFS and 0.4 arcmin for the HL-WFS. The symbols indicate the mean change in h_{opt,r_0} for all ≈10 000 measured C_N^2-profiles, while the error bars are the standard deviation.

diameter D_{tel}, this overlapping area $A_C(h,\alpha)$ can be calculated analytically:

$$A_C(h,\alpha) = \frac{D_{\mathrm{tel}}^2}{2}\arccos\frac{h_{\mathrm{layer}}\,\alpha}{D_{\mathrm{tel}}} - \frac{h_{\mathrm{layer}}\,\alpha\cdot D_{\mathrm{tel}}}{2}\sqrt{1-\left(\frac{h_{\mathrm{layer}}\,\alpha}{D_{\mathrm{tel}}}\right)^2}\,. \qquad (3.11)$$

The wavefront aberrations with a residual variance σ_{cl}^2 inside the pupil footprint of the guide star and thus within $A_C(h,\alpha)$ are corrected by the AO system. In the rest of the pupil footprint of the science object, the aberrations with a variance $\sigma_{\mathrm{layer}}^2$ are those of the uncorrected atmosphere. For the science object, the total residual wavefront aberrations σ_{sci}^2 are therefore given as a sum of σ_{cl}^2 and $\sigma_{\mathrm{layer}}^2$, weighted with their respective areas in the pupil footprint:

$$\sigma_{\mathrm{sci}}^2(h,\alpha) = \frac{A_C(h,\alpha)}{A_{\mathrm{tel}}}\,\sigma_{\mathrm{cl}}^2 + \frac{A_{\mathrm{tel}}-A_C(h,\alpha)}{A_{\mathrm{tel}}}\,\sigma_{\mathrm{layer}}^2\,. \qquad (3.12)$$

In this equation, σ_{cl}^2 for the guide star can be estimated from its Strehl ratio according to equation 2.21, and $\sigma_{\mathrm{layer}}^2$ of the non-corrected wavefront can be calculated from the observed seeing without AO correction via equations 2.15 and 2.18. Once the variance σ_{sci}^2 of the wavefront of the science object is determined, its Strehl ratio can be calculated with equation 2.21 and its FWHM with equations 2.18 and 2.15. This simple model does not take into account the spatial correlation of the Zernike modes and therefore cannot explain, for example, the observed elongation of the off-axis PSF in AO corrected images.

To estimate the off-axis performance of a layer-oriented MCAO system, a similar approach can be used. Again, the fraction of the overlap of the pupil footprint of the science object with, in this case, the footprint of all guide stars is determined (fig. 3.10, right panel). However, this fraction depends on the actual postion of

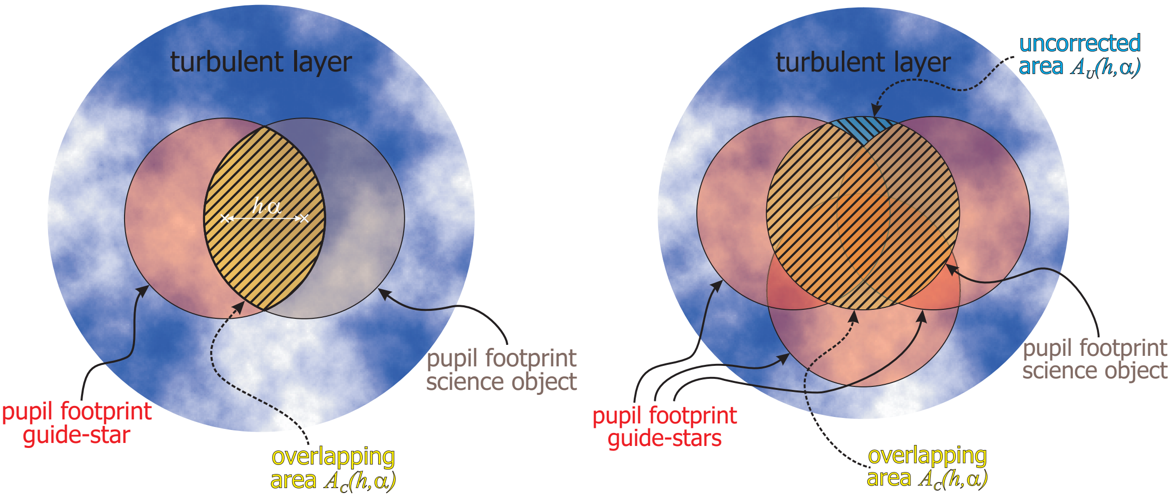

FIGURE 3.10: Figure to illustrate the overlapping region on a turbulent layer for the pupil footprints of the guide star and the science object for single-star AO (left) and MCAO system (right) with multiple guide stars.

the guide stars and cannot be described analytically in an easy way, as in equation 3.11. It has to be evaluated numerically. One possibility to estimate σ^2_{cl} is, similarly to above, from the on-axis performance, where the pupil footprint of the science object completely overlaps with those of the guide stars. The second possibility is to take the total wavefront variance in this layer $\sigma^2_{\mathrm{layer}}$ and filter it with the total filter functions $\mathbf{TFF}(h)$ as defined above:

$$\sigma^2_{\mathrm{cl}} = \sigma^2_{\mathrm{layer}} \cdot \mathbf{TFF}(h_{\mathrm{layer}}) \,. \tag{3.13}$$

3.5 CONCLUSION

In this chapter, we presented the concept of layer filter functions $\mathbf{LFF}(h)$ to describe the filtering of the wavefront aberrations in non-conjugated layers in a layer-oriented MCAO system. The wavefront sensor in such a system cannot see all the wavefront aberrations in these layers, but only those with low spatial frequencies, the others are smeared out. Only those wavefront aberrations can then be corrected with the deformable mirror. To take into account multiple DMs and their respective overall correction efficiency, the total filter functions $\mathbf{TFF}(h)$ are defined.

We also showed how these filter functions can be applied systematically to measured C_N^2-profiles and to derive an estimate for the performance of the MCAO system. In particular we described how the optimal conjugation heights of the DMs can be determined for various criteria. These optimal conjugation heights depend very little on the characteristics of the MCAO system such as the FoV, the number of corrected modes, and the bandwidth of the control loop. They are thus more an inherent characteristics of the C_N^2-profiles than of the MCAO system. Only the range of mis-conjugation h_{acc} for an acceptable reduction in the performance depends on the parameters of the MCAO system, it is larger for worse overall correction and for a smaller field-of-view of the layer-oriented WFS.

CHAPTER 4

Kalman Control Theory

power is nothing –
without control

Pirelli

4.1 INTRODUCTION

Once an AO system is set up, the practical question arises of how to transform in an optimal way the measurements of the wavefront-sensor to voltage commands for the Deformable Mirror. In this chapter, we review two such possibilities. The simplest algorithm, called the Least-Squares (LS) Reconstructor, just takes the measurements and tries to reconstruct the wavefront with the help of a calibration done in advance. We also present a more sophisticted algorithm, called Kalman filtering, which takes into account the measurement noise and a model for the spatial and temporal correlation of the wavefront aberrations, in order to increase the accuracy of the reconstructed wavefront. This filter is in particular very efficient in removing vibrations in the system. We will show how a version of this algorithm presented in the literature can be adapted to the pure modal calibration and control scheme of LINC-NIRVANA or MANU-CHAO and to a layer-oriented MCAO system. In this chapter the theoretical basis of the Kalman filter is given, experimental results with the MANU-CHAO system will be presented later in section 5.7.

4.2 CALIBRATION OF AO SYSTEMS

As mentioned in section 2.2.6, the modal approach is frequently used to describe wavefront aberrations. Usually a calibration is done to adjust the wavefront-sensor to the deformable mirror, account for the non-perfect representation of the Zernike modes by the DM, and for static effects in the wavefront-sensor.

In the linear regime of the wavefront sensor, the propagation of the modal coefficients $\mathbf{c}$ of the aberrated wavefront to the measured wavefront slopes $\mathbf{g}$ can be conveniently described by a matrix equation

$$\mathbf{g} = \mathbf{I} \cdot \mathbf{c} \,. \tag{4.1}$$

The interaction matrix $\mathbf{I}$ can be determined by calibrating the system with a diffraction-limited light-source (e.g. a single-mode fiber) in the focus of the telescope (Kasper, 2000). $\mathbf{I}$ can be filled by applying the single modes successively to the DM and measuring the response of the WFS. When only the nth mode is applied to the DM, the vector $\mathbf{c}$ contains only zeros, and one 1 at the position n of the applied mode. This means that the measured gradients make up the nth column of the interaction matrix $\mathbf{I}$.

4.3 LEAST-SQUARES RECONSTRUCTION

Once a calibration is done, the simplest way to reconstruct the wavefront is to use the inverse of equation 4.1:

$$\mathbf{c} = \mathbf{R} \cdot \mathbf{g} , \tag{4.2}$$

with the reconstruction matrix $\mathbf{R}$. The wavefront $W(x, y)$ is then given by a superposition of the calibrated modes $M_i(x, y)$

$$W(x y) = \sum_i c_i \cdot M_i(x, y) , \tag{4.3}$$

and the voltages $\mathbf{v}$ which have to be applied to the DM are:

$$\mathbf{v} = \mathbf{U} \cdot \mathbf{c} = \mathbf{U} \cdot \mathbf{R} \cdot \mathbf{g} . \tag{4.4}$$

With the injection matrix $\mathbf{U}$ which contains as its columns the voltages $\mathbf{v}_i$ to represent the single control modes. Since the matrix $\mathbf{U}$ was also used for the determination of the interaction matrix $\mathbf{I}$ in the calibration procedure, all quantities in equation 4.4 are related to the actual system.

There are several options to calculate the reconstruction matrix $\mathbf{R}$. One is the pseudo-inverse for the non-quadratic measured interaction matrix:

$$\mathbf{R}_{\mathrm{LS}} = \left(\mathbf{I}^T \cdot \mathbf{I}\right)^{-1} \cdot \mathbf{I}^T , \tag{4.5}$$

also called Least-Squares (LS) Reconstructor.

In closed-loop operation, the residual wavefront gradients $\mathbf{g}_{\mathrm{res},n}$ are measured at each loop step n and the voltages $\mathbf{v}_{\mathrm{res},n}$ which have to be applied additionally to the DM are calculated with equation 4.4. However, since there are delays between the measurement of the wavefront and the application of the voltages to the DM, these additional voltages are multiplied with a gain factor $0 < G < 1$:

$$\mathbf{v}_{n+1} = \mathbf{v}_n + \mathbf{v}_{\mathrm{res},n} = \mathbf{v}_n + G \cdot \mathbf{U} \cdot \mathbf{R}_{\mathrm{LS}} \cdot \mathbf{g}_{\mathrm{res},n} . \tag{4.6}$$

This gain factor has to be adapted to the loop parameters and atmospheric conditions. A higher gain factor makes the loop more aggressive, but also amplifies the measurement noise and thus results in a less stable loop. Due to the delays in a real system, a gain factor between 0.5 and 0.8 is typically used. In a more sophisticated implementation, the gain factor is adapted to the individual modes, with smaller values for high-order modes to suppress the propagated measurement noise, which affects especially these modes.

4.4 CONDITION NUMBER

Good calibration is extremely important and this is especially so for the LS reconstructor. A convenient quantity to describe the quality of the calibration and the useful number of reconstructed modes is the condition number $\kappa(\mathbf{I})$ of the interaction matrix $\mathbf{I}$.

Any matrix $\mathbf{A}$ with dimensions $n \times m$ and rank r, can be decomposed into

$$\mathbf{A} = \mathbf{U} \cdot \mathbf{S} \cdot \mathbf{V}^t , \tag{4.7}$$

with two orthogonal matrices $\mathbf{U}$ and $\mathbf{V}$ and a matrix $\mathbf{S}$, which has the r singular values $\sigma_1, \ldots, \sigma_r$ on its diagonal. The inversion of equation 4.1 can then be accomplished with the singular-value decomposition (SVD):

$$\mathbf{R}_{\mathrm{SVD}} = \mathbf{V} \cdot \mathbf{S}^+ \cdot \mathbf{U}^t , \tag{4.8}$$

where the matrix $\mathbf{S}^+$ is the pseudo-inverse of the matrix $\mathbf{S}$ with the inverse singular values $1/\sigma_1, \ldots, 1/\sigma_r$ on its diagonal. Equation 4.8 is mathematically equivalent to equation 4.5, but might be numerically more favorable. The condition number $\kappa(\mathbf{A})$ of the matrix $\mathbf{A}$ is given as the ratio of the largest over the smallest singular value

$$\kappa(\mathbf{A}) = \frac{\mathbf{min}\, \sigma_i|_i}{\mathbf{max}\, \sigma_i|_i} . \tag{4.9}$$

The condition number describes the sensitivity of the inverse linear system in equation 4.1 to small perturbations in either $\mathbf{I}$ or $\mathbf{c}$. In closed-loop operation, $\kappa(\mathbf{I})$ thus describes the propagation of the measurement error $\Delta\mathbf{g}$ in the measured gradients $\mathbf{g}$ to the error $\Delta\mathbf{c}$ in the modal coefficients $\mathbf{c}$. Formally, this can be written as (Golub and Loan, 1996):

$$\frac{\Delta\mathbf{c}}{\mathbf{c}} \leq \kappa(\mathbf{I}) \cdot \left[\frac{\Delta\mathbf{I}}{\mathbf{I}} + \frac{\Delta\mathbf{g}}{\mathbf{g}} \right] . \tag{4.10}$$

The error $\Delta\mathbf{c}$ in the reconstructed modal coefficients $\mathbf{c}$ is thus up to $\kappa(\mathbf{I})$ times the relative error in $\mathbf{I}$ or $\mathbf{g}$. A maximal acceptable value for the condition number is therefore usually between 5 and 10 (Kasper, 2000).

The condition number describes the similarities of the calibrated modes. If, for example, two modes look similar to the WFS, then two columns of the calibrated interaction matrix are similar, resulting in a large condition number. The numerical problems involved in inverting such a matrix (eqn. 4.8) and the sensitivity to the measurement noise (eqn. 4.10), results in a reduced performance and a less stable control loop. When operating the system in closed-loop with such an interaction matrix, the coefficients of the two modes cannot be determined independently, leaving these modes either un-corrected, or assigning them huge, opposing coefficients, destroying the reconstruction process and ultimately crashing the control loop.

4.5 THE KALMAN FILTER FOR ADAPTIVE OPTICS SYSTEMS

In the previous section, we already mentioned that the gain-factor G of the single modes for the LS Reconstructor can be adapted to the propagated measurement noise in the individual modes. In this section, we present an algorithm which accomplishes this automatically. This so-called Kalman filter takes the measurement noise into account and also includes a model of the spatial and temporal characteristics of the wavefront aberrations. Depending on the measurement noise in the individual modes, it can thus put more weight on the actual measurements or on the theoretical model.

The implementation of the Kalman filter presented here follows the approach of several recent papers (Le Roux et al., 2004; Petit et al., 2004, 2006), except for a modification to account for the pure modal control approach as it will be implemented in LINC-NIRVANA and MANU-CHAO. In the mentioned papers, the Kalman filter is developed for a mixture of zonal and modal control as implemented in NACO.

4.5.1 THEORETICAL BACKGROUND

Le Roux et al. (2004) give a very nice overview of the application of the Kalman filter to Adaptive Optics Systems. We therefore provide here only a brief summary to explain the principle, and show the required modifications and equations which have to be implemented in a control-system. For an in-depth discussion of the algorithm, we refer the reader to the paper by Le Roux et al. (2004).

As an usual approximation, the dynamical behavior of a system and its outputs can be described over short time-scales by a linear state-space model with a state-space vector, whose temporal evolution is given by a linear equation called the state equation. For an Adaptive Optics system with pure modal control, a convenient choice for the temporal state-space vector is given by

$$\mathbf{X}_n = \begin{bmatrix} \mathbf{\Phi}_{n+1}^{\mathrm{tur}} \\ \mathbf{\Phi}_{n}^{\mathrm{tur}} \\ \mathbf{\Phi}_{n-1}^{\mathrm{tur}} \\ \mathbf{\Phi}_{n-1}^{\mathrm{cor}} \\ \mathbf{\Phi}_{n-2}^{\mathrm{cor}} \end{bmatrix} , \tag{4.11}$$

where $\mathbf{\Phi}_n^{\mathrm{tur}}$ are the modal coefficients of the turbulent wavefront, and $\mathbf{\Phi}_n^{\mathrm{cor}}$ are the applied correction wavefronts to the DM at the loop step n. With this state-space vector $\mathbf{X}_n$, the state equation can be written as

$$\mathbf{X}_{n+1} = \begin{bmatrix} \mathbf{A}_{\mathrm{tur}} & 0 & 0 & 0 & 0 \\ \mathbb{1} & 0 & 0 & 0 & 0 \\ 0 & \mathbb{1} & 0 & 0 & 0 \\ 0 & 0 & 0 & 0 & 0 \\ 0 & 0 & 0 & \mathbb{1} & 0 \end{bmatrix} \mathbf{X}_n + \begin{bmatrix} 0 \\ 0 \\ 0 \\ \mathbb{1} \\ 0 \end{bmatrix} \mathbf{\Phi}_n^{\mathrm{cor}} + \begin{bmatrix} \mathbb{1} \\ 0 \\ 0 \\ 0 \\ 0 \end{bmatrix} \mathbf{Z}_{n+1} , \tag{4.12}$$

where $\mathbb{1}$ denotes the identity matrix and $\mathbf{A}_{\mathrm{tur}}$ describes the temporal correlation of the modal coefficients of the wavefront aberrations. The matrix $\mathbf{Z}_{n+1}$ describes the changes in the wavefront between two loop steps. It contains the average variance of the changes in the modal coefficients between two loop steps, which cannot be accounted by the linear model. The projection of the state-space vector $\mathbf{X}_n$ onto the measured wavefront slopes $\mathbf{S}_n$ is given by:

$$\mathbf{S}_n = \mathbf{I} \begin{bmatrix} 0 & 0 & \mathbb{1} & 0 & -\mathbb{1} \end{bmatrix} \mathbf{X}_n + \mathbf{Y}_n , \tag{4.13}$$

with $\mathbf{I}$ being the calibrated interaction matrix (sect. 4.2) and $\mathbf{W}_n$ the measurement noise, caused by, for example, read-out-noise of the CCD camera and Poisson-noise of the collected photons.

The two equations 4.12 and 4.13 can be written in compact form

$$\mathbf{X}_{n+1} = \mathbf{A}\,\mathbf{X}_n + \mathbf{B}\mathbf{\Phi}_n^{\mathrm{cor}} + \mathbf{D}\mathbf{Z}_{n+1} \tag{4.14a}$$

$$\mathbf{S}_n = \mathbf{E}\,\mathbf{X}_n + \mathbf{Y}_n\,. \tag{4.14b}$$

With the latest measurement $\mathbf{S}_n$ and the estimate of the state-space vector $\hat{\mathbf{X}}_{n/n-1}$ based on previous measurements $\{\mathbf{S}_{n-1}, \ldots, \mathbf{S}_0\}$, the prediction $\hat{\mathbf{X}}_{n+1/n}$ of the state-space vector for the next time-step is given by

$$\hat{\mathbf{X}}_{n+1/n} = \underbrace{\mathbf{A}\,\hat{\mathbf{X}}_{n/n-1}}_{\text{temporal correlation}} + \underbrace{\mathbf{B}\,\mathbf{\Phi}_n^{\mathrm{cor}}}_{\text{previous state}} + \underbrace{\mathbf{A}\,\mathbf{H}_n\left(\mathbf{S}_n - \mathbf{E}\,\hat{\mathbf{X}}_{n/n-1}\right)}_{\text{measurement, spatial correlation}}\,. \tag{4.15}$$

This is very similar to equation 4.6 of the LS reconstructor. It relates the measurement $\mathbf{S}_n$ by the WFS to the voltages (included in $\hat{\mathbf{X}}_{n+1/n}$), which have to be applied to the DM in the next time-step. The matrices $\mathbf{A}$, $\mathbf{B}$ and $\mathbf{E}$ are as defined above. The Kalman gain $\mathbf{H}_n$ is no longer just one number like G in equation 4.6, but rather is a matrix given by

$$\mathbf{H}_n = \mathbf{C}_{n/n-1}\,\mathbf{E}^T\left(\mathbf{E}\,\mathbf{C}_{n/n-1}\,\mathbf{E}^T + \mathbf{C}_Y\right)^{-1}, \tag{4.16}$$

with the covariance matrix $\mathbf{C}_Y$ of the measurement noise (sect. 4.5.2) and the covariance matrix $\mathbf{C}_{n/n-1}$ of the state vector estimation error. The latter one can be estimated with the Ricatti equation (Le Roux et al., 2004)

$$\mathbf{C}_{n+1/n} = \mathbf{A}\,\mathbf{C}_{n/n-1}\,\mathbf{A}^T + \mathbf{C}_Z - \mathbf{A}\,\mathbf{C}_{n/n-1}\,\mathbf{E}^T\left(\mathbf{E}\,\mathbf{C}_{n/n-1}\,\mathbf{E}^T + \mathbf{C}_Y\right)^{-1}\mathbf{E}\,\mathbf{C}_{n/n-1}\,\mathbf{A}^T, \tag{4.17}$$

which usually exhibits a relatively fast convergence, requiring only $\approx$10 to 20 iterations to achieve an acceptable accuracy. The Kalman gain $\mathbf{H}_n$ describes how well the measurements are matched by the a-priori model. To ensure that the global energy remains constant, the temporally propagated modal coefficients $\mathbf{A}_{\mathrm{tur}}^T\,\mathbf{C}_\Phi^A\,\mathbf{A}_{\mathrm{tur}}$ have to be subtracted from the theoretical modal covariance matrix $\mathbf{C}_\Phi^A$ for Zernike modes and Kolmogorov turbulence (sect. 4.5.2):

$$\mathbf{C}_Z = \mathbf{C}_\Phi^A - \mathbf{A}_{\mathrm{tur}}^T\,\mathbf{C}_\Phi^A\,\mathbf{A}_{\mathrm{tur}}\,, \tag{4.18}$$

with the temporal correlation matrix $\mathbf{A}_{\mathrm{tur}}$ of the control modes as defined above.

The voltages $\mathbf{v}$ which have to be applied to the Deformable Mirror can be calculated from

$$\mathbf{v} = \begin{bmatrix} \mathbf{U} & 0 & 0 & 0 & 0 \end{bmatrix}\mathbf{X}_{n+1}\,, \tag{4.19}$$

with the injection matrix $\mathbf{U}$ as defined in equation 4.4.

The Kalman filter is not sensitive to a large value of the condition number of the interaction matrix as in the LS reconstructor case. If, for example, one high-order mode looks very similar to a low-order mode on the WFS, the LS reconstructor would assign very similar modal coefficients to those two modes. In contrast, the Kalman filter realizes the unnatural high modal variance of the high-order mode and damps this mode by setting its gain factor to a very small value. This makes the loop more stable by avoiding the aliasing noise, and ultimately results in a higher performance. Furthermore, by including a temporal model of the atmosphere, large jumps in the modal coefficients between successive loop steps, caused by the measurement noise, are damped out.

4.5.2 THE REQUIRED ATMOSPHERIC AND SYSTEM PARAMETERS

Contrary to the LS Reconstructor, the Kalman filter requires additional input from a turbulence model and the system characteristics. In this section we describe how those can be obtained.

MODAL COVARIANCE MATRIX

To acquire the modal covariance matrix $\mathbf{C}_\Phi^A$ in equation 4.18, usually the theoretical normalized modal covariance matrix $\mathbf{C}_\Phi$ for the Kolmogorov model and Zernike modes, as defined in section 2.2.6 is used. However, $\mathbf{C}_\Phi$ has to be scaled by $(D_{\text{tel}}/r_0)^{5/3}$ to the prevailing seeing conditions. The Fried-parameter r_0 can be, for example, determined from waverfront sensor data as described in Fusco et al. (2004). This method basically relies on fitting the measured low-order modal covariance matrix to the theoretical one. Only the low-order modes are used, to limit the influence of the propagated noise, which especially affects high-order modes.

The amplification of the variances of the high-order modes by the measurement noise is also the reason why the measured modal covariance matrix (e.g. in open-loop) cannot be used directly. If such a distorted modal covariance matrix is given as input to the Kalman filter, it assumes that the measured, but unnaturally high modal coefficients are due to the atmosphere and not amplified by noise. In such a case, there will be no attenuation, but instead a further amplification of these modes, leading to a run-away effect and ultimately crashing the loop.

In a layer-oriented MCAO system, the filtered modal covariance matrix $\mathbf{C}_{\Phi,i,i}^*(\Delta h)$ for the single layers as defined in section 3.2.2 has to be used, with Δh denoting the difference between the altitude of the turbulent layer h_{layer} and the conjugation height of the DM h_{conj}. If the atmosphere consists not only of single layers, but rather has a vertical structure described by the C_N^2-profile, the total measured modal covariance matrix $\mathbf{C}_{\Phi,i,i}^{*,A}$ can be calculated via

$$\mathbf{C}_{\Phi,i,i}^{*,A} = \frac{\int C_N^2(h) \cdot \mathbf{C}_{\Phi,i,i}^*(h - h_{\text{conj}})\, dh}{\int C_N^2(h)\, dh} . \tag{4.20}$$

MEASUREMENT NOISE

The covariance matrix $\mathbf{C}_W$ of the measurement noise can be determined by a statistical analysis of the measured gradients in closed-loop. When considering the temporal auto-correlation $\mathbf{TA}[g_i](\Delta T)$ (eqn. 2.22) of the gradient g_i, any temporally uncorrelated measurement noise shows up only in the first bin $\mathbf{TA}[g_i](0)$. Using the analogy between the covariance and the auto-correlation for ΔT =0, the noise variance for each gradient can be determined from a linear or quadratic extrapolation of the first few n auto-correlation values $\mathbf{TA}[g_i](1, \ldots, n)$ to the origin, and taking the difference to the measured $\mathbf{TA}[g_i](0)$ (Kasper, 2000). The principle is illustrated in figure 4.1 and more details can be found in Egner (2003).

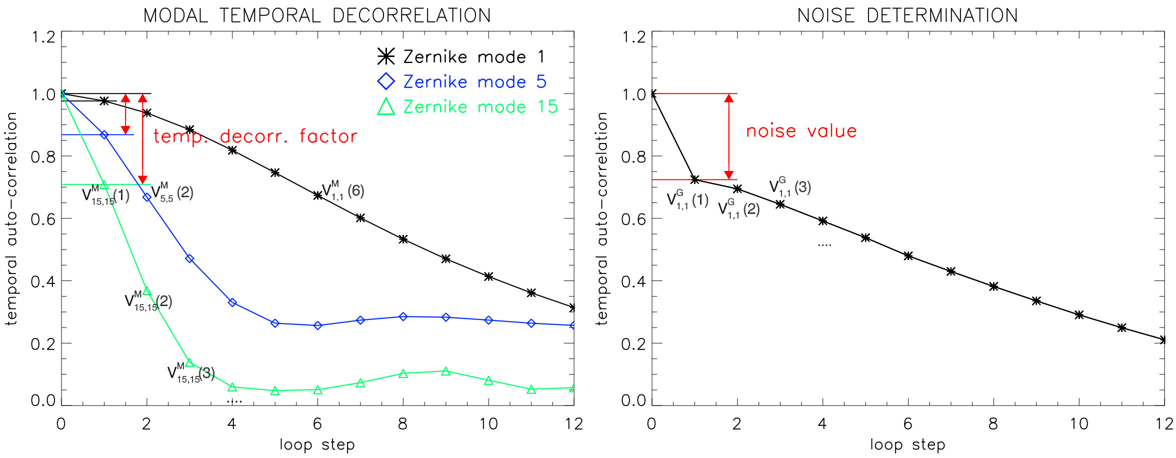

FIGURE 4.1: Sketch to illustrate how the modal decorrelation factor (**left**) and the noise of a sample gradient (**right**) can be extracted from an analysis of the temporal auto-correlation of the open-loop measurements of modal coefficients and wavefront slopes, respectively.

TEMPORAL CORRELATION MATRIX

The temporal correlation matrix $\mathbf{A}_{\text{tur}}$ describes how much the modal coefficients change on average between the single loop steps. In this case, $\mathbf{A}_{\text{tur}}$ is a diagonal matrix with the average correlation of the modal coefficients in loop step $n+1$ to those of loop step n. $\mathbf{A}_{\text{tur}}$ can be determined from a temporal auto-correlation analysis $\mathbf{TA}[c_i](\Delta T)$ of the measured modal coefficient c_i (fig. 4.1:

$$\mathbf{A}_{\text{tur},i,i} = \frac{\mathbf{TA}[c_i](0)}{\mathbf{TA}[c_i](1)} \,. \tag{4.21}$$

Similar to the temporal auto-correlation of the gradients, the measured auto-correlation $\mathbf{TA}[c_i](0)$ of the modal coefficients for $\Delta T = 0$ in open-loop also contains some noise, especially for high-order modes. However, we found that the filtering of this noise by multiplying the measured gradients with the LS reconstruction matrix $\mathbf{R}$ (eqn. 4.2) is sufficient and justifies this simplified approach.

4.6 THE KALMAN FILTER WITH VIBRATIONS

As pointed out by Petit et al. (2004), the Kalman filter can be adapted to efficiently filter out vibrations in the system. Since vibrations in an AO system can significantly reduce the performance (Petit et al., 2004; Kenworthy, 2005), and cannot be filtered out with a simple LS Reconstructor, we decided to examine the performance of the Kalman filter in the presence of vibrations.

4.6.1 THEORETICAL BACKGROUND

The theory for the Kalman filter to take also vibrations into account was presented by Petit et al. (2004). We therefore give only a brief summary here, and highlight the modifications necessary to adapt the algorithm to the calibration procedure of LINC-NIRVANA and MANU-CHAO.

For vibrations with a frequency f_{vib}, the additional modal weights a_n at time $n \cdot T$ can be described by

$$a_n \;=\; A \cos\left(2\pi \cdot f_{\text{vib}} \cdot n \cdot T \;+\; \phi\right) \,, \tag{4.22}$$

with time T between the successive loop steps and a starting phase ϕ for $t = 0$. It can be shown that for a sampling frequency f_{samp}, the temporal evolution of the vibrations in the measurements is given by (Petit et al., 2004)

$$a_{n+2} \;=\; 2 \cos\left(\frac{2\pi f_{\text{vib}}}{f_{\text{samp}}}\right) a_{n+1} \;-\; a_n \;. \tag{4.23}$$

Also the modal state-space vector has to be adapted, a convenient choice for an AO system with pure modal control is

$$\mathbf{X}_n \;=\; \begin{bmatrix} \mathbf{\Phi}_{n+1}^{\text{vib}} \\ \mathbf{\Phi}_{n}^{\text{vib}} \\ \mathbf{\Phi}_{n+1}^{\text{tur}} \\ \mathbf{\Phi}_{n}^{\text{tur}} \\ \mathbf{\Phi}_{n-1}^{\text{tur}} \\ \mathbf{\Phi}_{n-1}^{\text{cor}} \\ \mathbf{\Phi}_{n-2}^{\text{cor}} \end{bmatrix} \,, \tag{4.24}$$

with

$$\mathbf{\Phi}_n^{\text{cor}} \;=\; \mathbf{\Phi}_n^{\text{tur}} \;+\; \mathbf{\Phi}_n^{\text{vib}} \tag{4.25}$$

and a state model

$$\mathbf{X}_{n+1} \;=\; \begin{bmatrix} \mathbf{A}_{\text{vib}} & -\mathbb{1} & 0 & 0 & 0 & 0 & 0 \\ \mathbb{1} & 0 & 0 & 0 & 0 & 0 & 0 \\ 0 & 0 & \mathbf{A}_{\text{tur}} & 0 & 0 & 0 & 0 \\ \mathbb{1} & 0 & \mathbb{1} & 0 & 0 & 0 & 0 \\ 0 & 0 & 0 & \mathbb{1} & 0 & 0 & 0 \\ 0 & 0 & 0 & 0 & 0 & 0 & 0 \\ 0 & 0 & 0 & 0 & 0 & \mathbb{1} & 0 \end{bmatrix} \mathbf{X}_n \;+\; \begin{bmatrix} 0 \\ 0 \\ 0 \\ 0 \\ 0 \\ \mathbb{1} \\ 0 \end{bmatrix} \mathbf{\Phi}_n^{\text{cor}} \;+\; \begin{bmatrix} 0 \\ 0 \\ \mathbb{1} \\ 0 \\ 0 \\ 0 \\ 0 \end{bmatrix} \mathbf{V}_{n+1} \;. \tag{4.26}$$

The projection of $\mathbf{X}_n$ onto the measurement is given, similarly to above, by:

$$\mathbf{S}_n \;=\; \mathbf{G} \left[\begin{matrix} 0 & 0 & 0 & 0 & \mathbb{1} & 0 & -\mathbb{1} \end{matrix}\right] \mathbf{X}_n \;+\; \mathbf{W}_n \;. \tag{4.27}$$

4.6.2 THE REQUIRED ATMOSPHERIC AND SYSTEM PARAMETERS

For the Kalman filter with vibrations, the modal covariance matrix, the temporal correlation matrix, and the measurement noise can be determined with the same methods as described above. For the modal covariance matrix, some care has to be taken that the vibrations are not included for the calculation of the Fried parameter.

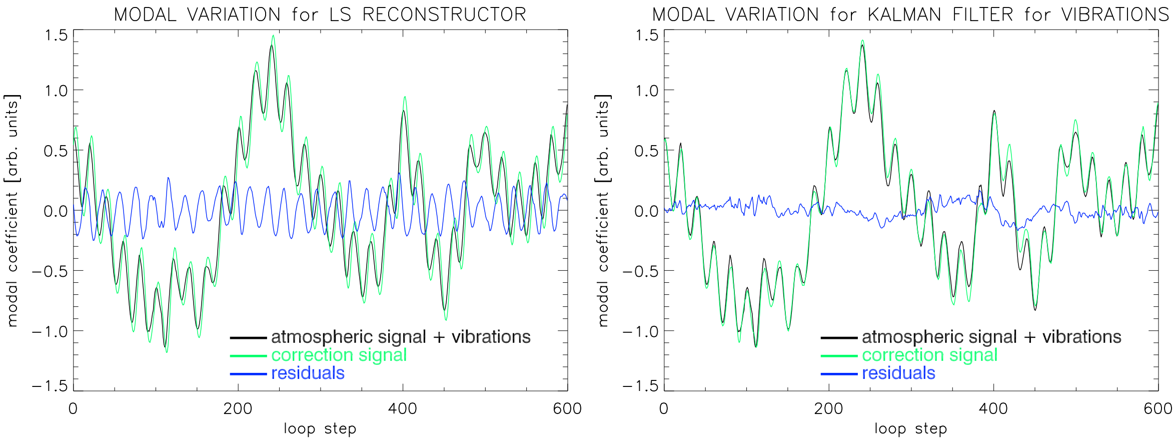

FIGURE 4.2: Temporal evolution of the mode with vibrations for Least-Squares Reconstructor (**left**) and Kalman filter (**right**) for 2 seconds.

We assume that the frequency of the vibrations is known. On the other hand, it is not necessary to know their amplitude or phase, but the Kalman filter rather adapts itself to these two parameters during the first few tens to hundred loop steps. Also, during closed-loop operation, the Kalman filter has some capability to compensate phase-jumps due to sporadic time-lags in the control loop.

4.6.3 NUMERICAL VERIFICATIONS

To investigate the maximum filtering efficiency of the Kalman filter, and verify the modifications of the algorithm, we performed a set of numerical simulations on open-loop data measured with the MANU-CHAO system (chapter 5). The vibrations were added numerically to these data and closed-loop simulations in IDL were performed with the same loop parameters as in the real system. Under these optimal conditions, where all required quantities for the Kalman filter are exactly known, the Kalman filter is indeed very effective in filtering out the vibrations, as shown in figure 4.2. By using some additional information and after some initial adaptation steps, the Kalman filter follows the vibrations very nicely, and thus almost completely filters them out. In contrast, the LS Reconstructor lags behind the vibrations and thus cannot achieve a good correction.

The good reduction of the vibrations can also be seen in the temporal power-spectral density of the mode with added vibrations, as shown in figure 4.3. The LS Reconstructor does not filter out the vibrations: their energy is almost completely conserved, which is entirely different for the Kalman filter.

4.7 CONCLUSIONS

In this chapter, we presented a review of the calibration and control of Adaptive Optics Systems. In particular, the Least-Squares (LS) Reconstructor and the Kalman filter were introduced. We showed how the Kalman filter can be adapted from published versions to the calibration and control scheme of LINC-NIRVANA and MANU-CHAO and to a layer-oriented MCAO system. Numerical simulations performed for additional vibrations in the system showed the clear superiority of the

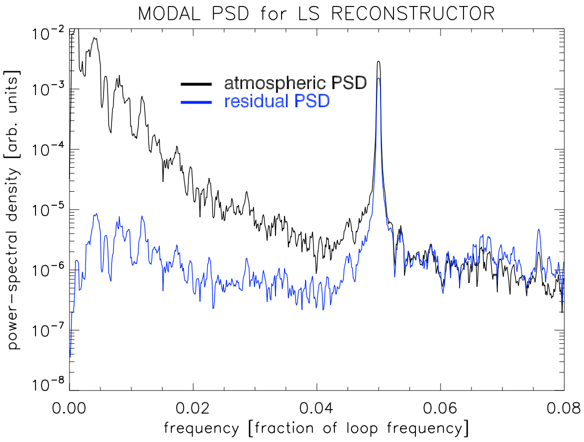

FIGURE 4.3: The power-spectral density (PSD) of one mode with added vibrations for the Least-Squares Reconstructor (**left**) and the Kalman filter (**right**).

Kalman filter over the LS Reconstructor in terms of performance.

The verification of the presented three variations of the Kalman filter with a laboratory experiment and the achievable performance in a real Adaptive Optics system in described in detail later in section 5.7.

CHAPTER 5

Characterizing an MCAO prototype for LINC-NIRVANA

your apocalypse was fab
for a girl who couldn't choose
between the shower or the bath

Tori Amos, "Hey Jupiter"

5.1 INTRODUCTION

Section 2.5.3 presented the benefits of a Multi-Conjugate Adaptive Optics system with respect to single-star AO. However, up to now, no MCAO or even a simpler GLAO system is in operation on the night-sky. To verify the concepts and to gain some experience with the alignment, operation and control of an MCAO system in the context of developing and building the LINC-NIRVANA instrument, a prototype for lab-testing was built. A GLAO system would be a first step towards a full-fledged MCAO system. GLAO also uses multiple guide stars, is based on the same principles, and contains all the relevant components. It thus allows us to verify the design concepts without the full complexity of an MCAO system.

Furthermore, a GLAO system, which uses several guide stars to measure and one DM to correct only the most turbulent layer, can already achieve a significant increase of the corrected field-of-view, as compared to single-star AO. With a GLAO lab experiment, the characteristics and performance of a stand-alone GLAO system can be evaluated, gaining valuable experience and verifying numerical simulations.

Extensive tests of a complete GLAO system in the lab have therefore been conducted and the results are presented in this chapter. This system contains a dynamic turbulence generator, a Deformable Mirror (DM), a dedicated control software package and four pyramids as wavefront-sensors (WFS). Operating this system in closed-loop, the layer-oriented (LO) principle with optical co-addition can be studied for the first time in detail under realistic atmospheric conditions. The system is characterized in static and dynamic operation, and the influence of non-conjugated turbulent layers, the effect of brightness variations of the guide stars

---

portions of this chapter appear in Egner et al. (2004) and Egner et al. (2006a).

and the impact of misalignments are studied. Furthermore, calibration strategies and the performance of the Kalman control algorithm are examined.

5.2 SYSTEM DESCRIPTION

The main components of the system are shown and described in figures 5.1 and 5.2. This section gives details on the individual system components.

5.2.1 THE LIGHT SOURCE

To simulate the guide stars, we used a metal plate with small holes as a mask in front of an halogen lamp. With several such plates, various guide star configurations can be easily and repeatably accomplished. For most of the experiments, we used the guide star configuration shown in figure 5.3, with the four guide stars distributed in a field of ≈30” diameter.

We also used various plates with different diameters of the holes to simulate various modulation amplitudes of the pyramids (sect. 2.4.1), and therefore to adjust the linear range of the pyramid to the amplitude of the wavefront aberrations induced by MAPS (sect. 5.3.3). The diameter of these holes were 0.1, 0.3 and 0.5 mm. With a pixel-scale of 1.7”/mm, this corresponds to an angular extension and therefore to a modulation amplitude of 0.17”, 0.51” and 0.85”, respectively, which is 3, 10 and 16 times the diameter of the Airy-disk.

A single mode fiber was attached to a central hole in the metal plate and illuminated by a laser with λ =835 nm. This fiber has a core-diameter of ≈5 μm and serves as a diffraction-limited reference for independently and unambiguously determine the loop performance. It is subsequently referred to as the science fiber.

5.2.2 MAPS

In order to dynamically test next-generation AO systems for Calar Alto, VLT and LBT, a dedicated atmospheric turbulence simulator was developed and built at the MPIA over the last few years (Butler et al., 2004; Hippler et al., 2006). This Multiple Atmospheric Phase screens and Stars (MAPS) system consists of a collimator, a reimager and several rotating phase screens. The optical design was optimized to simulate the focal plane of the VLT (8 m telescope, f/15, and same curvature of the focal plane) and to deliver diffraction-limited performance in the wavelength range from 0.5 μm to 2.2 μm over the complete 2 arcmin FoV. A CAD-drawing of the optical design appears in figure 5.4, and a picture of the actual implementation of MAPS as included in the lab-setup can be seen in figure 5.2.

THE PHASE SCREENS

One method to simulate the optical effects of atmospheric turbulence is to use phase screens with some sort of imprinted wavefront aberrations. Rotating a screen with a size much larger than the pupil diameter, gives a temporally evolving wavefront distortion. The rotation speed is set to match the desired wind speed of the turbulent layer. This so-called frozen-flow method (sect. 2.2.3) with internally fixed, but moving wavefront aberrations is a typical approximation made for numerical

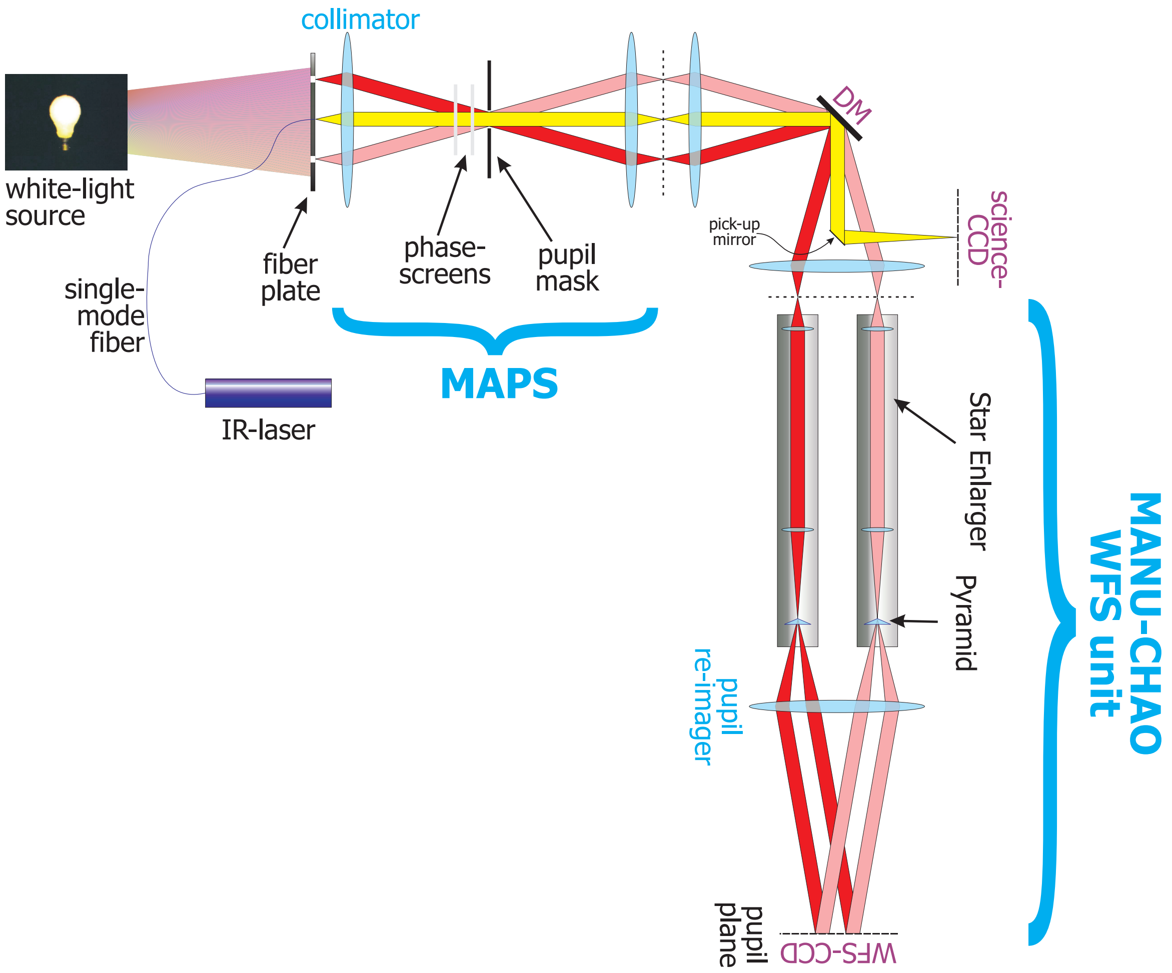

FIGURE 5.1: A very schematic sketch of the complete lab setup to show the main components. The relative sizes and angles are not to scale. The guide stars are simulated by a metal plate with small holes, which we illuminated from the back by a white light source. A single-mode fiber is also glued into this metal plate. The fiber is attached to an infrared laser and is used to simulate a diffraction-limited science object. Inside the turbulence simulator "MAPS", the light is first collimated, passes several phase screens to induce wavefront aberrations and is finally focused again. Another collimator images the pupil onto the Deformable Mirror, and the reflected light is focused by another set of optics. The light of the science object is reflected by a small pick-up mirror into the science camera, while the light of the guide stars enters the wavefront-sensor unit called "MANU-CHAO". The focal ratio on the tip of the pyramid is increased individually for each guide star with the help of two lenses. These are mounted together with the pyramid on a "Star-Enlarger" to move them to the position of the guide star in the field. In this lab-setup, a total of 4 pyramids is used. For reasons of clarity only two are shown here. A common lens re-images the pupils of all four pyramids on the wavefront-sensor CCD. In GLAO mode, the focus of this lens is adjusted to achieve perfect overlap of the pupil images of all four pyramids on the WFS-CCD.

simulations or lab experiments. Phase screens have the advantage that the wavefront aberrations are repeatable, thus allowing decisive comparison of different AO correction techniques.

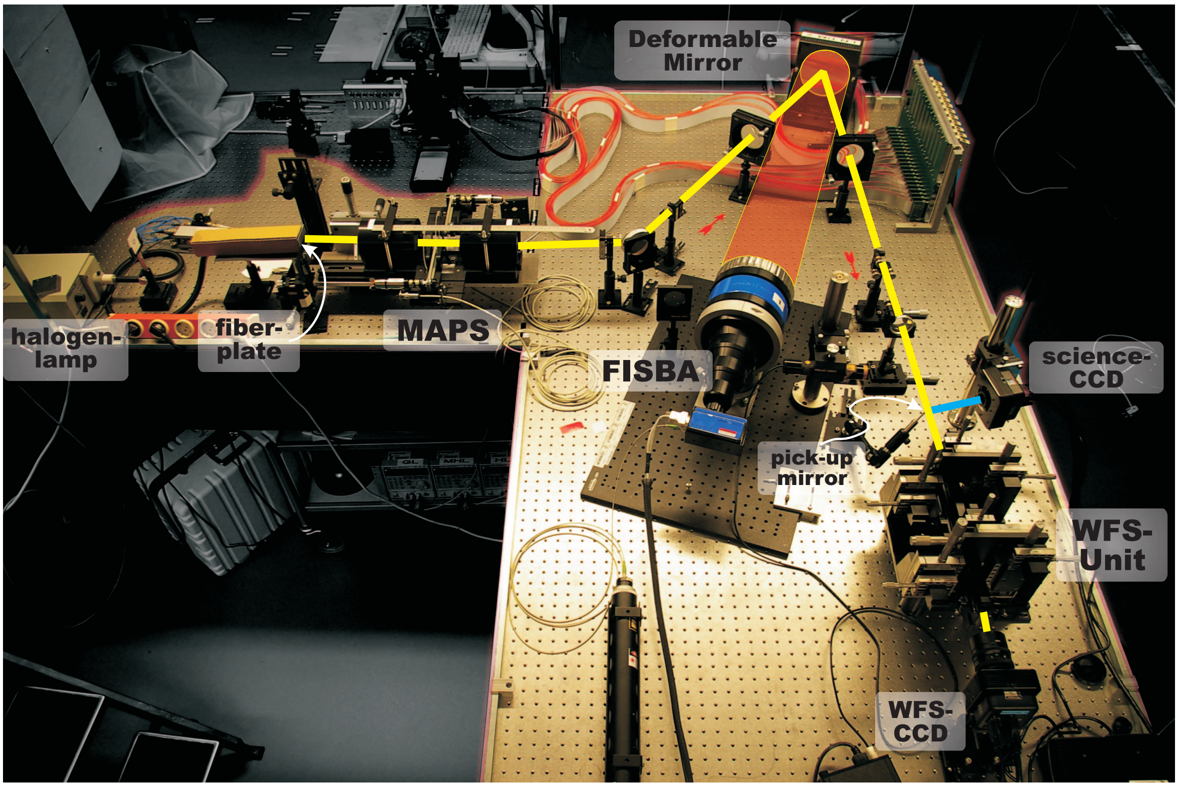

FIGURE 5.2: A photo showing the complete lab setup with the light-source (halogen lamp and fiber-plate), the turbulence generator (MAPS), some collimating optics, deformable mirror, re-focusing optics, science camera and wavefront-sensor unit. The FISBA interferometer is used for monitoring and calibration of the DM. The light-path is indicated by the thick yellow line.

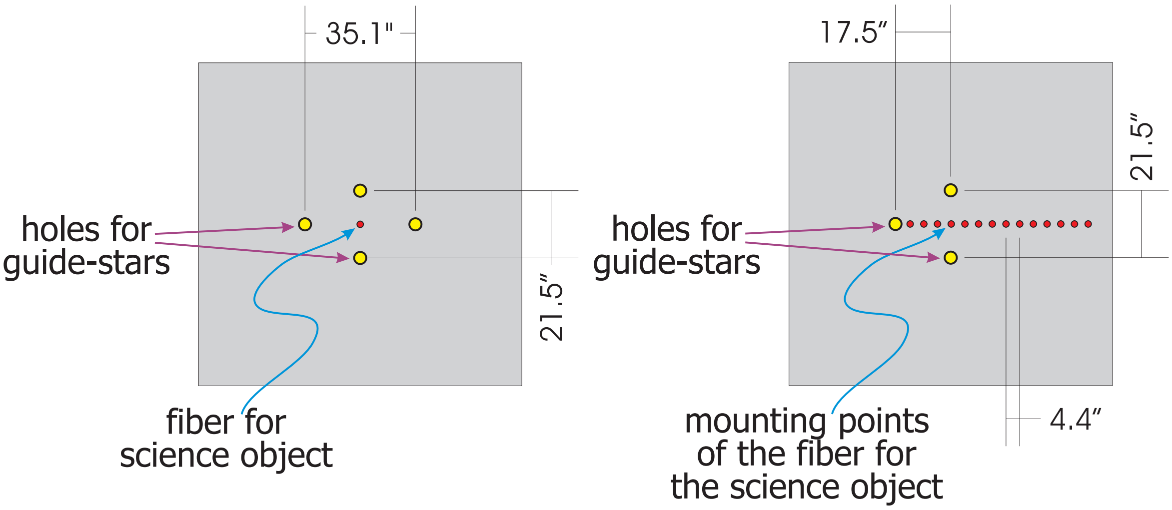

FIGURE 5.3: Sketch of the fiber plate for simulating the guide star asterism. **Left:** The fiber plate used for most of the measurements with four holes for simulating the guide stars. The single mode fiber for simulating the science object is glued at the center of this plate. **Right:** The fiber plate for measuring the performance in GLAO mode in the field. Only three guide stars were used, and the science fiber can be mounted to various positions along the x-axis.

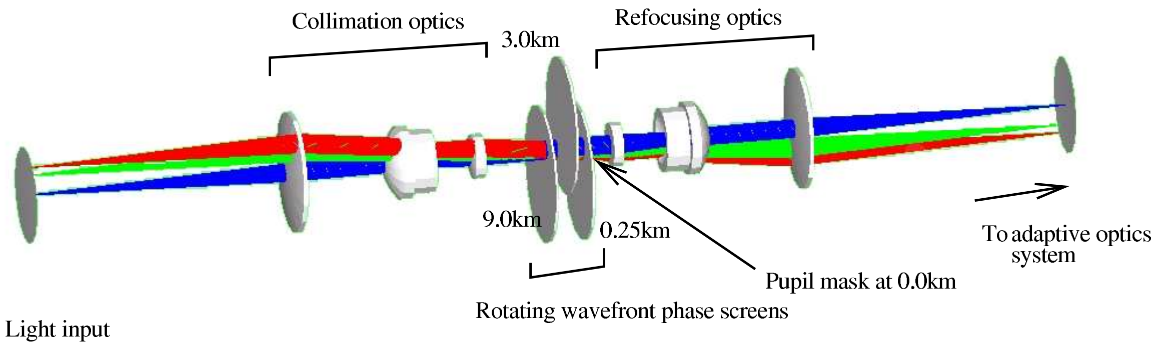

FIGURE 5.4: A CAD drawing of the optical design of the MAPS turbulence simulator. Starting from several point-sources, the light is collimated with a pupil diameter of up to 13 mm and then passes up to three rotating phase screens. These have a diameter of 10cm and are conjugated to different altitudes. Finally, a re-focusing optics re-images the stars to the focal plane, which then serves as input for the AO system. The total length of the system from the light-sources to the focal plane is 0.78 m.

Phase screen	**Fried Parameter r_0**	**Corresponding Seeing**
	mm @ λ=835 nm	**arcsec for MANU-CHAO**
Ground-Layer	0.63±0.03	0.50±0.02
High-Layer	1.11±0.04	0.30±0.01
both screens	0.52±0.03	0.61±0.03

TABLE 5.1: The measured Fried-Parameters of the two phase screens used in MAPS (Hippler et al., 2006). The corresponding seeing values for MANU-CHAO are given for the V-band (λ =0.5 μm) and assume a 3.5 m telescope at a science wavelength of 835 nm.

An overview of various techniques for the manufacturing of suitable phase-screens can be found in Egner (2003). Several options were investigated during the design phase of MAPS. The test results of various phase screen prototypes can be found for the ion-exchange technique in Butler et al. (2004) and Egner (2003), and for the etching technique in Hippler et al. (2006). After these tests, we decided to use the phase-screens manufactured by Silios using the etching technique, because they offered the best and most reliable performance.

The characteristics of the two phase screens used for this lab setup can be found in table 5.1. Figure 5.5 shows examples of short and long exposure images when using these phase screens, as measured with the science camera of MANU-CHAO. Since MANU-CHAO was originally designed to be ultimately mounted for an on-sky testing to the Telescopio Nazionale Galileo (TNG) (sect. 5.2.5), the scaling to angular dimensions on the sky assumes a 3.5 m telescope and a science wavelength of 835 nm.

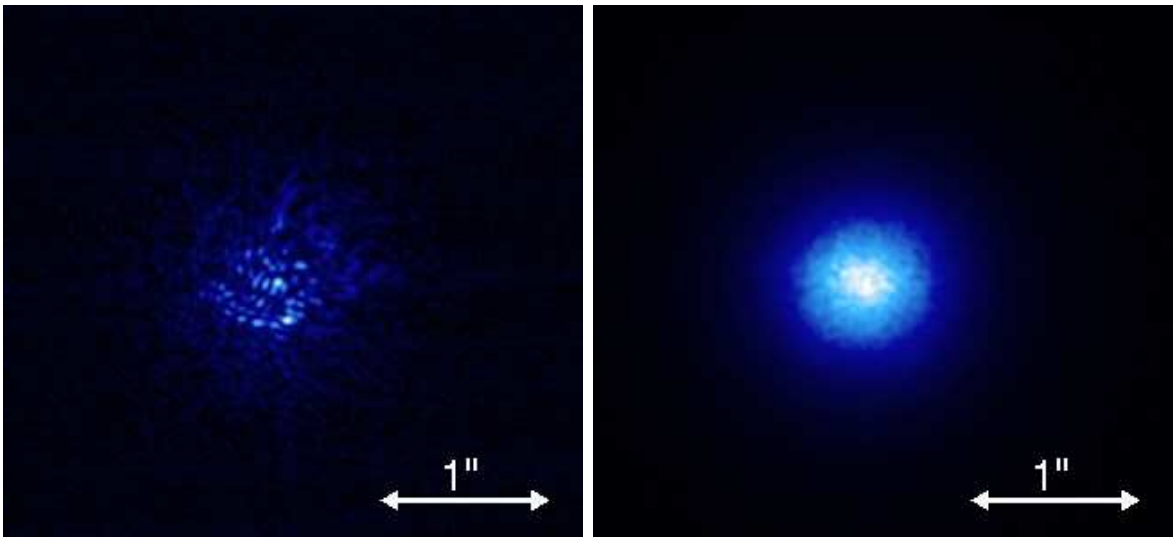

FIGURE 5.5: Two samples of the shape of the PSF of the science object when using the Ground-Layer phase screen in MAPS. The images were taken with the science camera of MANU-CHAO and indicate the angular size as would be measured at a 3.5 m telescope and a wavelength of 835 nm. For reasons of clarity, the contrast in these two images is square-root stretched and normalized. **Left:** A sample of a short-exposure PSF, which shows very nicely the speckle-pattern. **Right:** The average PSF over a full rotation of the phase screen, showing the smearing of the speckle-pattern into the seeing disk with a FWHM of ≈0.45".

5.2.3 THE TELESCOPE SIMULATOR

After the light passed the MAPS unit, it is collimated to form an image of the pupil on the DM and then re-focused to feed the MANU-CHAO WFS unit. To accomplish this, we designed a telescope simulator with Zemax, having the following requirements:

- A pupil image large enough to have $\approx 10\times 10$ actuators in the pupil on the DM;
- Telecentric f/32 output beam, i.e. exit pupil at infinity;
- Diffraction-limited polychromatic image of the pupil on the WFS CCD over the complete field-of-view;
- Diffraction-limited image of the on-axis, monochromatic science channel on the science CCD;
- Use of commercial lenses only.

To achieve these requirements, the collimating and re-focusing arm each consist of three lenses (fig. 5.6 top), delivering a diffraction-limited image over the complete field-of-view for monochromatic light (fig. 5.6 bottom). Even for white-light, the shift of the pupil images on the WFS CCD for different wavelengths is smaller than 0.625% of the pupil diameter. For 30×30 subapertures, this chromatic smearing is less than 0.2 subapertures, which is small enough to achieve diffraction-limited performance (see sect. 5.3.1 and Diolaiti et al., 2005b,b). However, the use of commercially and readily available lenses limit the diameter of the pupil image on the DM to 65 mm, resulting in 10×10 actuators across the pupil.

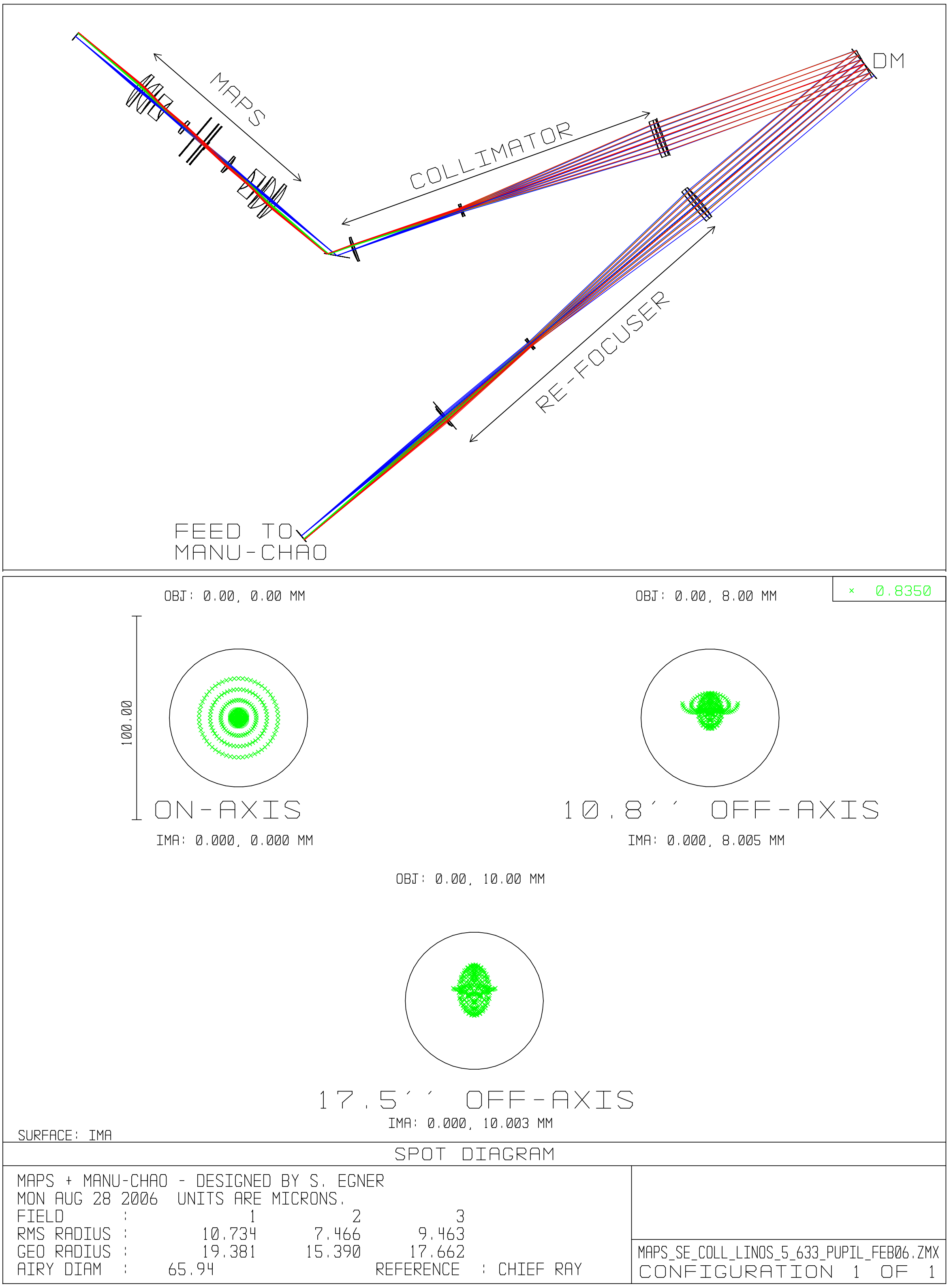

FIGURE 5.6: **Top:** Optical design of the collimator and re-focuser of the lab setup. **Bottom:** The PSF of point-sources at the position of the on-axis science object and the off-axis position of the guide stars in the plane labeled ”feed to MANU-CHAO” in the top picture. The circles indicated the size of the Airy-disk and highlight the diffraction-limited image quality of the combined system.

The angle between the incoming and the reflected light on the DM has to be as small as possible, but is limited by the FISBA interferometer to see the full DM and not be obstructed by the mounting of the lenses. Due to this opening angle, the DM is not perfectly conjugated to the pupil: the left side is a little bit before, while the right side is conjugated behind the pupil. However, for an angle of 37° between the two beams, and a beam diameter of 65 mm, this results in a conjugation-range of ±40 m, which is negligible for the degree of correction achievable with this system. Furthermore, transfered to MAPS, this corresponds to an accuracy in the position and wobble of the phase screens of less than 0.1 mm, which cannot be achieved with the current setup. Also during on-sky operation, is the complete DM conjugated to one single altitude only for observations at the zenith. The apparent elongation of the DM on the WFS is only 5% and with the used calibration scheme of the WFS not relevant.

5.2.4 THE DEFORMABLE MIRROR

To correct the wavefront aberrations induced by MAPS, we used one of the DMs of LINC-NIRVANA, which is a continuous face-sheet DM by Xinetics with 349 piezo-actuators on a quadratic grid. The DM together with its electronics has been extensively characterized at various temperatures, for such parameters as the surface flatness, the characteristics of the single actuators, and their robustness against damage. See Egner et al. (2004) and Stuik et al. (2004a) for a detailed description of the test-procedure. The test results are summarized in Egner (2004) and Egner (2005). Here, we cite only the main characteristics as relevant for this setup.

For monitoring and safety, the DM is continuously watched with a commercial Twymann-Green Interferometer by FISBA Optics during closed-loop operation of the system. To obtain one measurement of the DM surface with the FISBA would take ≈15 seconds and can thus not be done in real-time. However, we found it extremely useful to monitor the fringes of the FISBA, which are displayed in real-time, during the operation of the AO system. In this way problems with single actuators or with the reconstruction process can be easily identified and examined.

OPTICALLY FLAT PATTERN

An iterative routine using the FISBA interferometer was developed to generate the voltage pattern for all actuators, which is required for an optically flat surface of the DM. The routine is completely automatic. It measures the surface of the DM, projects it to the single actuators, and calculates the voltages required to achieve an optically flat surface. A residual rms of less than 17 nm could be achieved, which is at the measurement limit of the FISBA interferometer. Furthermore, the remaining surface roughness consists of higher spatial frequencies, smaller than the actuator pitch, and can thus not be compensated by adjusting the actuators. When operating the DM at room temperature, this flat pattern was found to remain constant over time. Over one year of operation, the surface roughness when applying the same voltage pattern never exceeded ≈30 nm rms, which is sufficient for the performance regime of MANU-CHAO.

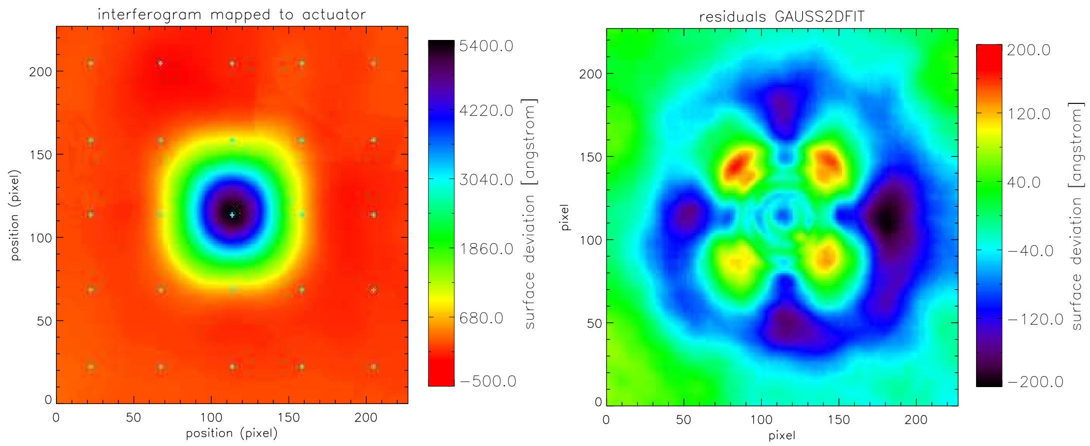

FIGURE 5.7: **Left:** The influence function of one sample actuator when being poked by +0.3 of full stroke. The position of the neighboring actuators are marked with small white plus signs. **Right:** The residuals after fitting the measured influence function with a two-dimensional Gaussian. The pattern is dominated by the non-circular shape of the influence function, but its rms is still smaller than that of optically flattened mirror surface.

INFLUENCE FUNCTIONS

To achieve optimal control of the DM, it is important to know the shape of the mirror surface when a single actuator is driven. As will be explained in section 5.3.2, the shape of this so-called influence function is required to calculate the voltages for an optimal representation of, for example, the Zernike modes with the DM. Figure 5.7 shows the influence function of one actuator. The influence functions of all of the actuators are very similar to each other. For example, their widths differ by just ≈1%. Only at the edge of the DM are some deviations apparent, caused by the lack of constraining actuators at one or two sides of the deflected actuator. The FWHM of the influence functions is 1.04 actuator spacings in the direction of the grid and 1.07 at 45 degrees to the grid. It is greater in the latter direction, because the adjacent actuator is farther away, and thus less constrains the individual actuator motion. At room temperature, the linearity of all of the actuators is very good: the motion response to input voltages drops by 6% at full stroke and can be described by a pure quadratic function. The main characteristics of the DM as measured at room temperature are summarized in table 5.2.

5.2.5 WAVEFRONT SENSOR UNIT

The core of the lab-setup presented here is the “MANU-CHAO” wavefront-sensor unit. MANU-CHAO implements the concept of a layer-oriented (LO) GLAO system with optical co-addition by using four pyramids to measure the wavefront aberrations of four natural guide stars. It was initially developed and assembled by the Adaptive Optics group at the Osservatorio Astrofisico di Arcetri (Ragazzoni et al., 2002; Farinato et al., 2004a) as a prototype for the LO-WFS of MAD (Marchetti et al., 2006). It was tested there in static operation by inserting phase-screens into the beam and comparing the retrieved wavefronts with those measured by a commercial interferometer. However, the real performance of a GLAO system can be determined only in closed-loop operation, which is described for the first time in this thesis.

Parameter	Measured value
Manufacturer	Xinetics Inc.
Number of actuators	349 (≈80 used for MANU-Chao)
Diameter of facesheet	150 mm
Actuator pitch	6.67±0.03 mm
Maximum stroke	4.9±0.05 micron
Achievable surface flatness	17 nm rms
Actuator non-Linearity	6% (purely quadratic)
Hysteresis	1%
Variation of the actuator gain	1% rms
FWHM of influence function in grid-direction	1.04 ± 0.01 actuator-distances
FWHM of influence function at 45° to grid	1.07 ± 0.01 actuator-distances
Influence on adjacent actuator	11.0±0.2%

TABLE 5.2: The main characteristics of the Xinetics Deformable Mirror, as determined at room-temperature. Some of the characteristics (especially maximum stroke, hysteresis, non-linearties, and achievable surface flatness) exhibit a strong dependence on temperature, in general deteriorating for lower temperatures (Egner, 2005).

The optical design of MANU-CHAO is made for an f/32 telecentric input beam of the Telescopio Nazionale Galileo (TNG) on La Palma. Choosing the optical design of MANU-CHAO to fit to the TNG offers the possibility of on-sky tests after the initial lab experiments have been successfully accomplished.

A requirement of a pyramid WFS is that the size of the guide star image on the tip of the pyramid is ≈10 times larger than the size of tip of the manufactured pyramid itself (sect. 2.4.1). A size of the tip of ≈10 μm thus requires an f/250 beam for a wavelength of 1 μm at an 3.5 m telescope. However, for a LO system, this cannot be achieved by increasing the f-ratio of the complete beam, because the diameter of the focal plane would increase by the same amount, requiring huge lenses to image the pupils onto the WFS-CCD. For a 2 arcmin FoV at a modern 8 m, f/15 telescope, this would result in a diameter of the focal plane and thus of the pupil re-imaging lens of more than 1 meter, which is economically not feasible.

A possible solution is to enlarge the f-ratio *locally* (Ragazzoni et al., 2005). This can be achieved with so-called Star Enlargers, as shown in figure 5.1. Each Star Enlarger contains two lenses and one pyramid. The first lens with a short focal length f_1, collimates the light, while the second lens with a longer focal length f_2 focuses the light onto the tip of the pyramid. In MANU-CHAO, both lenses are achromatic doublets with f_1 =25 mm and f_2 =150 mm, resulting in an increase of the f-ratio from f/32 to f/192. Each Star Enlarger is mounted on four manual stages to move it to the position of its associated guide star and to adjust its tilt to achieve optimal overlap of the pupil images of the single pyramids on the WFS-CCD. The pyramids were manufactured at the Osservatorio Astronomico di Brera-Merate by grinding commercial BK7 lenses. Their vertex angle is 1.0 degree.

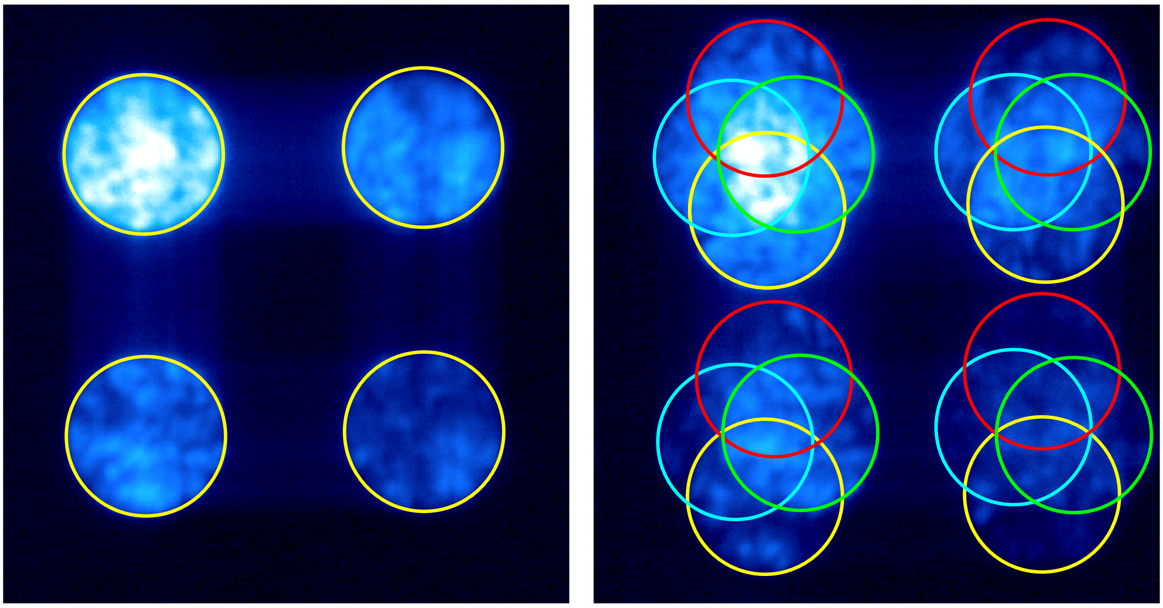

FIGURE 5.8: Examples of the pupil images produced by the four pyramids, measured with MANU-CHAO when the detector is conjugated to the ground (**left**) and to a high-layer (**right**). When being conjugated to the ground, the pupil images of all guide stars overlap perfectly. In contrast, they are shifted according to the positions of the stars in the field for high-layer conjugation, as indicated by the different colors of the overplotted circles.

Finally, a common lens with a focal length $f = 75$ mm images the pupils on the WFS-CCD (fig. 5.8). By adjusting the focus of this lens, the detector can be conjugated easily to different altitudes without having to change the complete setup.

5.2.6 CARMA – CONTROL SOFTWARE

In order to efficiently conduct lab experiments and concentrate on the science, it is extremely important to have an easy-to-use and stable graphical control software. For these reasons, a dedicated control software package called CARMA (Control And Reconstruction software for Multi-conjugate Adaptive optics) was developed and implemented in IDL. The array-based architecture of IDL keeps the effort of writing such a software package ($\approx$15 000 lines of code) relatively low. Debugging and compiling is much easier than for example in C. The disadvantages of the rather low speed and inability of real-time command execution is not an issue for this lab experiment. Here, the loop-frequency is limited by the frame-rates of the used CCDs, which are slow enough to accomplish all required calculations within one read-out time of the CCD, even with IDL. The rotation-speed of the phase screens in MAPS can anyways be adjusted to simulate any ratio between loop frequency and temporal evolution of the atmosphere.

The CARMA package contains all required modules for a complete control software package of an AO system, including a full graphical user interface (GUI). The settings of the single hardware components can be changed and all parameters of the control loops can be adjusted. Moreover, all relevant data can be displayed and logged to disk. Several analysis and debugging tools are available to the user. The control loop of CARMA is implemented in a modular design, therefore new control algorithms can be implemented relatively quickly and easily.

5.3 CALIBRATION ISSUES

Before operating MANU-CHAO in open- or closed-loop, it is important to find an optimal calibration strategy, to determine the required alignment accuracy, dynamic and linear range of the WFS and the DM, and the optimal basis functions for modal control. Otherwise, neither a reliable wavefront reconstruction in open-loop nor an acceptable performance in closed-loop, can be achieved. This section describes measurements and discussions related to these calibration issues.

5.3.1 ALIGNMENT ACCURACY

As explained in section 2.4.1, the mapping of the four pupil images produced by a pyramid to the grid of the WFS-CCD pixels can be off by up to 0.5 pixel. This causes aliasing of the signal from one subaperture on the telescope pupil into its neighbor, and reduces the sensitivity to high spatial frequencies. One possible cure in the case of MANU-CHAO is to use numerical binning of the pupil images, after these were cut out from the WFS-CCD images. For this system, the pupils each have a diameter of 60 pixel on the WFS-CCD, but only ≈80 actuators of the DM are used. To adjust the number of subapertures to those of the actuators and reduce the aliasing error, a binning of 4×4 was usually applied. In this way, the aforementioned mismatch can be reduced by the binning factor to an acceptable value of less than 1/5 of a subaperture.

Furthermore, the vertex angle of the individual pyramids are slightly different, resulting in non-perfect overlap of the pupil images of the single pyramids. This causes an effect similar to aliasing. In a layer-oriented system, there is again no possibility to correct for this pupil smearing. The impact can only be partially reduced by binning of the WFS-CCD.

To assess the impact of these effects, the condition number of the calibrated interaction matrix (sect. 4.3) and the performance in closed loop were measured with four pyramids in optical co-addition, compared to the single pyramid case. As shown in figure 5.9, both quantities are very similar and independent of the number of pyramids and the binning factor. This gives confidence that the matching of the pupil images to the pixels of the CCD and the overlap of the pupils of the four pyramids are sufficiently accurate for the performance range of this system.

Only for binning 8×8 and high-order modes, is the condition number significantly worse. The reason is that the pupil diameter on the detector is 60 pixels and thus not an integer number for this binning mode. Either information at the edge of the pupil is lost, or pure background noise is taken into account for the wavefront reconstruction, both deteriorating the performance.

The condition number in figure 5.9 shows a steep increase when using more than 40 modes, independent of the number of pyramids or binning factors. The maximum useful number of reconstructed modes is therefore ≈36, which is a typical number when using ≈100 actuators (Kasper, 2000). The primary reason is that higher spherical modes as represented by the DM look very similar to defocus, leading to a run-away effect and ultimately crashing the loop.

To further examine the impact of pupil smearing, artificial misalignments were introduced by shifting the software-mask to cut out the individual pupils from the un-binned WFS-CCD image. As mentioned, the numerical binning of 4×4 was applied only after the pupils were cut out from the WFS-CCD images. The mea-

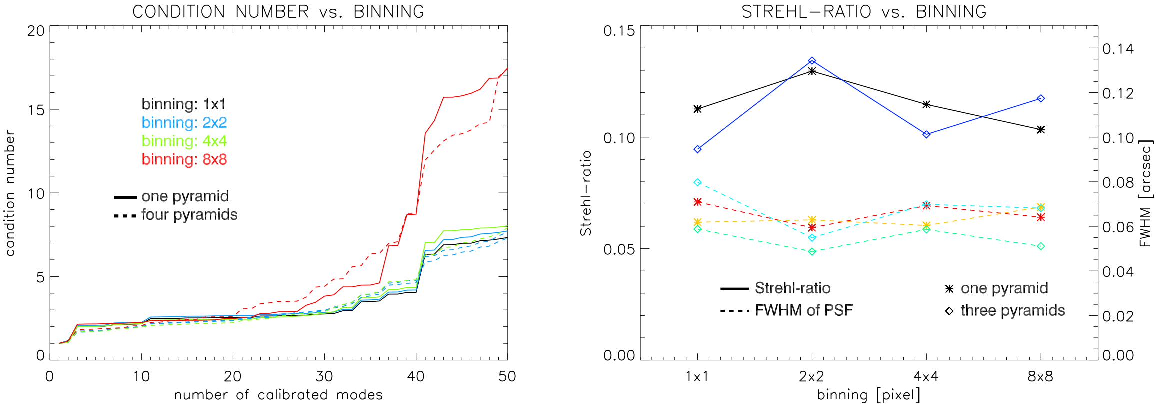

FIGURE 5.9: The condition number of the calibrated interaction matrix (**left**) and the performance in terms of Strehl and FWHM of the science channel PSF in closed-loop (**right**) for different binning factors when using 30 modes and the ground-layer phase screen.

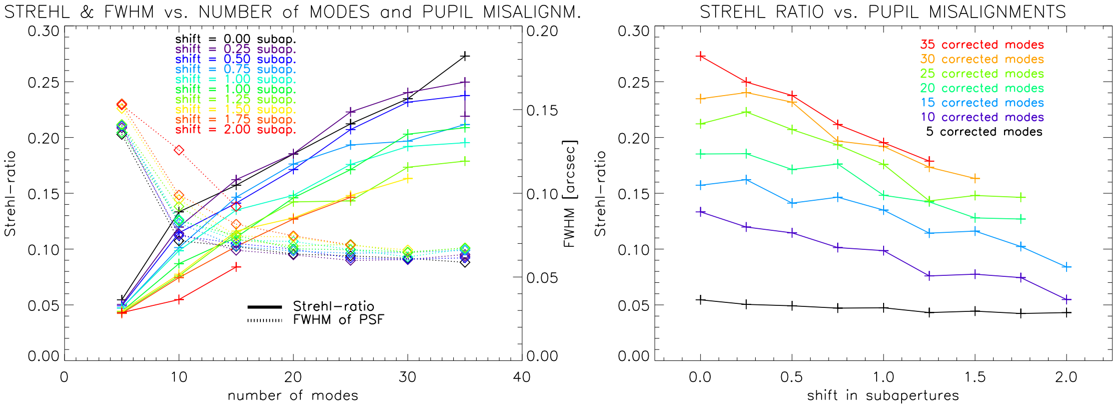

FIGURE 5.10: The measured performance in closed-loop as a function of the pupil misalignments. **Left:** The Strehl ratio and the FWHM of the PSF as a function of the number of reconstructed modes for various values of the misalignments. **Right:** The Strehl ratio as a function of the size of the pupil misalignments.

sured performance in closed-loop when shifting the mask for two of the four pupils is shown in figure 5.10. The Strehl ratio drops rapidly even for small misalignments and independently of the number of reconstructed modes. This means that all spatial frequencies are affected by such a misalignment. For very small misalignments (0.2 subapertures) the performance is less affected, because this is the inherent misalignment of the system caused by slight mismatches of the properties of actual used hardware components. These measurements confirm simulations, which suggest that the misalignments have to be smaller than 0.2 subapertures to achieve acceptable performance (Diolaiti et al., 2005a,b).

5.3.2 INJECTION MATRIX

For modal control of the system, we decided to use Zernike modes because of their easy mathematical handling and good representation of the wavefront aberrations induced by the atmosphere. Still the problem remains how to optimally represent Zernike modes with the DM.

The surface of the DM can be approximated by a linear superposition of the response of the individual actuators to the applied voltages. The response of actuator j is given by its influence function $I_j(x, y)$. To represent a given shape, for example Zernike mode $Z_n(x, y)$, with the DM, the weighting coefficients $U_{n,j}$ of these individual influence functions have to be determined:

$$Z_n(x, y) = \sum_j U_{n,j} \cdot I_j(x, y) \ . \tag{5.1}$$

With the measured sample actuator influence function $I(x, y)$ (fig. 5.7) as a template for $I_j(x, y)$, the voltages $U_{n,j}$ can be determined by a least-squares fit to the theoretical Zernike modes. The matrix $\mathbf{U}$ containing the voltages $U_{n,j}$ for all actuators and modes is subsequently called the injection matrix.

As mentioned above (sect. 5.2.3), we use only the inner 65 mm of the DM for this lab experiment. The voltages of the actuators in this inner portion are determined with the method just described to fully represent the Zernike modes. However, high-order Zernike modes have large deformations at the edge of the pupil. To adequately represent these deformations, it is not sufficient to leave the "invisible" actuators in the outer annulus at their bias voltage. Instead, we applied "next-neighbor slaving" to determine the voltages for these actuators. That is, starting from the "visible" actuators, the voltages of the outer actuators were set to the mean value of the closest controlled actuators. Furthermore, the voltages of the outer actuators were multiplied with a concentric attenuation factor to reduce the applied voltages towards the edge of the DM. This keeps the mean applied voltage of all actuators close to the bias voltage, avoiding problems with the DM electronics when introducing piston to the DM. A surface plot of the determined voltages appears in figure 2.5 on page 15.

To assess the quality and linearity of the representation of the Zernike modes by the DM, the individual modes were applied and the mirror surface was measured for each mode with the FISBA interferometer. As shown in figure 5.11, the linearity of the applied modes is better than a few nanometers rms. However, the rms of the individual applied modes is different by $\approx$15%. Zernike modes are orthonormal and should thus have all the same rms value. The deviations are caused especially for high-order modes by the inability of the simple model of equation 5.1 to properly take into account the interaction of the individual actuators with its neighbors. For high-order modes, the voltages applied to adjacent actuators can be greatly different, but due to the coupling by the facesheet, they show a smaller excursion than expected from pure linear behavior. However, since the WFS unit is calibrated with the applied modes on the DM, this effect has only very little influence on the performance of this particular AO system.

5.3.3 LINEAR RANGE AND OPTIMAL CALIBRATION AMPLITUDE

Since the linear range of the unmodulated pyramid WFS is rather small (Costa, 2005), the applied amplitude of the modes used for the calibration of the system (as described in sect. 4.2) has to be chosen small enough to stay within this linear range. On the other hand, the calibration amplitude should be as large as possible to minimize the noise caused by the residual surface roughness of the DM. Once the optimal modal basis has been found, it is thus essential to know the ideal calibration amplitude of the modes.

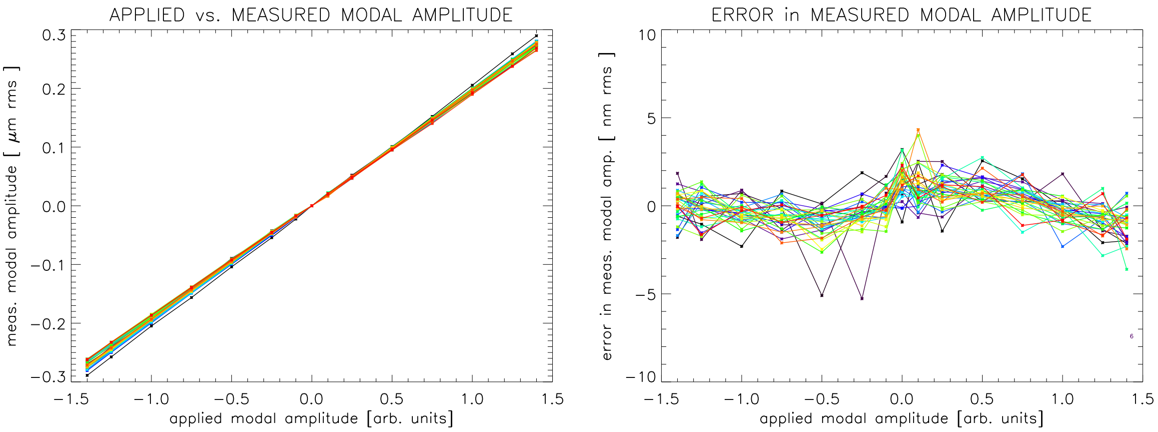

FIGURE 5.11: The quality of the representation of Zernike modes by the DM. **Left:** The measured versus the applied modal weight. **Right:** The relative deviation from linearity for the single modes.

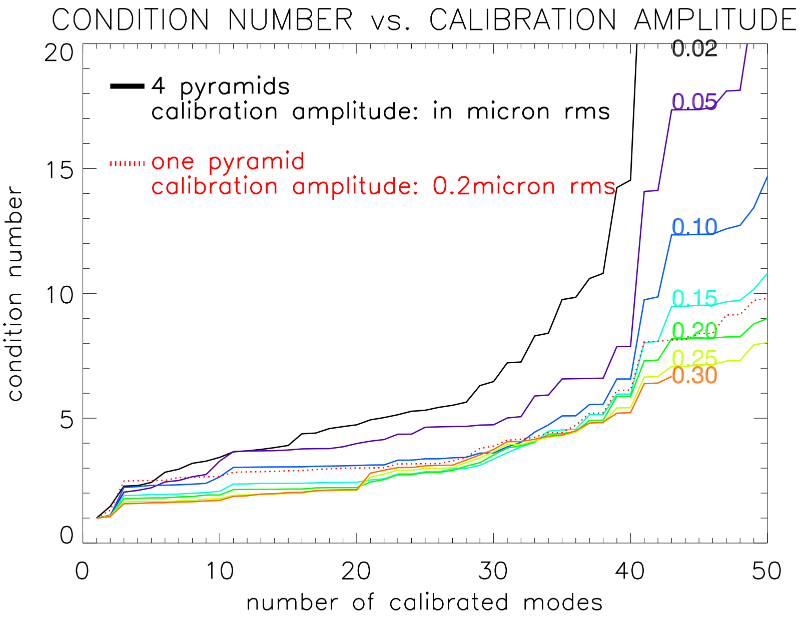

FIGURE 5.12: The condition number of the calibrated interaction matrix versus the number of modes and for different calibration amplitudes.

To find the optimal calibration amplitude for the system, we calibrated with different amplitudes and calculated the condition number of the measured interaction matrix. As can be seen in figure 5.12, the condition number gets smaller for larger calibration amplitudes, saturating for calibration amplitudes larger than $\approx 0.15\,\mu$m rms. This reflects the fact, that for smaller calibration amplitudes, the high spatial frequency surface aberrations of the DM are relatively more pronounced. Since this residual surface roughness of the DM is the same for all applied modes, the perceived modes on the WFS look more similar, increasing the condition number of the interaction matrix.

On the other hand, we determined the linear range of the pyramid by applying the modes with different amplitudes to the DM and measured the modal coeffi-

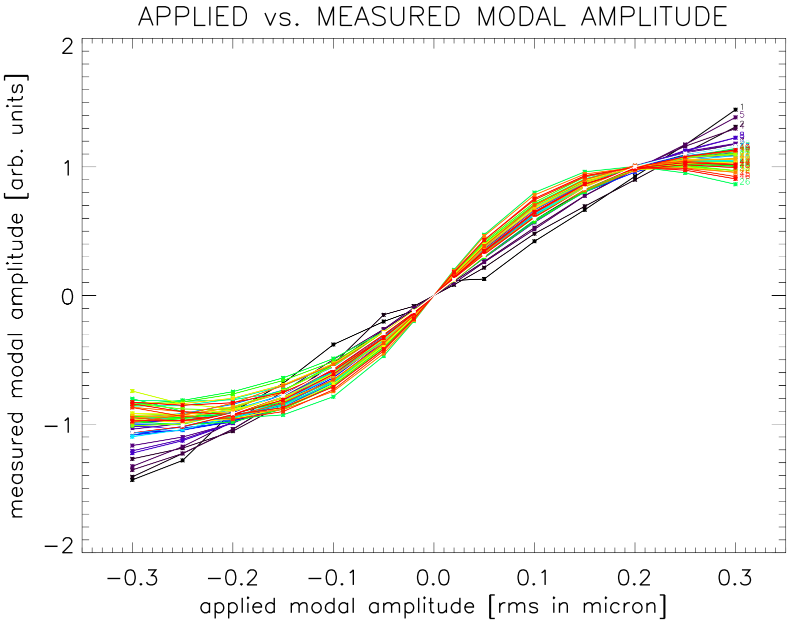

FIGURE 5.13: The linearity of the pyramid for the individual modes. For small amplitudes (below 0.1 μm rms) the pyramid over-estimates the weight of the modes, while it saturates above 0.2 μm rms. The amount of over-estimation and the starting point of the saturation is worse for high-order modes.

cients with the WFS. As shown in figure 5.13, the linear range for most of the high order modes is only up to 0.1 μm rms. If the system is calibrated with an amplitude greater than the linear range, then the measured modal coefficients are under-estimated in closed loop, having a similar effect as a smaller gain factor (see sect. 4.3). In this case, the control loop requires more loop steps to achieve the same degree of correction, and thus cannot follow rapidly evolving turbulence.

It should be mentioned that the observed non-linearities in figure 5.13 are entirely due to the pyramid WFS. As shown above (fig. 5.11), the deviation from linearity of the applied modes on the DM is less than 1%.

To determine the combined impact of these two effects, we measured the performance of the system in closed-loop for different calibration amplitudes and wind speeds. For larger wind speeds at the same loop frequency, the differences between successive loop steps is larger, emulating the effects of worse seeing. Figure 5.14 shows that it is in general better to calibrate with a small modal amplitude. Only for loop frequencies f_{loop} larger than ≈30 times the Greenwood-frequency f_G, does the control loop have enough time to compensate for the effectively reduced gain factor by multiple loop steps without loosing too much in performance.

5.4 STATIC VERIFICATION

One important verification step of an AO system is to compare the obtained wavefront measurements with a reference. This was accomplished by applying a semi-random pattern to the DM and comparing the measurements of MANU-CHAO with those of the FISBA interferometer. There are several options to reconstruct the wavefront from the wavefront slopes as measured with MANU-CHAO. The first is

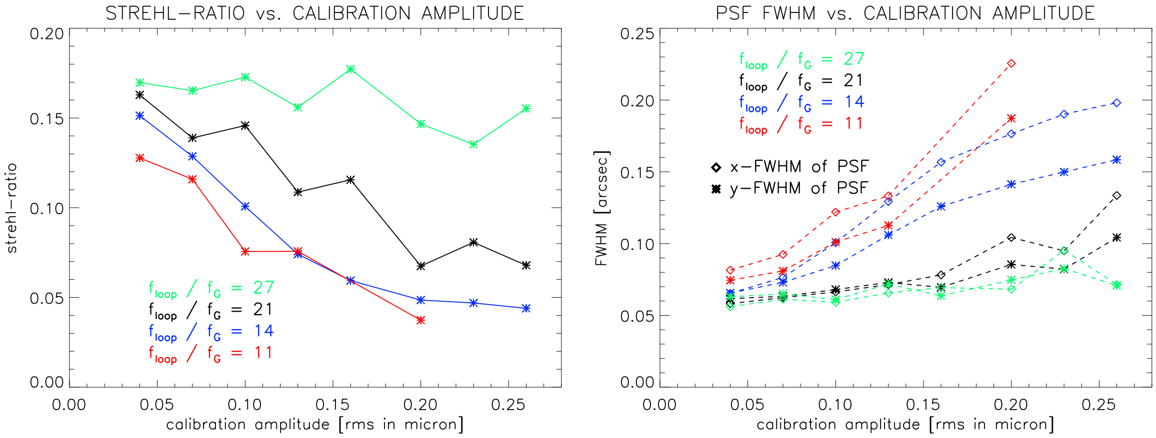

FIGURE 5.14: The performance in closed-loop in terms of Strehl ratio (**left**) and FWHM (**right**) as a function of the calibration amplitude and for different wind speeds. The curves correspond to different ratios of Greenwood-frequency f_G of the turbulence over loop frequency f_{loop}.

to make use of a property of the Laplace-Operator Δ, which connects the second derivative $\Delta W(x, y)$ of a function $W(x, y)$ to its Fourier-Transform $w(u, v)$ via

$$\mathbf{FT}\left[\Delta W(x, y)\right] = -\left(u^2 + v^2\right)\ w(u, v)\ . \tag{5.2}$$

The second derivative $\Delta W(x,y)$ of the wavefront can be computed with the difference quotient directly from the wavefront slopes. With equation 5.2, the Fourier-transform of the wavefront $w(u,v)$ is determined, which is in turn transformed back into the spatial domain to get the wavefront $W(x,y)$ itself. This procedure usually requires two to three iteration steps to achieve good results. More details about the Laplace operator in this context can be found in Gonzalez and Woods (2003) and Roddier and Roddier (1991).

The second possibility is to simulate a theoretical interaction matrix $\mathbf{I}_{\text{rmt}}$ for a pyramid wavefront sensor with, for example, the CAOS simulation package (Carbillet et al., 2004) and use the modal approach as described in section 4.3. The wavefront is then given by a linear superposition of the Zernike modes $Z_n(x, y)$. Finally the third method is to measure the interaction matrix $\mathbf{I}_{\text{cal}}$ directly as described in section 4.2.

A comparison of these three wavefront reconstruction algorithms for a static, Kolmogorov-like wavefront is shown in figure 5.16 for one pyramid and in figure 5.17 when using all four pyramids in optical co-addition. The Laplace operator generally shows a good matching between the measurements of MANU-CHAO and the FISBA interferometer. The simulated interaction matrix $\mathbf{I}_{\text{rmt}}$ on the other hand has problems with reconstructing the wavefront at the edge of the pupil. The reason is imperfections of the pyramids edges, which scatter light and thus create additional intensity variations in the pupil images, which are not related to the wavefront aberrations. This causes an amplification of high-spatial frequency noise and results in excessive coefficients for high-order Zernike modes. Since these high-order Zernike modes have most of their deflection at the edge of the pupil (fig. 2.5), the reconstructed wavefront shows large distortions at the edge. Nevertheless, the good matching between the reference measurements and the reconstructed wavefront of MANU-CHAO is obvious.

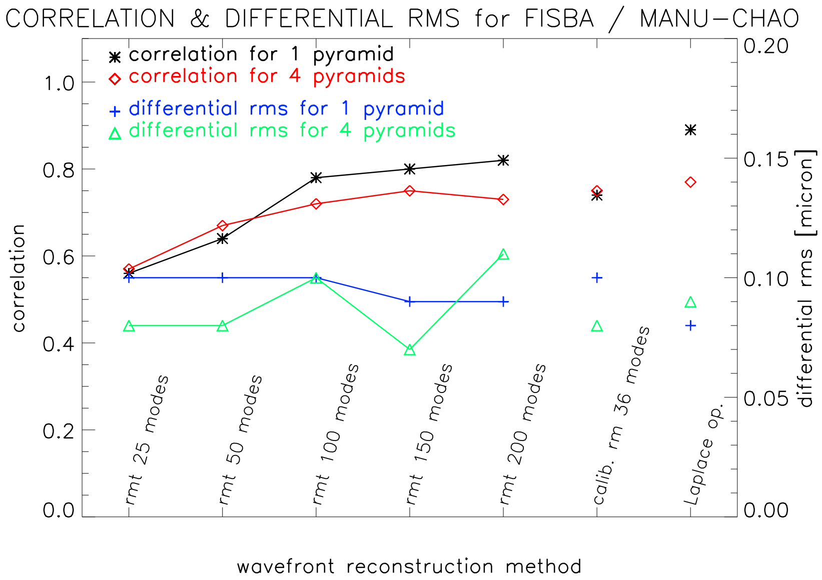

FIGURE 5.15: The correlation and the differential standard deviation between the Zernike coefficients as determined from measurements with the FISBA and MANU-CHAO for a semi-random wavefront. A simulated reconstruction matrix (rmt) with different number of modes, a calibrated reconstruction matrix with 36 modes, and the Laplace Operator were used to reconstruct the wavefront from the measurements by MANU-CHAO.

Due to the limited number of calibrated modes, the wavefront reconstructed with the calibrated interaction matrix $\mathbf{I}_{\text{cal}}$ has only limited similarity with the FISBA measurement, but clearly shows the main features. Nevertheless, for the same number of reconstructed modes, the performance of the system is better when using $\mathbf{I}_{\text{cal}}$ than for $\mathbf{I}_{\text{rmt}}$ (fig. 5.15).

To quantify the matching between the reference measurement with the FISBA and the reconstructed wavefront from MANU-CHAO, two methods were used. Both are based on the decomposition of the wavefronts into Zernike modes. The first method was to directly correlate the fitted modal weights $c_{i,\text{FISBA}}$ and $c_{i,\text{MANU-CHAO}}$ via

$$\mathbf{COR} = \mathbf{CC}\left[\mathbf{c}_{\text{FISBA}}, \mathbf{c}_{\text{MANU-CHAO}}\right](0) \; , \tag{5.3}$$

with the cross-correlation function $\mathbf{CC}[f(x), g(x)]$ as defined in equation 2.40. The resulting correlation is between 60% and 90%, increasing with the number of reconstructed modes (fig. 5.15).

The second method was to calculate the differential variance σ^2_{diff} between the two wavefronts via

$$\sigma^2_{\text{diff}} = \sum_{i=0}^{200} \left(\mathbf{c}_{\text{FISBA}} - \mathbf{c}_{\text{MANU-CHAO}}\right)^2 \; . \tag{5.4}$$

In figure 5.15 also the results using this method are shown, which are very similar to the correlation method. The differential rms is ≈0.10 μm, corresponding to a Strehl ratio of ≈60%, which is acceptable for the desired performance range of this system. Furthermore, this is smaller than the fitting error of ≈0.17 μm, even when correcting the maximum number of 36 modes. This gives us confidence that the wavefront aberrations can reliably be measured.

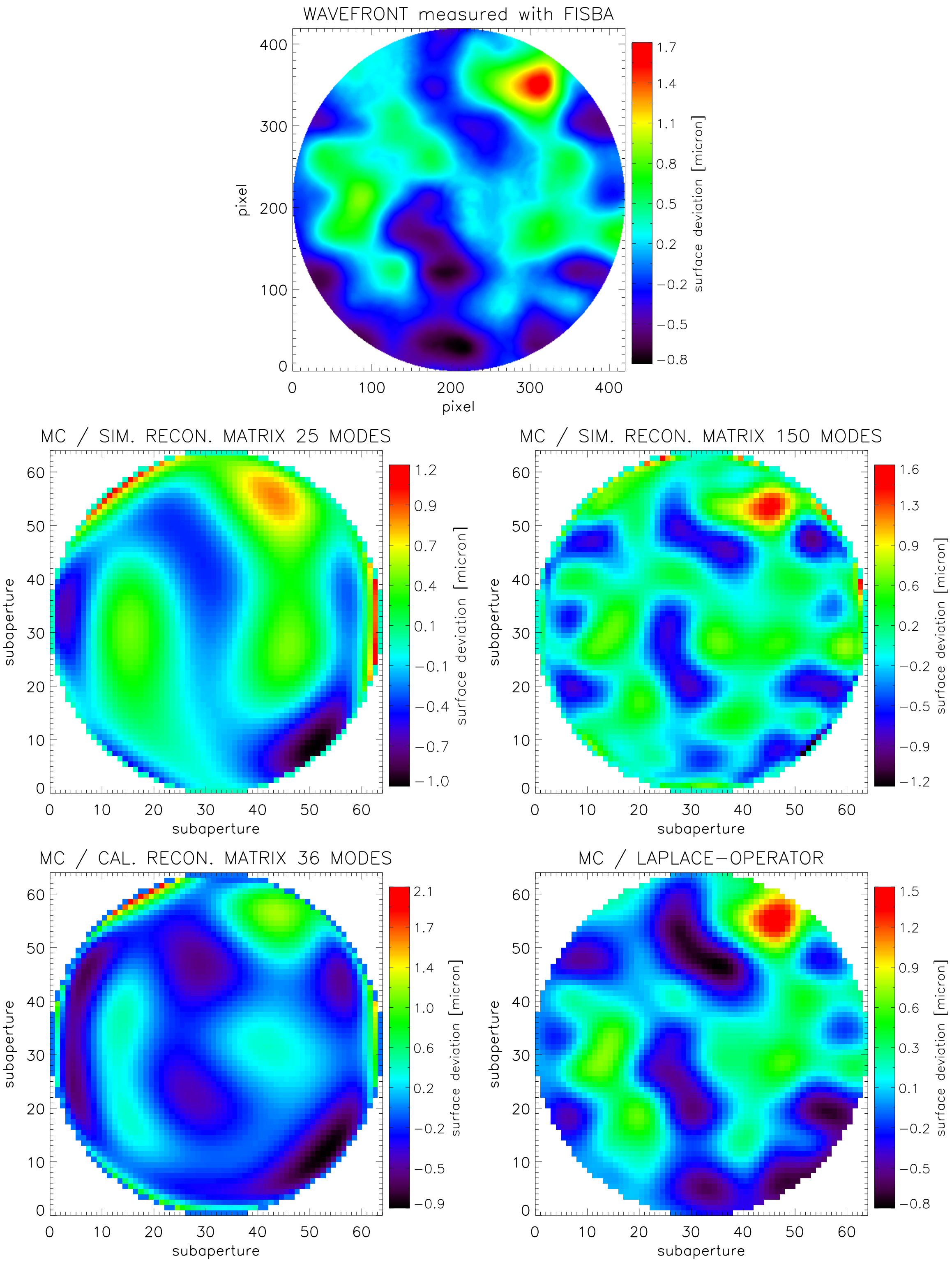

FIGURE 5.16: A static, random wavefront as measured with the FISBA Interferometer (**top**) and with MANU-CHAO using one pyramid and different methods to reconstruct the wavefront. Shown are the results obtained with a simulated reconstruction matrix with 25 modes (**middle left**) and 150 (**middle right**) Zernike modes, a calibrated reconstruction matrix using 36 modes (**bottom left**) and with the Laplace Operator (**bottom right**).

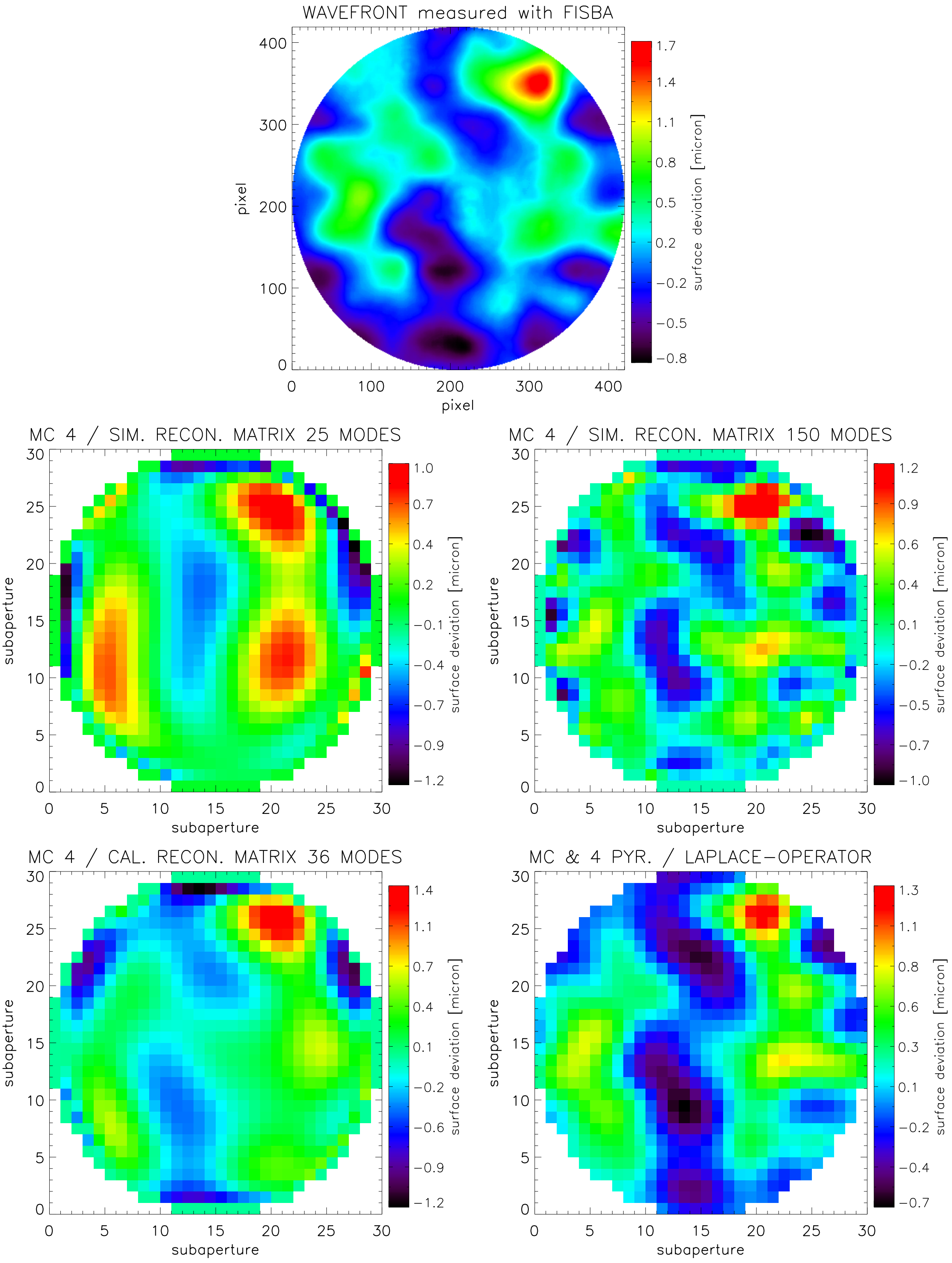

FIGURE 5.17: A static, random wavefront as measured with the FISBA Interferometer (**top**), and with MANU-CHAO using four pyramids in optical co-addition and different methods to reconstruct the wavefront. Shown are the obtained wavefronts with a simulated reconstruction matrix for 25 (**middle left**) and 150 (**middle right**) Zernike modes, a calibrated reconstruction matrix using 36 modes (**bottom**) and the Laplace-Operator (**top right**). To minimize aliasing noise, a binning of 2×2 was applied for these measurements.

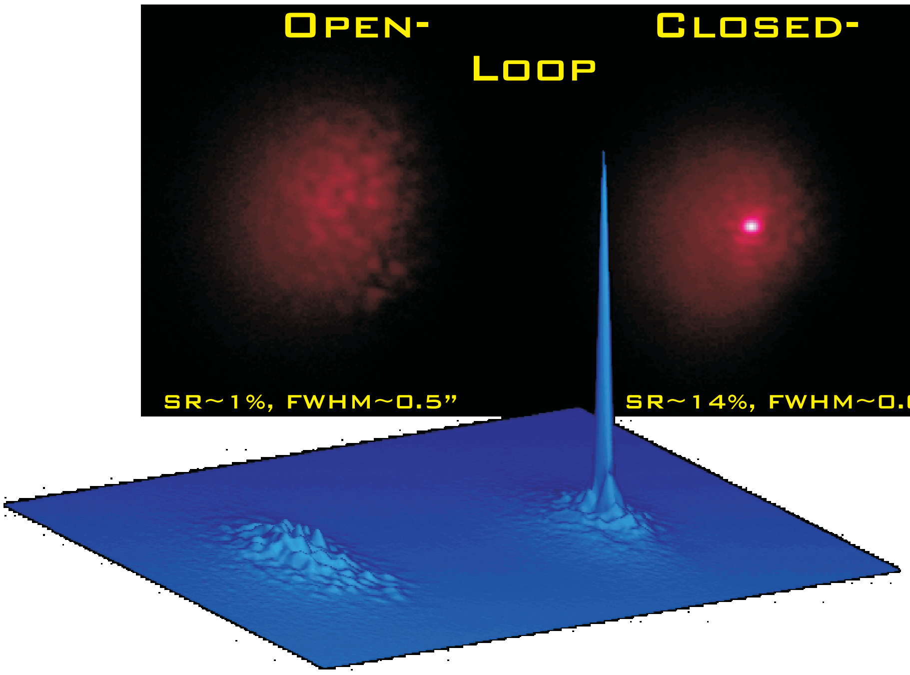

FIGURE 5.18: The observed PSF of the science channel in open-loop (**left panel**) and closed-loop (**right panel**) when using all four pyramids in optical co-addition mode and one phase screen conjugated to the pupil, thus simulating the on-axis case. The contrast in the upper images is square-root stretched to enhance the halo around the central core.

5.5 DYNAMIC MEASUREMENTS

Besides the reliability of static wavefront measurements is the quality of the correction in closed-loop operation the most important measure of the performance of an AO system. For all dynamic measurements presented here, the calibration procedure described in section 4.2 and the Least-Squares (LS) reconstructor were used. In figure 5.18, a comparison of the PSF of the science channel in open-loop (no correction) and closed-loop (with correction) is shown for on-axis, single-star AO operation. Without correction, the image is seeing-limited, with a FWHM of the PSF ϵ_{FWHM} of ≈0.5”. When correcting 36 Zernike modes, ϵ_{FWHM} is reduced to ≈0.07” and is thus almost diffraction-limited for this system. The fact that we are using a phase screen with a small value of r_0 at the science wavelength, results in only a rather modest Strehl ratio of ≈14% in closed-loop operation. The reason was to achieve the same spatial and temporal sampling as at the telescope under realistic atmospheric conditions.

By using a single phase screen and placing it conjugated to the pupil, the wavefront aberrations are independent of the position in the field, there is no isoplanatic effect (fig. 2.14 on page 28). In this way, the performance on-axis can also be simulated with this system, even though the two light-sources for the guide star and the science object do not coincide.

To further evaluate the performance of the system in closed-loop, the Strehl ratio and the FWHM of the science PSF was determined as a function of the number of reconstructed modes. Figure 5.19 shows the steady increase in performance, up to the useful maximum number of reconstructed modes (sect. 5.3.1), which is

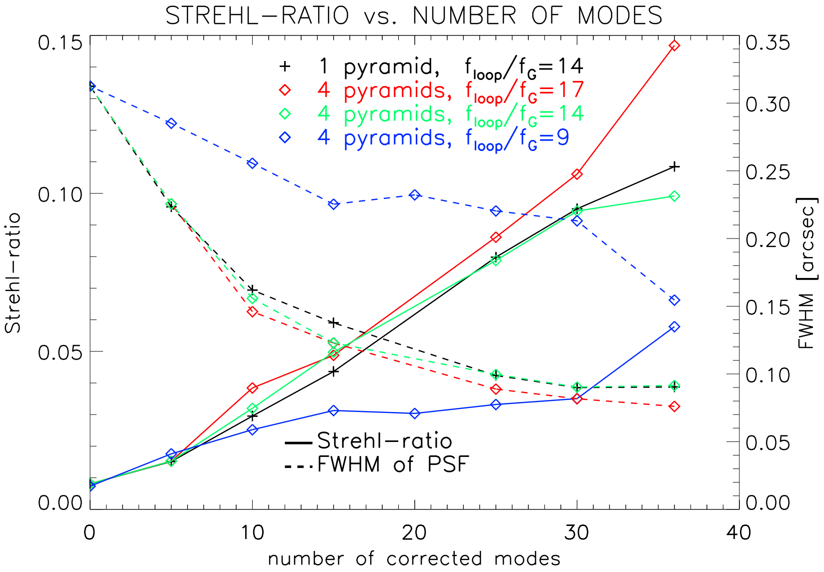

FIGURE 5.19: The measured Strehl ratio and FWHM of the science PSF in closed-loop as a function of the number of corrected modes for different ratios of the atmospheric Greenwood-frequency f_G and the loop frequency f_{loop}. One phase screen, conjugated to the pupil is used to simulate the on-axis case.

limited by the DM and not by the WFS itself. This means that the high spatial frequencies are sufficiently well preserved by the mapping of the pupil images on the discrete pixel grid of the WFS-CCD (sect. 5.3.1). Figure 5.19 also shows that the performance in this on-axis, high-flux regime is independent of the number of pyramids. The high spatial frequencies are therefore also preserved when optically co-adding the pupil images of the four pyramids.

5.6 GROUND-LAYER AO MEASUREMENTS

After these more general aspects, dynamic measurements of specifically the GLAO concept are presented in this section.

5.6.1 FILTERING OF NON-CONJUGATED HEIGHTS

A theory to describe how well single turbulent layers can be seen and thus corrected with an MCAO system was presented in chapter 3. To verify this theory experimentally, the conjugation height of the phase screens in MAPS were varied and the WFS-DM combination was kept conjugate to the pupil plane. The performance in closed-loop was then measured for various positions of the phase screen.

Figure 5.20 shows the result of these measurements and compares the Strehl ratio and the FWHM of the PSF ϵ_{FWHM} when operating in single-star and GLAO mode. We used the measured values of ϵ_{FWHM} for comparison to theoretical predictions, because for Strehl ratios below ≈15%, the simple Marechal estimate (eqn. 2.21) is no longer valid. In this regime, the Strehl ratio is not a simple function of the variance of the wavefront, but instead critically depends on the precise, but unknown structure of these aberrations. In these low-Strehl conditions, ϵ_{FWHM} is less sensitive to such effects, and is therefore a better measure for the performance.

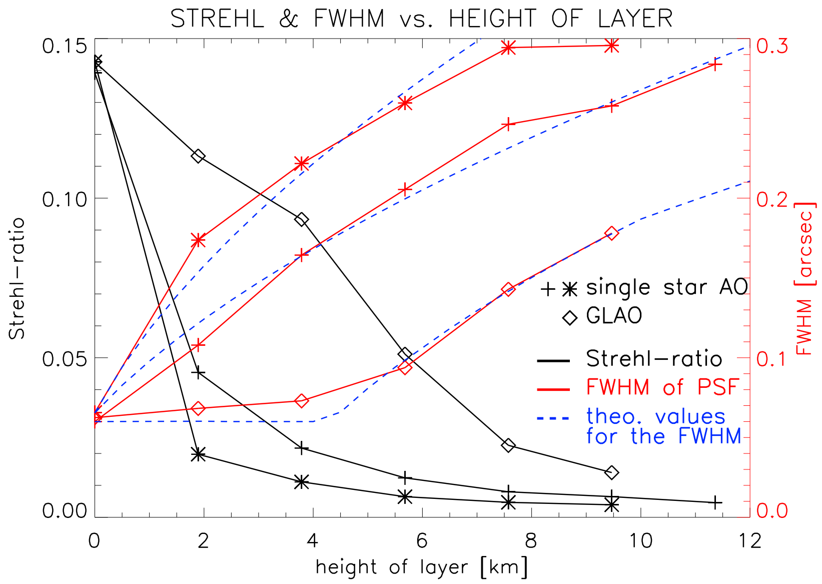

FIGURE 5.20: The Strehl ratio and FWHM of the PSF in closed-loop as a function of the height of the phase screen above the pupil plane for MANU-CHAO operating in GLAO mode. For comparison, the performance of a single-star AO system with the science-object at 14 and 17 arcsec distance from the guide star, respectively, is shown.

The theoretical value for ϵ_{FWHM} can be calculated from the variance of the wavefront aberrations σ^2_{sci} (eqn. 2.18 and 2.19). For single-star AO, σ^2_{sci} was calculated with equation 3.12, where the value of σ^2_{cl} was determined from the on-axis performance and $\sigma^2_{\mathrm{layer}}$ from open-loop measurements. For the GLAO mode, the theoretical performance was determined from $\sigma^2_{\mathrm{layer}}$, attenuated with the layer-filter functions $\mathbf{TFF}(h)$ for this system, as defined in chapter 3. Figure 5.20 shows that all measurements follow very nicely the theoretical predictions.

The fact that ϵ_{FWHM} in GLAO operation is constant if the altitude of the turbulent layer is less than ≈4 km, can be nicely explained with the help of the layer-filter functions (e.g. fig. 3.4). For a given number of reconstructed modes, the correction by the AO system is effective only up to a certain spatial frequency. When moving the turbulent layer away from the conjugation plane of the WFS, the uncorrected high spatial frequencies are smeared out first, while the corrected, lower spatial frequencies and thus the closed-loop performance are barely influenced.

5.6.2 MODAL COVARIANCE MATRIX

A good measure to describe this filtering effect of non-conjugated turbulent layers as a function of spatial frequency is the Zernike modal covariance matrix, whose theoretical values were calculated in section 3.2.2. Since Zernike modes are approximately sorted by spatial frequency (sect. 2.2.6), the temporal average variances of the individual modal coefficients correlate with the spatial power-spectral density of the wavefront aberrations.

To measure the modal covariance as a function of the height of the turbulent layer above the conjugation plane of the WFS, the altitude of the phase screen in MAPS was varied, while the WFS was kept conjugated to the pupil plane. For each position of the phase screen, the modal covariance in open- and closed-loop was

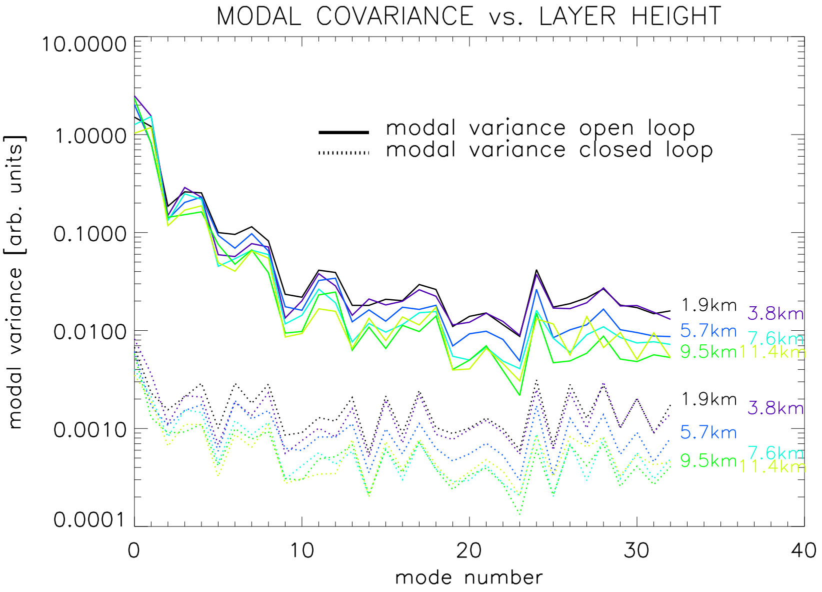

FIGURE 5.21: The temporal average variance of the modal coefficients in open- and closed loop as a function of the distance between the phase screen and the conjugation height of the WFS, measured with MANU-CHAO in GLAO mode.

determined. The result plotted in figure 5.21 clearly shows the increase of the filtering effect for increasing distance of the turbulent layer from the conjugation plane of the WFS. The open-loop data also show that the filtering effect is more pronounced for high-order modes. However, the overall filtering is not as strong as expected from theoretical predictions. The reason is that, an infinite number of guide stars was assumed in the theoretical calculations, which might be not a good approximation for this case with only four guide stars. For only four guide stars, the small number of overlapping pupils with slightly shifted positions is not sufficient to homogeneously smear out the spatial frequencies.

As seen in the previous section (fig. 5.20), the adaptation of the conjugation heights of the DMs to the vertical structure of the atmospheric turbulence is crucial to achieve optimal performance of an MCAO system. Since simultaneous SCIDAR measurements are not feasible for all MCAO observations, information about the vertical structure of the atmospheric turbulence has to be retrieved by different means. One idea is to use the measured modal covariance matrix of the high-layer (HL) DM. For maximum Strehl ratio on-axis, this DM has to be conjugated to the strongest turbulent layer in the free atmosphere. If all layers obey the Kolmogorov model, then the HL-DM has to be placed at the altitude where the ratio of the temporal averaged variances of the high- to the low-order modal coefficients is maximum. For a mis-conjugation, the high spatial frequencies are attenuated with respect to the low spatial frequencies, decreasing this ratio.

Considering the results in figure 5.21, the determination of the optimal conjugated height from the measured modal variances seems to be possible, with a vertical resolution of a few kilometers. However, it is doubtful if this is sufficient for this application (sect. 6.8). But, as explained above, for more guide stars and a larger FoV, the filtering effect should be more pronounced, making the distinction of closely separated layers easier and thus increasing the vertical resolution.

5.6.3 OFF-AXIS PSF STRUCTURE

One of the main advantage of a GLAO system (sect. 2.5.3) is that the shape of the PSF is supposed to be more uniform over the FoV as compared to single-star AO. For measuring the shape of the PSF in closed-loop and at different positions in the field, we used a dedicated metal plate in the light-source to mount the science fiber at various off-axis positions (fig. 5.3). Due to opto-mechanical constraints, only three guide stars could be used for these measurements.

As shown in figure 5.22, in GLAO mode and for one turbulent layer at 5.6 km above the pupil plane, ϵ_{FWHM} is less than twice the diffraction-limit over a field with 30 arcsec diameter. Compared to single-star AO, where ϵ_{FWHM} increases almost exponentially with distance to the guide star, this is a dramatic improvement in performance. For single-star AO, ϵ_{FWHM} is already at a distance of 3 arcsec from the guide star more than twice the diffraction-limit. The area of useful correction is thus increased in GLAO mode by a factor of ≈25. This confirms the notion that an homogenous performance can be achieved over the entire area covered by the footprints of the guide stars on the respective turbulent layer.

For the case of one turbulent layer at altitude h, the isoplanatic angle ϑ_0 in a singe-star AO system is given by (Hardy, 1998)

$$\vartheta_0 \;=\; 0.31\,\frac{r_0}{h}\;, \tag{5.5}$$

which results for h =5.6 km in ϑ_0 =2.5”. At a distance of 1.3” from the guide star, the Strehl-ratio is thus expected to drop from 15% to already 9.5%, as confirmed by the measurements.

Figure 5.23 shows images of the PSF at various distances to the guide star. In single-star operation mode, the PSF shows a significant elongation already a few arcsec away from the guide star. In GLAO operation mode this is dramatically better, the PSF remains circular up to a distance of ≈25 arcsec. The two figure 5.22 and 5.23 show that the elongation of the PSF increases with increasing distance from the guide star. This well-known effect is more pronounced for single-star AO, but is also present for a GLAO system, albeit much smaller and only for very large angular separations (> 25”). The elongation is caused by the different residual variance of the tilt in the direction toward and perpendicular to the guide star, as explained in e.g. chapter 7.4 of Hardy (1998).

We used the simple model described in section 3.4 to compare the measurements with theoretical expectations. With the positions $\vec{\alpha}_i$ of the guide stars and the conjugation altitude h of the layer, the corrected fraction $A_C(h, \vec{\alpha}_i)$ of the pupil footprint of the science object is determined numerically. Together with the temporal, fitting, and reconstruction errors, whose sum σ^2_{cl} can be retrieved from the on-axis performance, the total wavefront error σ^2_{sci} for the science object is calculated with equation 3.12. Finally, the theoretical value for ϵ_{FWHM} can be calculated from σ^2_{sci} with equations 2.18 and 2.19), resulting in the curves plotted in figure 5.22. The offset in ϵ_{FWHM} for the GLAO mode for the high-layer phase screen can be nicely explained with the layer-filter functions. For such a non-conjugated layer, the high-spatial frequencies are not seen by the WFS and thus cannot be corrected, resulting in reduced overall performance.

This simple model fails very close to the guide star. It does not take into account diffraction and thus predicts an infinitely small ϵ_{FWHM} at the position of the guide star. For a more accurate model in this regime, where $r_0 \approx D_{\text{tel}}$, the telescope

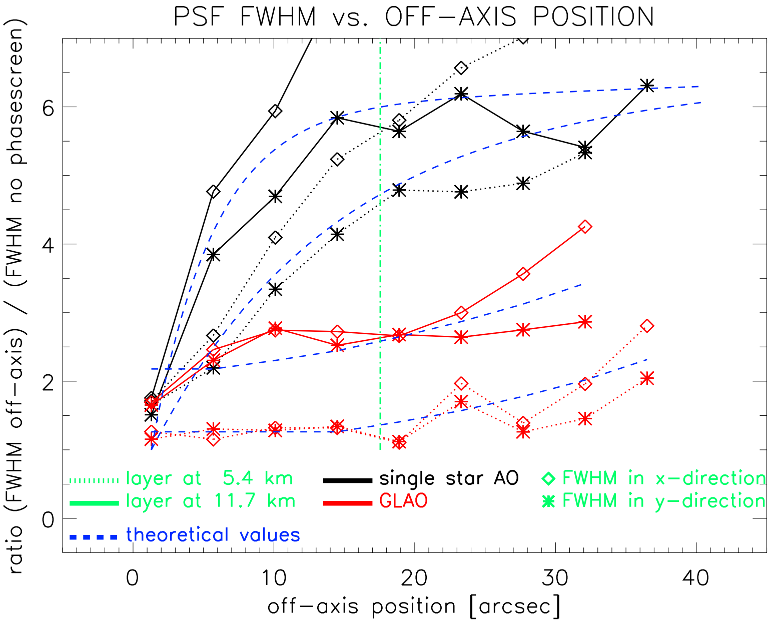

FIGURE 5.22: The FWHM of the PSF of the science object as a function of the distance to the guide star for single star AO and GLAO operation mode and for two different heights of the turbulent layer above the pupil plane. Three guide stars were used in GLAO mode (fig. 5.3) and the distance is given as the separation from the left-most guide star. The position along the x-axis of the two other guide stars is indicated by the vertical, dashed line.

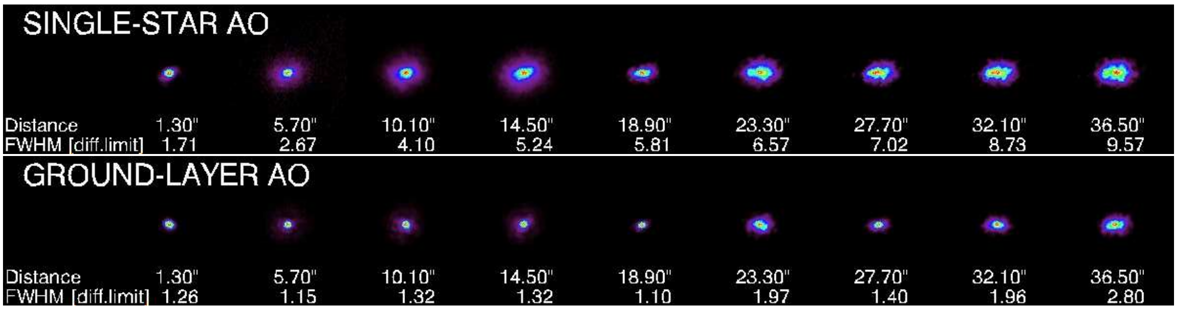

FIGURE 5.23: Images of the PSF of the science object as a function of the distance to the guide star for single star AO (**top**) and GLAO (**bottom**) operation mode for one turbulent layer at 5.4 km above the pupil plane. To highlight the shape of the single PSFs, they have been normalized to the same maximum intensity. The indicated FWHM is measured along the x-axis and is given in units of the diffraction-limit. For comparison, the open-loop FWHM is ≈6.5 times the diffraction-limit.

diameter D_{tel} has to be included in the calculation of ϵ_{FWHM} with equation 2.19. Furthermore, this model does not take into account the spatial correlation of the Zernike modes and thus predicts a circularly symmetric PSF. Nevertheless, for the purpose of this work, this simple model has sufficient accuracy.

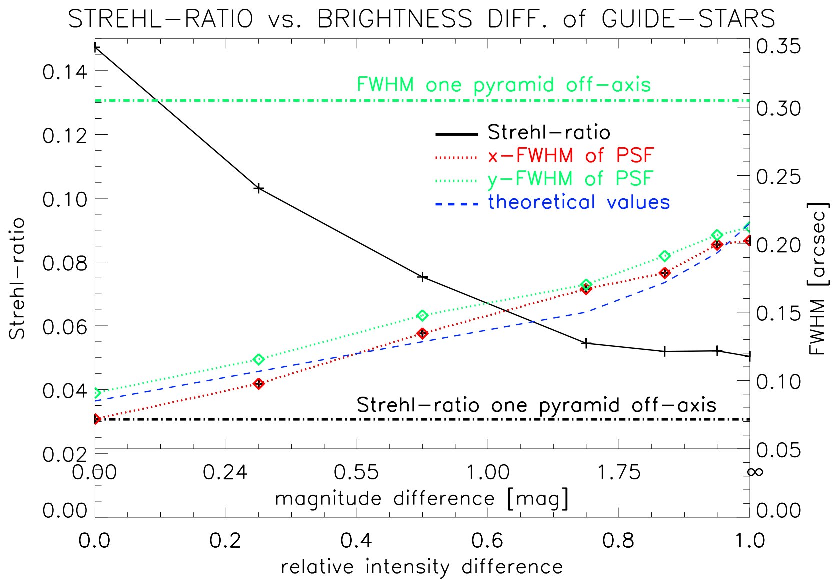

FIGURE 5.24: The measured Strehl ratio and FWHM of the PSF in GLAO operation mode as a function of the difference in the brightness of the guide stars. The brightness of three guide stars was the same and kept constant, while the fourth one was dimmed in discrete steps.

5.6.4 DIFFERENT BRIGHTNESS

One requirement of a layer-oriented MCAO system with optical co-addition is that all guide stars must have similar brightness. Otherwise, the measurements of the wavefront aberrations have more weight in the direction of the brightest guide star, biasing the reconstruction process toward its position and yielding a non-uniform distribution of the performance in the FoV.

To experimentally investigate this effect, one phase screen with a conjugated altitude of 10 km above the telescope and four guide stars were used. The brightness of one guide star was gradually reduced with the help of a variable filter. The measured performance is plotted in figure 5.24, showing a significant drop when the one guide star is only 0.25 mag fainter. If this guide star is fainter than $\approx$1.5 mag, as compared to the other three guide stars, it has practically no influence on the achievable performance. This confirms results obtained with end-to-end simulations of layer-oriented MCAO systems (Arcidiacono, 2004; Marchetti et al., 2003).

For a real system, the value of the Strehl ratio in the field depends critically on the position and brightness of the guide stars, and can be evaluated only through numerical simulations (see e.g. Arcidiacono, 2004); a simple semi-analytical estimate is generally not possible. Nevertheless, a rough estimate can be derived for the simple case presented here, with only one turbulent layer, four symmetrically arranged guide stars and an on-axis science object.

The usual assumption is that the best correction of the wavefront in the FoV is achieved at the position of the barycenter $\mathbf{p}_{\text{photons}}$ of photons from all guide stars. In the case that all stars have the same brightness, this barycenter $\mathbf{p}_{\text{hom}}$ coincides with the geometrical center $\mathbf{x}_{\text{stars}}$ of the guide star distribution. In contrast, when the stars have different brightness, the barycenter of the inhomogeneous distribution $\mathbf{p}_{\text{inhom}}$ is shifted, which in turn shifts the point of optimal correction away from

$\mathbf{x}_{\text{stars}}$. For a fixed science object located at $\mathbf{x}_{\text{stars}}$, as for this system, the correction performance therefore apparently degrades. To estimate ϵ_{FWHM} of this fixed science object, we reverse the situation and assume equal brightness of all guide stars, but the science object is shifted away from $\mathbf{x}_{\text{stars}}$ by the distance $|\mathbf{p}_{\text{hom}} - \mathbf{p}_{\text{inhom}}|$. Using the formulism described in the previous section for calculating the off-axis performance, ϵ_{FWHM} can be estimated. As shown in figure 5.24, this simple model fits reasonably well with the measured data.

For brightness differences of more than $\approx$1 mag, the model predicts a better performance than measured experimentally. The reason is that the CCD has a RON and limited dynamic range, which are not considered in the analytical model. The signal of the fainter star is therefore either lost in the RON or results in homogenous illuminated pupil images. In either case, the faint star does not provide additional information about the wavefront aberrations to improve the performance.

5.7 KALMAN FILTER FOR AO

For all previous closed-loop measurements, the established Least-Squares (LS) reconstructor was used. Another option for the control algorithm is the Kalman filter, whose theoretical basis was introduced in chapter 4. Measurements to verify the predicted performance increase of the Kalman filter are presented in this section.

5.7.1 KALMAN FILTER FOR CLASSICAL AO

To experimentally test the performance of the Kalman filter with the included spatial and temporal model of atmospheric turbulence for a Classical on-axis AO system, one guide star and one phase screen conjugated to the pupil plane were used. A plot with the performance of the Kalman filter and the LS reconstructor as a function of the number of corrected modes appears in figure 5.25. As predicted by simulations (e.g. Le Roux et al., 2004), the performance of the Kalman filter is slightly better than that of the LS reconstructor. This shows that the principle of the Kalman filter is sound and that the required additional quantities can be determined with sufficient accuracy with the methods described in section 4.5.2.

5.7.2 KALMAN FILTER FOR GLAO

Chapter 4 also introduced the adaptation of the Kalman filter to a layer-oriented MCAO system. For the experimental verification with MANU-CHAO, all four guide stars were used, and the performance was measured as a function of the conjugation altitude of the phase screen. For the modal covariance matrix, the theoretical values (sect. 3.2.2) were used, for the determination of the other required quantities, the methods described in section 4.5.2 were applied.

As shown in figure 5.26, the Kalman filter performs slightly better than the LS reconstructor. However, since the FoV of MANU-CHAO is relatively small, the filtering effect of non-conjugated layers is rather weak (sect. 5.6.2) and thus the performance increase when using the Kalman filter is not very significant.

However, the small gain in performance when using the Kalman filter in these two cases and the significant increase in complexity, computational power, and sensitivity to disturbances make the usefulness of its application in such cases

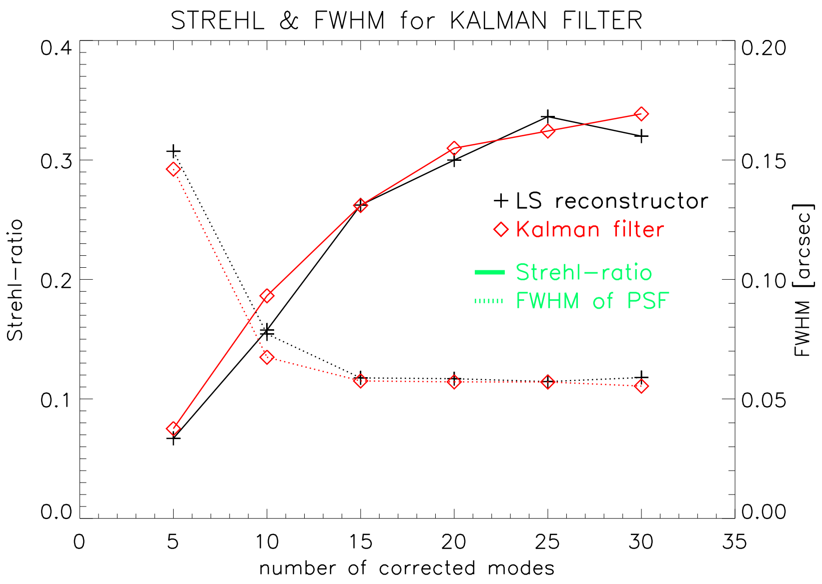

FIGURE 5.25: The performance of the Kalman filter and the Least-Squares (LS) reconstructor in closed-loop operation for an on-axis, single-star AO system.

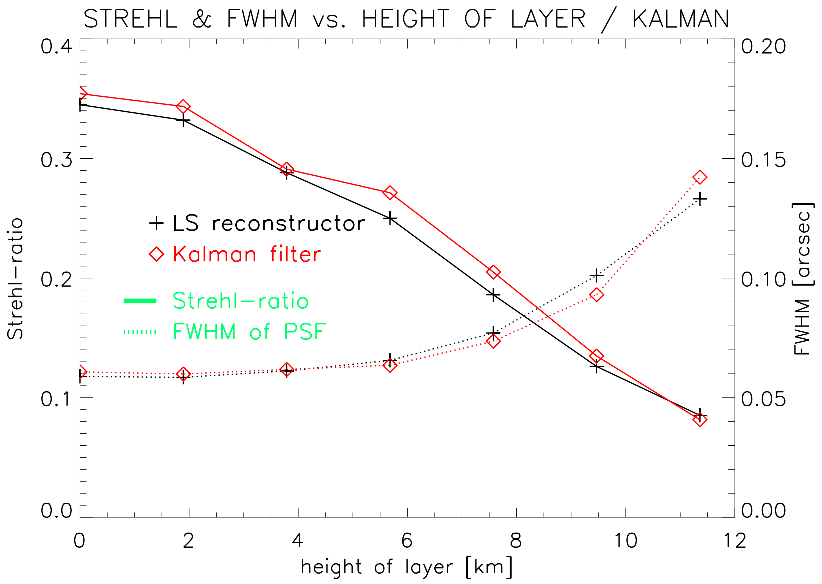

FIGURE 5.26: The performance of the Kalman filter and the Least-Squares (LS) reconstructor in closed-loop operation for GLAO operation.

rather doubtful. Most likely, other error sources in the system such as static aberrations and non-optimal control of the DM (including hysteresis, non-linearities and the mutual influence of the actuators) have a larger influence on the measured performance and are easier to correct. Only for very high Strehl ratios might the Kalman filter become an interesting option.

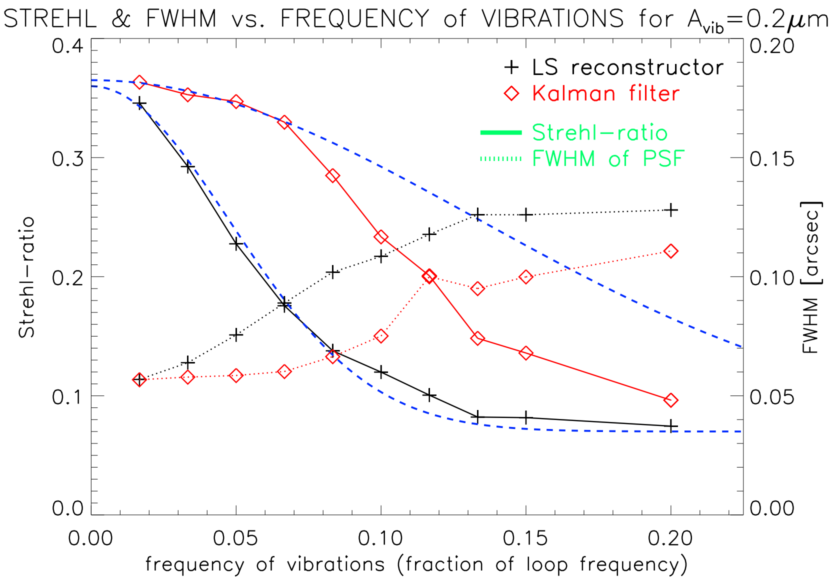

FIGURE 5.27: Performance of the Kalman filter and the Least-Squares (LS) reconstructor as a function of the frequency of the vibrations with a fixed amplitude.

5.7.3 KALMAN FILTER WITH VIBRATIONS

The Kalman filter achieves a significant increase in performance in simulations especially in the presence of vibrations. One guide star and one phase screen conjugated to the pupil plane were used for an experimental verification. Furthermore, two independent loops were implemented in the CARMA control software package. One loop applies the vibrations on the tilt mode to the DM, while the other runs at half the frequency and tries to correct the vibrations from the measurements acquired with the WFS. Since these two loops are independent and the applied vibrations are pure sine functions, the effects of vibrations can be measured systematically and without any additional harmonics. The additional quantities required for the Kalman filter are determined with the methods described in section 4.5.2, and the frequency of the vibrations is given as input to the control loop.

The performance of the Kalman filter as a function of the frequency of the vibrations is shown in figure 5.27. With the Kalman filter, the temporal bandwidth of the control loop is increased by a factor ≈2. This means that the frequency of the vibrations can be twice as high for the Kalman filter to achieve the same performance as the LS reconstructor.

Also plotted in figure 5.27 are the results of numerical simulations where vibrations were added numerically on measured open-loop data, and closed-loop operation was simulated with the same loop parameters as in the real system, but assuming perfect hardware components. The result of these simulations matches very well with the measured performance for the LS reconstructor, but predicts a significantly higher Strehl ratio for the Kalman filter, especially for vibrations with high frequencies. One reason for the experimentally worse performance of the Kalman filter compared to simulations is the jitter in the system between the two control loops. In MANU-CHAO the data of the CCD cameras have to be transfered via ethernet to the wavefront reconstruction computer, which sometimes introduces small delays. The other reason for the worse performance might be the insufficient accuracy of the additional required quantities for the Kalman filter in

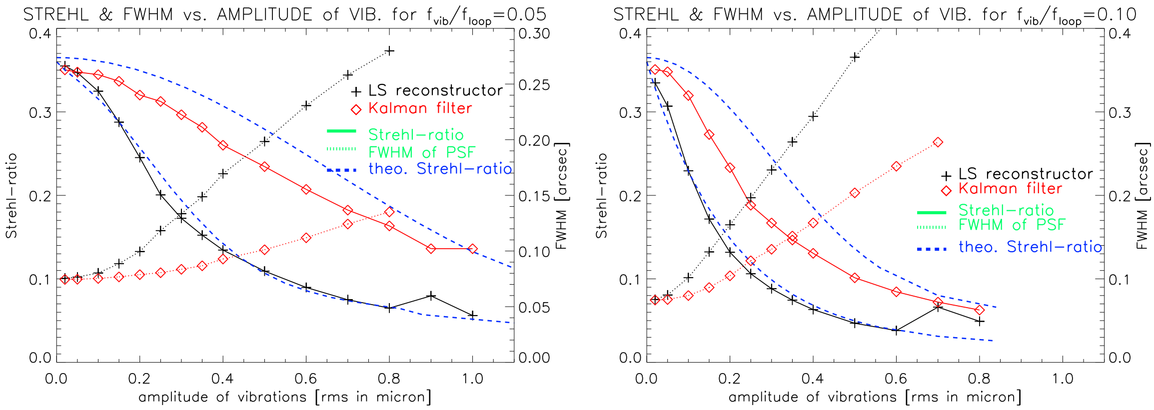

FIGURE 5.28: Performance of the Kalman filter and the Least-Squares (LS) reconstructor as a function of the amplitude of the vibrations for a fixed vibration frequency.

the real system. This leads to an assignment of some of the energy in the vibrations to the turbulence. Since the bandwidth of the Kalman filter for these aberrations is much lower, they are left uncorrected.

The Strehl ratios saturate at high frequencies, because the vibrations are left completely un-corrected. Since the amplitude of the vibrations is fixed, the elongation and thus the shape of the PSF in the long exposure image remain the same.

Figure 5.28 plots the performance of the two reconstruction algorithms as a function of the amplitude of the vibrations for a fixed vibration frequency. The performance of both control algorithms drops rather quickly with an increase in the amplitude of the vibrations, but the Kalman filter always performs significantly better. Due to the same problems mentioned above, the Kalman filter performs slightly worse than expected from simulations. Nevertheless, the amplitude of the vibration can be a factor of ≈2 larger for the Kalman filter to achieve the same performance as the LS reconstructor.

Figure 5.29 shows the filtering of the vibrations in terms of the temporal power-spectral density for the mode with the added vibrations. The LS reconstructor leaves the energy in the vibrations almost uncorrected, while the Kalman filter can attenuate the amplitude of the vibrations by a factor of ≈10, which is slightly worse than expected from numerical simulations (fig. 4.3).

In the presence of vibrations in the system, the Kalman filter is clearly superior to the LS reconstructor, albeit less than expected from numerical simulations. However, also for this algorithm, we found that it is extremely important to have accurate estimates of the additional parameters required. Otherwise the Kalman filter is prone to significant cross-talk with other modes and loop instabilities.

5.8 CONCLUSION & OUTLOOK

In this chapter, we presented the results obtained with a Ground-Layer Adaptive Optics (GLAO) experiment in the lab. A complete GLAO system was set up and dynamic measurements using four natural guide stars, in layer-oriented operation mode with optical co-addition were performed. For the first time, these concepts were successfully verified in closed-loop operation.

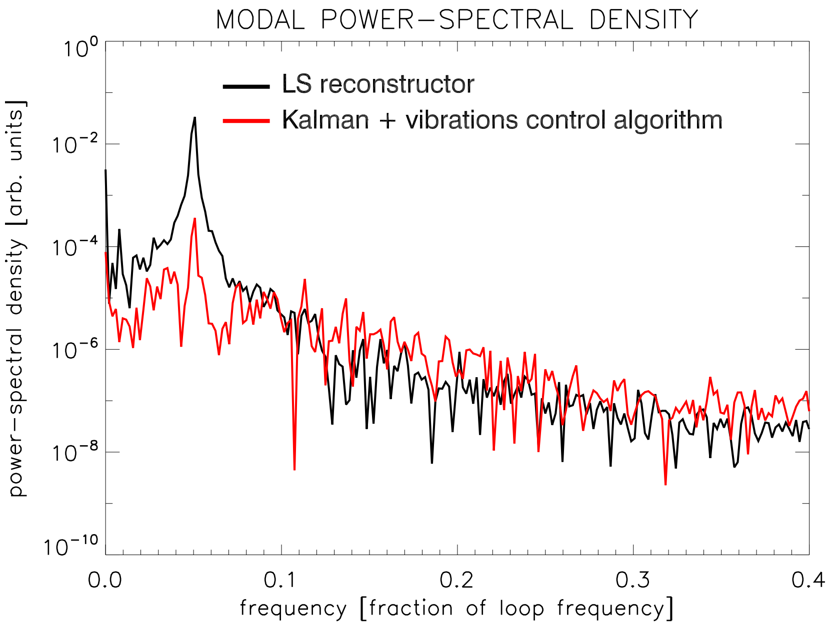

FIGURE 5.29: The residual temporal power spectral density of the tilt mode for the Least-Squares (LS) reconstructor and the Kalman filter in closed loop operation in the presence of vibrations with a frequency of 5% the loop frequency.

5.8.1 CALIBRATION ISSUES

The system and all its individual components were thoroughly characterized. One verification step was the comparison of static wavefront measurements to those obtained with a commercial interferometer, yielding correlations of up to 90%. Since the dynamic range of the pyramid was found to be small compared to the wavefront aberrations, a study on the optimal calibration amplitude was performed. Despite the larger influence of the residual surface aberrations of the DM, a smaller calibration amplitude was found to give better performance in closed loop. Furthermore, the effects of misalignments on the pupil images in the single star and GLAO operation mode was studied, showing the rapid drop in performance for even small shifts of the pupil images. This effect was found to be independent of the spatial frequency and is thus independent of the number of reconstructed modes.

5.8.2 GROUND-LAYER AO

The performance of this system in GLAO mode was extensively characterized in closed-loop. It was shown that the concept of layer-oriented GLAO with optical co-addition works, with results very similar to those predicted by numerical simulations. The filtering of non-conjugated layers matches very well with semi-analytical expectations based on layer-filter functions, presented in chapter 3. Moreover, the shape of the PSF in the field follows the predictions very neatly. The PSF is uniform over the entire field, covered by guide stars, leading to an increase in the area with useful correction by a factor at ≈25, as compared to single star AO.

Also the impact of differences in the brightness of the individual guide stars on the correction efficiency was studied. A star which is more than ≈1.5 mag fainter than the others was found to have no influence on the performance of the system.

5.8.3 KALMAN FILTER

With MANU-CHAO, we tested new concepts for the control of an Adaptive Optics system, in particular the Kalman filter. For single-star and ground-layer AO, the Kalman filter showed only slight superiority over the commonly used LS reconstructor. Nevertheless, in the presence of vibrations in the system, the Kalman filter clearly outperforms the LS reconstructor. Both the temporal and spatial bandwidth are increased by a factor of ≈ 2, slightly less than predicted by numerical simulations, especially for high frequency vibrations.

5.8.4 OUTLOOK

After the thorough characterization of the components, an extensive software package having been written and the system now running stably, MANU-CHAO is a unique test-bed for other concepts and new ideas in the context of Adaptive Optics. However, since this thesis is concentrated on the GLAO concept with multiple natural guide stars, they have not been pursued within the context of this work.

- Star-Oriented vs. Layer-Oriented GLAO:
  MANU-CHAO can be modified relatively easily to a star-oriented GLAO setup. In this way, a comparison of the two concepts could be accomplished in closed-loop operation. For example, one could examine whether the RON of the detectors is really a serious problem for the star-oriented approach, or if this could be compensated by the optimization of the performance in a certain direction with sophisticated control algorithms. Moreover, the impact of different brightnesses of the guide stars could be studied for both approaches.

- Laser Guide Stars:
  As mentioned in the introduction, laser guide stars (LGS) offer the prospect of significantly increased sky-coverage, and are thus in rapid development at a number of astronomical observatories. Especially Rayleigh LGS would allow us to measure the contribution of the ground-layer turbulence to the total wavefront aberrations with relatively few (maybe just one) guide stars. An experimental verification of this concept could also be relatively easily done with MANU-CHAO by changing the optical setup of MAPS. In this context, also more fundamental questions could be addressed, such as the performance of the pyramid WFS on extended and in particular non-circular guide stars, and the feasibility of optical co-addition for LGS.

- On-sky test of MANU-CHAO:
  After all lab-tests are now successfully completed, an on-sky test can be addressed. In the description of the optical design of MANU-CHAO, it was already mentioned that it was designed to match to the existing AO system at the TNG, making an on-sky test almost straight-forward. Currently, it would still be the first AO system with multiple guide stars working on sky.

- LINC-NIRVANA:
  For LINC-NIRVANA also a GLAO operation mode is foreseen by using only the Ground-Layer wavefront-sensor (GWS) and the deformable secondary mirror of the LBT. Since the GWS has a large field-of-view (6 arcmin), the achievable image quality will be homogenous over this large area, but rather low. However, the FoV of the science detector is only 10×10 arcsec^2 and the nearest

guide star will be at least 1 arcmin away from the center of the science field. A classical, single-star AO system, maybe with a LGS and using the just mentioned star as the tip-tilt star, will offer better performance. Since the science FoV is smaller than the isoplanatic angle, also such a classical AO system will deliver a homogenous performance over such a small field.

- GLAO for Calar Alto:
  Considering the promising results obtained with this lab experiment in terms of correctable field-of-view, one might want to start thinking about building an GLAO system for the 2.2 m or 3.5 m telescope on Calar Alto. Also at Calar Alto most of the turbulence is located close to the ground (Weiß, 2003). With a similar system as currently under development at the MMT (Lloyd-Hart et al., 2006) or the WHT (Rutten et al., 2003), which both use one Rayleigh laser guide star, a significant increase of the corrected field of view (up to 2 arcmin) and of sky-coverage can be achieved at an high observing efficiency. The technological challenges of the required laser systems appear to be solved and turn-key systems are now commercially available (Rutten et al., 2006). For an effective improvement of the seeing by a factor of 2 for wavelengths longer than R-band, 90% sky-coverage can be achieved up to $\approx 40^\circ$ galactic latitude and still $\approx$30% at the poles (Stuik et al., 2004b). As pointed out recently by Morris et al. (2006), combining a GLAO system with an Integral Field Spectrograph would be especially beneficial for extra-galactic research.

CHAPTER 6

Site-characterization for LINC-NIRVANA

in the desert in the dry,
before the breaking of the rain,
the temperature in the shade
has reached a hundred and ten again

Midnight Oil, "Bullroarer"

6.1 INTRODUCTION

The previous chapter (see e.g. sect. 5.6.1) demonstrated that the performance of an MCAO-System depends critically on the strength and vertical structure of the atmospheric turbulence. To investigate this in more detail, we present in this chapter measurements of the C_N^2-profiles above Mt. Graham with a Generalized SCIDAR, their statistical analysis, and the impact on the design and performance expectations of the MCAO system of LINC-NIRVANA. This is the first thorough analysis of the vertical structure of the atmospheric turbulence above the site of the LBT. Based on observations during 16 nights, spread over one year, Mt. Graham seems to be excellently suited for astronomical observations. Not only LINC-NIRVANA, but all instruments at the LBT can profit from this study, because their performance and the science return are affected by the atmospheric turbulence conditions, as presented in chapter 1 and section 2.2.

Using the measured C_N^2-profiles, a systematic approach to calculate the performance expectations of the LINC-NIRVANA instrument is presented. With the layer-transfer functions (chapter 3), describing the filtering of the turbulence-induced distortions by an AO system, the optimal conjugated heights for different criteria are calculated, and their short-term variability is studied. Finally, in this chapter, a new method is presented to measure with an existing G-SCIDAR the turbulence profile with 40 times increased vertical resolution in the first few hundred meters above the ground. The theoretical basis of this method, its on-sky validation and first results obtained at Mt. Graham are shown.

---

portions of this chapter appear in Egner et al. (2006b) and Egner et al. (2006c).

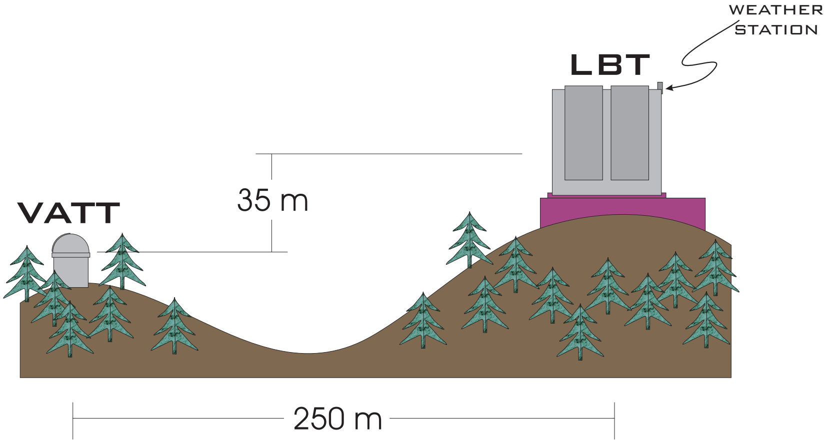

FIGURE 6.1: The topography and location of the VATT and the LBT on the peak of Mt. Graham. The VATT is located below the highest peak and its dome is as high as the trees. In contrast, the LBT is placed on the very top of the mountain and clearly stands above the trees. The primary mirror of the LBT is ≈35 meters above the VATT.

6.2 THE VATT-SCIDAR

The Generalized SCIDAR instrument used for this campaign was built by Dan McKenna of Steward University in Arizona (McKenna et al., 2003) and is mounted on the Vatican Advanced Technology Telescope (VATT) (West et al., 1997), which is located ≈250 m to the south of the LBT on the top of Mt. Graham (fig. 6.1). In this section, a brief overview of the G-SCIDAR instrument and the VATT telescope is given, because the properties of the telescope and its enclosure can have a significant impact on the interpretation of the results (sect. 6.3.1 and 6.7).

6.2.1 DESCRIPTION OF THE INSTRUMENT

The principle of the optical design of a G-SCIDAR appears in the introduction (fig. 2.7), and the actual implementation in the VATT-SCIDAR is shown in figure 6.2. The first optical element after the focal plane of the telescope is a zoom lens to collimate the light to a diameter matched to the detector in use. The detector itself is placed at a distance from the zoom-lens which corresponds to a conjugation height $h_{\mathrm{GS}} = -3.5\,\mathrm{km}$.

In the case of the VATT-SCIDAR, a combination of an image intensifier tube (IIT) and a CCD is used as a detector, to overcome the problem of the RON of the CCD at the prevailing low light-level conditions. The IIT can be gated externally with short pulses to achieve the required effective integration time of ≈1 ms, which is much shorter than the maximum frame-rate of 100 Hz of the CCD camera.

After initial alignment of the G-SCIDAR, which includes adjusting the size of the pupil image on the CCD, centering the pupil images, and locking the telescope tracking on an off-axis guide star, the data-acquisition is started. Usually 6 000 scintillation frames are taken at a frame-rate of 100 Hz. The resulting images are partially processed in real-time. After all scintillation frames have been accumulated, one normalized auto- (**AC**) and cross-correlation (**CC**) image is calculated and saved to disk. The raw data are discarded. This process is then repeated between 30 and 100 times, making up one observation block.

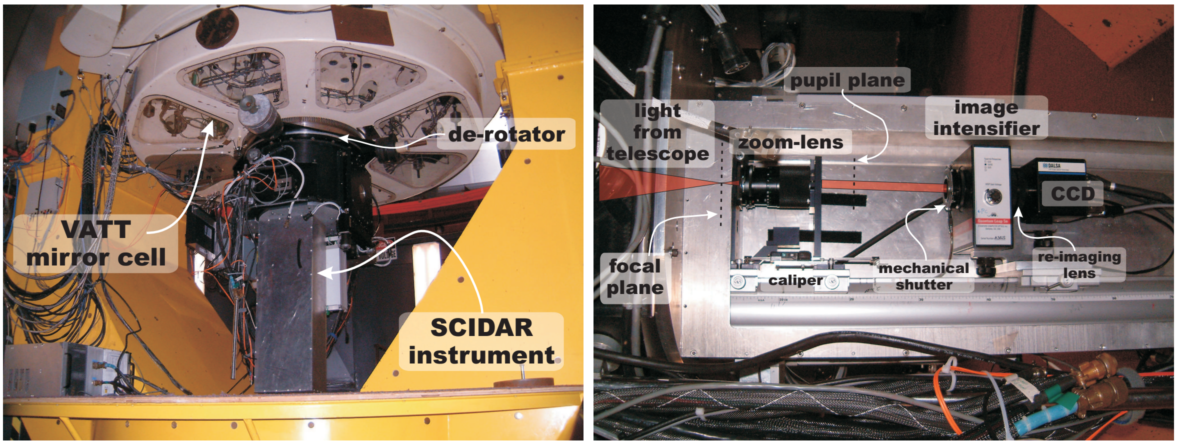

FIGURE 6.2: Photos showing the VATT-SCIDAR instrument. **Left:** The SCIDAR (silver box) mounted to the de-rotator at the Cassegrain focus of the VATT telescope. **Right:** The inside of the SCIDAR instrument.

6.2.2 The Vatican Advanced Technology Telescope

The VATT is a Gregorian-type telescope with a primary mirror of 1.83 m diameter and a Cassegrain focus with f/9. The primary mirror is spin-cast, with a honeycomb back-structure. It is supported by pneumatic actuators to keep its optimal shape and constantly vented with cold air from the back-side to adjust its temperature to ambient conditions. The basically hollow honeycomb structure significantly reduces the mass and makes a large surface for the actively cooled, blown-in air, altogether greatly reducing the thermal inertia of the mirror. If the mirror is warmer than the ambient air, turbulence develops just above the mirror, causing additional wavefront aberrations. These aberrations generated inside the dome and the telescope are called “dome-seeing” and have to be added to the seeing caused by the atmosphere to determine the image quality in pictures taken with the telescope.

For monitoring weather conditions, there is a weather station installed on the roof of the VATT with an LCD display in the control room. There is another weather station on the roof of the LBT (see fig. 6.1), with a GUI on the control computer of the VATT showing the basic weather parameters, such as temperature, humidity, wind speed and wind direction, averaged over a few minutes. The temperature on the mountain is relatively stable: the variations between day and night are rarely more than a few degrees and within one night the maximum temperature differences are typically less than 2°C.

A guide camera for fine-tracking is integrated in the de-rotator of the telescope. With the help of a pick-off mirror, a suitable bright star can be selected at a distance of up to 15 arcmin from the optical axis. This camera delivers the residual positions, which are used for guiding, every two seconds. It also reports the FWHM of the guide star. However, since the VATT has a rather short f-ratio, static aberrations (especially astigmatism) quickly increase with the angular distance from the optical axis. Therefore the apparent size of the guide star and thus the deduced seeing values are larger than on-axis. Moreover, focusing of the guide camera is done manually, which might further increasing the apparent seeing. This has to be taken into account when comparing the seeing values measured with the guide camera and those determined from the G-SCIDAR data.

6.3 THE DATA-REDUCTION PIPELINE

The G-SCIDAR instrument delivers one **AC** and **CC** frame approximately every minute, yielding a substantial amount of data. Considering the number of images (≈600 **AC** and **CC** frames per night) and the required computing power, an efficient reduction of these data is mandatory. For these reasons, an almost completely automatic data-reduction pipeline was developed and implemented in IDL. In this section, we give an overview of the design and capabilities of this pipeline and the steps undertaken to verify the results.

6.3.1 PRINCIPLE OF DATA-REDUCTION

As explained in section 2.3, the C_N^2-profile can be extracted from the **AC** images, while the wind speed profile can be determined from the **CC** images.

CALCULATION OF THE C_N^2 PROFILES

For the calculation of the C_N^2-profiles, the first step in the data-reduction process is the calculation of the **T**-matrices as defined in equation 2.47. These depend only on the parameters of the binary and the pupil sampling. Since the diameter of the pupil image on the detector is always the same, these matrices must be calculated only once for each binary.

The next step is to extract the **AC** profile along the direction of the binary from the **AC** images. Using a slice through the **AC** frame perpendicular to the axis of the binary, the central peak and the background level is subtracted from the **AC** profile. This slice is also used to determine the noise in the **AC** images and thus to estimate the number of useful iterations in the inversion step and the quality of the final retrieved C_N^2-profiles.

For the inversion of the Fredholm equation 2.46, we used the conjugate gradient method (Press et al., 2002). The required estimate of the C_N^2-profile as a starting point for this method is determined from an SVD inversion of a down-sampled **AC** profile (Klückers et al., 1998; Weiß, 2003). The conjugate gradient method is an iterative process, which is stopped once sufficient accuracy is achieved or a maximum number of iterations is reached. Both criteria are influenced by the noise-level determined from the **AC** profiles. To check the accuracy of the determined C_N^2-profiles, the expected **AC** profile is calculated from the C_N^2-profile and compared to the measured **AC** profile. Determining the **AC** profile from the C_N^2-profile is numerically easy, because it involves only a matrix multiplication.

The vertical size of one pixel is for the VATT-SCIDAR much smaller than the theoretical vertical resolution Δh_{GS} of the G-SCIDAR (eqn. 2.49 and 2.48). To suppress the noise, the C_N^2-profile is convolved to match the theoretical vertical resolution. This is done in Fourier-space with a Gaussian kernel with variable width Δh_{GS}.

DETERMINATION OF THE WIND PROFILES

The extraction of the wind speed profile relies on the analysis of the **CC** images, as explained in section 2.3.1. Although the extraction of the wind speed profile from the **CC** images is in principle possible, in practice it is rather difficult. The reason is that due to wind shear, the correlation peaks of the triplets are no longer

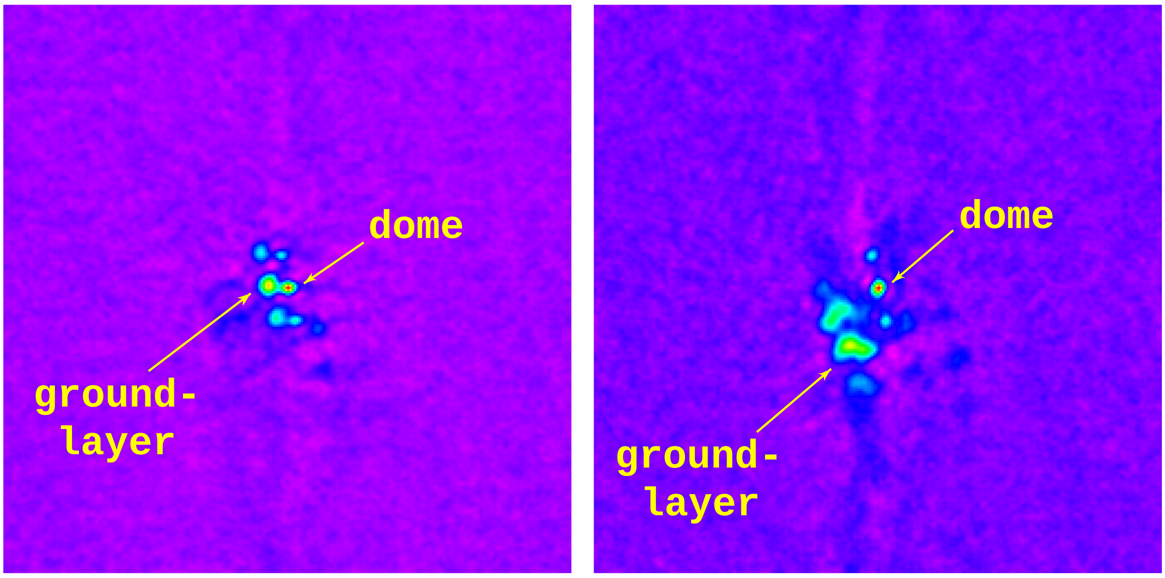

FIGURE 6.3: An example of a "good" (**left**) and a "bad" (**right**) cross-correlation image. In the "good" **CC** image, the correlation peaks of the ground-layer are circular and well defined. The positions of the three peaks of the triplet associated with the ground-layer can thus be extracted, which is not the case for the "bad" **CC** images.

well defined. An accurate determination of the center position and intensity of the correlation peaks is therefore not possible. Figure 6.3 shows two examples of "good" and "bad" **CC** images. Only in the "good" images are the triplets associated with different layers separated. The correlation peaks are well defined and can thus be used for the extraction of the wind speed profile and the dome-seeing.

Even though new algorithms have been developed recently to extract the wind speed profile based on the analysis of the **CC** images in Fourier space or their decomposition into wavelets (Fuensalida et al., 2006; Garcia-Lorenzo and Fuensalida, 2006), these algorithms are not yet mature enough to automatically reduce all **CC** frames. Therefore, we developed a semi-automatic and robust data-reduction algorithm. The user first has to select the "good" **CC** images. The extraction of the correlation peaks' positions and intensities is then done automatically.

Once the "good" **CC** frames are selected by the user, each frame is rotated to align the triplet axis with the x-axis. Then, for each line along the x-axis, the maximum is fitted with a one-dimensional Gaussian and subtracted. As long as the maximum of the residuals is above a given threshold, this step is repeated. The fitted center positions of the found peaks are then used as an best guess for the center of a two-dimensional Gaussian fit to determine the center of the correlation peak in both directions.

When the center positions and intensities of all correlation peaks are found, a logical analysis of the fitting results is performed to extract only the triplets and throw away the fits to noise peaks. In this step, the algorithm checks if there are three correlation peaks along the axis of the binary, with two lateral peaks at the same distance from the central peak and having similar intensities. As a last step, the user has to confirm if the fit is acceptable, that is, all correlation peaks are found and well fitted with acceptable residuals. Otherwise, the user can change the initial parameters for the fitting routine. If these conditions are fulfilled, the wind speed, wind direction and height of the layer is calculated according to equations 2.36 and 2.37.

In the majority of the **CC** images of our data, the correlation peaks are not well defined: in only 20% of the images could a useful wind speed profile be extracted. This is comparable to what is found by other groups (Avila et al., 2006), when counting only the frames where the triplets are unambiguously identified. Usually, we found that the wind shear causes the correlation peaks to smear after a few seconds. When averaging over shorter times for the **CC** images, the wind speed profile might be extracted, but because of the fewer averaged scintillation images, the noise in the **AC** images becomes unacceptably high for the calculation of the C_N^2-profiles. As will be shown later (sect. 6.6.1), the fact that the wind speed profile could not be determined for every **CC** image is not critical for the calculation of the astro-climatic parameters.

CALCULATION OF THE DOME-SEEING

To determine the dome-seeing, we used a similar method to that proposed by Avila et al. (2001), which relies on the analysis of the intensities of the **CC** peaks. The vertical resolution ($\Delta h_{\mathrm{GS}} \approx 1\,\mathrm{km}$) of the C_N^2-profile as retrieved from the **AC** images is not high enough to discern the turbulence inside the dome from the turbulence in the lowest part of the atmosphere. However, in the case of the **CC** images, the triplets associated with the single turbulent layers are also shifted according to the wind speed in that layer (see e.g. fig. 2.8). The vertical resolution Δh_{GS} is still the same, but layers with different wind speeds can thus be separated, even if they are very close in altitude. Assuming that the wind speed outside the dome is not zero, the triplets at an altitude $h = 0 \pm \Delta h_{\mathrm{GS}}/2$ and with non-zero wind speed are associated with the ground-layer outside the dome. On the contrast, the triplet at the same altitude, but with zero wind speed is associated with the turbulence inside the dome.

Since the intensities of the central peak of the triplets is a measure of the strength of the turbulence and thus the C_N^2 in the corresponding layer, the contribution of the dome-seeing to the total measured turbulence within $h = 0 \pm \Delta h_{\mathrm{GS}}/2$ can be determined from a comparison of the respective intensities of the correlation peaks. The fraction a_{DS} of the turbulence, which is near the ground and outside the dome can therefore be calculated with the intensities I_{dome} of the central peaks of the triplets belonging to the dome and the sum of the intensities I_{outside} of all triplets associated with the ground-layer turbulence outside the dome. This fraction a_{DS} is:

$$a_{\mathrm{DS}} = \frac{I_{\mathrm{outside}}/\alpha(\Delta T_{cc})}{I_{\mathrm{outside}}/\alpha(\Delta T_{cc}) + I_{\mathrm{dome}}} . \tag{6.1}$$

The factor $\alpha(\Delta T_{cc})$ corrects for the faster de-correlation of the turbulence outside the dome with respect to the turbulence inside the dome. The value of $\alpha(\Delta T_{cc})$ was determined by taking **CC** images with differing values of the temporal lag ΔT_{cc} over a few minutes. This assumes that the intensity of the turbulence in these two layers remains the same within this time-span. For each of these **CC** images, we calculate the ratio of the center peak intensities

$$R_i(\Delta T_{cc}) = \frac{I_{i,\mathrm{outside}}(\Delta T_{cc})}{I_{i,\mathrm{dome}}(\Delta T_{cc})} . \tag{6.2}$$

The factor $\alpha(\Delta T_{cc})$ is determined from a linear fit to all couples $[\Delta T_{cc},\ R_i(\Delta T_{cc})]$.

Using the slopes m and the offset t of this linear fit, $\alpha(\Delta T_{cc})$ is given by

$$\alpha(\Delta T_{cc}) \; = \; 1 \; + \; \frac{m}{t} \cdot \Delta T_{cc}. \tag{6.3}$$

Since, due to the temporal de-correlation, the slope m is negative, $\alpha(\Delta T_{cc})$ is always smaller than 1. From our data we determined

$$\alpha(\Delta T_{cc}) \; = \; 1 - (0.035 \pm 0.003) \cdot \Delta T_{cc}, \tag{6.4}$$

for ΔT_{cc} in units of frames when using a 100 Hz frame-rate.

Finally, to correct the first resolution element of the C_N^2-profiles for dome-seeing, we have to multiply by a_{DS}:

$$C_N^{2*}(h) \; = \; \begin{cases} C_N^2(h) \; \cdot a_{\text{DS}} & \text{for} \quad |h| \; < \; \Delta h_{\text{GS}}/2 \\ \\ C_N^2(h) & \text{for} \quad h \; > \; \Delta h_{\text{GS}}/2 \end{cases} , \tag{6.5}$$

while the dome-seeing ϵ_{dome} can be calculated via (eqn. 2.15)

$$\epsilon_{\text{dome}} \; = \; \left[0.409 \cdot \frac{(2\pi)^2}{\lambda^{1/3}} \sec \zeta \int_{-\Delta h_{\text{GS}/2}}^{+\Delta h_{\text{GS}/2}} C_N^2(h) \cdot (1 \; - \; a_{\text{DS}}) \, dh \right]^{3/5} . \tag{6.6}$$

6.3.2 VERIFICATION OF THE PIPELINE

In order to compare the results obtained at Mt. Graham to those of other SCIDAR instruments operated at other astronomical sites, it is extremely important to verify the output of the data-reduction pipeline. For these reasons, we used three independent methods to verify the results.

VERIFICATION OF THE C_N^2 PROFILES

The first validation method was to compare the retrieved C_N^2-profiles of our pipeline with those of the G-SCIDAR group at the University of Mexico. R. Avila kindly provided a sample of **AC** frames measured at the focus of the 2.1 m telescope at San Pedro Martir with the GS/LUAN (Avila et al., 1998). From these **AC** frames, we calculated the C_N^2-profiles using both the GS/LUAN and our data-reduction pipelines. A comparison of two such retrieved C_N^2-profiles appears in figure 6.4. As can be seen, the vertical distribution and the strength of the turbulence of the two profiles match very well. To quantify the difference between the two profiles, we calculated the relative error $\Delta\epsilon_{\text{X}}$ of the seeing ϵ in different layers of the atmosphere

$$\Delta\epsilon_{\text{X}} \; = \; \frac{\epsilon_{\text{LBT}} \; - \; \epsilon_{\text{LUAN}}}{\epsilon_{\text{LUAN}}} \tag{6.7}$$

For the total atmosphere, the mean relative error $\langle \Delta\epsilon_{\text{TOT}} \rangle$ for all sample C_N^2-profiles is 2%. For the ground-layer (up to 1.5 km above the telescope), $\langle \Delta\epsilon_{\text{BL}} \rangle$ is 4%, and for the free atmosphere (above 1.5 km), $\langle \Delta\epsilon_{\text{FA}} \rangle$ is 5%. The relative errors $\Delta\epsilon_{\text{X}}$ for all sample profiles are randomly distributed, with no systematic trend. Thus, our and the GS/LUAN pipeline provide comparable results starting from the same input. Moreover, the good matching of the two C_N^2-profiles indicate that the resulting C_N^2-profile is only slightly affected by the numerical method used to invert the Friedholm equation (eqn. 2.46). The pipeline of GS/LUAN uses the maximum entropy algorithm, while we use the conjugate gradient method for the inversion.

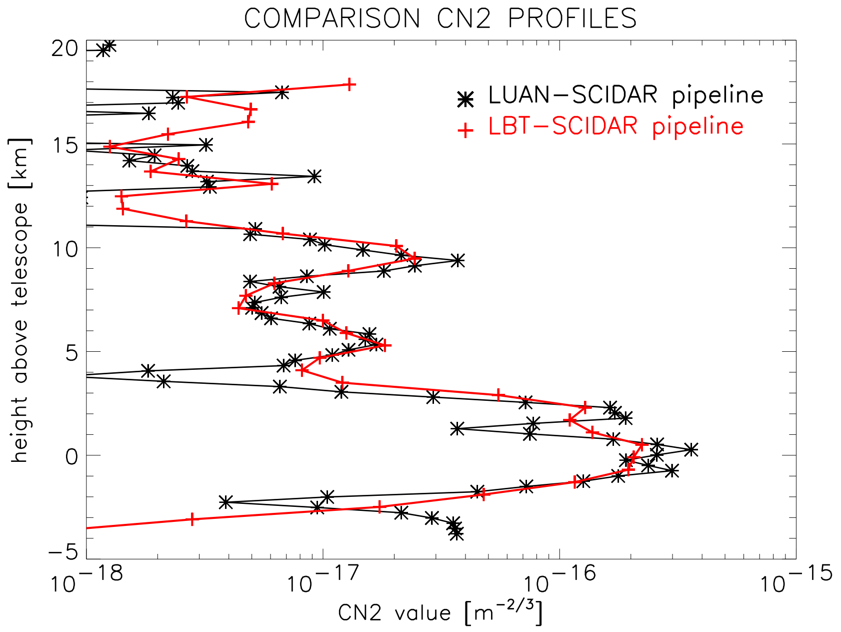

FIGURE 6.4: Comparison of the C_N^2 profiles as calculated with the data-reduction pipeline of the LUAN-SCIDAR by R. Avila and our pipeline developed for the VATT G-SCIDAR.

VERIFICATION OF THE INTEGRATED VALUES

With the first validation method, we verified that our pipeline delivers correct results starting from the same input. However, it could be that the VATT-SCIDAR instrument has some peculiarities, resulting in a systematic error in the C_N^2-profiles. For this reason we compared the values of the seeing ϵ_{SCIDAR} determined from the G-SCIDAR C_N^2-profiles with the seeing ϵ_{guider} as measured with the guide camera of the VATT. Since the PSF of the guide star can suffer from significant static aberrations (sect. 6.2.2), ϵ_{guider} might slightly over-estimate the true seeing.

As shown for a typical night in figure 6.5, for γ Ari and λ Ori, ϵ_{guider} and ϵ_{SCIDAR} match very well: both follow the same temporal evolution of the seeing. Unfortunately, saving the data of the guide camera is not yet automatized: it has to be done manually. For this reason, no data taken with the guide camera are available for the other two stars. However, the measured ϵ_{SCIDAR} are continuous at the transition between the stars (e.g. at around 00:30 local time), indicating that the retrieved values for ϵ_{SCIDAR} are independent of the actual star used for the G-SCIDAR.

VERIFICATION OF THE WIND PROFILES

To verify the wind speed profiles retrieved from the G-SCIDAR **CC** images, data from meteorological archives was used. The European Center for Medium Weather Forecast (ECMWF) maintains a database with the outputs of meteorological models interpolated to a regular latitude / longitude grid. For Mt. Graham, the closest such grid-point (33°00’00”N / 110°00’00”W) is located ≈35 km to the north. Considering the spatial resolution of the meteorological model of ≈100 km, this separation is acceptable.

The G-SCIDAR can determine the wind speed v_{SCIDAR} only of the turbulent layers and not of the entire atmosphere. Furthermore, the wind speed at the ground is

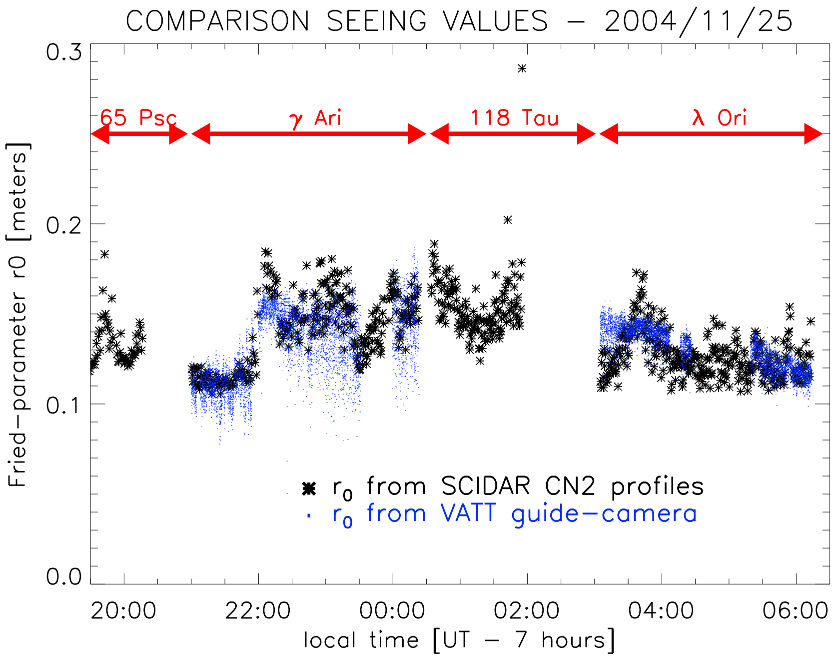

FIGURE 6.5: Comparison of the values of the Fried Parameter r_0 (including dome-seeing) at λ =0.5 μm, as determined from the G-SCIDAR C_N^2 profiles and the VATT Guide Camera.

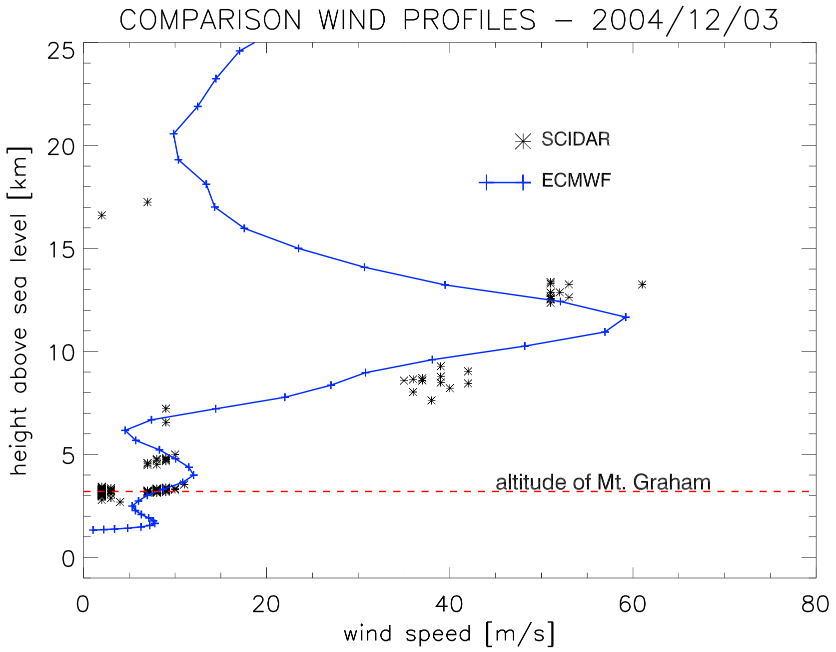

FIGURE 6.6: Comparison for a typical night of the wind profiles as extracted from the G-SCIDAR data and as taken from the archive of the ECMWF.

influenced by the local orography, for example the flow of the wind over the top of the mountain and the interaction of the wind with vegetation, and thus it cannot be predicted with the ECMWF models. Nevertheless, as shown in figure 6.6, the wind speeds of the turbulent layers match very well with the data from the ECMWF for the free atmosphere (higher than ≈1 km above the telescope).

No.	Dates	No. of nights	No. of profiles	Observers
1	24 – 26 Nov. 2004	3	2707	DM, SE
2	03 Dec. 2004	1	383	DM
3	26 Apr. 2005	1	554	DM
4	19 – 24 May 2005	6	2481	EM, SE
5	06 – 15 Dec. 2005	5	3786	SD, SE
Total		**16**	**9911**	

TABLE 6.1: The basic parameters for the individual observing runs. The observers were DM: Dan McKenna, EM: Elena Masciadri, SD: Sebastian Daemgen, SE: Sebastian Egner.

Another problem is that the wind speed profile v_{ECMWF} from the ECMWF database is available only at [0:00, 6:00, 12:00, 18:00] GMT and thus not for the same time as the single C_N^2-profile measurements. For our observations, the variations of the wind speed in the free atmosphere were less than $\approx 5\,\mathrm{m/s}$ during one night. This justifies the comparison of the mean v_{SCIDAR} profile with the v_{ECMWF} profile at 6:00 GMT (23:00 local time) in figure 6.6 and in appendix B.

6.4 OBSERVING PARAMETERS

For the site-characterization campaign at Mt. Graham, there have been 5 observing runs to date, with a total of 16 useful nights and almost 10 000 measured C_N^2-profiles (see tab. 6.1 for details). The observing nights were distributed over one year and cover almost all seasons. However, because of the limited number of observation runs, most of the data were taken on successive nights. This makes the determination of seasonal trends in the C_N^2-profiles and in the astro-climatic parameters rather difficult, as the influence of peculiar weather conditions lasting for a few nights cannot be separated from the true seasonal variation.

As mentioned in section 2.3, the achievable vertical resolution Δh_{GS} and maximum attainable height h_{max} of the retrieved C_N^2-profiles depend on the separation ϕ of the binary observed with the G-SCIDAR. On the one hand, h_{max} should be at least $\approx 20\,\mathrm{km}$. On the other hand, a Δh_{GS} near the ground of $\approx 1\,\mathrm{km}$ is desirable. Figure 6.7 plots h_{max} and Δh_{GS} at the ground as a function of ϕ for the parameters of the VATT telescope and the G-SCIDAR instrument. As can be seen, to satisfy both conditions, ϕ has to be between 6 and 10 arcsec.

For a good signal-to-noise ratio (SNR) on the detector, the binary has furthermore to have a certain minimum brightness. Even though the VATT-SCIDAR uses an IIT, the short integration times of 1 msec still make it necessary to observe stars brighter than 5th magnitude in V-band to have enough photons in each frame to surmount the $\approx 20\mathrm{e}^-$ RON of the CCD. Moreover, to achieve good SNR of the correlation frames, the two components of the binary must have similar brightness.

All binaries which fullfill both conditions were selected from the Washington Double Star Catalogue (WDSC). This usually yielded enough suitable stars to cover the entire night with observations at a maximum zenith distance of 30°. A list of all observed binary stars, along with their properties, appears in table 6.2. This table

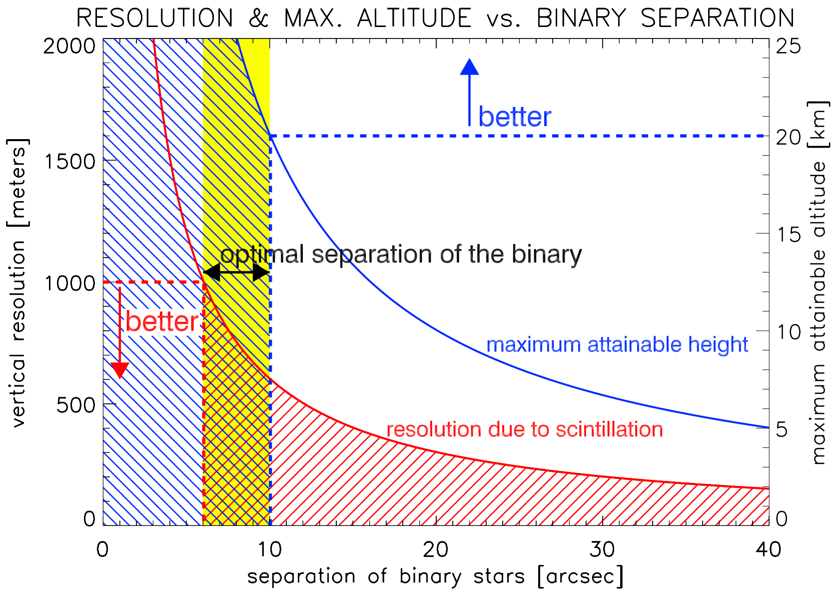

FIGURE 6.7: The achievable vertical resolution and the maximum attainable height for the VATT G-SCIDAR versus the separation of the observed binary.

Name	**Right asc.**	**Declination**	**Magnitude**	**Sep.**	**Observed**
	hh mm ss.s	±dd mm ss.s	V-mag$_1$ / mag$_2$	arcsec	run
Psc 65	00 49 52.82	+27 42 38.9	6.33 / 6.34	4.2	1, 2
Psc ψ	01 05 42.00	+21 28 00.0	5.27 / 5.45	30.0	5
Ari γ	01 53 31.81	+19 17 37.9	4.52 / 4.58	7.4	1, 2, 5
Tau 118	05 29 16.50	+25 09 00.8	5.83 / 6.68	4.7	1, 2
Ori λ	05 35 08.28	+09 56 03.0	3.51 / 5.60	4.3	1
Castor	07 34 35.86	+31 53 17.8	1.93 / 2.97	4.2	5
Cnc ζ	08 12 12.85	+17 38 52.8	5.05 / 6.20	5.9	1, 5
Leo γ	10 19 58.35	+19 50 29.4	2.37 / 3.64	4.5	5
Boo π	14 40 43.60	+16 25 03.0	4.88 / 5.79	5.5	3, 4
Ser δ	15 34 48.15	+10 32 19.9	4.17 / 5.16	4.0	4
Her 95	18 01 30.41	+21 35 44.8	4.85 / 5.20	6.3	3, 4
Cyg β	19 30 43.28	+27 57 34.9	3.37 / 4.68	34.7	4
Del γ	20 46 39.20	+16 07 27.0	4.36 / 5.03	9.1	1

TABLE 6.2: The observed stars for the G-SCIDAR runs.

also lists the two binary stars with a much larger separation (≈30"), which were observed for the High Vertical Resolution Generalized SCIDAR (HVR-GS) method described in section 6.7.

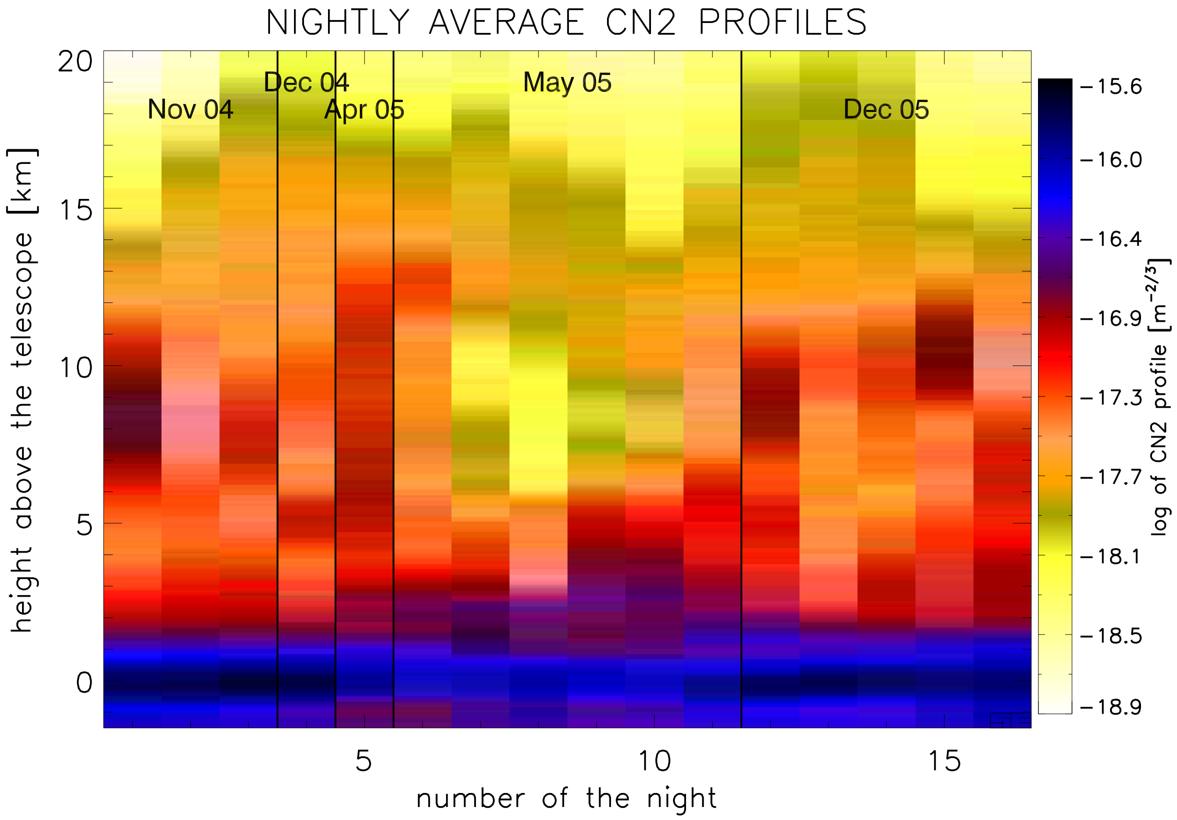

FIGURE 6.8: The mean C_N^2-profiles for all nights. The dome-seeing is removed and the C_N^2 intensity is plotted color-coded in logarithmic scale with yellow denoting weak, and blue strong turbulence.

6.5 TURBULENCE PROFILES

The first step in the evaluation of the atmospheric turbulence above Mt. Graham is the statistical analysis of the retrieved C_N^2-profiles.

6.5.1 VERTICAL TURBULENCE STRUCTURE

Appendix A contains plots of the temporal evolution of atmospheric turbulence during the individual nights with the measured C_N^2-profiles and the median C_N^2-profiles. In this section, only the mean C_N^2-profiles for the individual nights (fig. 6.8) and the median C_N^2-profile using all data (fig. 6.9) are shown. For all these plots, the dome-seeing has already been subtracted (sect. 6.3.1).

The ground-layer dominates the C_N^2-profile for most nights (fig. 6.8), except for 2 to 3 nights in May 2005. During summer (April and May 2005), other distinct turbulent layers are located at ≈3 and ≈5 km above the ground (fig. 6.10). The altitude of these layers is ≈1 km higher in winter (November & December 2004, December 2005). In contrast, the altitude of the jet-stream layer changes dramatically between the seasons: it is between 6 and 12 km in winter, but between 11 and 17 km in summer. This is similar to what was found at San Pedro Martir (Masciadri and Egner, 2004). San Pedro Martir is ≈500 km to the WSW of Mt. Graham and should have similar characteristics for the jet-stream layer. Unfortunately, the nights in summer were consecutive nights, which means that the observed effects

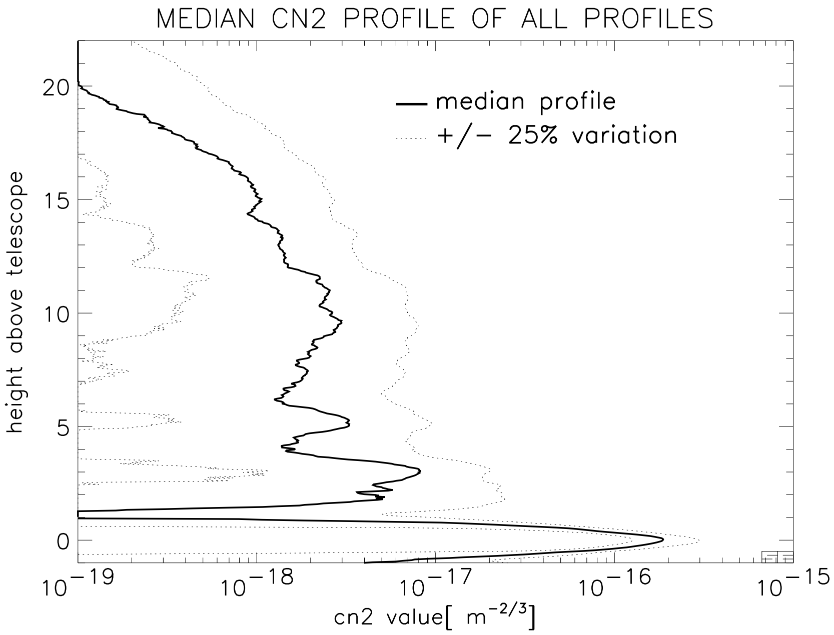

FIGURE 6.9: The median C_N^2-profile calculated from all measured data (solid line) and ±25% deviation.

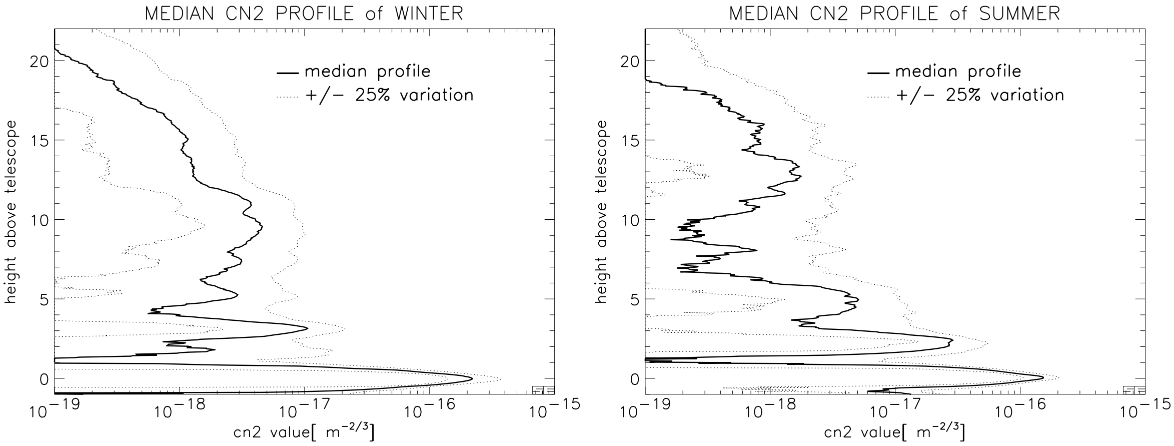

FIGURE 6.10: The median C_N^2-profile for winter (**left**), including data from the G-SCIDAR observing runs in November and December 2004 and December 2005. Data from the G-SCIDAR runs in April and May 2005 are included in the median C_N^2-profile for summer (**right**).

could be due to peculiar weather conditions during these few nights and might not reflect a true seasonal trend. Only for a few nights did the measurable turbulence extend above 20 km.

6.5.2 CONTRIBUTION BY THE GROUND-LAYER

Since the ground-layer dominates the C_N^2-profile for most nights (fig. 6.8), and thus has the largest impact on the image quality or performance of an AO system, a more detailed analysis of the strength of the ground-layer has been performed. The fraction of the total atmospheric turbulent energy which is concentrated in the

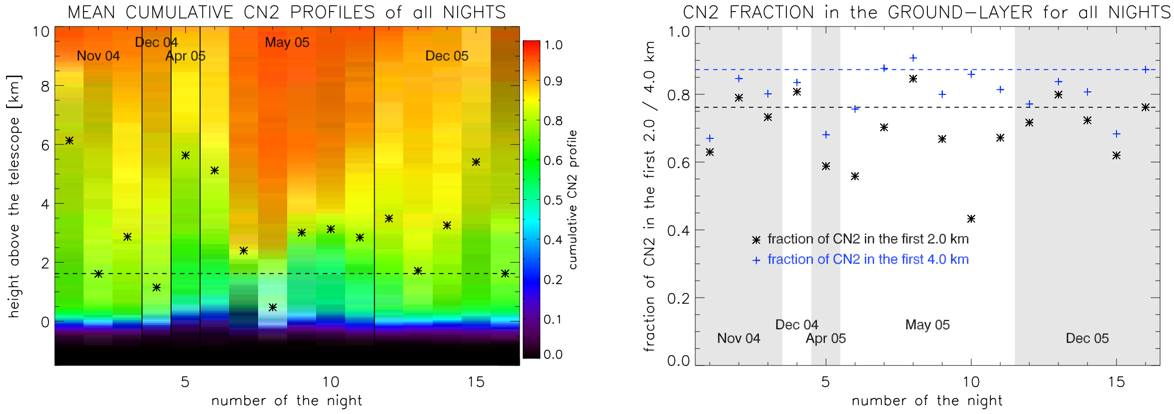

FIGURE 6.11: **Left:** The mean cumulative C_N^2-profile $\mathbf{C}(h)$ for each night. The stars are the median height for 75% of the turbulence being below this altitude for each night, the line is the same but for all C_N^2-profiles. **Right:** The percentage of the C_N^2-profile below 2 and 4 km above the telescope for each night (symbols) and the mean for data (lines).

ground-layer is best described by the normalized cumulative C_N^2-profile $\mathbf{C}(h)$:

$$\mathbf{C}(h) = \frac{\int_0^h C_N^2(h')\,dh'}{\int_0^\infty C_N^2(h')\,dh'} \,. \tag{6.8}$$

Figure 6.11 plots the mean $\mathbf{C}(h)$ for each night. Also indicated are the heights h_{75}, below which 75% of the total C_N^2 is concentrated. Considering all C_N^2-profiles, h_{50} is $\approx$150 m and h_{75} is $\approx$1.6 km. This means that on average half of the turbulence is below $\approx$150 m. Since this is much lower than Δh_{GS} of the C_N^2-profiles, no precise number can be given. Figure 6.11 also shows the fraction of the total C_N^2, which is located below 2 and 4 km, respectively. We find that, on average, $\approx$77% of the total C_N^2 are below 2 km and 87% below 4 km above the telescope.

6.5.3 AVERAGE DISCRETIZED C_N^2 PROFILE

In order to compare the vertical turbulence structure found above Mt. Graham to other astronomical sites, a "typical" C_N^2-profile is required. This profile should have the same value for the astro-climatic parameters (ϵ_0, τ_0, ϑ_0 and ϑ_P) as the median value found using all measured C_N^2-profiles (tab. 6.6 on page 121). However, as shown in table 6.3, using the median of all measured C_N^2-profiles grossly underestimates the median seeing. On the other hand, the mean C_N^2-profile significantly overestimates it. This section will explain how to find a suitable "typical" C_N^2-profile.

The main purpose of such a "typical" C_N^2-profile is as an input for simulations of, for example, the performance of AO Systems. This usually requires several, infinitesimal thin phase screens to simulate the atmospheric turbulence (see e.g. Arcidiacono, 2004; Bertram, 2005, and chapter 5). Assuming frozen flow, the induced wavefront aberrations of the phase screens are fixed but moving with a certain wind speed over the telescope pupil. For these simulations, a discretized C_N^{2D}-profile is thus required, with 7 to 9 layers, the Fried-Parameter $r_{0,i}$ and the wind speed v_i for each layer.

Method	**Seeing**
	arcsec
Mean seeing	0.72
Median seeing	0.67
Seeing from mean C_N^2-profile	0.75
Seeing from median C_N^2-profile	0.52
Standard deviation of seeing	0.17
Seeing from “average discretized” C_N^2-profile	0.68

TABLE 6.3: The “average” seeing for one night (26 Nov 2004) as determined with different methods. Taking the mean $C_N^2(h)$ profile over-estimates the median seeing, while taking the median $C_N^2(h)$ profile significantly under-estimates it. The “average discretized” C_N^2-profile solves this problem and should be used as an input for simulations of AO systems at this site.

To simulate the performance of an MCAO system under various seeing conditions, not only a “typical” C_N^2-profile is required, but also discretized C_N^{2D}-profiles representing “good” and ”bad” seeing conditions. As described in the previous section, for Mt. Graham the ground-layer is the strongest layer and thus also dominates the resulting value of the seeing ϵ (sect. 6.5.1). Simply scaling the complete C_N^2-profile to represent bad seeing conditions thus overestimates the high-layer turbulence and results in a reduced isoplanatic angle ϑ_0. This is especially important for MCAO simulation, since ϑ_0 has significant influence on the performance and the dependence of the achievable Strehl ratio in the field.

To calculate “typical” discretized C_N^2-profiles, we followed the method proposed by Tokovinin and Travouillon (2006). Using the independence of the turbulence in the ground-layer from that in the free atmosphere (as shown later in sect. 6.6.7), all C_N^2-profiles are first split into a ground-layer component (0 – 1 km above the telescope) and the free atmosphere (above 1 km). These are then treated independently. In each part, the cumulative distribution of r_0 is calculated from all C_N^2-profiles. For a “typical” $C_{N,\mathrm{average}}^2(h)$ profile, the mean of the C_N^2-profiles associated with values of r_0 between 45% and 55% in the cumulative distribution is calculated for the ground-layer and the free atmosphere. Similarly, to calculate a typical “good” and “bad” C_N^2-profile, the C_N^2-profiles associated with r_0 values of 20% $-$ 30% (for the good) and 70% $-$ 80% (for the bad) are averaged to find $C_{N,\mathrm{good}}^2(h)$ and $C_{N,\mathrm{bad}}^2(h)$, again separately for the ground-layer and the free atmosphere.

The last step is to discretize the $C_{N,X}^2(h)$ profiles, where the subscript X denotes “average”, “good” or “bad”. The altitudes h_i of the discrete layers are selected to match peaks in the $C_{N,\mathrm{average}}^2(h)$ profiles and the Fried Parameter $r_{0,i}$ are calculated for each layer from the $C_{N,X}^2(h)$ profiles via

$$r_{0,i} = \left[0.423 \left(\frac{2\pi}{\lambda}\right)^2 \int_{(h_i+h_{i-1})/2}^{(h_i+h_{i+1})/2} C_{N,X}^2(h)\, dh \right]^{-3/5} . \qquad (6.9)$$

Height	**r_0 value**			**wind speed**
km	m			m/s
	good	**average**	**bad**	**mean**
0.0	0.29	0.24	0.20	8.4
0.5	0.56	0.46	0.41	14.3
3.0	0.86	0.74	0.61	18.6
5.0	1.27	0.92	0.69	26.6
10.0	1.05	0.76	0.58	28.5
15.0	1.36	1.20	1.09	12.7
20.0	3.70	3.12	3.11	21.7
Total Seeing ["]	**0.56**	**0.68**	**0.82**	
Isopl. Angle ["]	**3.38**	**2.71**	**2.26**	
Coh. Time [msec]	**4.54**	**3.60**	**2.90**	

TABLE 6.4: The "average discretized" C_N^{2D}-profile consisting of the Fried-Parameter r_0 (at λ =0.5 μm) and the wind speed at discrete altitudes. One C_N^{2D}-profile is determined for good, bad and average seeing conditions, respectively.

The final "average discretized" $C_{N,X}^{2D}(h)$ profiles for good, bad and average seeing conditions appear in table 6.4. Also shown in this table are the astro-climatic parameters determined from the the discretized C_N^{2D}-profiles. Their values match very well the median values obtained from all measured C_N^2-profiles (tab. 6.4).

When using the good and the bad "typical" C_N^{2D}-profiles, one has to keep in mind that the ground-layer (the layers at 0.0 and 0.5 km) are independent of the high-altitude layers (at 3.0 to 20.0 km). This means first that for simulations any combination can be used, depending on the precise system aspects to be studied. But this also means that for example the left column in table 6.4 represents good conditions of the ground-layer and the free atmosphere at the same time, which corresponds to only 25% · 25%=6.25% of the total time.

As mentioned above, simulations are usually done with internally fixed phase screens moving with the wind speed v_i. Therefore, also an average wind speed v_i for each turbulent layer i has to be determined. Such a "typical" v_i can be calculated from the mean wind speed profiles $v_j^*(h)$ for the night j, by taking the mean over a small volume around the height of the layer h_i and over all nights:

$$v_i \;=\; \left\langle \, \langle v_j^*(h) \rangle \Big|_{(h_i+h_{i-1})/2 < h < (h_i+h_{i+1})/2} \right\rangle_j . \tag{6.10}$$

The "typical" wind speeds for each layer determined in this was are also given in table 6.4. Since during the observation runs we conducted so far, the variation of the wind speed profile was rather low (appendix B), only the mean wind speeds v_i are given, without their variations. More observations with a SCIDAR are required to reliably determine the scatter. In this context, we do not favor the analysis of meteorological databases, like for example already done for other astronomical sites like for Dome C in Antarctica (Geissler and Mascidari, 2006; Geissler, 2005) or the Canary Islands (Chueca et al., 2004; Garcia-Lorenzo et al., 2005), because there might be a correlation between the wind speed and the strength of the turbulence (Athey et al., 2006). For this reason, only the wind speed profiles of the nights with G-SCIDAR measurements should be taken into account.

6.5.4 WIND SPEED PROFILES

The mean wind speed profiles for each night can be found in appendix B, which contains both the results of G-SCIDAR observations and data from the ECMWF. For most of the nights, there is a single peak at an altitude of ≈8 to 13 km, with a maximum wind speed of ≈40 to 60 m/s. However, especially for the nights in May 2005, the wind speed in the troposphere was ≈20 m/s and thus much lower. It seems that there is little variation of the altitude of the maximum wind speed; only the value of the wind speed is changing. In contrast, the wind direction in this part of the atmosphere does not change over the year. It was always from the west, with a maximum deviation of ±20 degrees. The altitude of maximum wind speed coincides only for 4 out of 16 nights with a peak in the C_N^2-profile. Again, we still have too few data to discern if these findings are caused by short-term weather variations or if they reflect a real seasonal trend.

6.6 ASTRO-CLIMATIC PARAMETERS

For astronomers, the detailed structure of the C_N^2-profiles and wind profiles is only of minor importance, since observers are primarily interested in the resulting image quality. They need to know the seeing ϵ (eqn. 2.15) and be able to predict the performance of an AO system, which depends also on the isoplanatic angle ϑ_0 (eqn. 2.55) and the wavefront coherence time τ_0 (eqn. 2.8). Similarly, for interferometric observations, the isopistonic angle ϑ_P (eqn. 2.58) is important.

The values given for the astro-climatic parameters in this section are all for a wavelength of $\lambda = 0.5\mu$m, except when noted otherwise. Furthermore, the stated errors indicate the standard-deviation of their respective variation for all C_N^2-profiles.

For the following calculation of the astro-climatic parameters, only the dome-seeing corrected C_N^{2*}-profiles were used, as explained in section 6.3.1. Due to the limited vertical resolution of the G-SCIDAR, the C_N^{2*}-profiles apparently extend a few hundred meters below the ground. In order to correctly include the ground-layer, all the turbulence assigned to negative altitudes was put into the first resolution element above the ground to obtain the transformed $C_N^{2T}(h)$ profiles:

$$C_N^{2T}(h) = \begin{cases} C_N^{2*}(h) & \text{for} \quad h > 0 \\ \\ C_N^{2*}(0) + \int\limits_{-1.0\mathrm{km}}^{0.0\mathrm{km}} C_N^{2*}(h')\,dh' & \text{for} \quad h = 0 \end{cases} . \qquad (6.11)$$

Corresponding to the vertical resolution of the G-SCIDAR, the lower limit in the integral was set to −1.0 km. However, varying this parameter between −0.5 km and −2.0 km, changes the resulting seeing by typically only ≈3%, which is comparable to the differences between various inversion algorithms (sect. 6.3.2). The

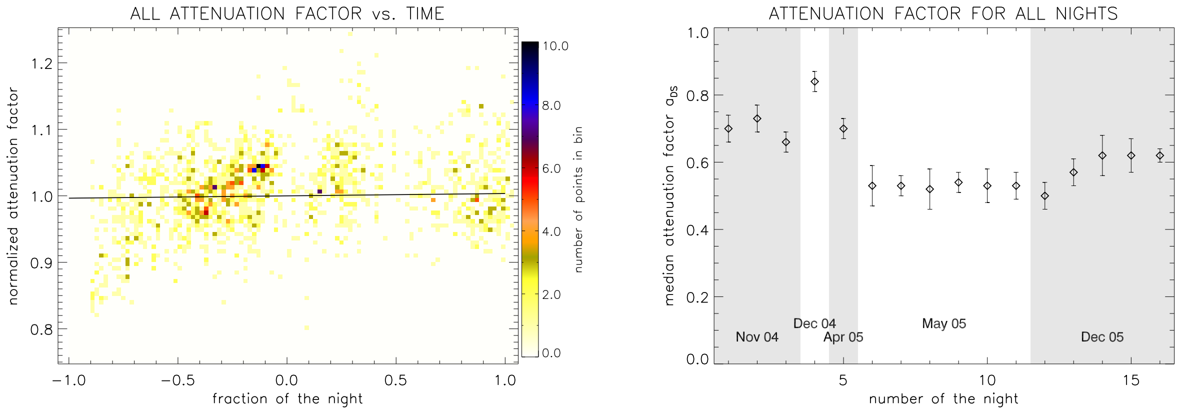

FIGURE 6.12: Left: The normalized attenuation factor a_{DS} for all data. Here, -1.0 corresponds to the end of astronomical twilight in the evening and $+1.0$ to its beginning in the morning. **Right:** The attenuation factor for all nights. A value of a_{DS} =0.6 means that 60% of the turbulence in the first resolution element is located outside the dome, and 40% is inside the dome.

transformation of the C_N^2-profiles via equation 6.11 preserves the total integral of the C_N^2-profiles and therefore does not change the value of e.g. the seeing ϵ. But the transformation has a strong impact on the value of the coherence time τ_0, because the required wind speed measurements are naturally only available above the ground.

6.6.1 DOME-SEEING

Before meaningful values of the astro-climatic parameters, representing the atmospheric characteristics of this site, can be determined, the C_N^2-profiles have to be corrected for the dome-seeing (sect. 6.3.1). However, as explained above (sect. 6.3.1), we cannot extract a wind profile or a value for the attenuation factor a_{DS} for every C_N^2-profile. The median value for a_{DS} for one night was therefore used for all C_N^2-profiles for that night. To justify this assumption, first the temporal variation of a_{DS} over the course of the individual nights was determined. As shown in figure 6.12, a_{DS} normalized to the median of each night and summarized for all nights shows only a negligible systematic trend of 0.7%. Figure 6.12 also shows the retrieved value of a_{DS} for the individual nights, which exhibits significant seasonal variations. It is $\approx$10 to 25% lower in summer than in winter.

In order to estimate the error on the astro-climatic parameters determined in this section when using the median value of a_{DS} for all C_N^2-profiles during one night, we repeated the calculation of the astro-climatic parameters, but using the 10% and 90% value in the distribution of a_{DS}. The results for the seeing ϵ and the coherence time τ_0 appear in figure 6.13. Except for the nights in May, the error in the astro-climatic parameters is in both cases $\approx$1/3 of the intrinsic variations. It should be stressed that using an average value for a_{DS} does therefore not lead to a systematic error, in the median value of the astro-climatic parameters, but only increases their scatter. The isoplanatic ϑ_0 and isopistonic angle ϑ_P are not sensitive to turbulence near the ground and thus are almost independent of the dome-seeing.

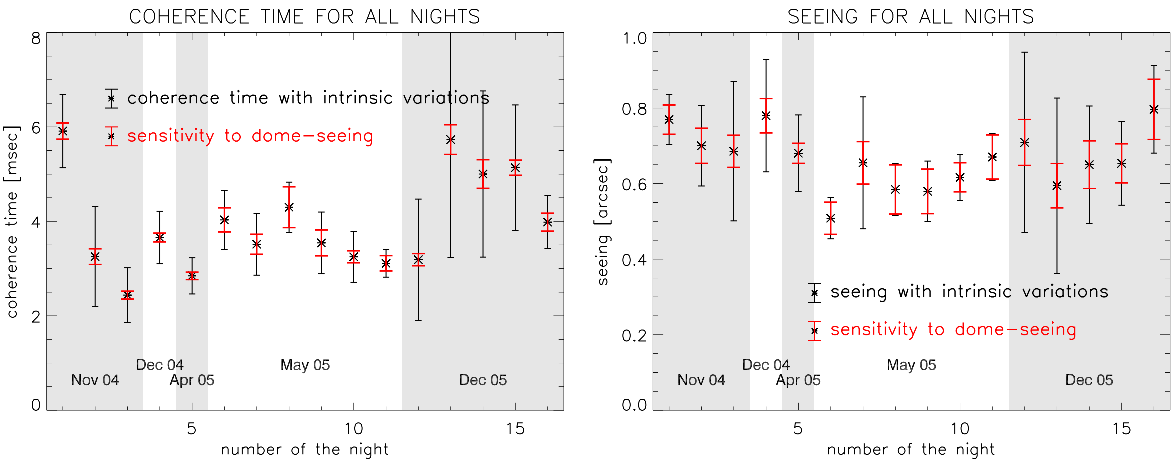

Figure 6.13: The sensitivity of the seeing ϵ (**left**) and the wavefront coherence time τ_0 (**right**) to the dome-seeing for the individual nights. The red error bars indicate the change in the median value of these two parameters when fixing the attenuation factor a_{DS} to 10%, 50% and 90% level of its distribution during each night. For most nights, this effect is much smaller than the intrinsic variation, represented by the black error bars.

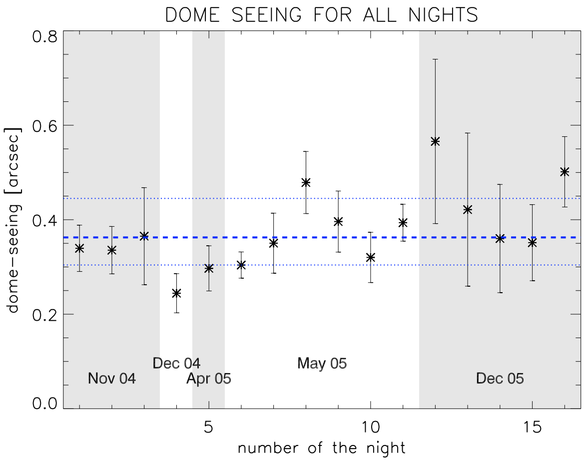

Figure 6.14: The dome-seeing ϵ_{dome} for the individual nights. The error bars indicate the variation of the dome-seeing during the individual nights, the dashed line is the median and the dotted lines are the first and third quartile of the dome-seeing for all data.

Altough the dome-seeing is not a “real” astro-climatic parameter, we list it here for completeness. Its median value was found to be 0.36±0.13” (fig. 6.14), and is thus comparable to that at other telescopes (e.g. Avila et al., 2001). It should be mentioned here that the seeing adds in a non-linear fashion (eqn. 2.15). For example, a dome-seeing of 0.36” and an intrinsic atmospheric seeing of 0.67” results in a total seeing in the images taken with the telescope of 0.80”.

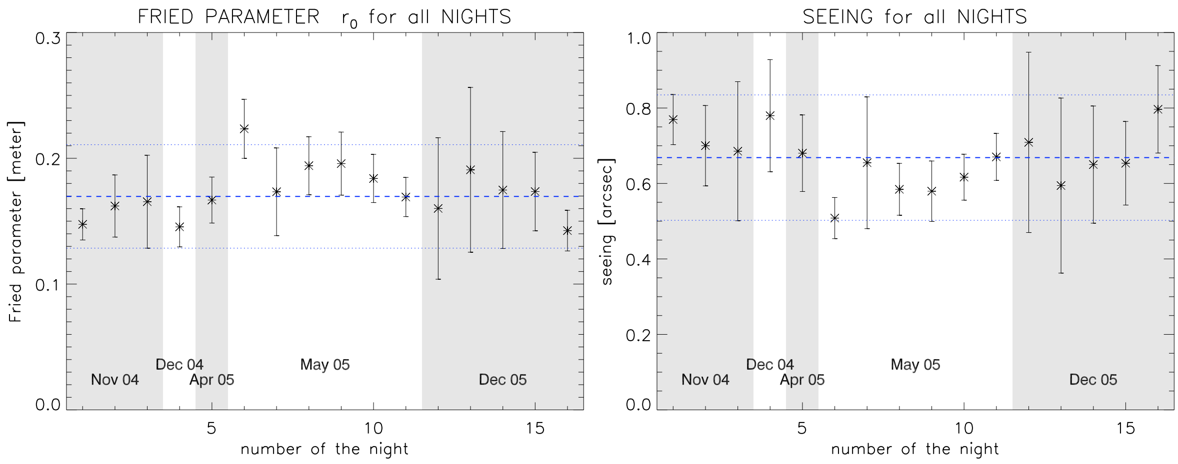

FIGURE 6.15: The median seeing ϵ and the Fried Parameter r_0 for the individual nights. The error bars represent the standard-deviation of the respective variations during the single nights. The dashed lines indicate the median value and the dotted lines enclose one standard deviation of all C_N^2-profiles.

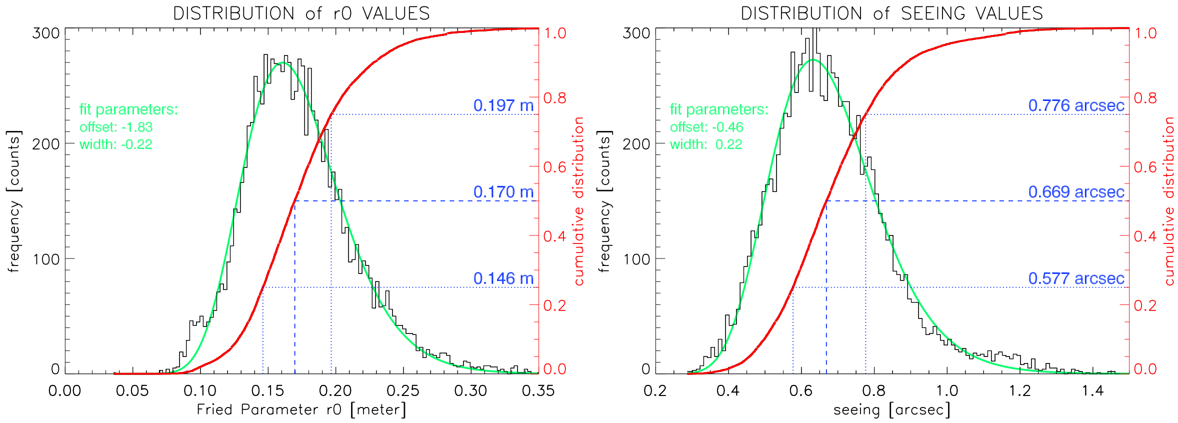

FIGURE 6.16: The cumulative distribution of the seeing ϵ and the Fried Parameter r_0, along with a log-normal fit. The dashed lined show the quartiles. This means, for example, that the seeing is better than 0.58" 25% of the time, and better than 0.78" 75% of the time, with a median of 0.67".

6.6.2 SEEING

The Fried parameter r_0 and the seeing ϵ can be calculated from the C_N^2 profiles using equations 2.17 and 2.15. The mean values and variations of r_0 and ϵ for the individual nights are plotted in figure 6.15, and can also be found in table 6.6. The median seeing for all data is 0.67 ± 0.17". It seems that the seeing is $\approx$0.08" better in spring and summer than in winter. However, this is based on only one observation run with 6 consecutive nights for summer. The cumulative distributions of ϵ and r_0 appear in figure 6.16. Their distribution is excellently described by a log-normal function (eqn. 2.16, Conan et al., 2002).

To assess the contributions of the different parts of the atmosphere to the total seeing, the seeing was calculated in different atmospheric layers. The altitude of these layers was chosen to confirm with the analysis at other sites (e.g. Avila et al., 2003) and the results match extremely well with those at San Pedro Martir. As can

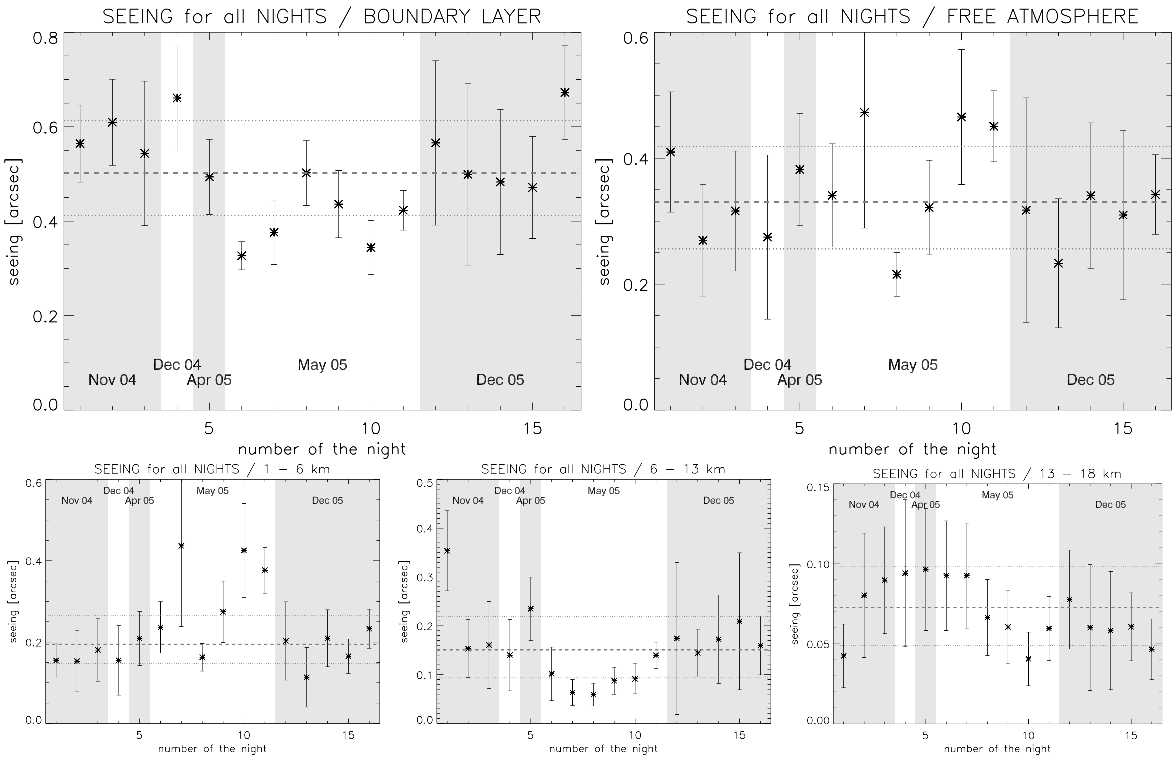

FIGURE 6.17: The seeing in the boundary layer (0 – 1 km), in the free atmosphere (above 1km) and in the layers (1 – 6 km), (6 – 13 km), (13 – 18 km) above the telescope for the single nights. The error bars represent the standard-deviation during the individual nights, the dashed line indicates the median and the dotted lines the first and third quartiles for all C_N^2-profiles.

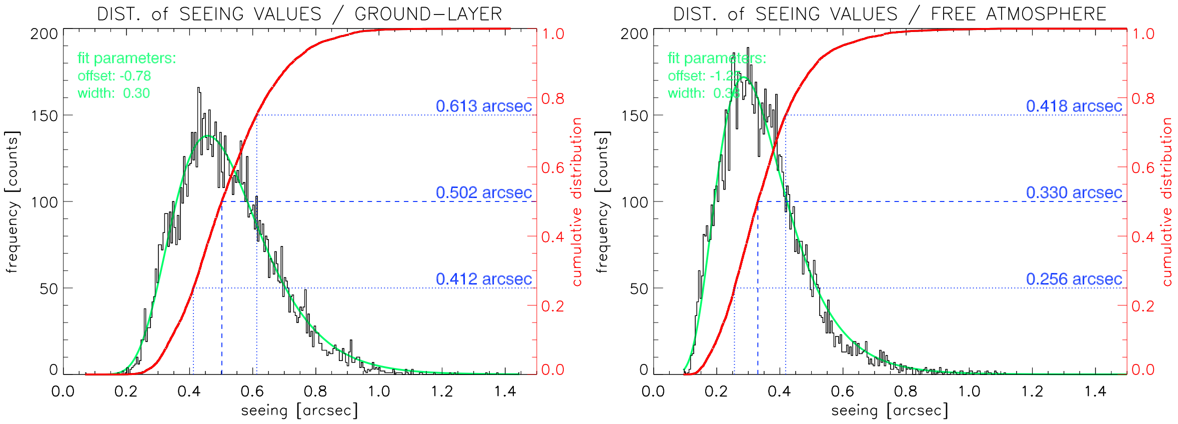

FIGURE 6.18: The histogram and the cumulative distribution of the seeing in the boundary layer (0 – 1 km above the telescope) and in the free atmosphere (above 1.0 km). Also shown is a fit to a log-normal distribution.

be seen in figure 6.17, the observed seasonal trend of ϵ is mainly due to variations in the ground-layer, while the seeing in the free atmosphere is rather constant throughout the year. The cumulative distribution of the seeing in the ground-layer and in the free atmosphere appear in figure 6.18.

Method	# nights	Quartiles			Reference
		25% ["]	50% ["]	75% ["]	
DIMM	166	0.51	0.66	0.85	Merrill et al. (1986)
PSF FWHM	40		0.70		Cromwell et al. (1988)
PSF FWHM	49		1.04		Taylor et al. (2004)
PSF FWHM	2		0.78		Ulich and Davison (1985)
G-SCIDAR	16	0.58	0.69	0.78	this work

TABLE 6.5: Literature values for the seeing measured with different methods at Mt. Graham at a wavelength λ =0.5 μm. Except for Taylor et al. (2004), these values match very well with the seeing values determined from the G-SCIDAR observations presented in this work.

The retrieved values of ϵ from G-SCIDAR measurements are very similar to those measured during previous site-testing campaigns at Mt. Graham (see table 6.5). Merrill et al. (1986) used a DIMM instrument, while Cromwell et al. (1988) and Ulich and Davison (1985) determined the seeing from the measured FWHM of a stellar PSF at the focus of a small telescope. Only Taylor et al. (2004) found a significantly larger value for ϵ. However, they analyzed the image quality at the VATT, which includes in addition to aberrations caused by the atmosphere, other contributions such as dome-seeing, static aberrations, telescope vibrations, focusing and tracking errors. The induced additional wavefront distortions could thus significantly increase the perceived seeing. Assuming a dome-seeing of 0.36", as measured during the G-SCIDAR campaign (sect. 6.6.1), their results would correspond to a clear-air seeing of 0.90". This is still higher than the other values, but could be explained by the focusing problems mentioned by Taylor et al. (2004).

It is interesting to note that the seeing can exhibit dramatic changes of up to 0.6" over only a few minutes (appendix A). During some nights, especially at the beginning of 8 December 2005, the seeing shows quasi-periodic oscillations with a period of a few minutes and amplitude of 0.4". These changes are probably caused by so-called "gravity waves". Under certain atmospheric conditions, air parcels flowing over the mountain start to oscillate in altitude with a period of 4.5 to 5 minutes (Nappo, 2002). Simulations based on meteorological models would be required to confirm this, but are beyond the scope of this thesis.

Another noteworthy fact is the general improvement of the seeing ϵ over the course of the night. In figure 6.19, ϵ of all nights, normalized to the median of the individual nights is plotted as a function of the fraction of the night. Apparently, ϵ is $\approx$18% better at the end of the night than at the beginning, similar to to what is found at Mauna Kea (Subaru Telescope, 2006). This can be explained by the required time for the thermalization of the mountain surface to the ambient temperature. As long as the surface is not at the same temperature as the air, heat is transfered from the soil and vegetation to individual air parcels, which creates optically active turbulence (eqn. 2.1). Since the ground-layer dominates the total turbulence profile (fig. 6.11 and 6.17), less temperature variations in this layer can ultimately lead to an improvement of the seeing. Any influence of the dome or the telescope is excluded, because the dome-seeing was subtracted for all C_N^2-profiles.

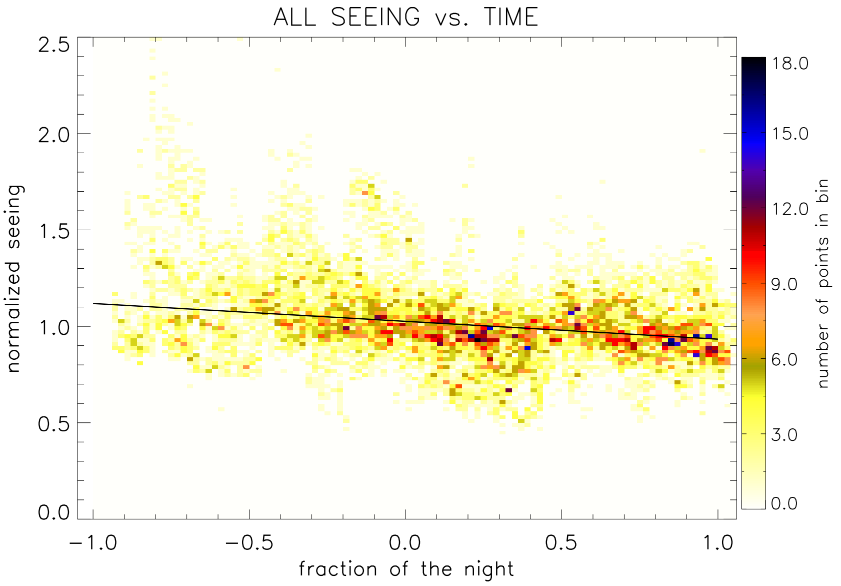

FIGURE 6.19: The normalized seeing over the course of the night for all data.

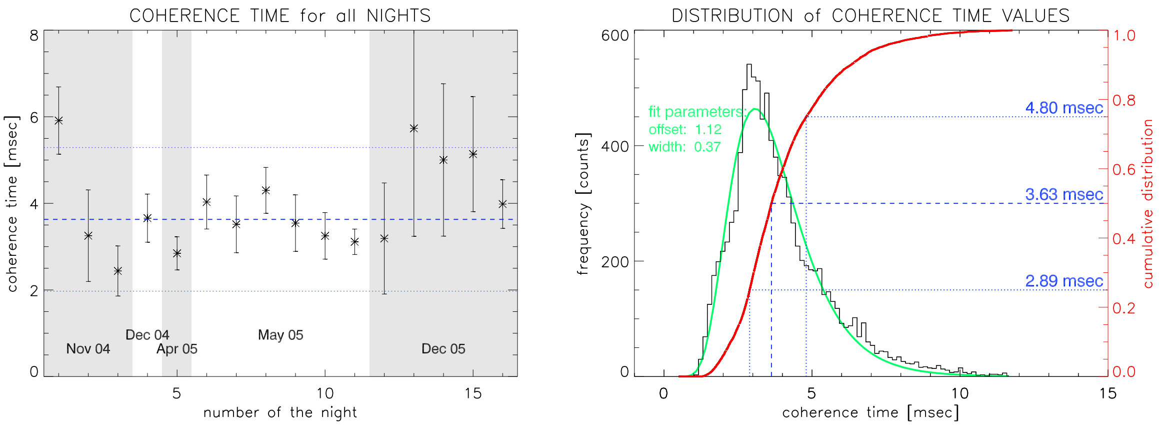

FIGURE 6.20: The median value of the wavefront coherence time τ_0 for the individual nights and its cumulative distribution for all C_N^2-profiles.

6.6.3 WAVEFRONT COHERENCE TIME

The calculation of the wavefront coherence time τ_0 involves both the C_N^2-profile and the wind speed profile (eqn. 2.8). Since it is not possible to determine a wind speed profile for every C_N^2-profile (sect. 6.3.1), we used the average wind speed profile for each night. This average profile consists of two parts. The lower part (below 2 km above the telescope) was the average wind speed profile as measured with the G-SCIDAR during that particular night. For the upper part we used wind speed data from the ECMWF archive (valid for 17:00, 23:00 and 05:00 local time), linearly interpolated to the observing time of the C_N^2-profile. This approximation does not introduce a systematic error in the coherence time, but only a broadening of its distribution.

The median value of τ_0 for the individual nights is shown in 6.20 and table 6.6, the median value for all C_N^2-profiles was found to be 3.63±1.66 msec. Figure 6.20 also shows the cumulative distribution of τ_0. For some nights in winter, the

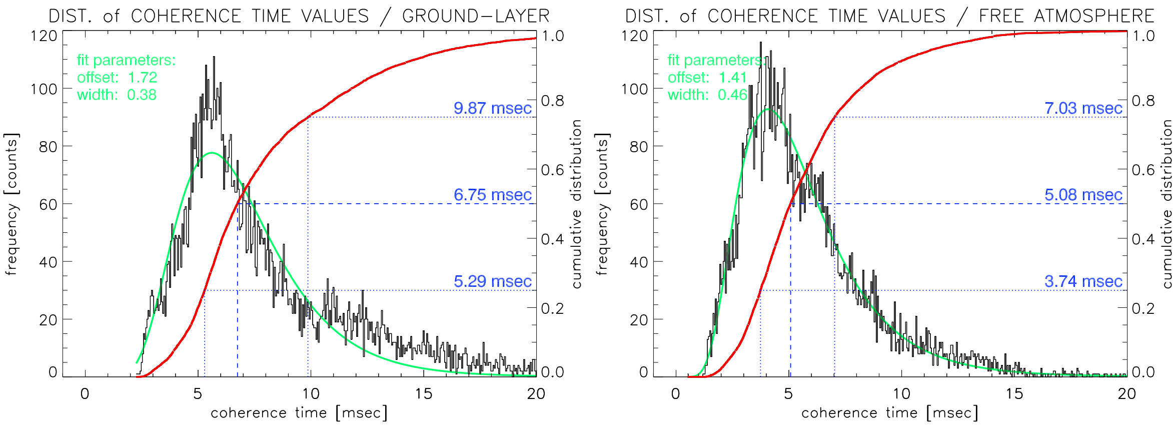

FIGURE 6.21: The histogram and the cumulative distribution of the wavefront coherence time for the boundary layer (0 – 1 km above the telescope) and the free atmosphere (above 1 km). Also shown is a fit to a log-normal distribution and the quartiles of the distribution.

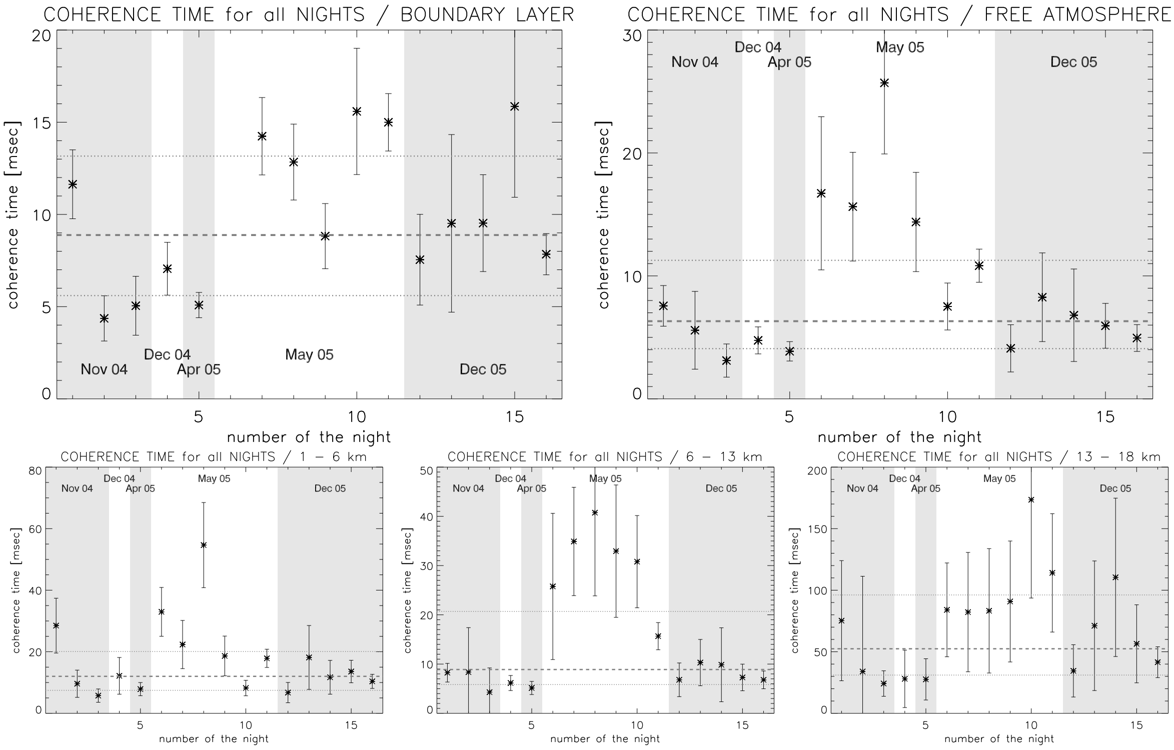

FIGURE 6.22: The wavefront coherence time in the boundary layer (0 – 1 km) and the free atmosphere (above 1 km), and in the layers (1 – 6 km), (6 – 13 km) and (13 – 18 km) above the telescope for the individual nights. The error bars represent the standard-deviation during the individual nights, the dashed line indicates the median and the dotted lines the first and third quartiles for all C_N^2-profiles.

coherence time is ≈50% higher than in summer. Again we do not yet have enough data for a clear seasonal trend. The values of τ_0 range from 1 to 10 msec, with occasional dramatic variations by a factor ≈4 within a few minutes.

The value of τ_0 was also calculated for different layers of the atmosphere to determine their respective contribution to the total value. As shown in figures 6.21

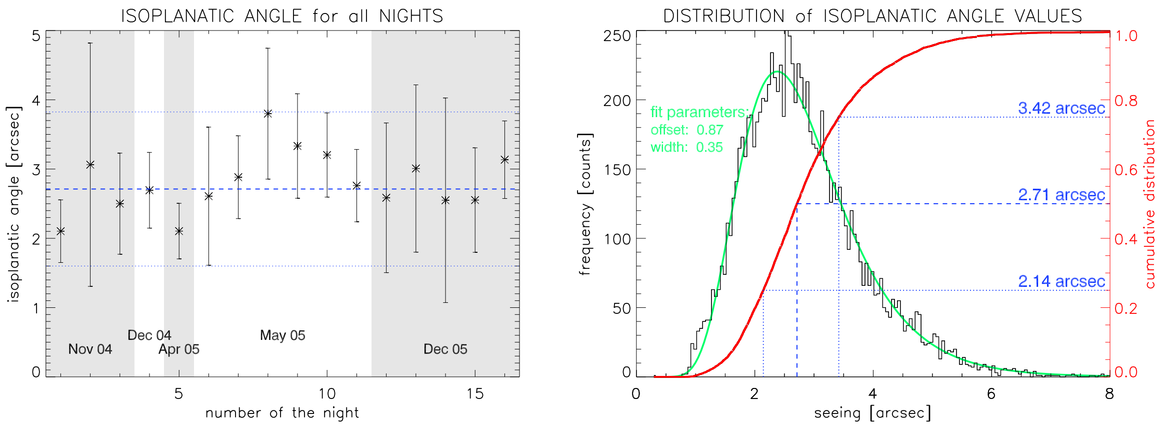

FIGURE 6.23: The median value of the isoplanatic angle ϑ_0 for all nights and its cumulative distribution for all C_N^2-profiles. The variation during the individual nights is indicated by the error bars and the quartiles of the distribution by the dashed and dotted lines.

and 6.22, the higher wind speeds in the troposphere more than compensate the smaller value of the C_N^2 in this region. This results in a comparable value for τ_0 in the ground-layer and in the free atmosphere. Figure 6.22 also shows that τ_0 in the upper part of the atmosphere (above 6 km above the telescope) is significantly higher, by a factor of 2 to 4, in summer than in winter. The reason is the much higher wind speed in this region of the atmosphere during the observing runs in winter (appendix B). This seasonal trend in the high part of the atmosphere is similar to what was found at San Pedro Martir (Masciadri and Egner, 2004).

6.6.4 ISOPLANATIC ANGLE

The isoplanatic angle ϑ_0 can be calculated from the C_N^2-profiles via equation 2.55. Its median value and variations for single nights are shown in table 6.6 and in figure 6.23, along with the cumulative distribution. The median value of ϑ_0 is 2.71 ± 1.11”, and it is 0.5” larger in summer than in winter. Over all nights, the range of ϑ_0 is between 1 and 6 arcsec in the visible ($\lambda = 0.5\,\mu$m).

6.6.5 ISOPISTONIC ANGLE

The isopistonic angle depends not only on the atmospheric turbulence profile, but according to equation 2.58, also on the turbulence outer scale L_0 and the specific parameters of the interferometer. Since ϑ_P is especially important for LINC-NIRVANA, we used the parameters of the LBT ($D = 8.4$ m, $\Delta = 22.8$ m), $L_0 = 25$ m and a wavelength of $\lambda = 0.5\,\mu$m for the calculations here.

The median value of ϑ_P and its variation, as well as the cumulative distribution, appear in figure 6.24 and table 6.6. Considering all measured C_N^2-profiles, the median value of ϑ_P is 8.3 ± 2.8” for the used parameters, with a range of 3 to 18”. It was found that in summer, ϑ_P is larger than in winter by ≈40%.

With the help of the figures 6.25 and 6.26, the values of the isopistonic angle ϑ_P given here can be transfered to different values of L_0 and λ. In figure 6.25, the dependence of ϑ_P on λ and L_0 is plotted for the median C_N^2-profile as measured at Mt. Graham. For values of L_0 larger than ≈15 m, ϑ_P is almost a linear function of

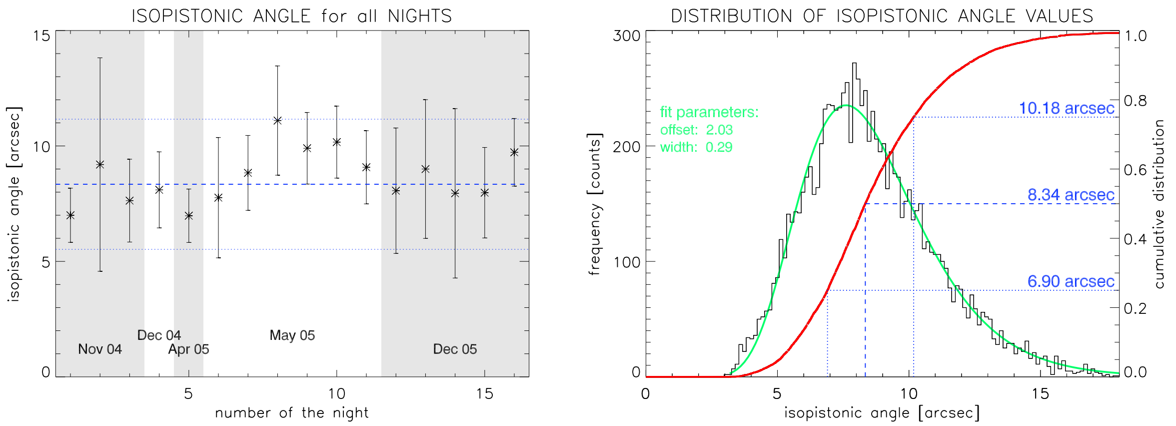

FIGURE 6.24: The median value of the isopistonic angle ϑ_P for the parameters of the LBT and for visible wavelengths, and the cumulative distribution for all C_N^2-profiles.

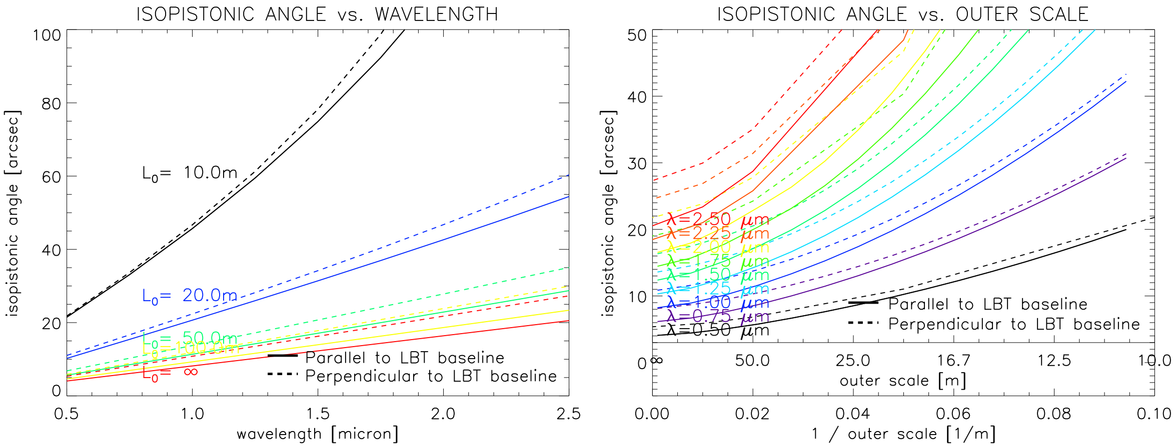

FIGURE 6.25: **Left:** The dependence of the isopistonic angle ϑ_P on the wavelength λ for different values of the outer scale L_0. **Right:** The isopistonic angle ϑ_P as a function of the outer scale L_0 for different wavelengths λ.

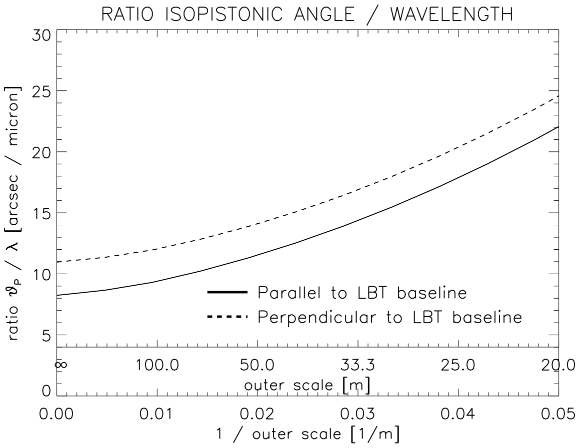

FIGURE 6.26: The mean ratio of isopistonic angle ϑ_P over wavelength λ as a function of the outer scale L_0.

Date	**Seeing**	**Coh. time**	**Isoplan. Angle**	**Isopist. Angle**
	arcsec	msec	arcsec	arcsec
24. Nov 2004	0.75 ± 0.07	5.9 ± 0.8	2.1 ± 0.5	7.0 ± 1.2
25. Nov 2004	0.67 ± 0.11	3.3 ± 1.1	3.1 ± 1.8	9.2 ± 4.6
26. Nov 2004	0.69 ± 0.18	2.4 ± 0.6	2.5 ± 0.7	7.6 ± 1.8
03. Dec 2004	0.78 ± 0.14	3.7 ± 0.6	2.7 ± 0.6	8.1 ± 1.6
26. Apr 2005	0.67 ± 0.10	2.9 ± 0.4	2.1 ± 0.4	7.0 ± 1.2
19. May 2005	0.51 ± 0.05	4.0 ± 1.6	2.6 ± 1.0	7.8 ± 2.6
20. May 2005	0.65 ± 0.17	3.5 ± 0.7	2.9 ± 0.6	8.8 ± 1.6
21. May 2005	0.58 ± 0.08	4.3 ± 0.5	3.8 ± 0.9	11.1 ± 2.4
22. May 2005	0.58 ± 0.09	3.5 ± 0.7	3.3 ± 0.8	9.9 ± 1.5
23. May 2005	0.62 ± 0.06	3.3 ± 0.5	3.2 ± 0.6	10.2 ± 1.6
25. May 2005	0.67 ± 0.06	3.1 ± 0.3	2.8 ± 0.5	9.1 ± 1.6
06. Dec 2005	0.71 ± 0.24	3.2 ± 1.3	2.6 ± 1.1	8.1 ± 2.7
07. Dec 2005	0.59 ± 0.23	5.7 ± 2.5	3.1 ± 1.2	9.0 ± 3.0
08. Dec 2005	0.65 ± 0.16	5.0 ± 1.8	3.1 ± 1.5	7.9 ± 3.7
09. Dec 2005	0.65 ± 0.11	5.1 ± 1.3	2.6 ± 0.8	8.0 ± 2.0
13. Dec 2005	0.80 ± 0.12	4.0 ± 0.6	3.1 ± 0.6	9.7 ± 1.5
All data	**0.67 ± 0.17**	**3.6 ± 1.7**	**2.7 ± 1.1**	**8.3 ± 2.8**

TABLE 6.6: The median values of all astro-climatic parameters for all the individual nights in the visible (λ =0.5 μm). The given errors correspond to the standard deviation during the individual nights. Also given are the median values and standard deviations, when using all measured C_N^2-profiles.

λ. The ratio ϑ_P/λ as a function of L_0 is shown in figure 6.26. This gives a median value of 38±15" for ϑ_P in the K-band (λ =2.2 μm). For $L_0 = \infty$, the median ϑ_P is 3.3±1.4" in the visible and 15±5" in the K-band, which is comparable to the isoplanatic angle ϑ_0 (sect. 6.6.4).

6.6.6 TEMPORAL CORRELATIONS

We used the temporal auto-correlation (**TA**, eqn. 2.23) and the temporal structure function (**SF**, eqn. 2.26) to characterize the time-scales for changes in the astro-climatic parameters. This does not reflect changes in the wavefront, which are characterized by the wavefront coherence time τ_0, but rather the change of these statistical parameters over time.

To calculate the decorrelation times for the temporal cross-correlation τ_{TA} and the structure function τ_{SF}, only blocks with of least two hours of continuous observation were used. The data within these blocks were interpolated to a regular

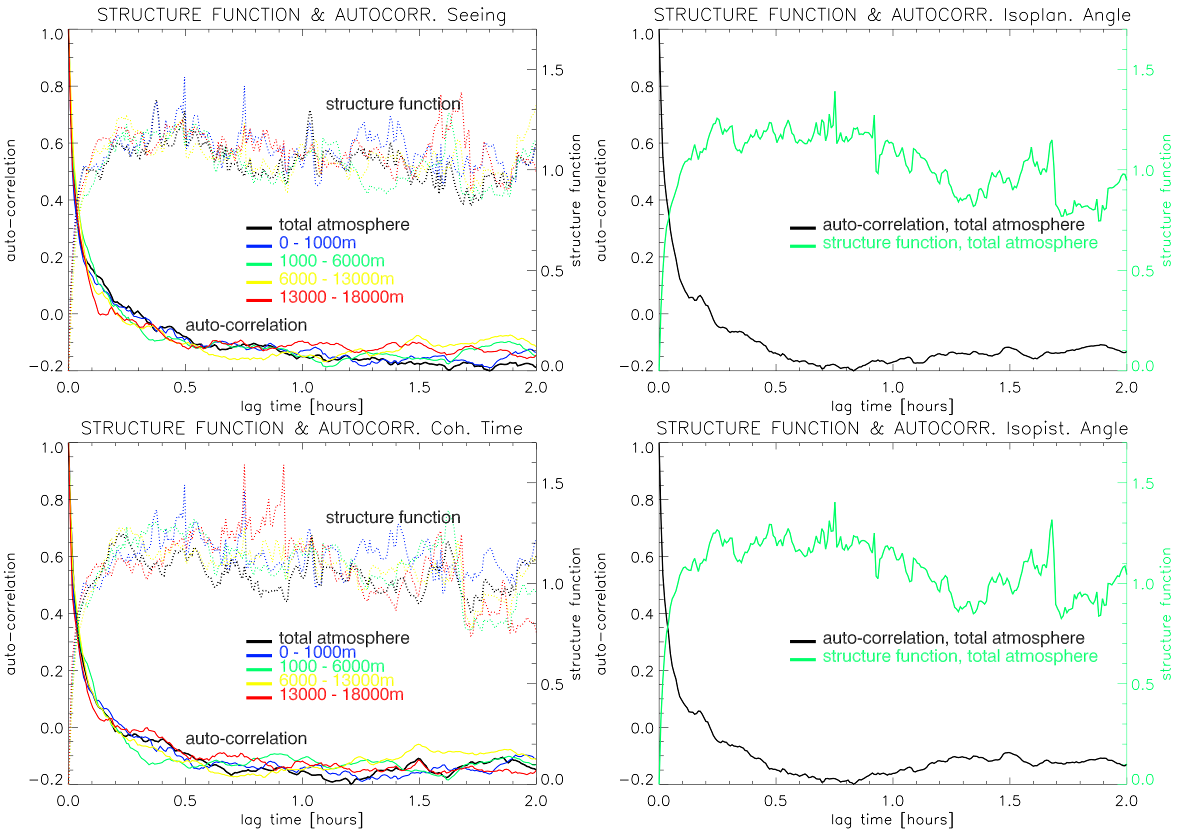

FIGURE 6.27: The temporal auto-correlation and the structure function for the astro-climatic parameters.

time-grid (1.0 minutes), as required for the calculations. Using equations 2.22, 2.23, 2.25 and 2.26, the de-correlation times τ_{TA} and τ_{SF} are calculated. The resulting temporal cross-correlation $\mathbf{TA}(\Delta t)$ and $\mathbf{SF}(\Delta t)$ for all astro-climatic parameters are plotted in figure 6.27. As can be seen, τ_{TA} is one or two minutes, while τ_{SF} is between 5 and 7 minutes, independent of the astro-climatic parameter or the atmospheric layer. This represents much more rapid changes than found at other sites. Avila et al. (2004); Tokovinin et al. (2003) report τ_{TA} between 0.5 and 2 hours. The reason for this discrepancy is not known, but since two independent methods were used for the calculations, with similar results, this should be an intrinsic characteristic of the site.

6.6.7 VERTICAL CORRELATIONS

The common understanding of the creation of optically active turbulence is that the ground-layer turbulence is caused by the interaction of the wind with the local orography at the ground, such as surface structure and vegetation. In contrast, the turbulence in the free atmosphere is caused by mixing of high wind speeds in the jet-stream. The turbulence in these two parts of the atmosphere should thus be independent. To test this hypothesis, the correlation between the seeing in the ground-layer (up to 1 km above the telescope) and in the free atmosphere (above 1 km) was calculated. As shown in figure 6.28 there is a correlation of only 7% between the two parts of the atmosphere, similar to what was found by Tokovinin et al. (2005). However, when calculating the correlation between the seeing in the

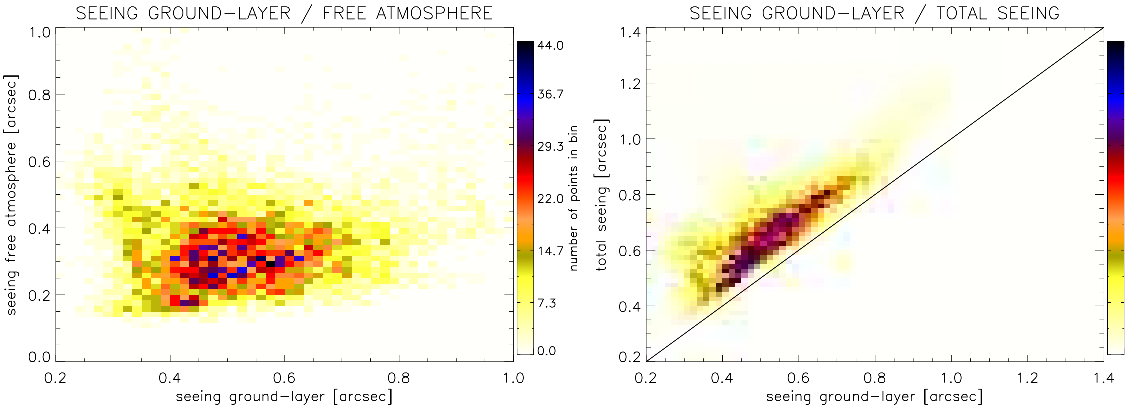

FIGURE 6.28: The correlation between the seeing in the ground-layer (up to 1 km above the telescope) and the free atmosphere (above 1 km) (**left**) and the seeing in the ground-layer and the total seeing (**right**).

ground-layer and the total seeing, a clear correlation of 80% is apparent (fig. 6.28), reflecting the dominance of the ground-layer in the C_N^2-profiles.

6.6.8 COMPARISON TO OTHER SITES

Here, we compare the measured astro-climatic parameters to those measured at other sites. However, there are many different techniques to measure these parameters, each with advantages and disadvantages. For this reason, only the results of G-SCIDAR observations appear in table 6.7. As with Mt. Graham, the G-SCIDAR measurements at other sites represent a small number of nights, usually only between 20 and 30. Furthermore, these measurements are mostly concentrated in a few observing runs, since they require a substantial investment of manpower and telescope infrastructure. This results in reduced significance of the statistical results. Nevertheless, from table 6.7, it is obvious that Mt. Graham can readily compete with the best sites in the world, in terms of the astro-climatic parameters. Considering the fact that the seeing ϵ_0 measured at Mt. Graham is comparable to that at other sites, but the isoplanatic angle ϑ_0 is larger, further supports the dominance of the ground-layer at Mt. Graham (6.5.2).

6.7 HIGH-RESOLUTION C_N^2 PROFILES

In previous sections, we presented and analyzed C_N^2-profiles measured with a Generalized SCIDAR in standard configuration, thus achieving a vertical resolution of $\Delta h_{\mathrm{GS}}(0) \approx 1$ km (see fig. 6.7). However, for some applications, it would be highly desirable to obtain C_N^2-profiles with much higher vertical resolution. Such high-resolution C_N^2-profiles would be particularly useful for the design and development of the next-generation Adaptive Optics Systems (e.g. Ground-Layer AO or Multi-Conjugated AO), which correct individual turbulent layers. To achieve optimal performance, it is essential to know the location and strength of these individual layers, and especially the detailed structure of the Ground-Layer, which usually contains most of the turbulence (see sect. 5.6.1).

Site	Duration	Seeing	Isoplan. Angle	Coh. time	Reference
		arcsec	arcsec	msec	
Mauna Kea	20 nights	0.50^1	1.9^1	—	Racine and Ellerbroek (1995)
San Pedro Martir	27 nights	0.71	1.6	6.5	Avila et al. (2004, 2003)
Cerro Pachon	24 nights	0.85	2.1	4.8	Avila et al. (2000); Vernin et al. (2000)
Cerro Tololo	22 nights	0.85	2.1	—	Vernin et al. (2000); Avila et al. (2000)
La Palma	34 nights	0.78 - 1.42	1.3	—	Fuensalida et al. (2004b)
La Silla	30 nights	1.30^2	2.1	—	Sadibekova et al. (2006)
Mt. Graham	**16 nights**	**0.67±0.17**	**2.71±1.11**	**3.63±1.66**	

TABLE 6.7: The median astro-climatic parameters measured with SCIDAR instruments at different astronomical observatories as a comparison to the values as determined for Mt. Graham. All values are given for the visible at $\lambda = 0.5\,\mu$m. The errors for Mt. Graham indicate the standard deviation of the parameters for all measured C_N^2-profiles.
Notes: ① Measured with classical SCIDAR and thus insensitive to the ground-layer. ② Including dome-seeing.

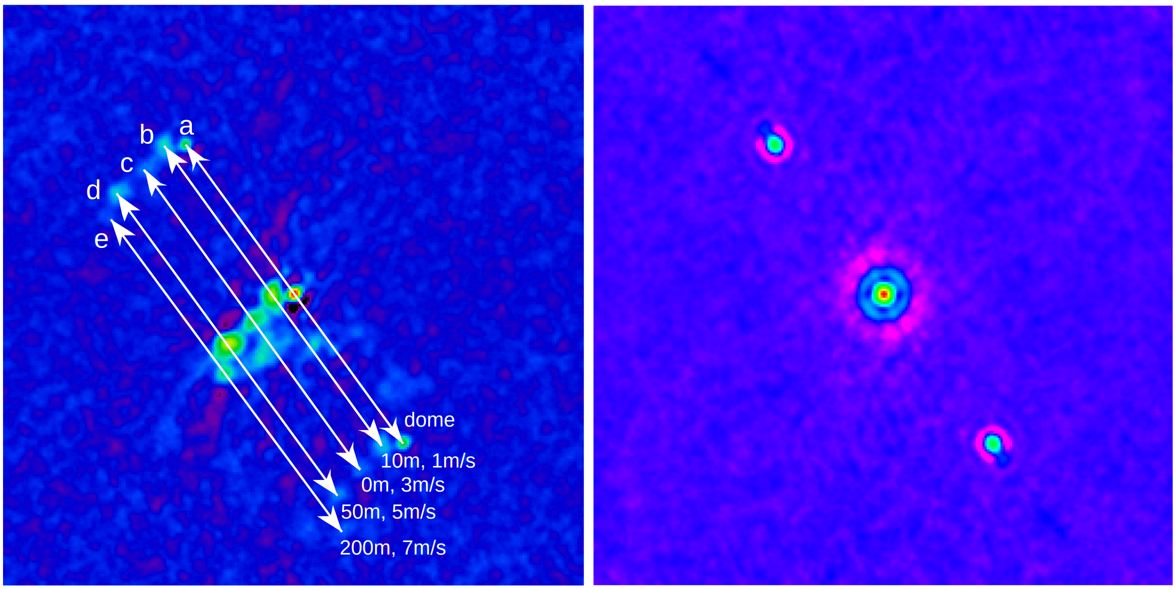

FIGURE 6.29: **Left:** Sample cross-correlation image of β Cyg as measured with the G-SCIDAR at the VATT. The retrieved heights above the telescope and the wind speeds are indicated tor the detected triplets. The uncertainty in the height of single layers is $\approx$25 m. **Right:** The corresponding auto-correlation image, where the correlation peaks of the individual layers overlap.

Several methods to measure the C_N^2-profile near the ground with high vertical resolution have been proposed: SOund Detection And Ranging (SODAR), meteorology masts and High-resolution SCIDAR (Avila and Chun, 2004). However, all these methods either do not directly measure the optical effects of the turbulence, making the obtained data difficult to calibrate and interpret, or they cannot be performed with an existing SCIDAR instrument. In this section, a new method is presented, which uses an existing G-SCIDAR instrument and can achieve a vertical resolution of a few tens of meters in the first few hundred meters above the telescope.

6.7.1 High vertical resolution method (HVR-GS)

As explained in section 2.3, the vertical resolution Δh_{GS} of the SCIDAR is limited by the size of the correlation peaks in the auto-correlation (**AC**) frames. If the peaks associated with different turbulent layers could be somehow separated, the vertical resolution might be improved. Such a possibility is given by analysing the temporal cross-correlation (**CC**) images for the calculation of the $C_N^2(h)$ profiles, as opposed to the **AC** images. When the wind speed in two layers is different, the corresponding peaks in the **CC** images are no longer only separated by their different heights, but also by their different wind speed and wind direction. As illustrated in figure 6.29, the correlation triplets associated with two different layers are no longer only displaced along the axis of the binary, but, under favorable conditions, also shifted by the wind speed $\mathbf{v}_{\mathrm{wind}}$ of the two layers. In contrast, the correlation peaks of the individual layers overlap in the **AC** image, making it impossible to resolve the single layers.

Similar to the calculation of the wind speed (sect. 6.3.1), the height h_{layer} of the layer can be calculated from the separation of the lateral peaks d_{triplet} in the associated triplets (eqn. 2.38). The vertical resolution is then limited only by the accuracy in determining the distance d_{triplet} of the lateral peaks for each triplet. For a peak sampled with at least a few pixels, the center position can usually be determined with an uncertainty that is much smaller then the FWHM of the peak. Since the FWHM of the correlation peaks is the limiting factor for the vertical resolution in conventional operation of the G-SCIDAR (i.e. by analysing the **AC** images), this new method, which relies on the center position of the peaks, offers the prospect to increase the vertical resolution by a significant factor.

With this High Vertical Resolution Generalized SCIDAR (HVR-GS) method, the height h_i of the single layers can be determined very precisely. However, it is difficult to get the absolute C_N^2 value of the corresponding turbulent layer directly from the intensities of the correlation peaks in the **CC** images (see section 2.3.1 for a detailed explanation). To determine the $C_{N,cc}^2(h_i)$ from the **CC** images, the measured triplet intensities $I_{i,\text{outside}}$ in the **CC** images are scaled with a common factor f_{scale} (assuming the same temporal decorrelation of all layers) to get the same total amount of turbulence as in the dome-seeing corrected $C_{N,ac}^{2*}(h)$ profiles (as determined from the **AC** images with the verified data-reduction pipeline):

$$\int\limits_{-\Delta h_{\text{GS}}(0)/2}^{h_{GL}} C_{N,ac}^{2*}(h)\, dh \;=\; f_{\text{scale}} \cdot \sum_i I_{i,\text{outside}} \cdot h_i^{-5/6}, \tag{6.12}$$

where h_{GL} is the height of the highest layer identified in the **CC** images. The intensity $I_{i,\text{outside}}$ of the central peaks of the triplets (in the absence of smearing due to wind shear) depends on the 5/6th power of the height h of the turbulent layer above the telescope (Roddier, 1981). To correct for this effect, the intensities of the central peaks of the triplets $I_{i,\text{outside}}$ are scaled by $h_i^{-5/6}$. Furthermore, the thickness Δh_i of all turbulent layers was assumed to be the same for all layers, which seems to be valid for our observations (see below).

Summarizing, in equation 6.12, the $C_{N,ac}^{2*}$ is calculated from the **AC** images, h_i is determined from the separation d_i of the lateral peaks for each triplet and $I_{i,\text{outside}}$ is the measured intensity of the central peak for each triplet. Using these inputs, the scaling factor f_{scale} can be determined via equation 6.12 for each correlation frame. The value of $C_{N,cc}^2(h_i)$ for the individual turbulent layers is then given by

$$C_{N,cc}^2(h_i) \;=\; f_{\text{scale}} \cdot I_{i,\text{outside}} \cdot h_i^{-5/6}. \tag{6.13}$$

Similarly, the seeing in the individual layers can be determined via (eqn. 2.15)

$$\epsilon_i \;=\; \left[\frac{0.409 \cdot (2\pi)^2}{\lambda^{1/3}} \cdot f_{\text{scale}} \cdot I_{i,\text{outside}} \cdot h_i^{-5/6}\right]^{3/5}. \tag{6.14}$$

6.7.2 HVR-GS ON-SKY VALIDATION

To validate the HVR-GS method, a wide binary was observed for roughly 1 hour per night for a total of 2 nights during two SCIDAR measurement campaigns in May and December 2005. The observed binary star in May was β Cyg and in December ψ Psc, with a separation of 35" and 30", respectively (tab. 6.2). By using such a wide binary, the achievable vertical resolution can already be improved by a factor of 5, even with the G-SCIDAR in standard configuration, compared to a standard binary with a separation of 7". With the conjugation height h_{GS} set to -3800 meters, the resolution $\Delta h_S(0)$ of conventional G-SCIDAR is ≈200 – 230 meters (eqn. 2.48). For the HVR-GS, one pixel on the detector corresponds to a vertical range Δh_p of 45 and 52 meters for these binaries, respectively (eqn. 2.49).

In contrast to normal G-SCIDAR operation, in which typically 6 000 frames (corresponding to 1 minute) are averaged to get one **AC** and **CC** image (sect. 6.2.1), for the HVR-GS method, only 500 frames were used. The reason was to limit the smearing of the correlation peaks in the **CC** image due to a variation in the wind speed and wind direction during the averaging time. This results in increased noise in the **AC** images and thus in the $C^2_{N,cc}$ profiles.

The first step in the data reduction process was to select from all measured **CC** images the frames in which the **CC** peaks have a circular shape. The other frames were discarded, because in these cases it would not be possible to distinguish between a vertical extent of the turbulent layer and a variation of the wind speed and wind direction during the averaging time. Furthermore, the total intensities of the single correlation peaks would be impossible to determine precisely.

Then, all peaks in the selected **CC** images were fitted with a 2-dimensional Gaussian to determine their central position. The accuracy of this procedure was determined by using the correlation triplet associated with the dome. This triplet is always at the same altitude and is not shifted due to the wind, and should thus always give the same center positions of the three correlation peaks. When repeating the fitting procedure for different **CC** images, the standard deviation of the peaks' center positions for this triplet was determined to be ≈0.4 pixel. According to equation 2.38, the accuracy in determining the center position of the lateral peaks limits the achievable vertical resolution of the HVR-GS method. Using equation 2.49, the vertical resolution $h_{\text{HVR-GS}}$ can be calculated via

$$\Delta h_{\text{HVR-GS}} = 0.4\sqrt{2}\cdot\Delta h_p = 0.4\sqrt{2}\cdot\frac{D_{\text{tel}}}{n_{\text{pixel}}\cdot\sin\phi}. \qquad (6.15)$$

For a binary separation ϕ of 35" and n_{pixel} ≈230 pixel across the pupil image, this results in a vertical resolution $\Delta h_{\text{HVR-GS}}$ ≈25 m, which is a factor of 40 better than for the G-SCIDAR in the standard configuration.

From the **CC** images, the intensity I_i of the central peak of each triplet and the $C^2_{N,ac}(h)$ profile from the **AC** images was determined. With the dome-seeing-corrected $C^{2*}_{N,ac}(h)$ profiles (sect. 6.3.1), the scaling factor f_{scale} was calculated from equation 6.12. The highest turbulent layer visible in the measured **CC** images was at ≈600 m, thus h_{GL} =600 m was chosen as the upper limit for the integration in equation 6.12. Finally, by using equation 6.13 and 6.14, the $C^2_{N,cc}(h_i)$ profile and the seeing ϵ_i in the single turbulent layers can be calculated.

6.7.3 RESULTS OF HVR-GS AND DISCUSSION

From the data taken with the wide binary, the $C^{2*}_{N,ac}(h)$ profiles can be retrieved with the data-reduction pipeline from the **AC** images, just as in conventional G-SCIDAR. Figure 6.30 shows the temporal evolution of the $C^2_{N,ac}(h)$ profile during ≈45 minutes of the night of 21 May 2005. When using such a wide binary, the vertical resolution $\Delta h_S(0)$ of G-SCIDAR is improved from ≈1 km (as in fig. 6.9) to ≈200 meters.

Figure 6.29 shows a typical **CC** image and the identified triplets, with the retrieved height and wind speed indicated. A plot of the equivalent seeing in the

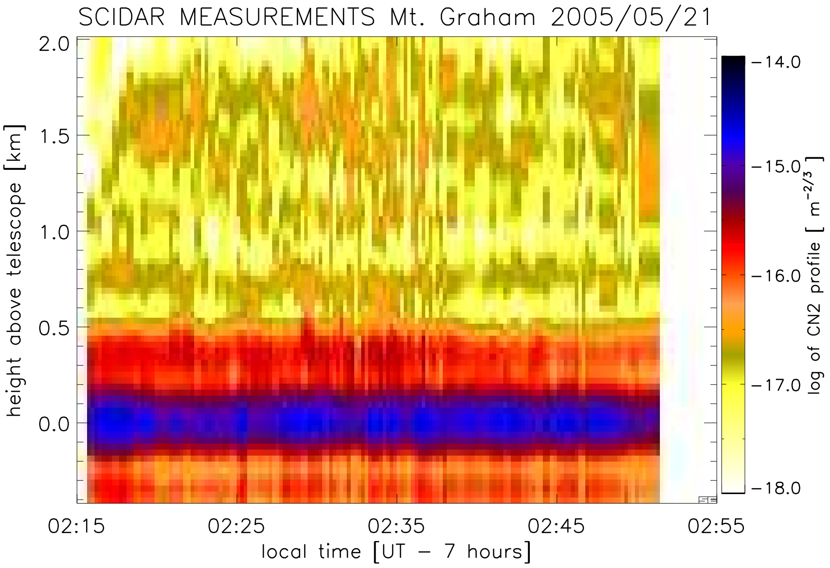

FIGURE 6.30: The temporal evolution of the $C_{N,ac}^{2*}(h)$ profile as determined from the autocorrelation images when using a wide binary with a separation of 35”. This is the conventional G-SCIDAR result.

individual layers for all measured profiles for one night appears in figure 6.31. In all profiles, a weak layer at the height of the VATT is visible, and the most turbulent layer is located at ≈50 m above the ground. As can be seen from the schematic topography shown in figure 6.1, the primary mirror of the LBT is ≈35 m above the VATT and thus above the first weak layer, but still below the strong layer at ≈50 m above the ground. Above the strong layer at ≈50 meters, the strength of the turbulence drops rapidly, with only one more distinct turbulent layer at ≈350 meters. The height of this layer matches the layer seen in the $C_{N,ac}^{2*}(h)$ profiles as determined from the **AC** images (fig. 6.30). This provides us a further confirmation of the reliability of the HVR-GS method.

An anemometer placed ≈50 m above the VATT on the roof of the LBT (see fig. 6.1), measured a wind speed of 5 to 7 m/s at the time of the **CC** image shown in figure 6.29. It thus matches very well the derived wind speed of the turbulent layer at ≈50 meters above the VATT, as determined with the HVR-GS method.

From the individual turbulence profiles shown in figure 6.31, it can be seen that the ground-layer apparent in the C_N^2-profiles with standard G-SCIDAR, is actually composed of many thin layers. Since the **CC** correlation peaks associated with individual layers are in our observations not extended along the binary axis, but have their intrinsic width, it seems that these layers are even thinner than the vertical resolution of the HVR-GS method, and are thus <25 meters thick.

Using the average cumulative $C_{N,cc}^2$-profile (defined in eqn. 6.8) retrieved from the HVR-GS (fig. 6.32), the average seeing in the 35 m altitude difference between the top of the VATT and the primary mirror of the LBT can be estimated. From the high-resolution profiles $C_{N,cc}^2(h_i)$, it is found that ≈27% of the C_N^2 in the first 600 m is below the first 35 m. During this particular night, the median seeing of the total atmosphere as measured with a G-SCIDAR at the VATT was 0.60”, with 0.55” in the first 600 m. If we assume that the turbulence profile at the LBT is the same as that measured at the VATT, this translates into a seeing of 0.52” above the primary mirror of the LBT.

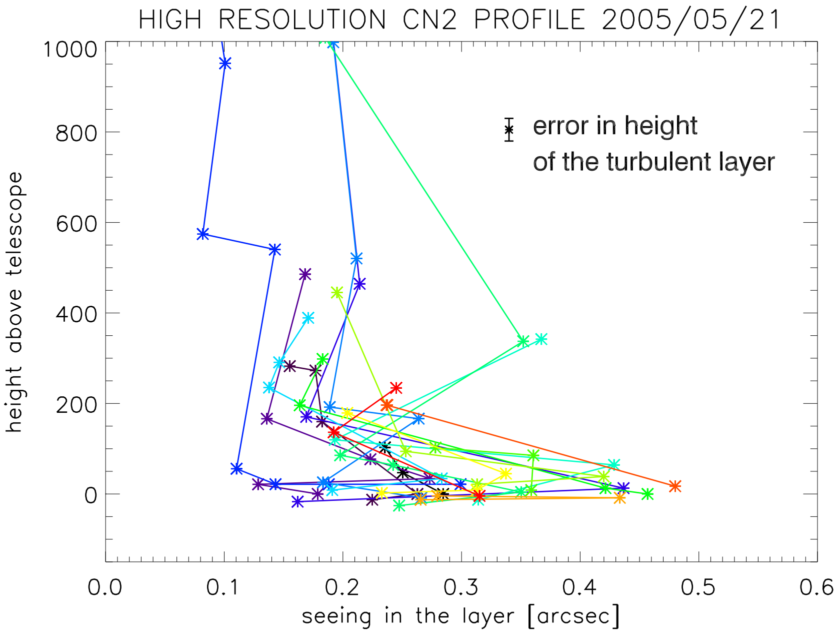

FIGURE 6.31: The seeing in single layers as retrieved from the data of 21 May 2005 with the high-vertical resolution SCIDAR method. The vertical resolution is ≈25 m (as indicated by the error bar).

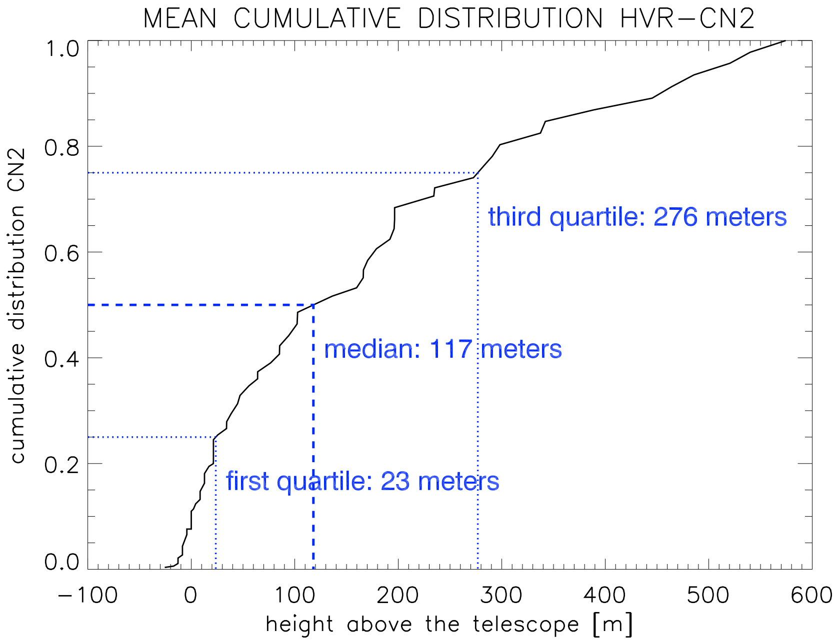

FIGURE 6.32: The cumulative C_N^2-profile measured with the High vertical resolution G-SCIDAR (HVR-GS) method near the ground.

One limitation of the HVR-GS method is that the turbulence profile can be extracted only under favorable wind conditions and thus might not represent typical conditions. To estimate if this causes an selection-bias, we compared the seeing determined from the $C_{N,ac}^{2*}$ profiles for the times when an extraction with the HVR-GS method was possible and when not. The median seeing in the first 2 km for all $C_{N,ac}^{2*}$ profiles shown in figure 6.30 is 0.64±0.10". Considering only those $C_{N,ac}^{2*}$

profiles, when an extraction with the HVR-GS method from the associated **CC** images was possible, the seeing is 0.66±0.10". The HVR-GS method does therefore not favor particularly good or bad seeing conditions. However, with the limited amount of data taken with this method so far, it is not yet possible to exclude an selection-bias on the vertical structure.

Nevertheless, even for the fraction when such HVR-GS $C^2_{N,cc}(h)$ profiles can be extracted, the turbulence profiles shown in figures 6.31 and 6.32 stress the importance of the actual position of a telescope on a mountain and the height of the telescope above the ground. A difference of 50 m in height can make a large difference in the resulting atmospheric seeing and thus image quality. However, one has to keep in mind that even small differences between the temperature of the ambient air and the dome or the primary mirror of a telescope can cause severe dome-seeing. Since the observed wind speeds at the LBT are usually dramatically higher than at the VATT, this requires greater effort to keep the air-flow through the dome of the LBT laminar and thus the dome-seeing low. Only then can the better atmospheric conditions actually be transformed into a better image quality.

6.8 IMPACT ON LINC-NIRVANA MCAO PERFORMANCE

Once the C^2_N-profiles and thus the vertical structure of the atmospheric turbulence have been determined, the impact on interferometry of LINC-NIRVANA and on the performance of its MCAO system be examined in more detail.

6.8.1 OPTIMAL CONJUGATED HEIGHTS OF THE DMS

As mentioned in the introduction (sect. 2.6.2), LINC-NIRVANA will make use of an MCAO system with two DMs in each arm. One is the deformable secondary of the LBT, whose conjugation altitude $h_{\mathrm{conj,GL}}$ is fixed at 100 m. The second DM is implemented in LINC-NIRVANA itself and its conjugation height $h_{\mathrm{conj,HL}}$ can be freely adjusted to between 4 and 15 km above the telescope.

To achieve best performance and optimize the opto-mechanical design of the instrument, it is essential to know the optimal conjugation heights $h_{\mathrm{opt},j}$ of the DMs, the impact of mis-conjugations, and the time-scales on which $h_{\mathrm{opt},j}$ have to adapted.

CALCULATION PRINCIPLE

To study these effects, the semi-analytical model presented in chapter 3 was used with the parameters of the Layer-Oriented (LO) MCAO system of LINC-NIRVANA. We assumed N_{modes} =400 controlled modes for the Ground-Layer (GL) DM and 180 modes for the High-Layer (HL) DM, which is a reasonable number for a bright guide star. But, as described in section 3.3, the precise number N_{modes} has no influence on $h_{\mathrm{opt},j}$.

Depending on the science-case, the optimal performance of an MCAO system might be defined differently. For compact sources, the maximum Strehl ratio on-axis is important, while a homogenous Strehl ratio over the complete field-of-view is desired for extended objects. The criteria for optimizing the conjugation heights of the DMs are thus maximum Strehl ratio in the first case and maximum isoplanatic angle in the latter. Since the science FoV of LN is rather small (10") and thus of the order of ϑ_0 without MCAO correction, the Strehl ratio in this field will be probably rather uniform. However, the important quantity here is the FoV of the WFS, which is much larger (120" and 360", respectively). When optimizing for Strehl ratio, the performance at the barycenter of the guide stars is maximized, but this does not have to coincide with the location of the science FoV, where the performance can be much lower. A trade-off between optimal Strehl ratio and isoplanatic angle has thus to be made, depending on the given object, scientific objectives and the location of suitable guide stars.

OPTIMAL HEIGHTS FOR STREHL

Following the method described in section 3.3, the residual Fried-Parameter $r_{0,\mathrm{res}}$ was calculated from the filtered C_N^2-profiles as a function of $h_{\mathrm{conj,HL}}$. The conjugated height of the HL-DM, where $r_{0,\mathrm{res}}$ is maximized, is then considered to be the optimal conjugation height for Strehl ratio $h_{\mathrm{opt,HL},r_0}$.

Since $h_{\mathrm{conj,GL}}$ is fixed, no in-depth analysis of $h_{\mathrm{opt,GL},r_0}$ was performed. Nevertheless, for the hypothetical cases that $h_{\mathrm{conj,GL}}$ can be adjusted, $h_{\mathrm{opt,GL},r_0}$ was determined for GLAO and MCAO mode. In both cases, $h_{\mathrm{opt,GL},r_0}$ is indeed $\approx$100 m for all C_N^2-profiles. However, due to the limited vertical resolution Δh_{GS} of the G-SCIDAR C_N^2-profiles, especially in the ground-layer, the accuracy in $h_{\mathrm{opt,GL},r_0}$ is limited to 100 – 200 m and thus is not sufficient for a detailed study. Since the major layers near the ground are much thinner than Δh_{GS} (sect. 6.7), their turbulent energy is apparently spread over a large vertical range of $\approx$1 km. If the layer-filter function is narrower than Δh_{GS} (e.g. for a wide FoV and a large N_{modes}), then the filtering of the C_N^2-profiles by the GL-DM is less efficient for the semi-analytical model than in reality. This results in an underestimate of the achievable Strehl ratio on-axis, but does not influence $h_{\mathrm{opt,HL},r_0}$ determined below. The conclusion of a very small $h_{\mathrm{opt,GL},r_0}$ is also supported by the high-vertical-resolution C_N^2-profiles obtained with the HVR-GS technique (sect. 6.7.3). These profiles show that the altitude of the most turbulent layer and thus $h_{\mathrm{opt,GL},r_0}$ is $\approx$50 m above the ground.

The acceptable range $\Delta h_{\mathrm{acc,HL},r_0}$ for the mis-conjugation of the high-layer DM is defined as the maximum separation between $h_{\mathrm{conj,HL}}$ and $h_{\mathrm{opt,HL},r_0}$ for a relative reduction of the residual $r_{0,\mathrm{res}}$ of less than 15%. In figure 6.33, the median $\langle h_{\mathrm{opt,HL},r_0}\rangle$ and $\langle \Delta h_{\mathrm{acc,HL},r_0}\rangle$ are plotted for all nights. The figure shows that $\langle h_{\mathrm{opt,HL},r_0}\rangle$ ranges between 2 km in summer and 10 km winter, and that $\langle \Delta h_{\mathrm{acc,HL},r_0}\rangle$ is usually a few kilometers. However, since an optimistic value for the number of corrected modes was assumed, this is more a lower limit and $h_{\mathrm{acc,HL},r_0}$ for the same relative drop in performance could be larger in reality. Of course, the overall performance will also be reduced when correcting fewer modes. The criterion used to find $\langle h_{\mathrm{opt,HL},r_0}\rangle$ was to minimize the total reduction in performance when considering all profiles for a particular night:

$$\mathbf{min}\left(\sum_i R\Big(C_{N,i}^2(h),\ h_{\mathrm{conj,HL}}\Big)\right)\Bigg|_{h_{\mathrm{conj,HL}}} \qquad \Longrightarrow \qquad \langle h_{\mathrm{opt,HL},r_0}\rangle\ . \tag{6.16}$$

The sum is over all C_N^2-profiles for the considered night, and $R\Big(C_{N,i}^2(h),\ h_{\mathrm{conj,HL}}\Big)$ is the relative reduction in performance (measured with $r_{0,\mathrm{res}}$, $\vartheta_{0,\mathrm{res}}$, $\vartheta_{P,\mathrm{res}}$) when fixing the HL-DM to the conjugation height $h_{\mathrm{conj,HL}}$ and using C_N^2-profile number i.

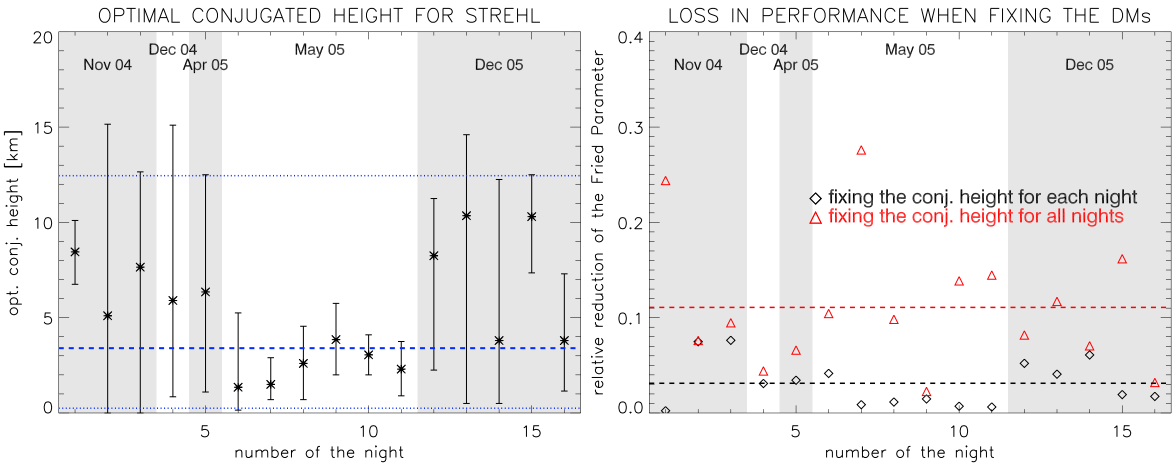

FIGURE 6.33: **Left:** The optimal conjugated height $h_{\text{opt,HL},r_0}$ of the high-layer DM for maximum Strehl ratio on-axis for the individual nights. The error bars indicate the median range of less than 15% reduction in the residual $r_{0,\text{res}}$ for each night. The dashed line denotes the median $\langle h_{\text{opt,HL},r_0} \rangle$ for all C_N^2-profiles and the dotted lines are the first and third quartiles (25% and 75%) in its distribution. **Right:** The relative loss in the residual Fried Parameter $r_{0,\text{res}}$ when fixing the conjugation height of the high-layer DM to the median optimal conjugation height $\langle h_{\text{opt,HL},r_0} \rangle$ of one night and for all nights. The dashed lines indicate the median values for all C_N^2-profiles.

For the operation of the instrument, it is important to know if the performance when fixing $h_{\text{conj,HL}}$ throughout the night is still acceptable or if a real-time adaption of $h_{\text{conj,HL}}$ should be implemented. As shown in figure 6.33, $r_{0,\text{res}}$ decreases by ≈3%, when fixing $h_{\text{conj,HL}}$ to the respective median $\langle h_{\text{opt,HL},r_0} \rangle$ of the individual nights. However, since $\langle h_{\text{opt,HL},r_0} \rangle$ is quite different for the individual nights, $r_{0,\text{res}}$ decreases by 11% when fixing $h_{\text{conj,HL}}$ to the median derived from $h_{\text{opt,HL},r_0}$ of all C_N^2-profiles. Nevertheless, this reduction is still much smaller than the intrinsic variations of r_0 without AO correction (fig. 6.15).

OPTIMAL HEIGHTS FOR ISOPLANATIC ANGLE

In the case that the Strehl ratio should be as homogenous as possible over the field, the isoplanatic angle has to be maximized. To calculate the optimal conjugation height $h_{\text{opt,HL},\vartheta_0}$ of the high-layer DM for maximum $\vartheta_{0,\text{res}}$, the same procedure as in the previous section was used. The conjugation height $h_{\text{conj,GL}}$ of the GL-DM was again fixed at 100 m. Since ϑ_0 is rather independent of the ground-layer, the problems related to the limited vertical resolution of the used C_N^2-profiles are negligible here.

The obtained values for $h_{\text{opt,HL},\vartheta_0}$ and $\Delta h_{\text{acc,HL},\vartheta_0}$ are plotted for all nights in figure 6.34. The median value $\langle h_{\text{opt,HL},\vartheta_0} \rangle$ was found to be ≈10.7 km for all data, with variations of a few kilometers among the individual nights, but no clear seasonal trend. Figure 6.35 shows $\vartheta_{0,\text{res}}$, calculated from each filtered, residual C_N^2-profile, when adjusting $h_{\text{conj,HL}}$ to the just determined optimal conjugation height $h_{\text{opt,HL},\vartheta_0}$ for that C_N^2-profile. Compared to figure 6.23, $\vartheta_{0,\text{res}}$ is increased by a factor ≈2 by the correction of the MCAO system.

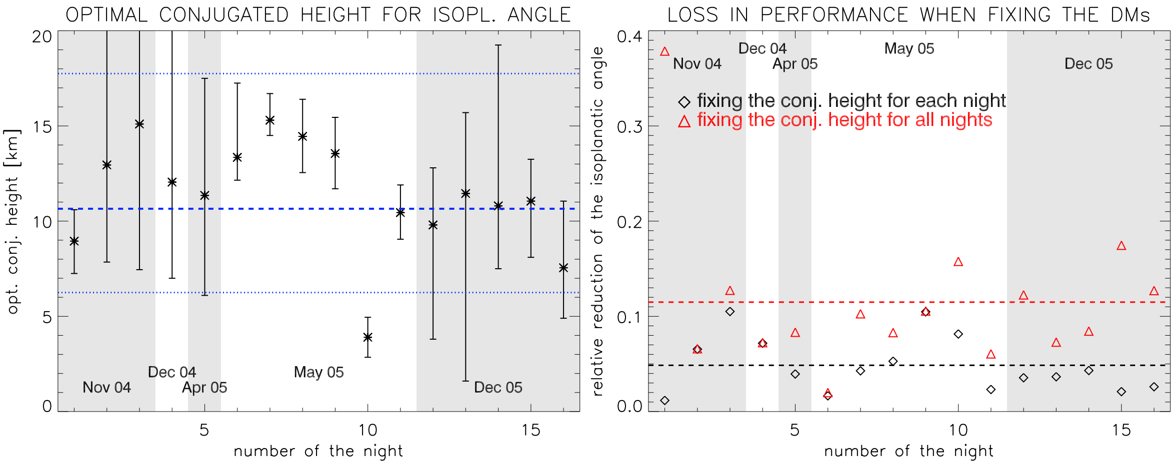

FIGURE 6.34: **Left:** The optimal conjugated height $h_{\text{opt,HL},\vartheta_0}$ of the high-layer DM for maximum isoplanatic angle for the individual nights. The error bars indicate for each night the median range of mis-conjugation for a reduction in $\vartheta_{0,\text{res}}$ of less than 15%. The dashed line is the median of $h_{\text{opt,HL},\vartheta_0}$ of all C_N^2-profiles and the dotted lines are the first and third quartile of its distribution. **Right:** The relative loss in the isoplanatic angle when fixing the conjugation height of the high-layer DM to the median optimal conjugation height $\langle h_{\text{opt,HL},\vartheta_0}\rangle$ of one night and for all C_N^2-profiles. The dashed lines indicate the median values for all C_N^2-profiles.

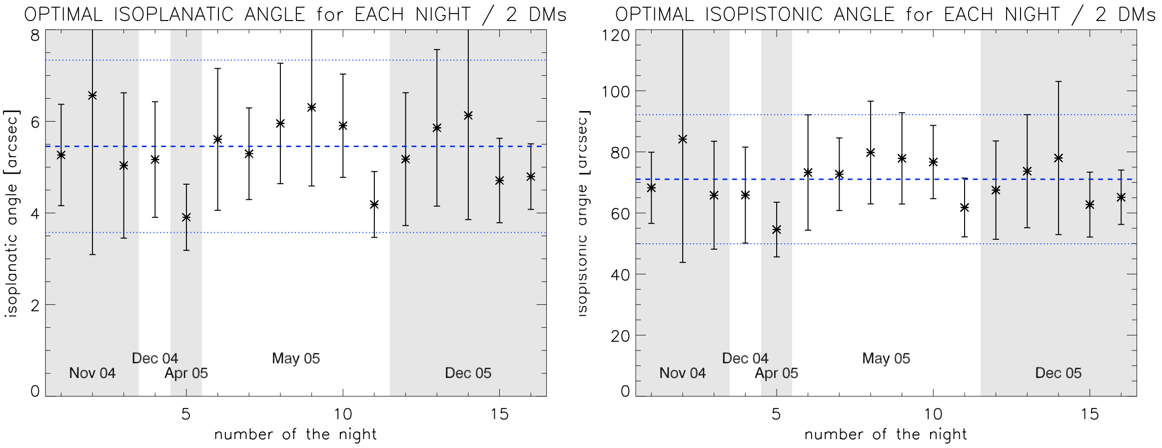

FIGURE 6.35: **Left:** The average isoplanatic angle $\vartheta_{0,\text{res}}$ for the individual nights, when setting the HL-DM to the optimal conjugation height for each C_N^2-profile. The error bars indicate for each night the median range of mis-conjugation for a reduction in $\vartheta_{0,\text{res}}$ of less than 15%, the dashed line is the median for all profiles and the dotted lines the first and third quartiles of its distribution. **Right:** The same, but for the isopistonic angle $\vartheta_{P,\text{res}}$.

When fixing $h_{\text{conj,HL}}$ to the median $\langle h_{\text{opt,HL},\vartheta_0}\rangle$ for the individual nights, the residual $\vartheta_{0,\text{res}}$ is reduced on average by ≈5% for all nights. Fixing $h_{\text{conj,HL}}$ to the median $\langle h_{\text{opt,HL},\vartheta_0}\rangle$ of all C_N^2-profiles results in a drop of ϑ_0 by ≈11% (fig. 6.34).

As mentioned in chapter 3, the method of the layer-transfer functions **LTF** used in this thesis is not the only analytical technique to determine the optimal conjugated heights of the DMs. Another such technique was proposed by Tokovinin et al. (2000). In figure 6.36 appears a comparison of these two models in terms of the optimal conjugated heights $h_{\text{opt,HL},\vartheta_0}$ for maximal isoplanatic angle $\vartheta_{0,\text{res}}$. For this

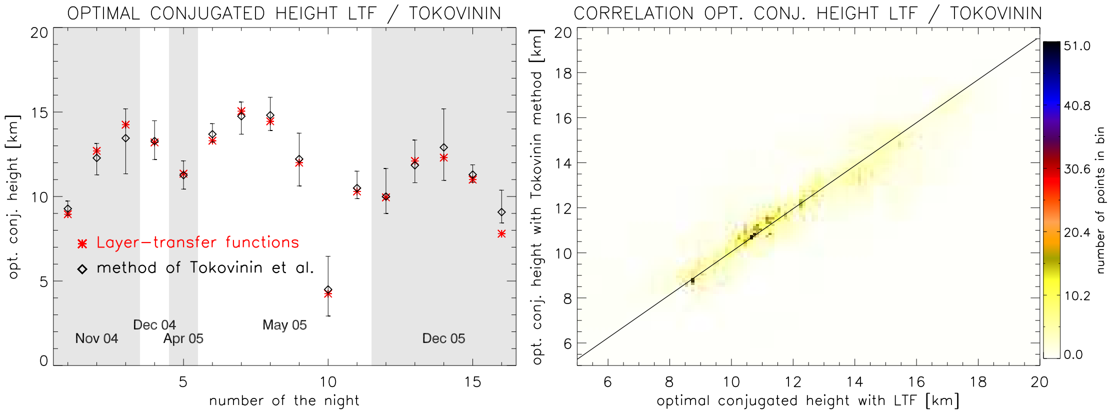

Figure 6.36: **Left:** The median optimal conjugated heights $h_{\mathrm{opt,HL},\vartheta_0}$ for the high-layer DM for maximum isoplanatic angle ϑ_0 with the method of Tokovinin et al. (2000) and with the layer-transfer functions as defined in chapter 3 for the individual nights. **Right:** The correlation in the optimal conjugated heights as determined with the two methods. Using all measured C_N^2-profiles, this yields a correlation of 92%.

comparison, $h_{\mathrm{conj,HL}}$ of the MCAO system can be freely adjusted, while $h_{\mathrm{conj,GL}}$ was fixed at 100 m, as above. As can be seen, the difference between the results obtained with the **LTF** and the algorithm of Tokovinin et al. (2000) is small: only for two nights is the difference larger than 1 km, for the other nights it is of the order of a few hundred meters. This is much smaller than the vertical resolution of the $C_N^2$2 profiles or the variation of $h_{\mathrm{opt,HL}}$ during the individual nights. Also plotted in figure 6.36 is the correlation of $h_{\mathrm{opt,HL}}$ between the two models, yielding a correlation of 92%. The results obtained with these two technique are therefore comparable. The determined values of $h_{\mathrm{opt,HL},\vartheta_0}$ in this chapter can be therefore readily compared with those obtained at other sites (Masciadri and Egner, 2004; Fuensalida et al., 2004a), for which the algorithm by Tokovinin et al. (2000) was used. The model using the **LTF** has the advantage that $h_{\mathrm{opt,HL}}$ can be determined for different criteria, like optimal Strehl-ratio on-axis, optimal isoplanatic angle $\vartheta_{0,\mathrm{res}}$ or isopistonic angle $\vartheta_{P,\mathrm{res}}$. For reasons of consistency, in this thesis only the **LTF** method is used.

OPTIMAL HEIGHTS FOR ISOPISTONIC ANGLE

For the operation of a Fizeau interferometer like LINC-NIRVANA with active fringe-tracking, it is important to know the isopistonic angle ϑ_P. The calculation of the optimal conjugation height of the HL-DM $h_{\mathrm{opt,HL},\vartheta_P}$ for maximum $\vartheta_{P,\mathrm{res}}$ for MCAO correction was done in a similar way to the isoplanatic angle. Figure 6.37 shows the median $\langle h_{\mathrm{opt,HL},\vartheta_P}\rangle$ for the individual nights, and figure 6.35 the achievable $\vartheta_{P,\mathrm{res}}$, when setting $h_{\mathrm{conj,HL}}$ to the just determined $h_{\mathrm{opt,HL},\vartheta_P}$ of each C_N^2-profile. This is an increase by a factor ≈2, as compared to figure 6.24 without MCAO correction.

Fixing $h_{\mathrm{conj,HL}}$ to $\langle h_{\mathrm{opt,HL},\vartheta_P}\rangle$ during each night results in an average decrease of ϑ_P of ≈4%, while fixing $h_{\mathrm{conj,HL}}$ to the median $\langle h_{\mathrm{opt,HL},\vartheta_P}\rangle$ of all C_N^2-profiles, decreases ϑ_P by ≈10%.

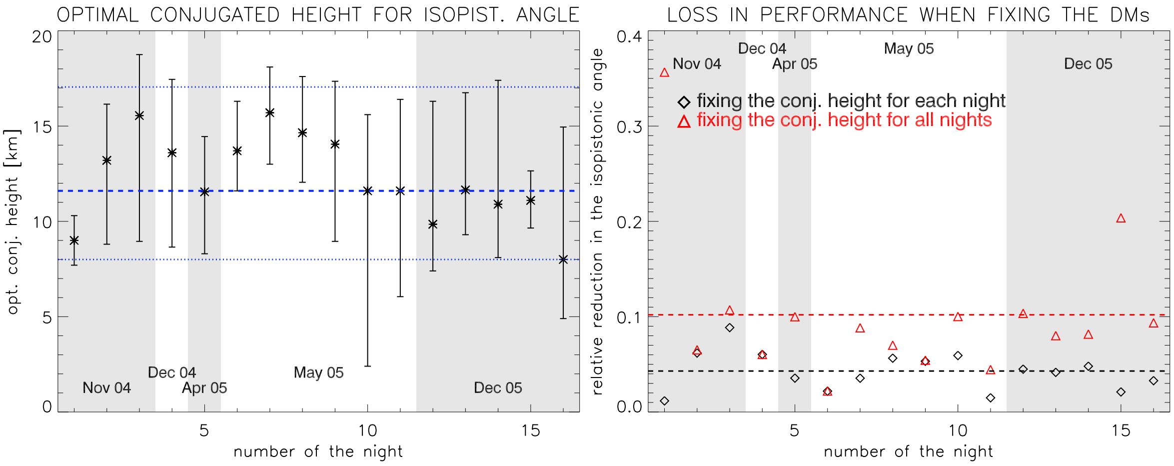

FIGURE 6.37: **Left:** The optimal conjugated heights $h_{\text{opt,HL},\vartheta_P}$ of the high-layer DM for maximum isopistonic angle $\vartheta_{P,\text{res}}$ for the individual nights. The error bars indicate for each night the median range of mis-conjugation for a reduction in $\vartheta_{P,\text{res}}$ of less than 15%. The dashed line is the median of $h_{\text{opt,HL},\vartheta_P}$ for all C_N^2-profiles and the dotted lines are the first and third quartile of its distribution. **Right:** The relative loss in the isopistonic angle $\vartheta_{P,\text{res}}$ when fixing the conjugation height of the high-layer DM to the median optimal conjugation height $\langle h_{\text{opt,HL},\vartheta_P}\rangle$ of one night and for all C_N^2-profiles. The dashed lines indicate the median values for all C_N^2-profiles.

Optimization Criteria	**Opt. conj. height**	**Reduction when fixing**	
	HL-DM	**nightly**	**all data**
	km	**%**	**%**
Fried Parameter $r_{0,\text{res}}$	3.4	3	11
Isoplanatic Angle $\vartheta_{0,\text{res}}$	10.7	5	12
Isopistonic Angle $\vartheta_{P,\text{res}}$	11.7	4	10

TABLE 6.8: The median optimal conjugation heights of the High-Layer DM for different criteria. Also given is the relative reduction in performance when fixing the conjugation height of the DM to the median $\langle h_{\text{opt,HL},i}\rangle$ for the individual nights and for all C_N^2-profiles.

SUMMARY AND DISCUSSION

The median optimal conjugation heights of the HL-DM are given in table 6.8 for the different optimization criteria (best Strehl ratio, as given by the maximal residual Fried parameter $r_{0,\text{res}}$, isoplanatic angle $\vartheta_{0,\text{res}}$ and isopistonic angle $\vartheta_{P,\text{res}}$ for the MCAO corrected image). Fixing the DMs to their median optimal conjugation altitude $\langle h_{\text{opt,HL},j}\rangle$ of each night results in a decrease of only 3 to 5%. In contrast, fixing $h_{\text{conj,HL}}$ to the median of all nights, results in a much larger drop of ≈11%. Real-time adjustment of $h_{\text{conj,HL}}$ might be thus not necessary, but $h_{\text{conj,HL}}$ should probably be adapted to the turbulence profile of each night, independent of the optimization criteria.

The optimal conjugation height $h_{\text{opt,HL},i}$ is quite different for the three optimization criteria (tab. 6.8). The reduction in $r_{0,\text{res}}$, $\vartheta_{0,\text{res}}$ and $\vartheta_{P,\text{res}}$ when optimizing the

Optimization Criteria	**Reduction in performance for**		
	r_0 [%]	ϑ_0 [%]	ϑ_P [%]
Fried Parameter $r_{0,\mathrm{res}}$	—	12	14
Isoplanatic Angle $\vartheta_{0,\mathrm{res}}$	29	—	0.5
Isopistonic Angle $\vartheta_{P,\mathrm{res}}$	29	0.5	—

TABLE 6.9: The impact of optimizing the conjugation height $h_{\mathrm{conj,HL}}$ of the HL-DM for one criteria on the performance as measured with the others. For example, when optimizing $h_{\mathrm{conj,HL}}$ for maximum isoplanatic angle, the median relative reduction for all C_N^2-profiles in the residual Fried parameter $r_{0,\mathrm{res}}$ is 29%.

performance for a different criterion is therefore important. As shown in table 6.9, $r_{0,\mathrm{res}}$ is reduced by 30% when setting $h_{\mathrm{conj,HL}}$ to $h_{\mathrm{opt,HL},\vartheta_0}$, which means for the parameters used here, a drop in the Strehl ratio from ≈40% to ≈20%. Depending on the specific science-case, a trade-off has thus to be made. Using the measured C_N^2-profiles, the shape of the PSF in the field could then be determined with the methods proposed by Veran et al. (1997); Weiss et al. (2002a).

6.8.2 LOOP-FREQUENCY AND NUMBER OF MODES

For the operation of the MCAO system of LINC-NIRVANA, it is not only important to know the optimal conjugation height h_{opt} of the DMs, but also the optimal number of corrected modes $N_{\mathrm{modes,opt}}$ and the frequency $f_{\mathrm{loop,opt}}$ of the control loop.

Calculating the wavefront coherence time in single layers (as in sect. 6.6.3) is too general for the determination of the required loop-frequency for the DMs of LINC-NIRVANA, because this method takes all the turbulence in a certain atmospheric volume into account. It thus depends critically on the thickness of this volume, which is chosen arbitrarily. In order to calculate a meaningful value for the required loop-frequency for the DMs, we use the layer-filter functions $\mathbf{LFF}(\Delta h)$ as defined in chapter 3. With these functions, the fraction of the total turbulence which is seen by a LO-WFS and which could thus be corrected by the DM, can be calculated for a given C_N^2-profile. For each WFS / DM combination of the system, a specific Greenwood frequency f_G^* is defined, which considers only the measurable fraction of the turbulence:

$$f_G^* = \left[0.102 \left(\frac{2\pi}{\lambda}\right)^2 \int C_N^2(h) \cdot \mathbf{LFF}(|h - h_{\mathrm{DM}}|) \cdot v^{5/3}\, dh\right]^{3/5} . \tag{6.17}$$

The temporal error $\sigma_{\mathrm{temp}}^{2*}$ of the correctable turbulence can be calculated analogous to equation 2.54, but using f_G^* instead of f_G:

$$\sigma_{\mathrm{temp}}^{2*} = \kappa_{\mathrm{loop}} \left(\frac{f_G^*}{f_{\mathrm{loop}}}\right)^{5/3} . \tag{6.18}$$

The fraction of the turbulence which cannot be measured with a LO-WFS does not introduce a temporal error, but rather adds σ_{nm}^2, which depends on the FoV and N_{modes}, to the total residual error σ_{res}^2, as defined in equation 2.52.

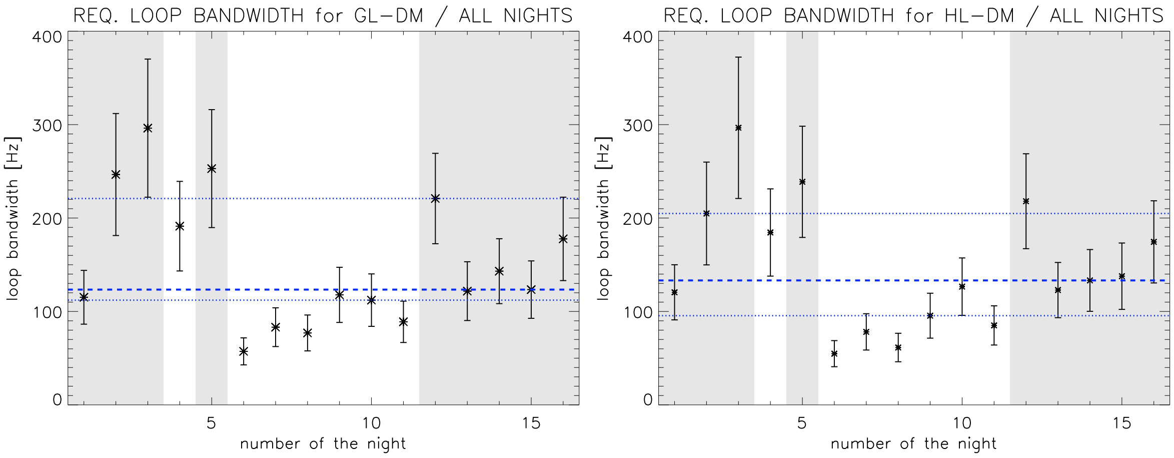

FIGURE 6.38: The optimal control bandwidth in K-band for the ground-layer (**left**) and high-layer (**right**) control loop of a MCAO system for all nights. The error bars indicate the standard deviation during the individual night, the dashed line the median for all C_N^2-profiles and the dotted lines the first and third quartiles of its distribution.

For all measured C_N^2-profiles, f_G^* was calculated for the GL-DM and HL-DM, which were conjugated to $h_{\text{conj,GL}} = 100\,\text{m}$ and $h_{\text{opt,HL},r_0}$, as determined in the previous section. Assuming a moderate $\kappa_{\text{loop}} = 0.5$, and $\sigma^{2*}_{\text{temp}} = 0.3\,\text{rad}^2$ as an acceptable value for the temporal error, the required loop frequencies $f_{\text{loop,opt,GL}}$ and $f_{\text{loop,opt,HL}}$ can be calculated with equation 6.18. The chosen value for $\sigma^{2*}_{\text{temp}}$ corresponds to a moderate Strehl ratio of ≈40% in K-band, with similar values for σ^2_{fit} and σ^2_{rec} (eqn. 2.52).

REQUIRED LOOP FREQUENCY

The median of the optimal loop frequencies $f_{\text{loop,opt,HL}}$ and $f_{\text{loop,opt,GL}}$ for all the nights is plotted in figure 6.38. These frequencies vary between 70 and 300 Hz, but are always very similar for the two control loops. This fact is also apparent in the almost equal wavefront coherence times τ_0 of the ground-layer turbulence (which is corrected by the ground-layer DM) and the free atmosphere (which is corrected by the high-layer DM) as shown in figure 6.21. Furthermore, the HL-DM has a narrower FoV and can thus correct turbulence in a larger vertical range. The optimal loop frequency shows for both DMs a variation by a factor 3, with lower values in summer than in winter.

OPTIMAL NUMBER OF MODES

As explained in section 2.4.3, the parameters of an AO system are usually tuned to achieve similar values for the three main error sources ($\sigma^2_{\text{fitting}}$, σ^2_{temp} and σ^2_{rec}). Setting $\sigma^2_{\text{fitting}}$ (eqn. 2.53) equal to $\sigma^{2*}_{\text{temp}}$ (eqn. 6.18), allows us to determine the optimal number of reconstructed modes $N_{\text{modes,opt}}$ for a given loop frequency f_{loop}:

$$\sum_{i=1}^{N_{\text{modes,opt,j}}} \mathbf{C}_{\Phi,i,i} \cdot \left(\frac{D_{\text{tel}}}{r_0^*}\right)^{5/3} = \kappa_{\text{loop}} \left(\frac{f_G^*}{f_{\text{loop}}}\right)^{5/3}, \tag{6.19}$$

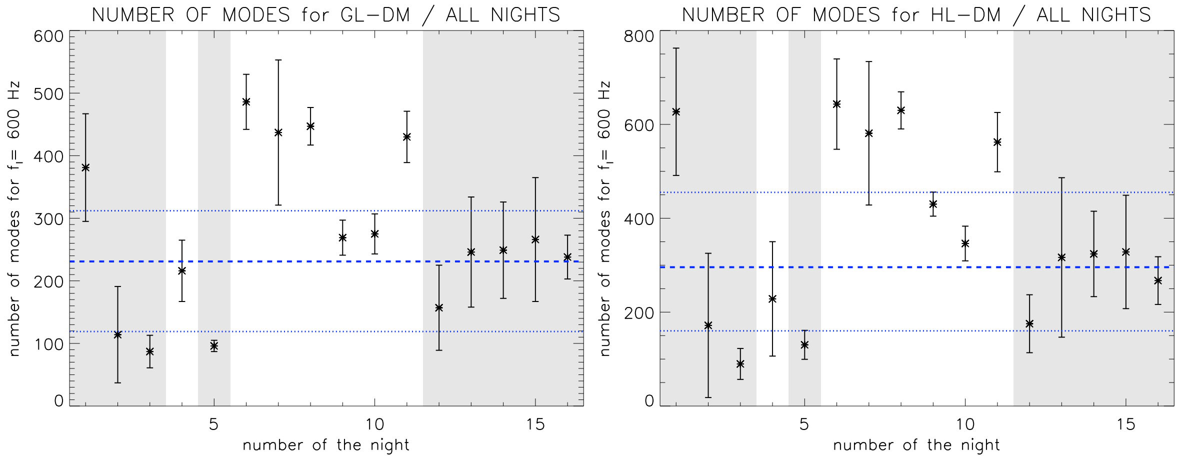

FIGURE 6.39: The optimal number of modes for the ground-layer (**left**) and the high-layer (**right**) control-loop for a loop-frequency of 600 Hz and for all nights.

with r_0^* denoting the Fried-parameter of the turbulence seen by the LO-WFS. For the following calculations, $h_{\mathrm{conj,GL}}$ was fixed at 100 m, while the HL-DM was placed at its conjugation altitude $h_{\mathrm{opt,HL},r_0}$ for maximal Strehl-ratio on-axis. The value of f_G^* was determined with equation 6.17 and r_0^* was calculated from the difference between the measured and the filtered C_N^2-profiles (chapter 3) for the K-band.

For the HL-DM, we have to consider that the footprint of the metapupil can be much larger than the footprint of the pupil of a single star (fig. 2.16). In order to correct the full metapupil on the HL-DM up to the same spatial frequencies, more modes than $N_{\mathrm{modes,opt,HL}}$ have to be reconstructed, because $N_{\mathrm{modes,opt,HL}}$ represents the number of modes which have be corrected within the pupil footprint of each star. Since the radial order j_n of the Zernike mode n is a good measure for the maximum corrected spatial frequencies, the required number $N_{\mathrm{modes,opt,full,HL}}$ to correct the full metapupil can be found by scaling $j_{\mathrm{N_{opt}}}$ with the diameter D_{mp} of the metapupil:

$$j_{\mathrm{N_{modes,opt,full,HL}}} = j_{\mathrm{N_{modes,opt,HL}}} \cdot \frac{D_{\mathrm{mp}}}{D_{\mathrm{tel}}} = j_{\mathrm{N_{modes,opt,HL}}} \cdot \frac{D_{\mathrm{tel}} + h_{\mathrm{conj,HL}} \cdot \mathrm{FoV}}{D_{\mathrm{tel}}}\,, \tag{6.20}$$

where $h_{\mathrm{conj,HL}}$ was set to $h_{\mathrm{opt,HL},r_0}$. The radial order $j_{\mathrm{N_{modes,opt,HL}}}$ can be determined from $N_{\mathrm{opt,HL}}$ via equation 2.32 and finally $N_{\mathrm{opt,full,HL}}$ from the inverse of equation 2.32 with $j_{\mathrm{N_{modes,opt,full,HL}}}$.

The median values of $N_{\mathrm{modes,opt,full,HL}}$ and $N_{\mathrm{modes,opt,GL}}$ for f_{loop} =600 Hz are shown in figure 6.39 for the individual nights. Again, the numbers are very similar for the two DMs. Even though the turbulence in the high-layer is much weaker than at the ground (sect. 6.5.1), the HL-WFS has a narrower FoV and thus sees turbulence in a larger vertical range than the GL-WFS. The footprint of the FoV on the HL-DM is furthermore larger than on the GL-DM, altogether requiring more modes for the HL-DM to achieve the same correction. The median optimal number of modes as a function of the loop-frequency is shown in figure 6.40. For the same reasons, the required number of modes to fullfill $\sigma^2_{\mathrm{fitting}} \approx \sigma^2_{\mathrm{temp}}$ grows much faster for the HL-DM than for the GL-DM, especially for higher f_{loop}.

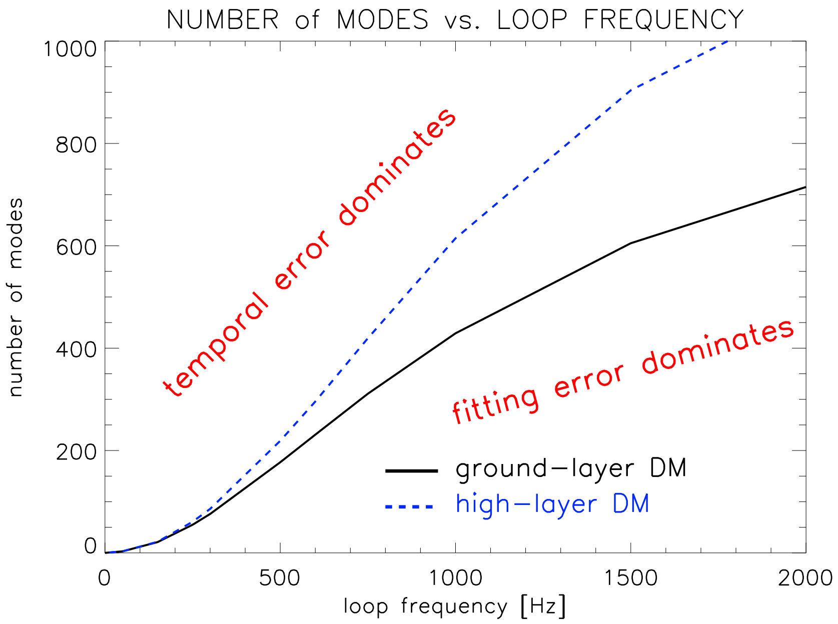

FIGURE 6.40: The mean required number of corrected modes as a function of the loop frequency. In the region above the curve, the temporal error dominates. This means that the performance cannot be improved by correcting more modes. In contrast, the fitting error dominates in the region below the curve. Here, the performance cannot be increased by increasing the loop frequency, but it is rather limited by the number of corrected modes. The lines represent the case that both errors have equal size.

6.9 CONCLUSION & OUTLOOK

In this chapter, we presented the results of a site-characterization campaign with a Generalized SCIDAR at Mt. Graham covering 16 nights distributed over one year.

6.9.1 SITE-CHARACTERIZATION

The retrieved, dome-seeing corrected, astro-climatic parameters (seeing ϵ =0.67”, isoplanatic angle ϑ_0 =2.7” and wavefront coherence time τ_0 =3.6 msec, all for λ =0.5 μm) are comparable with other excellent astronomical sites. The isopistonic angle was found to be 8.3” in the visible, for an outer scale of L_0 =25 m and the parameters of the LBT.

At Mt. Graham, most of the turbulence is concentrated near the ground: 77% is below 2 km above the telescope. The C_N^2-profile is thus always dominated by the ground-layer, with weaker layers at ≈2 - 3 km and 4 - 5 km above the telescope. The turbulent layer associated with the jet-stream exhibits a significant seasonal change in altitude, it is located between 6 and 12 km in winter, but between 11 and 17 km in summer, very similar to San Pedro Martir.

Also most of the astro-climatic parameters show a seasonal trend. For astronomical observations they are more favorable in summer: in the data we have so far, it seems that ϵ_0, ϑ_0 and ϑ_P are between 10 and 40% better in summer than in winter. For τ_0 of the total atmosphere, no clear seasonal trend is apparent. The observed seasonal trend is currently based on only one run for summer and thus might not reflect a true seasonal variation. Also the correlation times of the astro-climatic parameters have been determined. For these, we find values on the order of only a few minutes, shorter than at other sites.

Similar to other sites, we found no correlation between the turbulence in the ground-layer (up to 1 km above the telescope) and in the free atmosphere (above 1 km).

6.9.2 HIGH-VERTICAL RESOLUTION SCIDAR

We presented a new method to determine the C_N^2-profile in the first 2 km above the telescope with a vertical resolution of ≈25 m, an improvement by a factor of ≈40 compared to conventional SCIDAR. First results of this high-vertical resolution technique (HVR-GS) obtained with the SCIDAR instrument at the VATT on Mt. Graham are shown. The observed turbulent layers are rather thin (< 25 meters), with a weak layer just above the dome of the VATT and the strongest layer being located at ≈50 m above the VATT. Assuming that the turbulence profile at the LBT is the same as that measured at the VATT, this translates into an improvement of the seeing by 0.08” above the primary mirror of the LBT. Furthermore, the observed internal structure of the ground-layer turbulence underlines the sensitivity of the achievable image quality on the actual position of the telescope on a mountain: 50 m difference in height can have a large impact.

6.9.3 IMPACT ON LINC-NIRVANA

With the help of the layer-filter functions defined in chapter 3, the impact of the measured C_N^2-profiles on the MCAO system of the LINC-NIRVANA instrument was studied. In particular, the optimal conjugation heights h_{opt} of the Deformable Mirrors were calculated for various optimization criteria.

The optimal conjugation altitude of the high-layer DM for maximal Strehl ratio on-axis shows significant variations night by night and also a clear seasonal trend. It is ≈2 km in summer, and ≈8 km in winter. The range of mis-conjugation for the high-layer DM for a degradation of 15% in performance in terms of residual Fried Parameter is a few kilometers, with significantly higher values in winter. Due to the low vertical resolution of the measured C_N^2-profiles, h_{opt} of the Ground-Layer DM for maximal Strehl ratio cannot be determined very precisely, and is estimated to be always ≈100 m above the ground, as also confirmed by the results of the HVR-GS technique.

To achieve a homogenous Strehl ratio in the field, and thus maximum isoplanatic angle ϑ_0, the high-layer DM should be conjugated to ≈11 km above the telescope in winter and ≈15 km in summer. The range of mis-conjugation for a 15% reduction in ϑ_0 is again a few kilometers, with higher values in winter than in summer. Since the values for both the isoplanatic angle ϑ_0 and the isopistonic angle ϑ_P are influenced by the turbulence in the high layers, the results obtained for ϑ_P are very similar to those for ϑ_0.

Fixing the conjugation height of the high-layer DM to the median optimal conjugation height for each night reduces the performance on average by ≈4%, with similar values for r_0, ϑ_0 and ϑ_P. Similarly, when fixing the conjugation height of the high-layer DM to the median optimal conjugation height for all data, reduces the achievable values of r_0, ϑ_0 and ϑ_P on average by ≈11%. A real-time adaptation of $h_{\text{conj,HL}}$ might thus not be necessary for LINC-NIRVANA, but $h_{\text{conj,HL}}$ probably has to be adapted to the vertical turbulence profile of each night.

The required frequencies $f_{\rm loop}$ of the MCAO control loops turned out to be similar for both DMs. There is a factor of 3 variation in $f_{\rm loop}$, with lower values in summer than in winter. To achieve a good correction, the high-layer DM has to correct significantly more modes than the ground-layer DM. Even though the turbulence in the high-layer is much weaker than at the ground, the much larger pupil footprint on the high-layer DM results in up to twice the number of reconstructed modes for this DM.

6.9.4 OUTLOOK

This thesis is only the first step in characterizing the atmospheric turbulence above Mt. Graham. With more data, also the following questions might be answered:

- Up to now we measured the C_N^2-profiles only during 16 nights. More data is required to obtain a statistically significant database, not only of the derived astro-climatic parameters, but also of the typical vertical structure of the turbulence above Mt. Graham and the impact on LINC-NIRVANA.
- Most of the retrieved results exhibit a distinct seasonal trend. Unfortunately, this is based on only one observing run in May and could thus be caused by peculiar weather conditions during these few nights. Furthermore, no data is available so far for spring.
- Depending on the wind direction, the air-flow over the mountain might be more or less turbulent. If the air is pressed upward a narrow gorge, more turbulence might evolve than in the case of laminar flow over the mountain. With more SCIDAR data and temporally better sampled, accompanying measurements of the wind speed and wind direction at the ground, such effects could be examined. Recently, a correlation between the wind speed and the C_N^2 in the ground-layer was reported (Athey et al., 2006), which might also be verified with such wind data.
- As suggested by Munoz-Tunon et al. (1997), optically active turbulence in the free atmosphere might be related to gravity waves. By combining C_N^2-profiles measured with a SCIDAR and the data from radio-soundings launched regularly from Tucson airport, such a connection could be studied in detail.
- For the high-vertical resolution technique (HVR-GS) only a very limited set of data is available up to now. With more observations, the typically inner structure of the ground-layer could be studied in more detail and the presence of a very strong turbulent layer very close to the ground could be verified.

> It's a thousand pages, give or take a few,
> I'll be writing more in a week or two.
> I can make it longer if you like the style,
> I can change it round but I want to be a paperback writer.
>
> *The Beatles, "Paperback writer"*

APPENDIX A

The C_N^2-Profiles

He'd buy a hundred pounds of yeast and some copper line,
everybody knew that he made moonshine

Steve Earle, "Copperhead Road"

In this appendix all the retrieved C_N^2-profiles from the measurements of the G-SCIDAR at the VATT on top of Mt. Graham are shown. Each plot shows the temporal evolution of the C_N^2-profile over the course of one night in color-coded logarithmic intensity. Blue color represents strong turbulence, red medium and yellow weak turbulence. The altitude is given above the top of Mt. Graham, which is ≈3200 m above sea-level.

Also included in the plots are the values of the astro-climatic parameters seeing ϵ_{FWHM}, the wavefront coherence time τ_0 and the isoplanatic angle ϑ_0 in the visible (λ =0.5 μm). The isopistonic angle ϑ_P is given for the parameters of the LBT, an outer scale of L_0 =25 m and at visible wavelengths. The G-SCIDAR delivers one measurement every 30 to 60 seconds, yielding a few hundred C_N^2-profiles for each night. More details about the parameters for the measurements can be found in table 6.1 and 6.2.

Also given in this appendix are the median C_N^2-profiles for each night, together with the first and third quartiles.

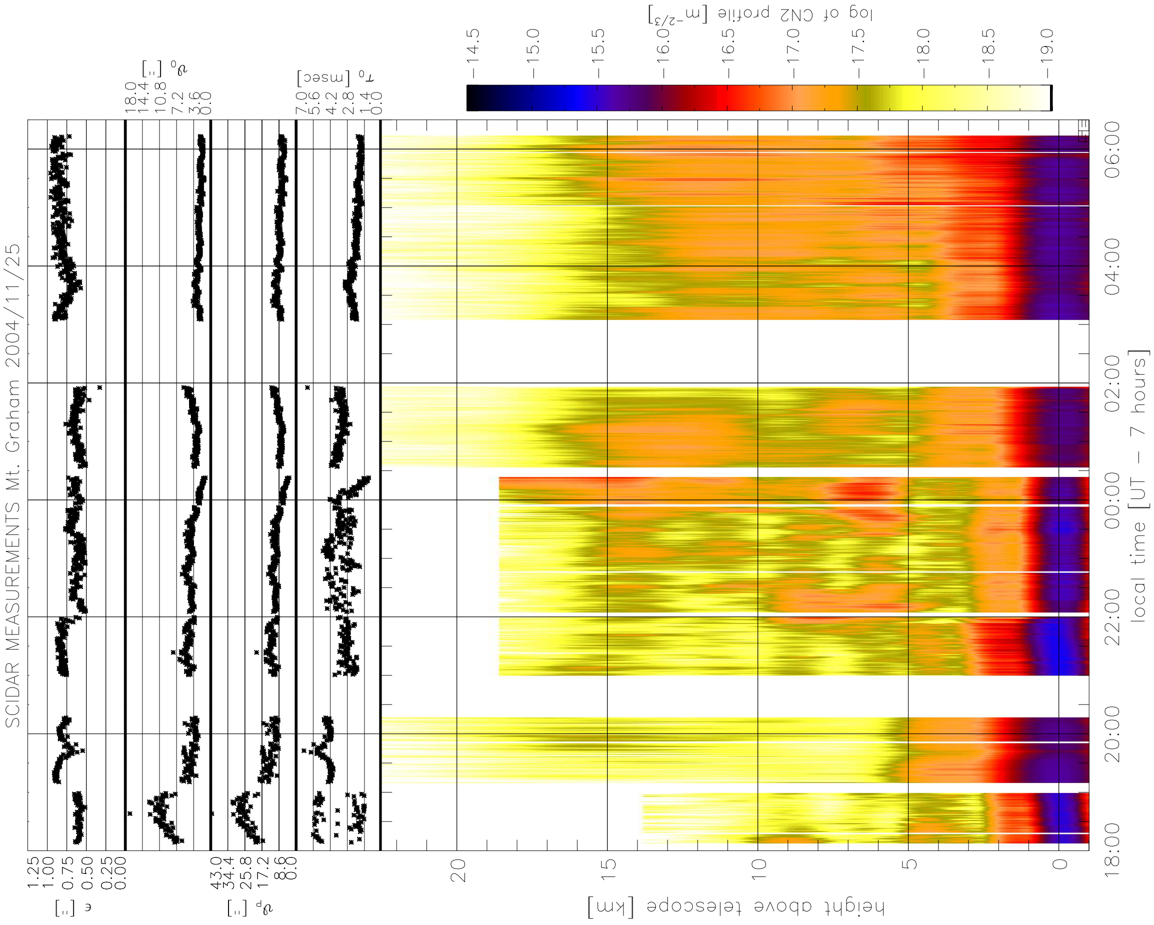
SCIDAR MEASUREMENTS Mt. Graham 2004/11/25
ε ["]
1.25
1.00
0.75
0.50
0.25
0.00
ϑ_p ["]
43.0
34.4
25.8
17.2
8.6
ϑ_0 ["]
18.0
14.4
10.8
7.2
3.6
0.0
τ_0 [msec]
7.0
5.6
4.2
2.8
1.4
0.0
height above telescope [km]
20
15
10
5
0
local time [UT − 7 hours]
18:00
20:00
22:00
00:00
02:00
04:00
06:00
log of CN2 profile [m^-2/3]
−14.5
−15.0
−15.5
−16.0
−16.5
−17.0
−17.5
−18.0
−18.5
−19.0

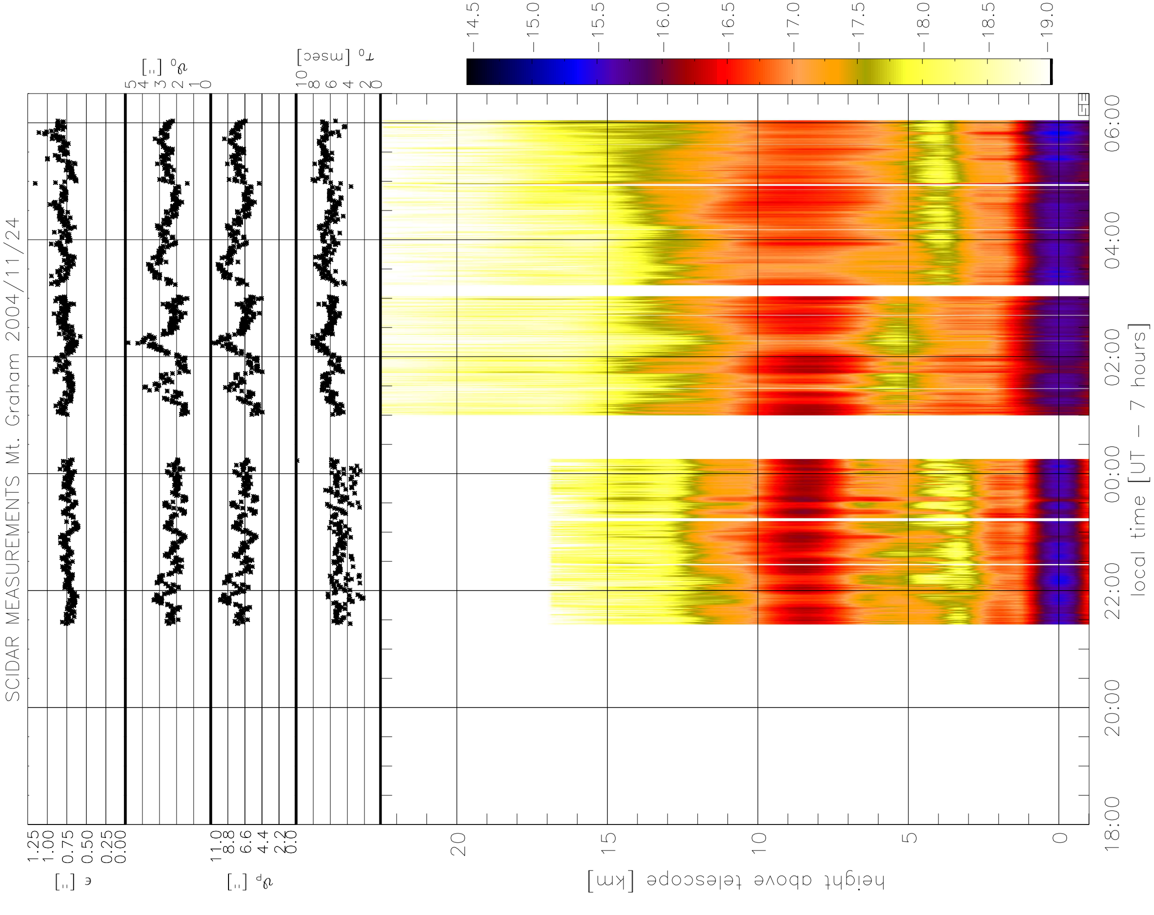
SCIDAR MEASUREMENTS Mt. Graham 2004/11/24
ε ["]
1.25
1.00
0.75
0.50
0.25
0.00
ϑ_p ["]
11.0
8.8
6.6
4.4
2.2
0.0
ϑ_0 ["]
5
4
3
2
1
0
τ_0 [msec]
10
8
6
4
2
0
height above telescope [km]
20
15
10
5
0
local time [UT − 7 hours]
18:00
20:00
22:00
00:00
02:00
04:00
06:00
log of CN2 profile [m^-2/3]
−14.5
−15.0
−15.5
−16.0
−16.5
−17.0
−17.5
−18.0
−18.5
−19.0

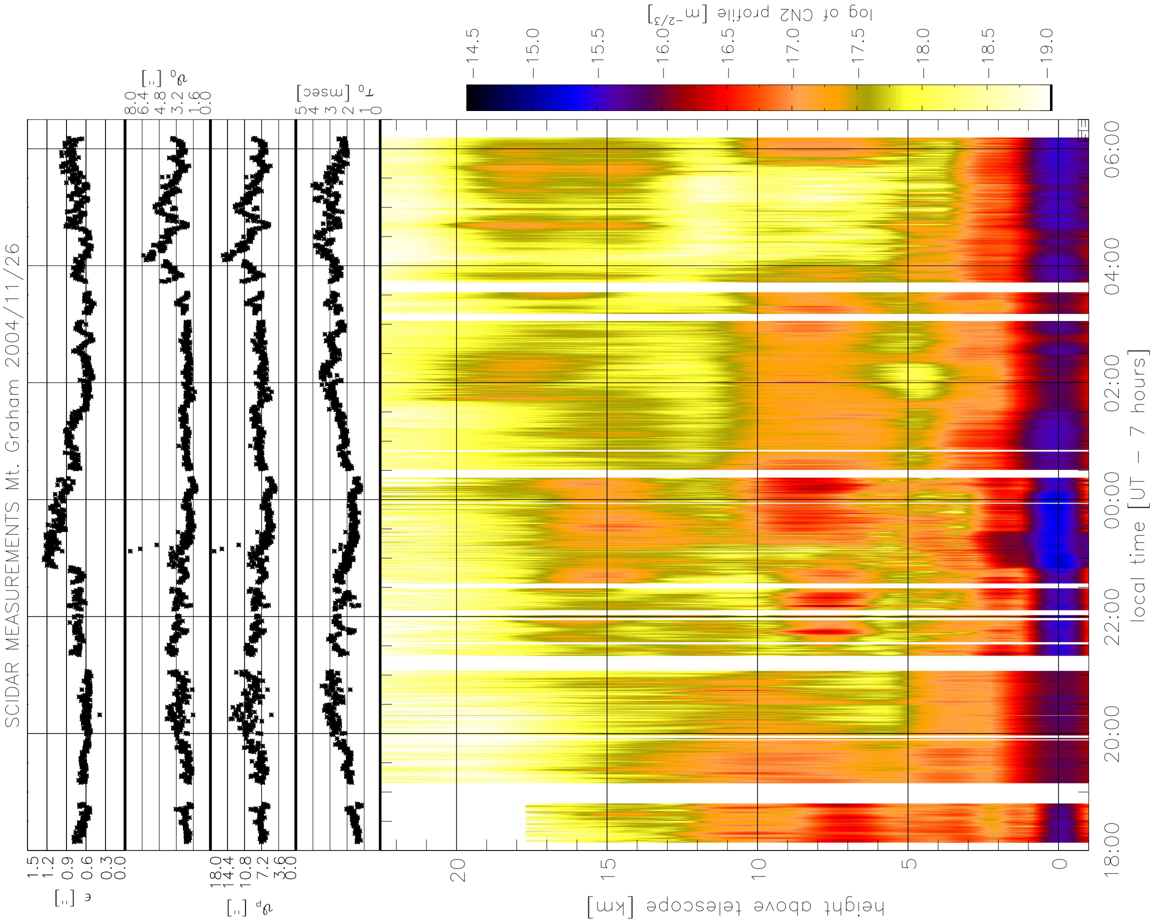
SCIDAR MEASUREMENTS Mt. Graham 2004/11/26
ε ["]
1.5
1.2
0.9
0.6
0.3
0.0
ϑ_p ["]
18.0
14.4
10.8
7.2
3.6
0.0
ϑ_0 ["]
8.0
6.4
4.8
3.2
1.6
0.0
τ_0 [msec]
5
4
3
2
1
0
height above telescope [km]
20
15
10
5
0
18:00
20:00
22:00
00:00
02:00
04:00
06:00
local time [UT − 7 hours]
log of CN2 profile [m^-2/3]
−14.5
−15.0
−15.5
−16.0
−16.5
−17.0
−17.5
−18.0
−18.5
−19.0

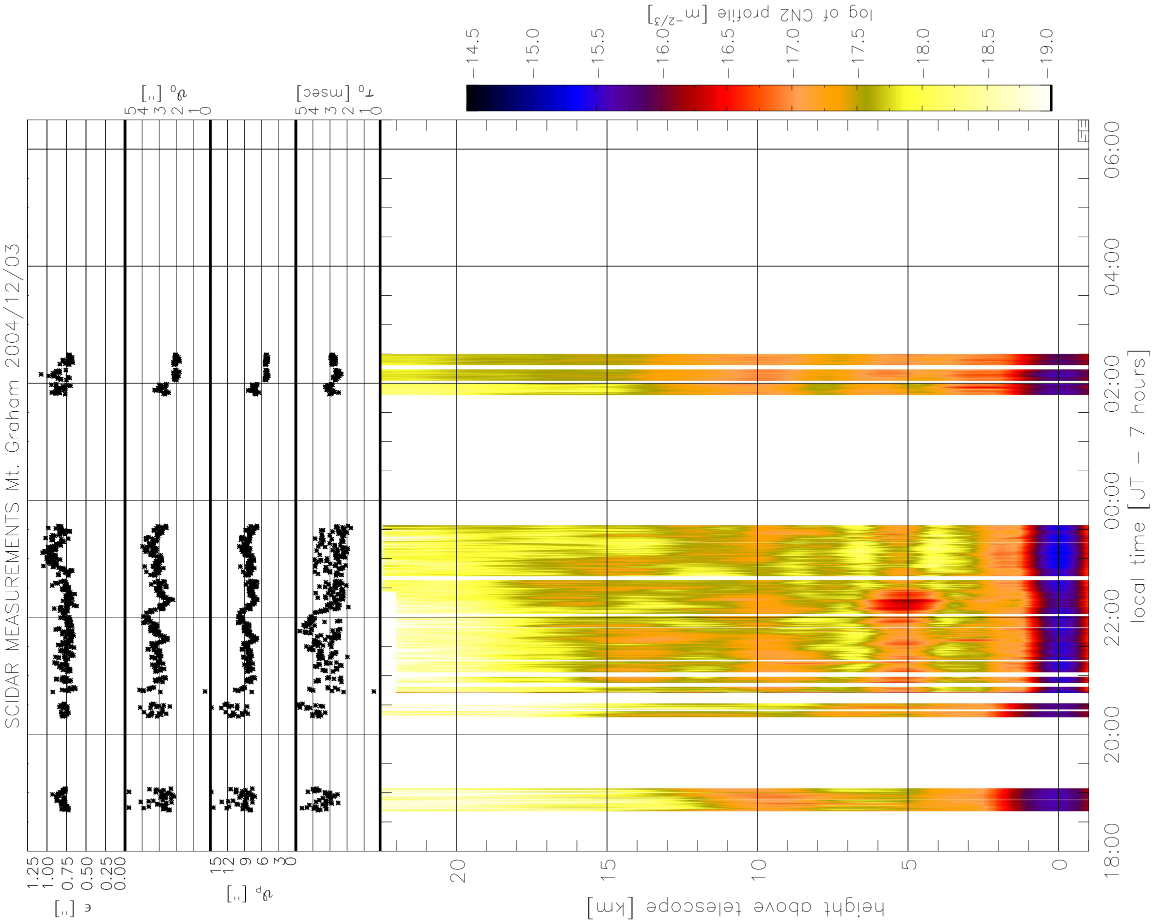
SCIDAR MEASUREMENTS Mt. Graham 2004/12/03
ε ["]
1.25
1.00
0.75
0.50
0.25
0.00
ϑ_p ["]
15
12
9
6
3
0
ϑ_0 ["]
5
4
3
2
1
0
τ_0 [msec]
5
4
3
2
1
0
height above telescope [km]
20
15
10
5
0
18:00
20:00
22:00
00:00
02:00
04:00
06:00
local time [UT − 7 hours]
log of CN2 profile [m^-2/3]
−14.5
−15.0
−15.5
−16.0
−16.5
−17.0
−17.5
−18.0
−18.5
−19.0

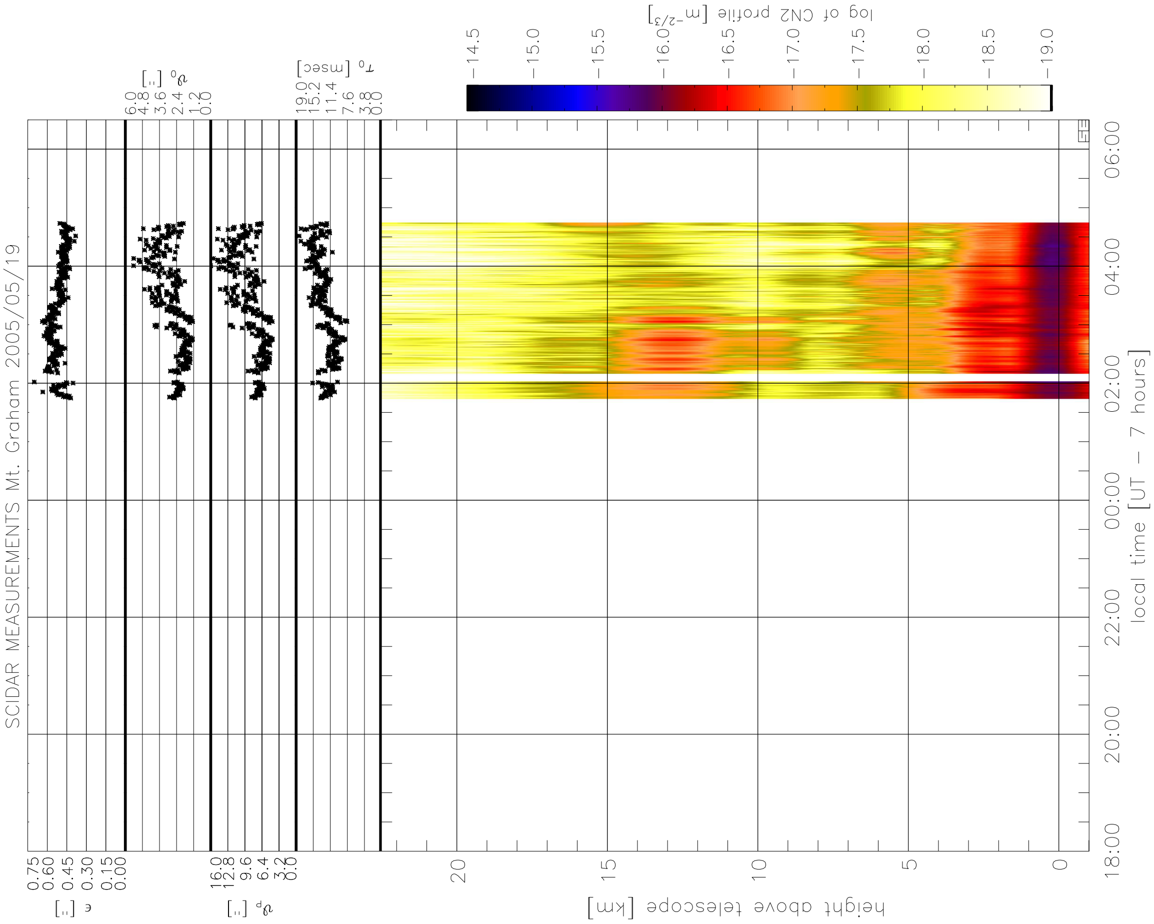
SCIDAR MEASUREMENTS Mt. Graham 2005/05/19
ε ["]
0.75 0.60 0.45 0.30 0.15 0.00
ϑ_0 ["]
6.0 4.8 3.6 2.4 1.2 0.0
ϑ_p ["]
16.0 12.8 9.6 6.4 3.2 0.0
τ_0 [msec]
19.0 15.2 11.4 7.6 3.8 0.0
height above telescope [km]
20 15 10 5 0
log of CN2 profile [$m^{-2/3}$]
−14.5 −15.0 −15.5 −16.0 −16.5 −17.0 −17.5 −18.0 −18.5 −19.0
18:00 20:00 22:00 00:00 02:00 04:00 06:00
local time [UT − 7 hours]

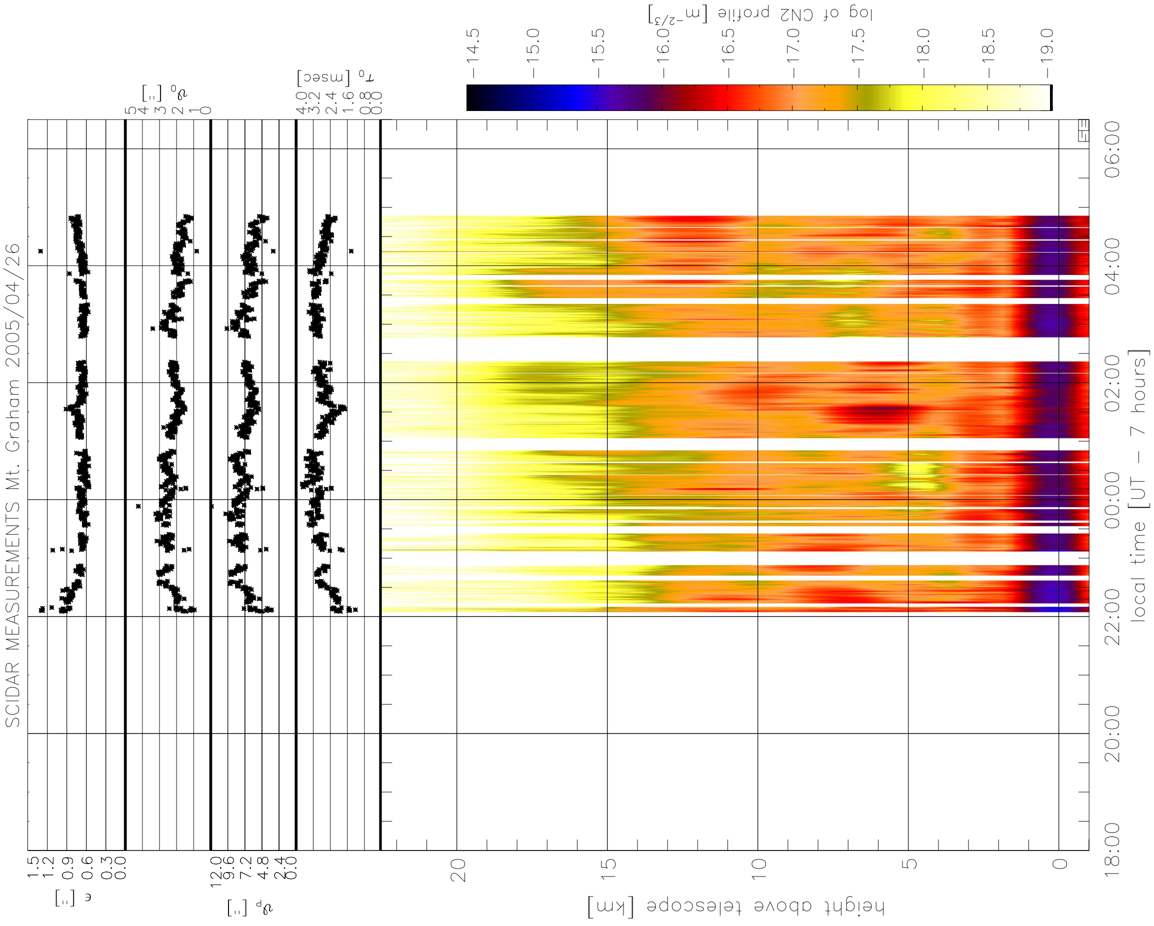
SCIDAR MEASUREMENTS Mt. Graham 2005/04/26
ε ["]
1.5 1.2 0.9 0.6 0.3 0.0
ϑ_0 ["]
5 4 3 2 1 0
ϑ_p ["]
12.0 9.6 7.2 4.8 2.4 0.0
τ_0 [msec]
4.0 3.2 2.4 1.6 0.8 0.0
height above telescope [km]
20 15 10 5 0
log of CN2 profile [$m^{-2/3}$]
−14.5 −15.0 −15.5 −16.0 −16.5 −17.0 −17.5 −18.0 −18.5 −19.0
18:00 20:00 22:00 00:00 02:00 04:00 06:00
local time [UT − 7 hours]

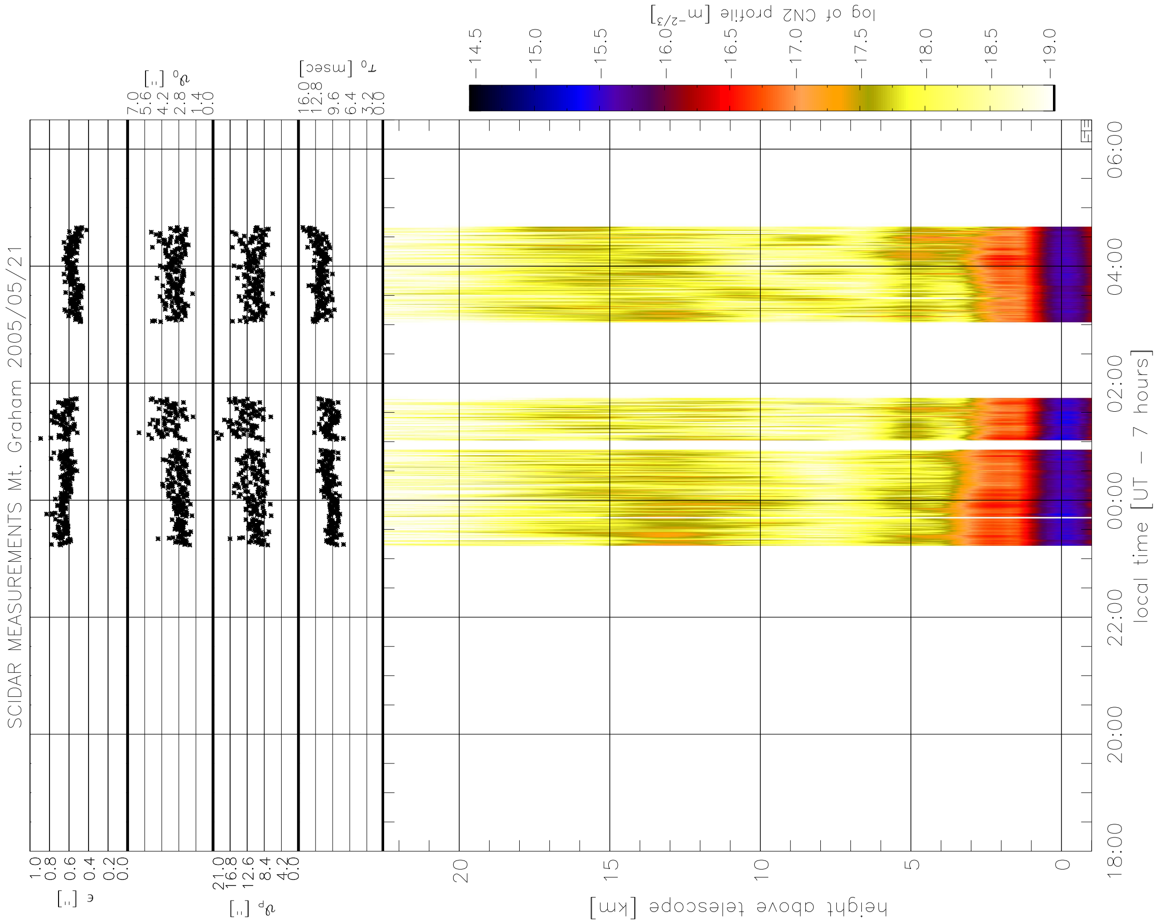
SCIDAR MEASUREMENTS Mt. Graham 2005/05/21
ε ["]
1.0
0.8
0.6
0.4
0.2
0.0
ϑ0 ["]
7.0
5.6
4.2
2.8
1.4
0.0
ϑp ["]
21.0
16.8
12.6
8.4
4.2
0.0
τ0 [msec]
16.0
12.8
9.6
6.4
3.2
0.0
height above telescope [km]
20
15
10
5
0
local time [UT − 7 hours]
18:00
20:00
22:00
00:00
02:00
04:00
06:00
log of CN2 profile [m^-2/3]
−14.5
−15.0
−15.5
−16.0
−16.5
−17.0
−17.5
−18.0
−18.5
−19.0

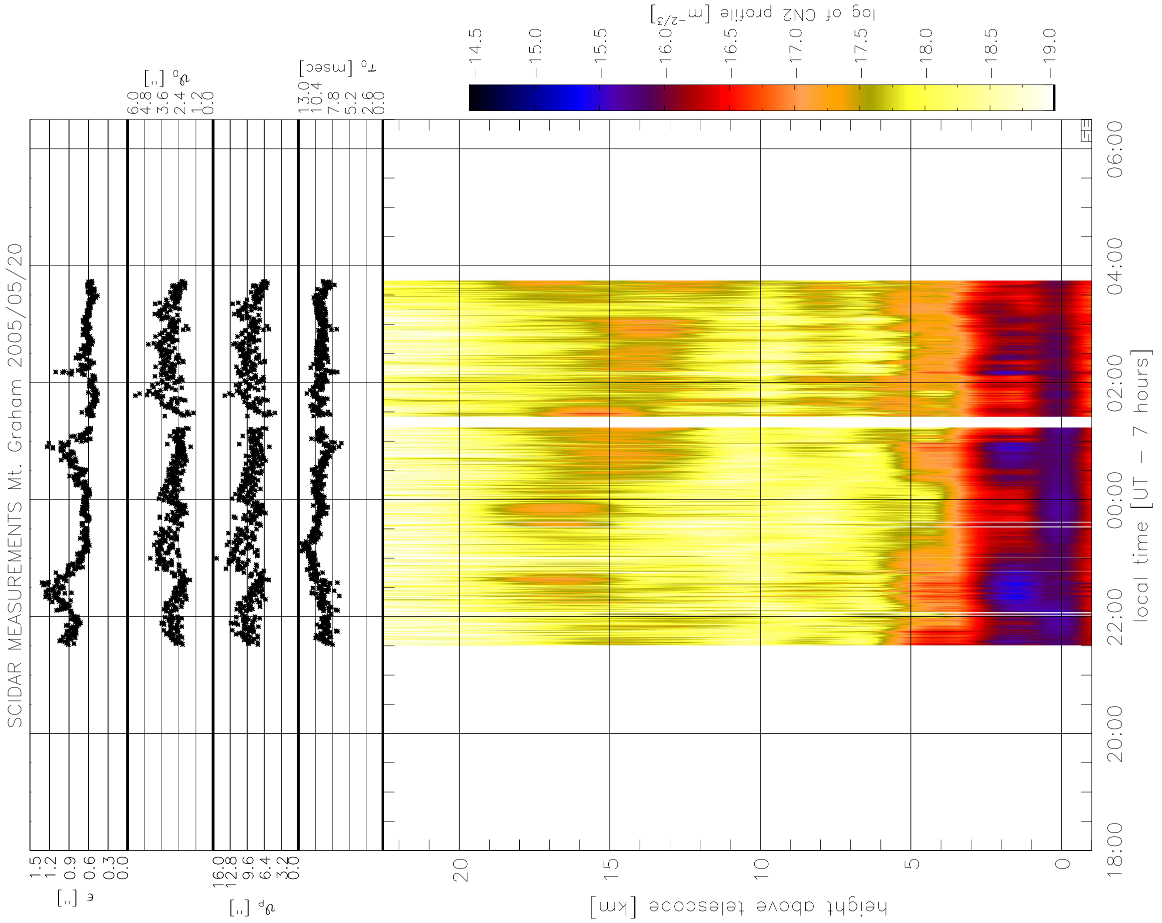
SCIDAR MEASUREMENTS Mt. Graham 2005/05/20
ε ["]
1.5
1.2
0.9
0.6
0.3
0.0
ϑ0 ["]
6.0
4.8
3.6
2.4
1.2
0.0
ϑp ["]
16.0
12.8
9.6
6.4
3.2
0.0
τ0 [msec]
13.0
10.4
7.8
5.2
2.6
0.0
height above telescope [km]
20
15
10
5
0
local time [UT − 7 hours]
18:00
20:00
22:00
00:00
02:00
04:00
06:00
log of CN2 profile [m^-2/3]
−14.5
−15.0
−15.5
−16.0
−16.5
−17.0
−17.5
−18.0
−18.5
−19.0

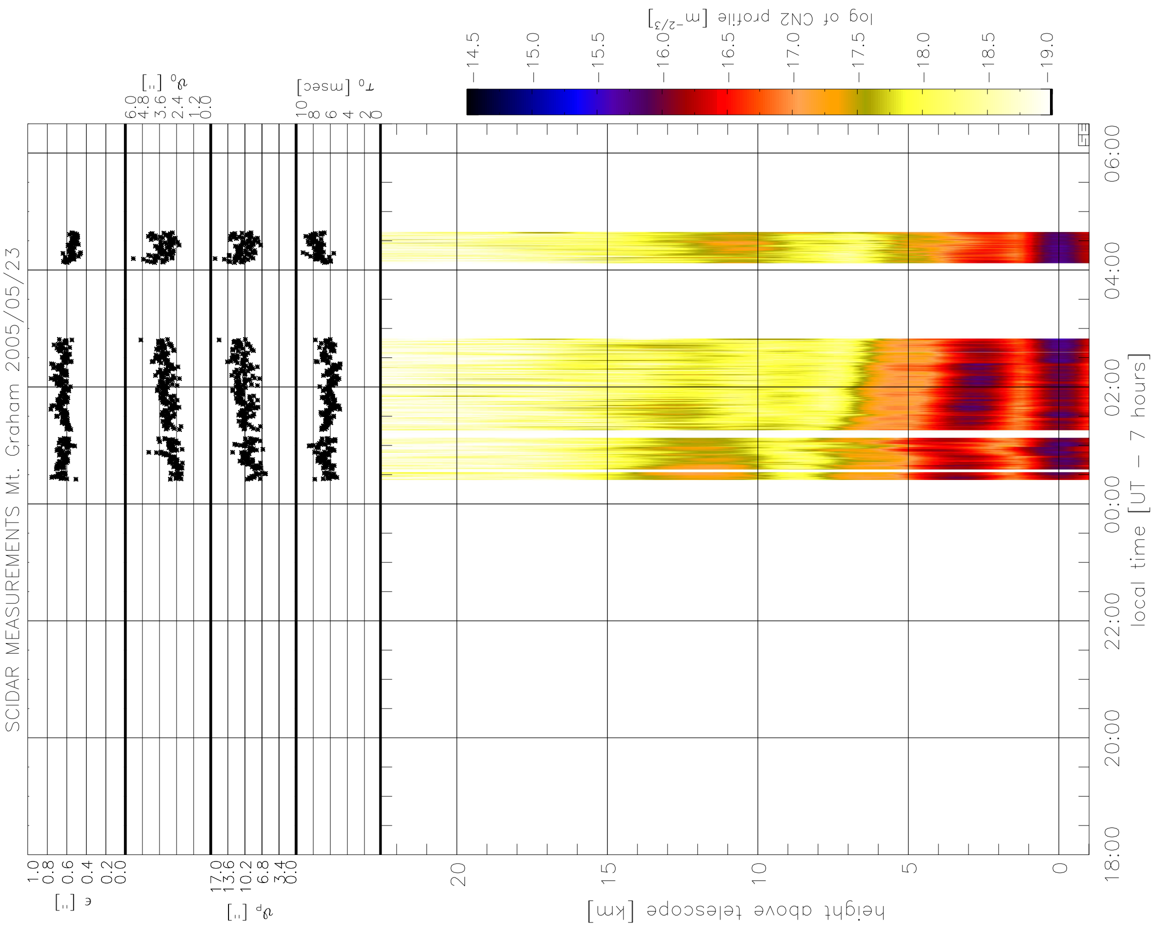
SCIDAR MEASUREMENTS Mt. Graham 2005/05/23
ε ["]
1.0 0.8 0.6 0.4 0.2 0.0
ϑ₀ ["]
6.0 4.8 3.6 2.4 1.2 0.0
ϑₚ ["]
17.0 13.6 10.2 6.8 3.4 0.0
τ₀ [msec]
10 8 6 4 2 0
height above telescope [km]
20 15 10 5 0
local time [UT − 7 hours]
18:00 20:00 22:00 00:00 02:00 04:00 06:00
log of CN2 profile [m^-2/3]
−14.5 −15.0 −15.5 −16.0 −16.5 −17.0 −17.5 −18.0 −18.5 −19.0

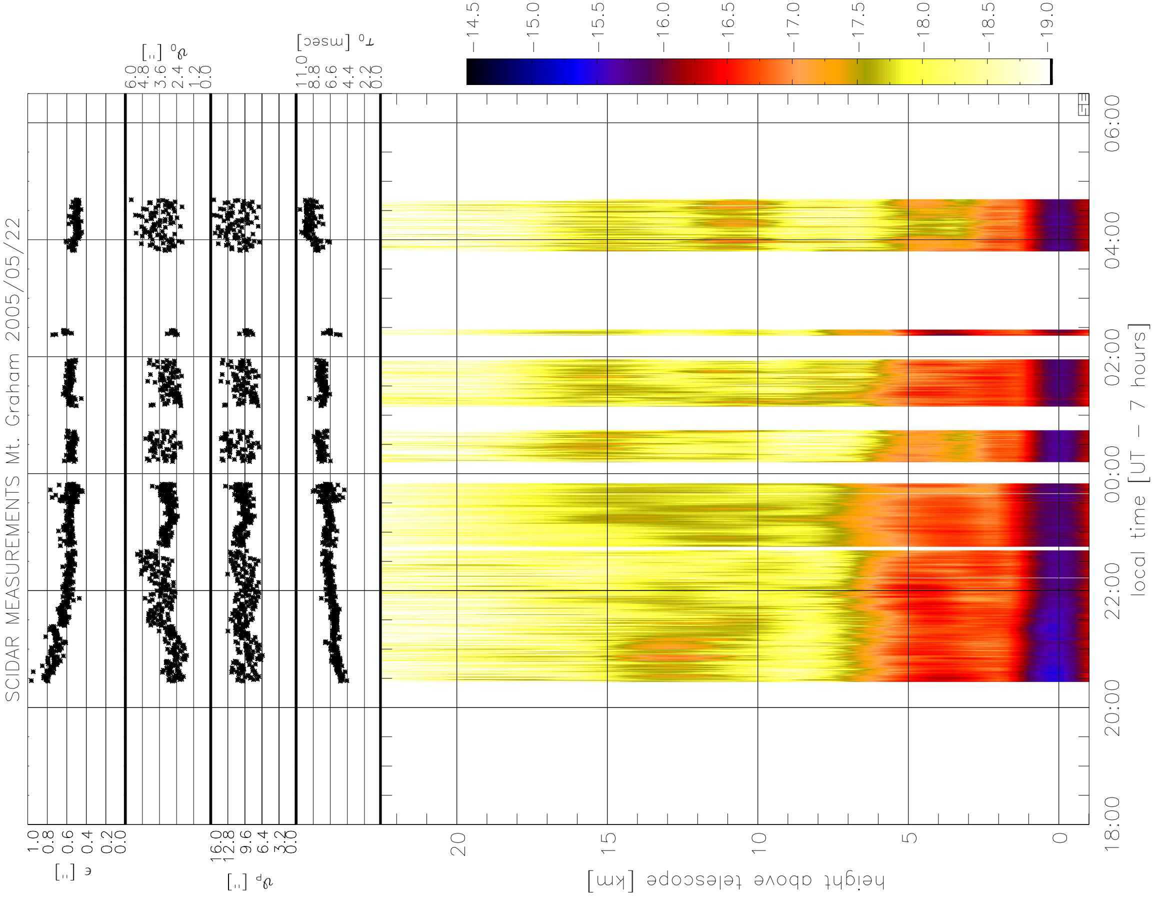
SCIDAR MEASUREMENTS Mt. Graham 2005/05/22
ε ["]
1.0 0.8 0.6 0.4 0.2 0.0
ϑ₀ ["]
6.0 4.8 3.6 2.4 1.2 0.0
ϑₚ ["]
16.0 12.8 9.6 6.4 3.2 0.0
τ₀ [msec]
11.0 8.8 6.6 4.4 2.2 0.0
height above telescope [km]
20 15 10 5 0
local time [UT − 7 hours]
18:00 20:00 22:00 00:00 02:00 04:00 06:00
log of CN2 profile [m^-2/3]
−14.5 −15.0 −15.5 −16.0 −16.5 −17.0 −17.5 −18.0 −18.5 −19.0

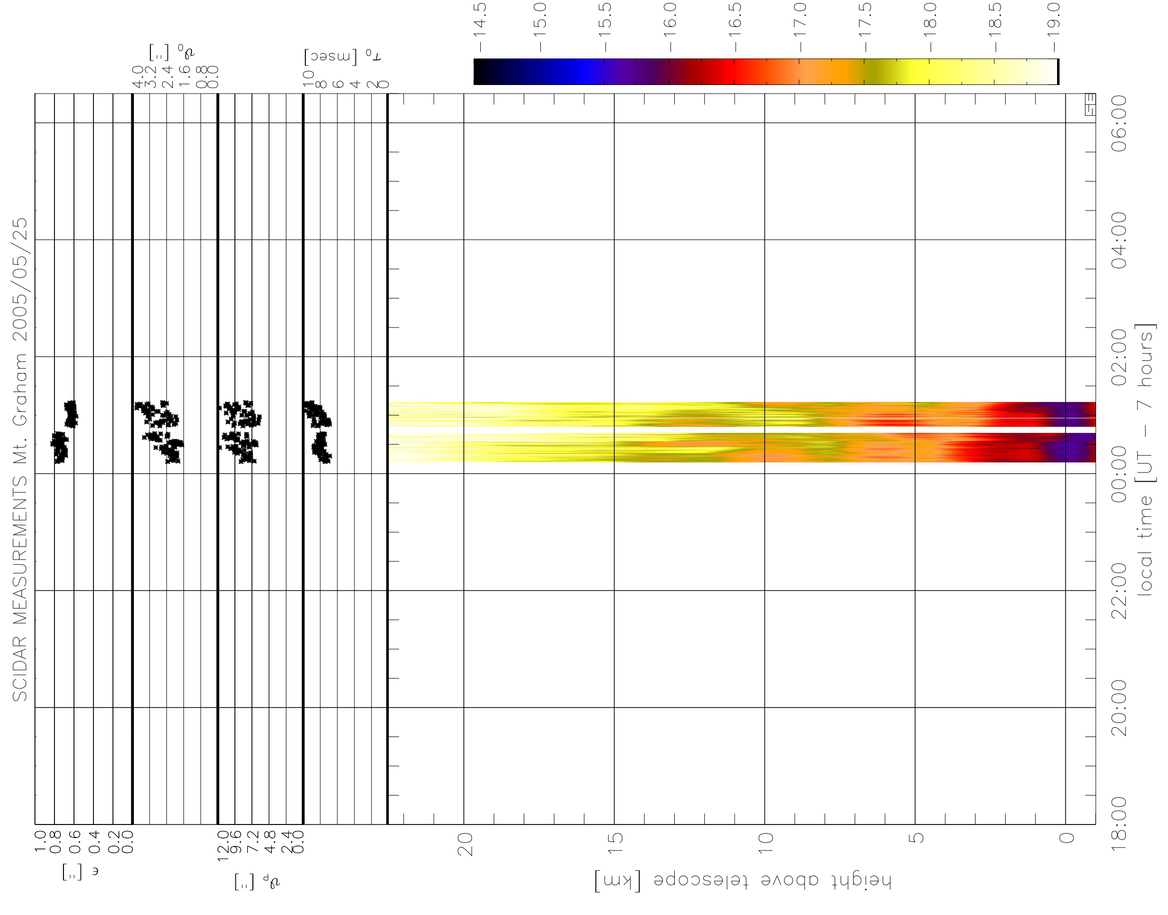
SCIDAR MEASUREMENTS Mt. Graham 2005/05/25
ε ["]
1.0
0.8
0.6
0.4
0.2
0.0
ϑ₀ ["]
4.0
3.2
2.4
1.6
0.8
0.0
ϑₚ ["]
12.0
9.6
7.2
4.8
2.4
0.0
τ₀ [msec]
10
8
6
4
2
0
height above telescope [km]
20
15
10
5
0
log of CN2 profile [m^-2/3]
−14.5
−15.0
−15.5
−16.0
−16.5
−17.0
−17.5
−18.0
−18.5
−19.0
18:00
20:00
22:00
00:00
02:00
04:00
06:00
local time [UT − 7 hours]

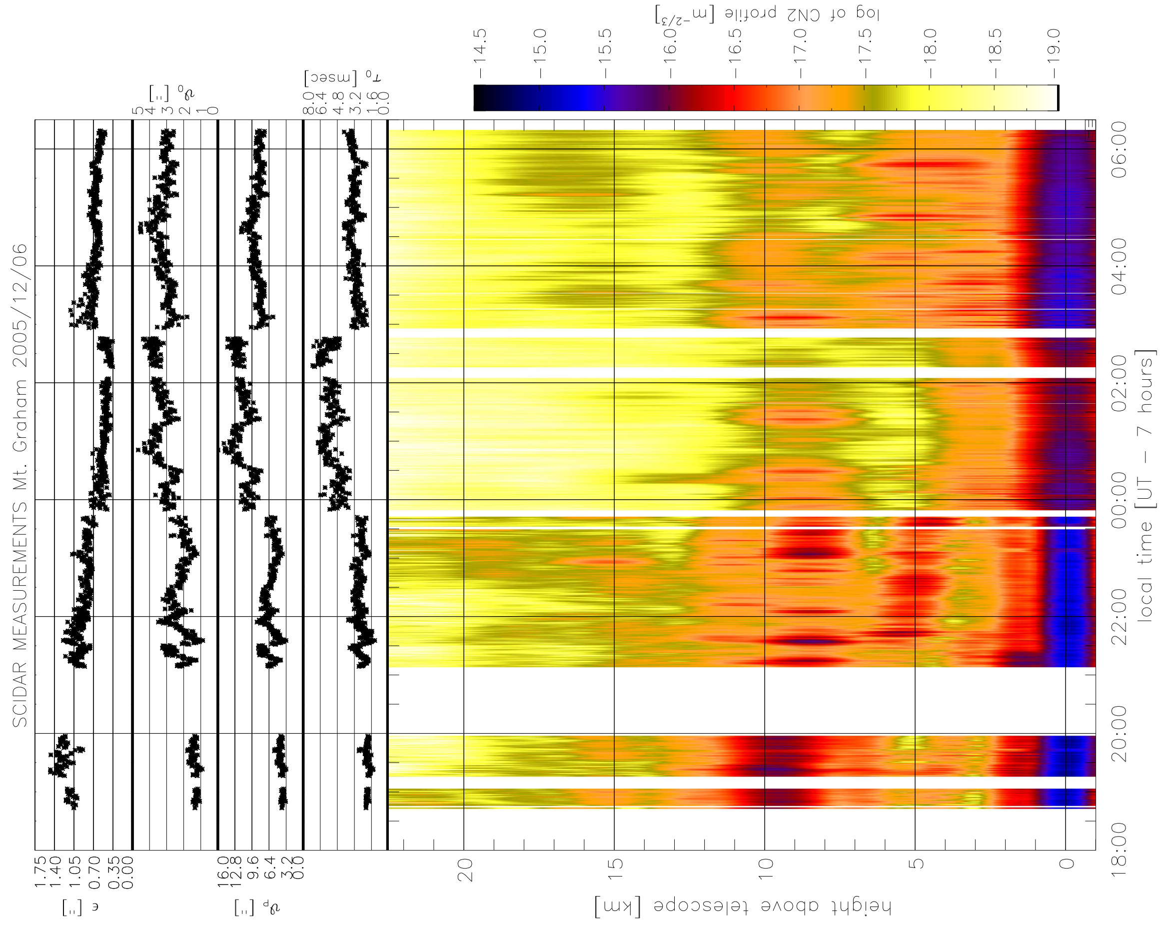
SCIDAR MEASUREMENTS Mt. Graham 2005/12/06
ε ["]
1.75
1.40
1.05
0.70
0.35
0.00
ϑ₀ ["]
5
4
3
2
1
0
ϑₚ ["]
16.0
12.8
9.6
6.4
3.2
0.0
τ₀ [msec]
8.0
6.4
4.8
3.2
1.6
0.0
height above telescope [km]
20
15
10
5
0
log of CN2 profile [m^-2/3]
−14.5
−15.0
−15.5
−16.0
−16.5
−17.0
−17.5
−18.0
−18.5
−19.0
18:00
20:00
22:00
00:00
02:00
04:00
06:00
local time [UT − 7 hours]

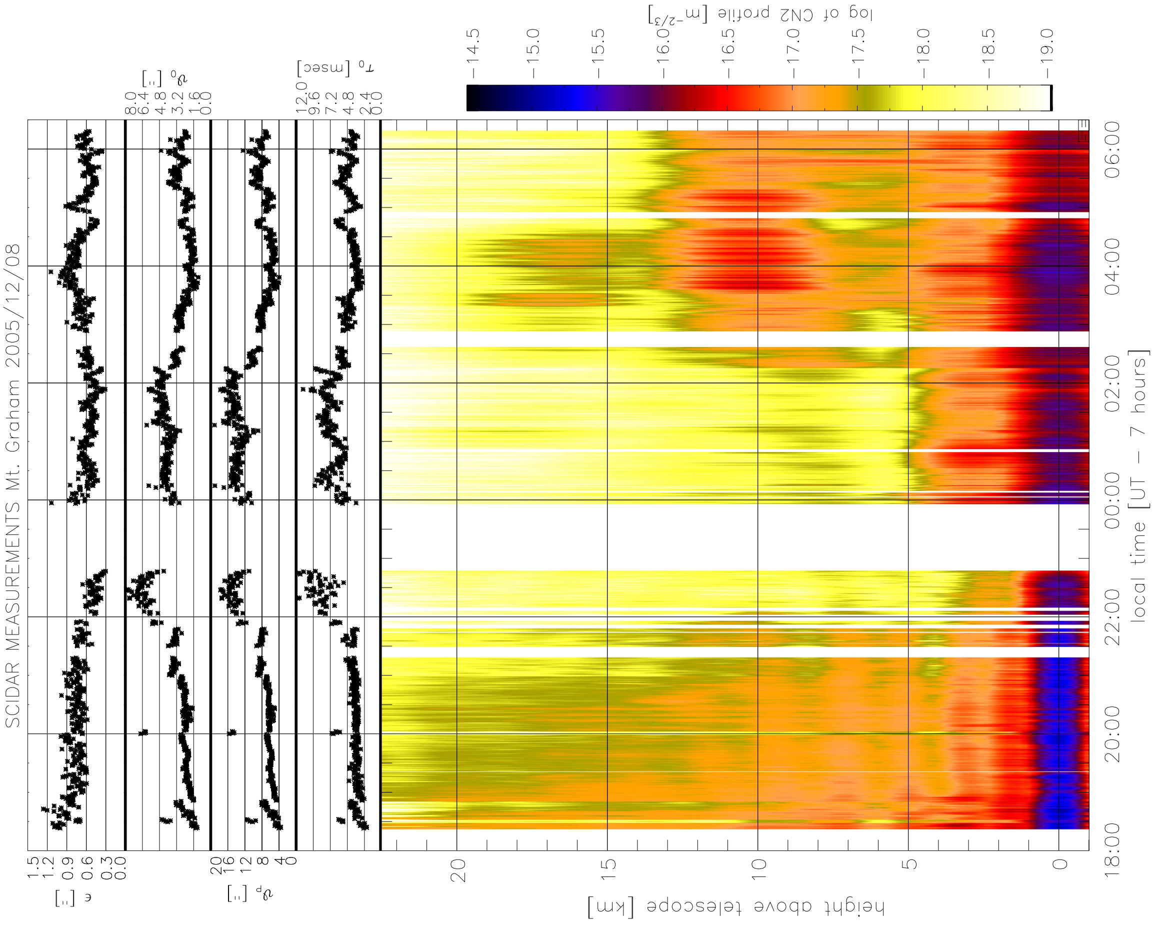
SCIDAR MEASUREMENTS Mt. Graham 2005/12/08
ε ["]
1.5
1.2
0.9
0.6
0.3
0.0
ϑ_0 ["]
8.0
6.4
4.8
3.2
1.6
0.0
ϑ_p ["]
20
16
12
8
4
0
τ_0 [msec]
12.0
9.6
7.2
4.8
2.4
0.0
height above telescope [km]
20
15
10
5
0
18:00
20:00
22:00
00:00
02:00
04:00
06:00
local time [UT − 7 hours]
log of CN2 profile [$m^{-2/3}$]
−14.5
−15.0
−15.5
−16.0
−16.5
−17.0
−17.5
−18.0
−18.5
−19.0

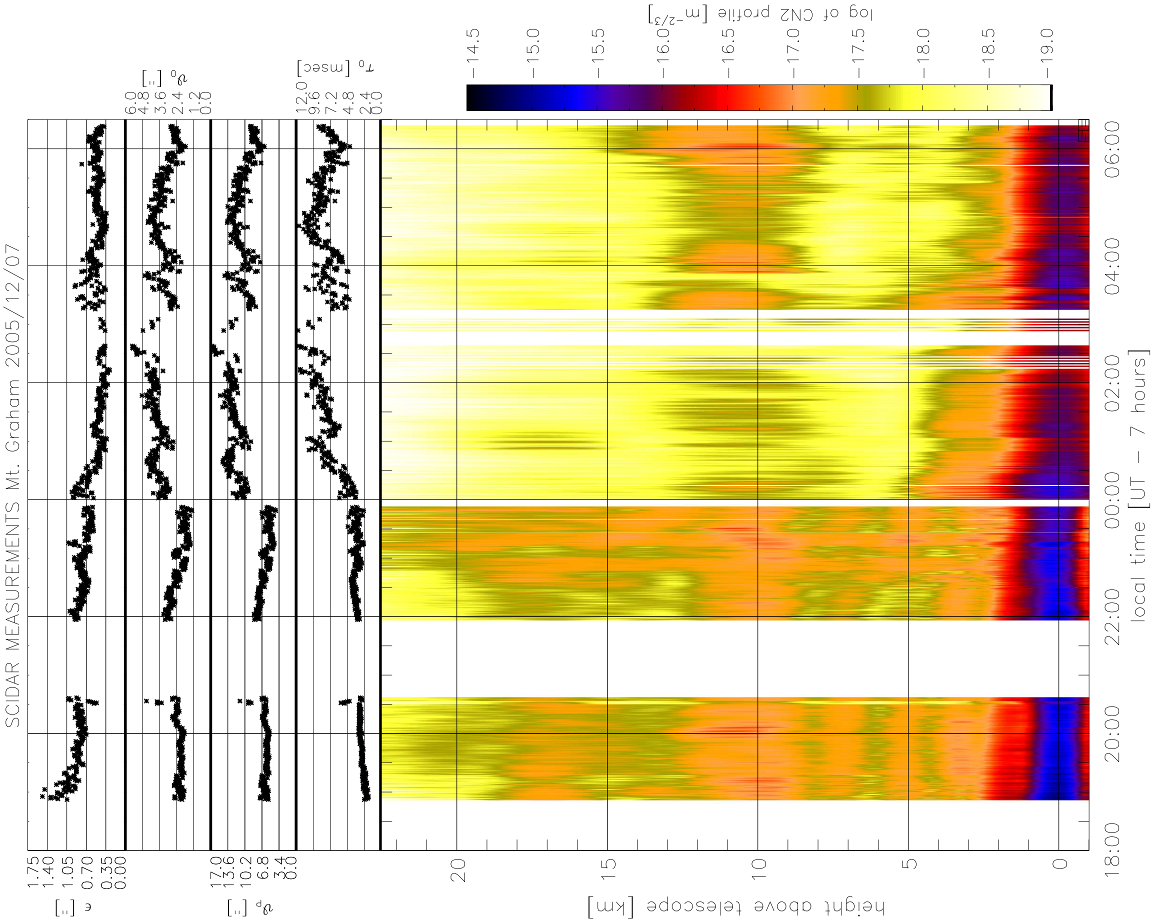
SCIDAR MEASUREMENTS Mt. Graham 2005/12/07
ε ["]
1.75
1.40
1.05
0.70
0.35
0.00
ϑ_0 ["]
6.0
4.8
3.6
2.4
1.2
0.0
ϑ_p ["]
17.0
13.6
10.2
6.8
3.4
0.0
τ_0 [msec]
12.0
9.6
7.2
4.8
2.4
0.0
height above telescope [km]
20
15
10
5
0
18:00
20:00
22:00
00:00
02:00
04:00
06:00
local time [UT − 7 hours]
log of CN2 profile [$m^{-2/3}$]
−14.5
−15.0
−15.5
−16.0
−16.5
−17.0
−17.5
−18.0
−18.5
−19.0

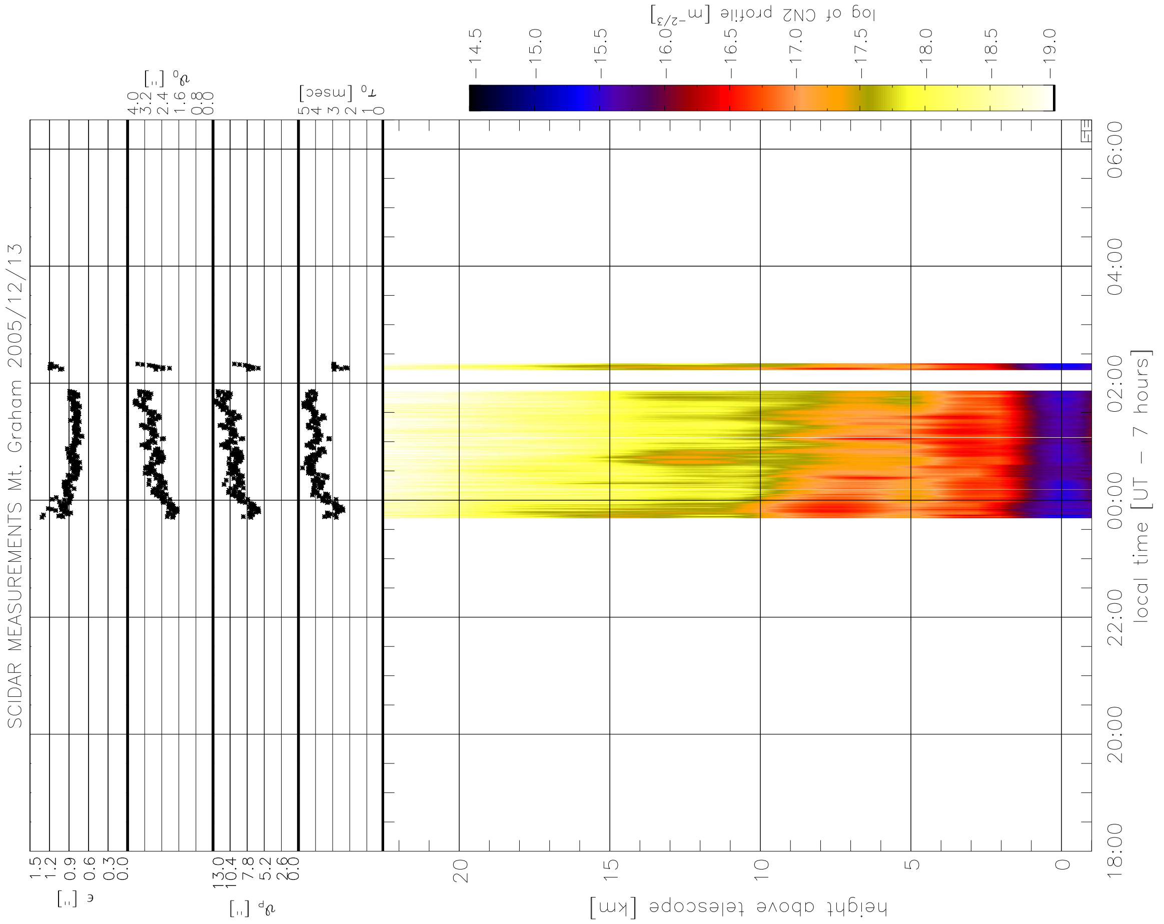
SCIDAR MEASUREMENTS Mt. Graham 2005/12/13
ε ["]
1.5
1.2
0.9
0.6
0.3
0.0
ϑ₀ ["]
4.0
3.2
2.4
1.6
0.8
0.0
ϑ_p ["]
13.0
10.4
7.8
5.2
2.6
0.0
τ₀ [msec]
5
4
3
2
1
0
height above telescope [km]
20
15
10
5
0
local time [UT − 7 hours]
18:00
20:00
22:00
00:00
02:00
04:00
06:00
log of CN2 profile [m^-2/3]
−14.5
−15.0
−15.5
−16.0
−16.5
−17.0
−17.5
−18.0
−18.5
−19.0

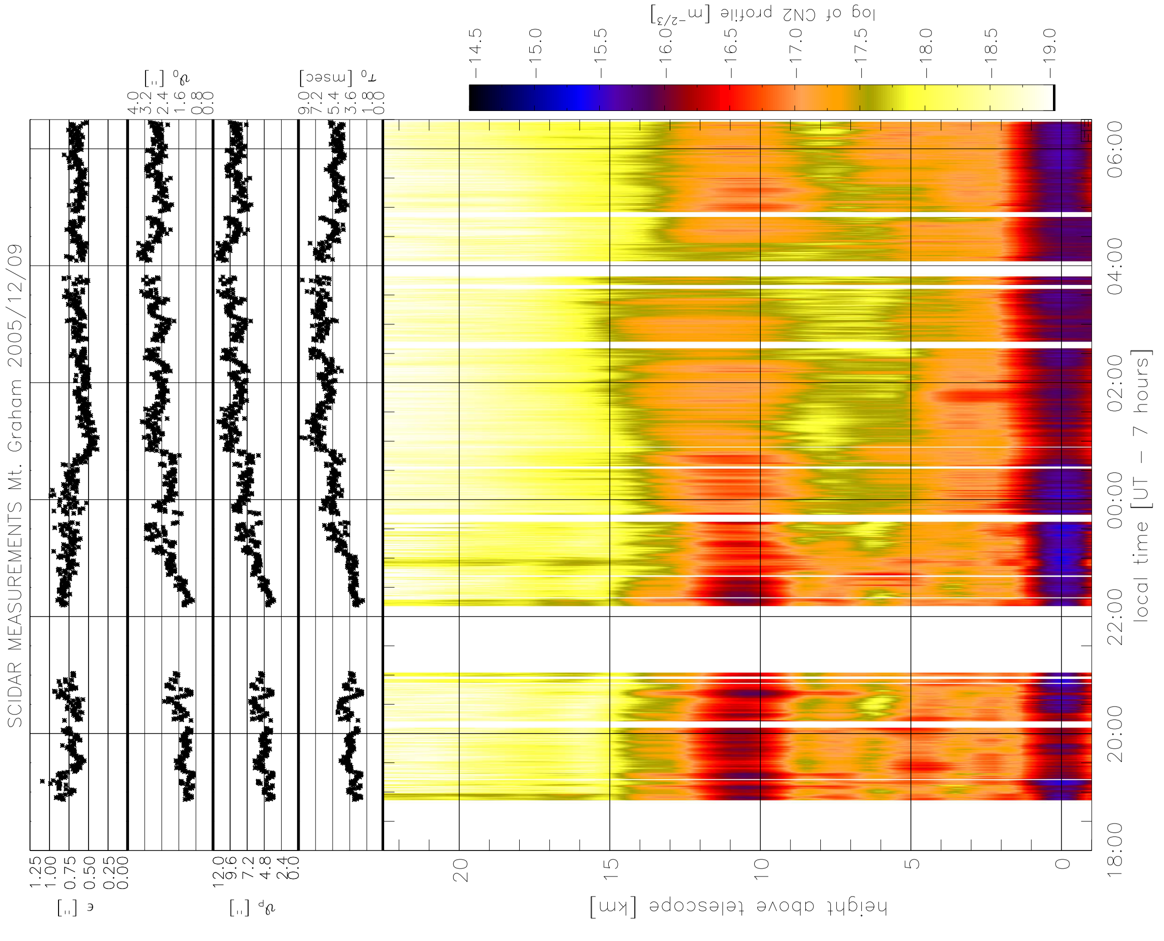
SCIDAR MEASUREMENTS Mt. Graham 2005/12/09
ε ["]
1.25
1.00
0.75
0.50
0.25
0.00
ϑ₀ ["]
4.0
3.2
2.4
1.6
0.8
0.0
ϑ_p ["]
12.0
9.6
7.2
4.8
2.4
0.0
τ₀ [msec]
9.0
7.2
5.4
3.6
1.8
0.0
height above telescope [km]
20
15
10
5
0
local time [UT − 7 hours]
18:00
20:00
22:00
00:00
02:00
04:00
06:00
log of CN2 profile [m^-2/3]
−14.5
−15.0
−15.5
−16.0
−16.5
−17.0
−17.5
−18.0
−18.5
−19.0

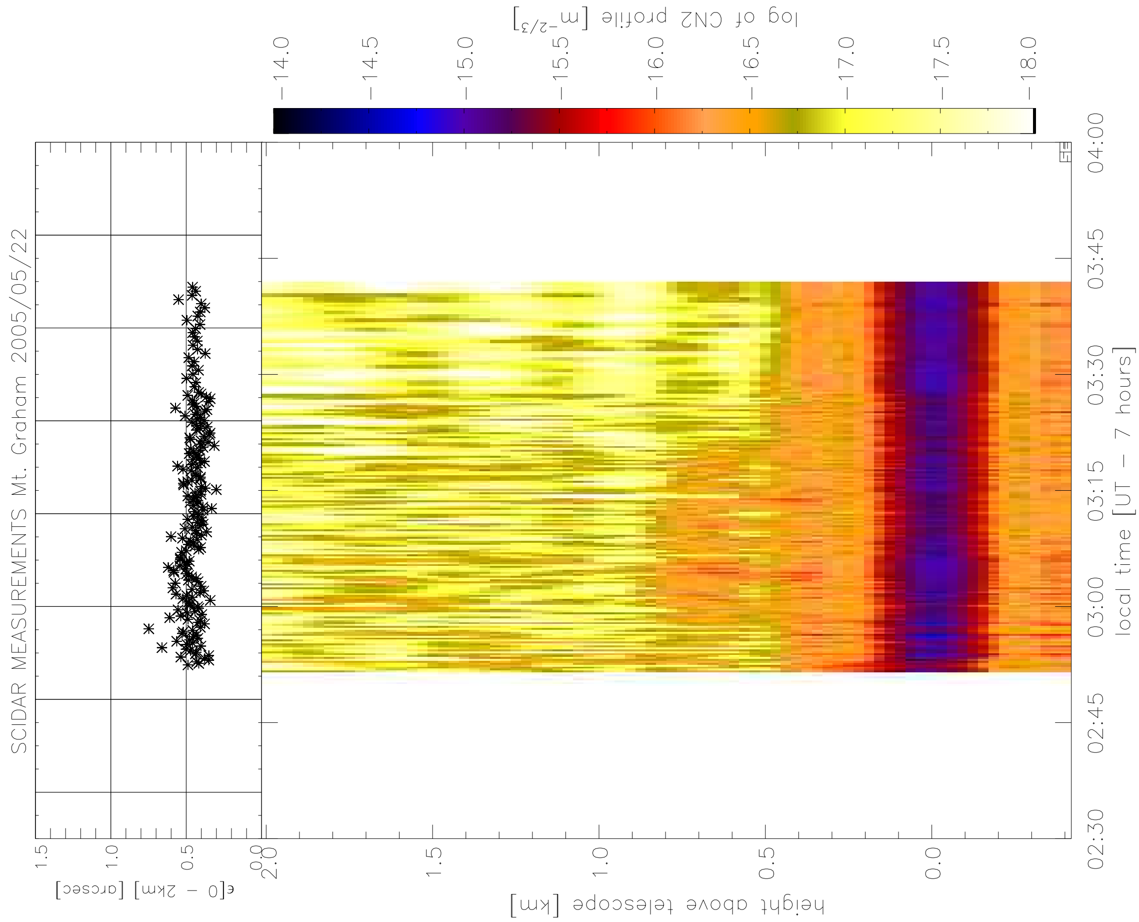
SCIDAR MEASUREMENTS Mt. Graham 2005/05/22
ε[0 – 2km] [arcsec]
1.5
1.0
0.5
0.0
height above telescope [km]
2.0
1.5
1.0
0.5
0.0
local time [UT – 7 hours]
02:30
02:45
03:00
03:15
03:30
03:45
04:00
log of CN2 profile [m$^{-2/3}$]
−14.0
−14.5
−15.0
−15.5
−16.0
−16.5
−17.0
−17.5
−18.0

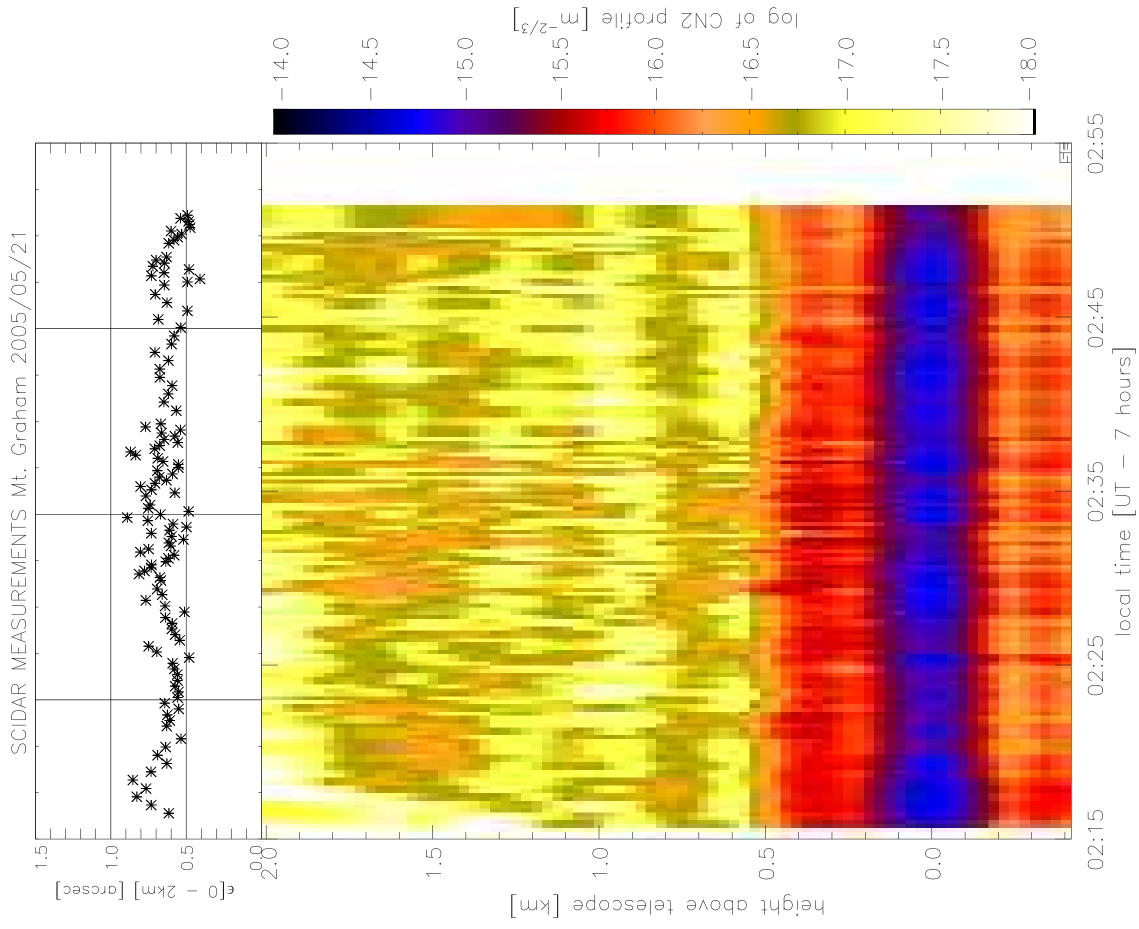
SCIDAR MEASUREMENTS Mt. Graham 2005/05/21
ε[0 – 2km] [arcsec]
1.5
1.0
0.5
0.0
height above telescope [km]
2.0
1.5
1.0
0.5
0.0
local time [UT – 7 hours]
02:15
02:25
02:35
02:45
02:55
log of CN2 profile [m$^{-2/3}$]
−14.0
−14.5
−15.0
−15.5
−16.0
−16.5
−17.0
−17.5
−18.0

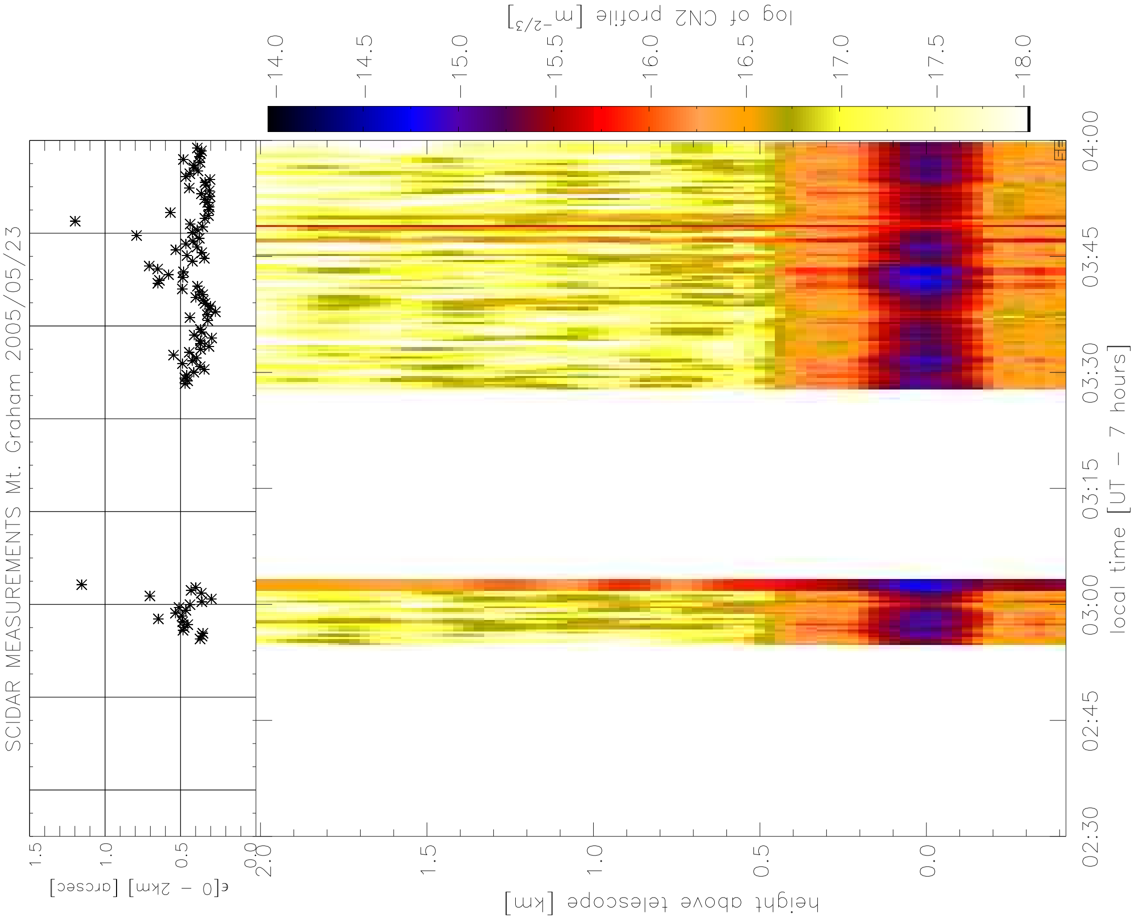
SCIDAR MEASUREMENTS Mt. Graham 2005/05/23
log of CN2 profile [$m^{-2/3}$]
−14.0
−14.5
−15.0
−15.5
−16.0
−16.5
−17.0
−17.5
−18.0
height above telescope [km]
2.0
1.5
1.0
0.5
0.0
local time [UT − 7 hours]
02:30
02:45
03:00
03:15
03:30
03:45
04:00
ε[0 − 2km] [arcsec]
1.5
1.0
0.5
0.0

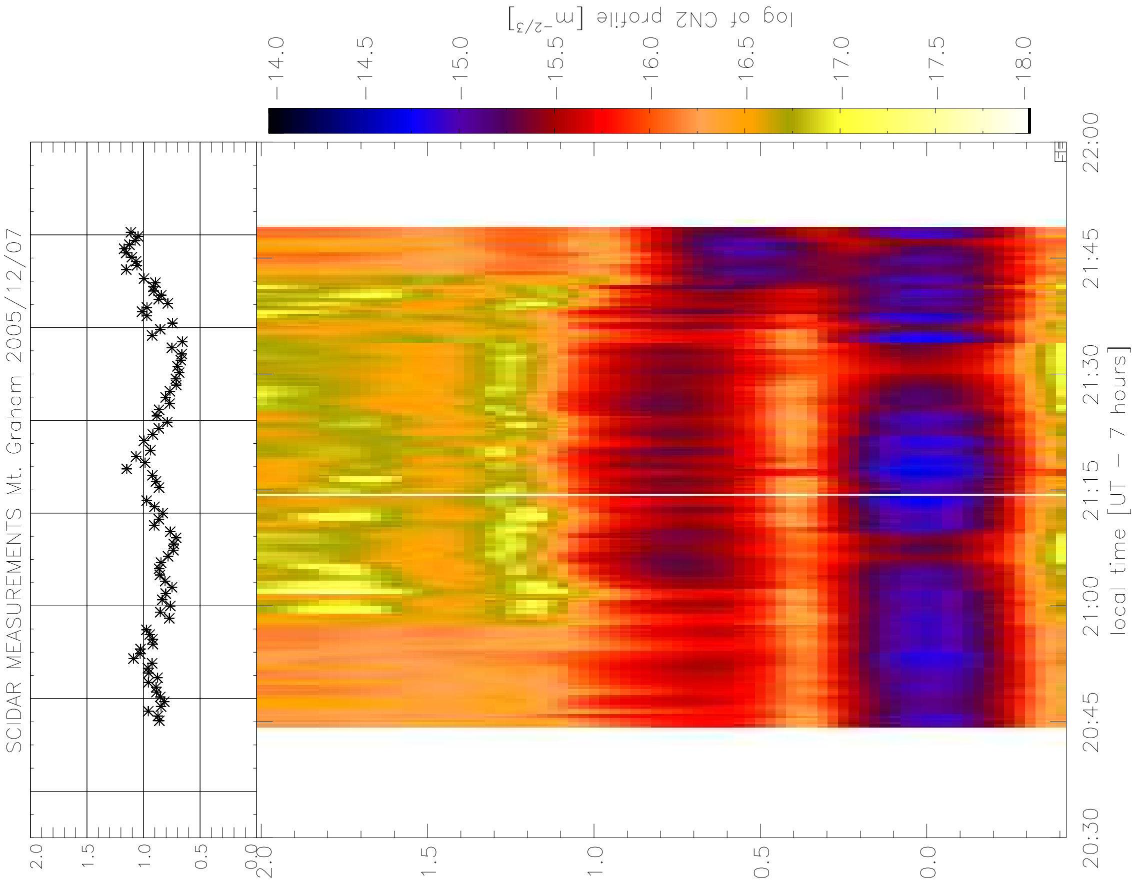
SCIDAR MEASUREMENTS Mt. Graham 2005/12/07
ε[0 – 2km] [arcsec]
2.0
1.5
1.0
0.5
0.0
height above telescope [km]
2.0
1.5
1.0
0.5
0.0
local time [UT – 7 hours]
20:30
20:45
21:00
21:15
21:30
21:45
22:00
log of CN2 profile [m^-2/3]
–14.0
–14.5
–15.0
–15.5
–16.0
–16.5
–17.0
–17.5
–18.0

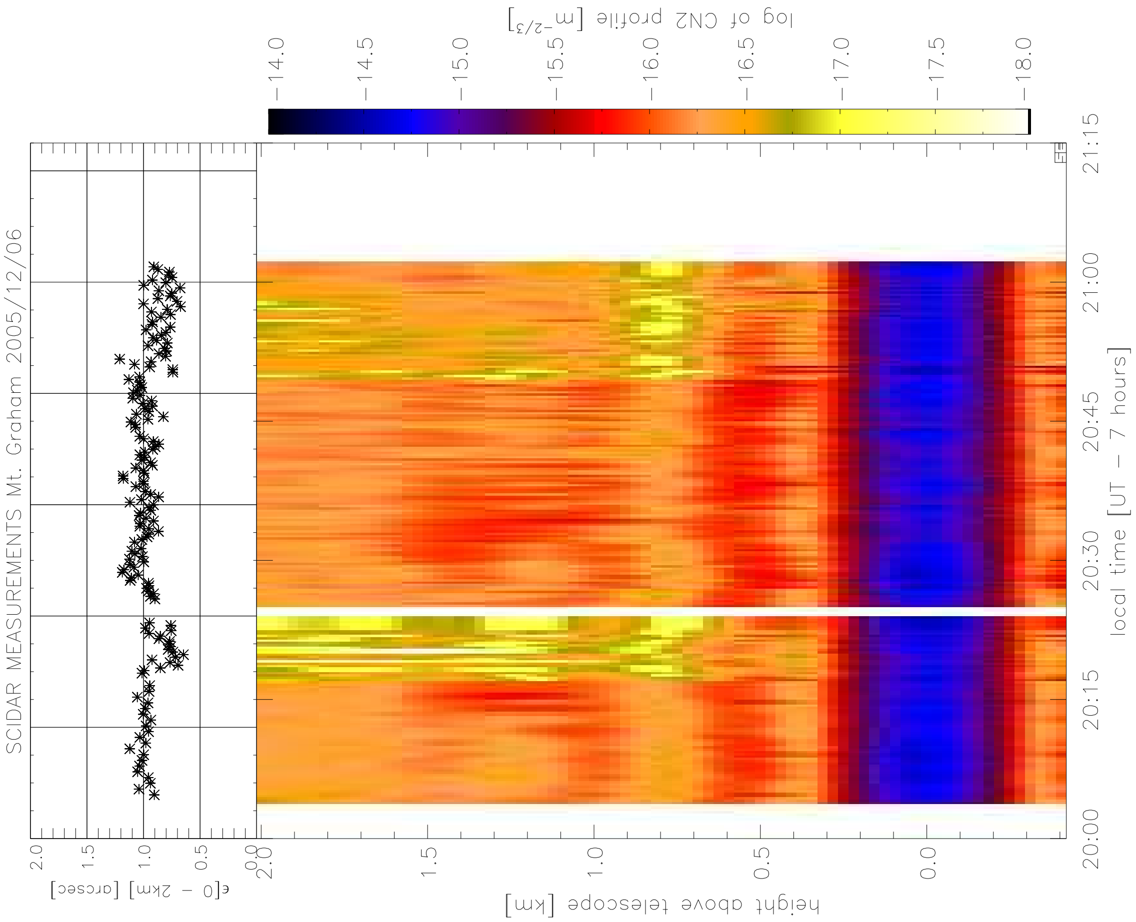
SCIDAR MEASUREMENTS Mt. Graham 2005/12/06
ε[0 – 2km] [arcsec]
2.0
1.5
1.0
0.5
0.0
height above telescope [km]
2.0
1.5
1.0
0.5
0.0
local time [UT – 7 hours]
20:00
20:15
20:30
20:45
21:00
21:15
log of CN2 profile [m^-2/3]
–14.0
–14.5
–15.0
–15.5
–16.0
–16.5
–17.0
–17.5
–18.0

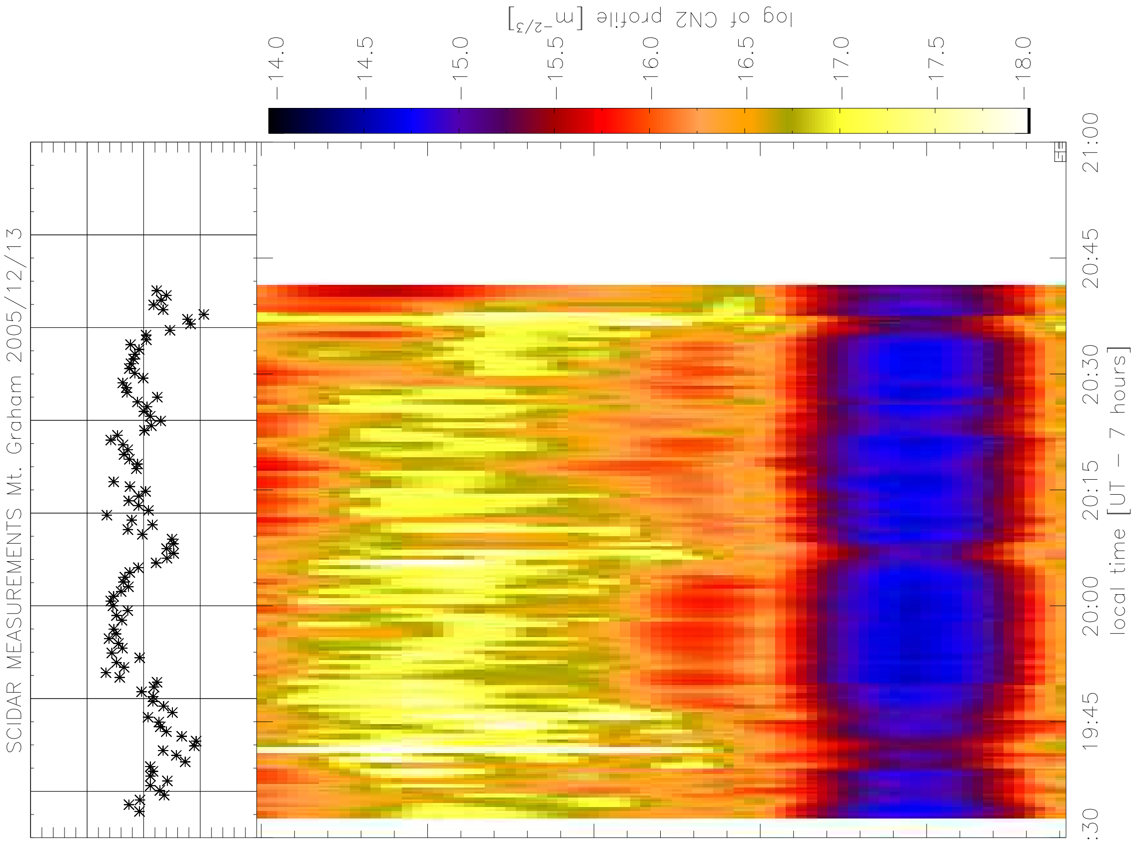
SCIDAR MEASUREMENTS Mt. Graham 2005/12/13
ε[0 – 2km] [arcsec]
0.0
0.5
1.0
1.5
2.0
height above telescope [km]
0.0
0.5
1.0
1.5
2.0
local time [UT – 7 hours]
19:30
19:45
20:00
20:15
20:30
20:45
21:00
log of CN2 profile [m^-2/3]
−14.0
−14.5
−15.0
−15.5
−16.0
−16.5
−17.0
−17.5
−18.0

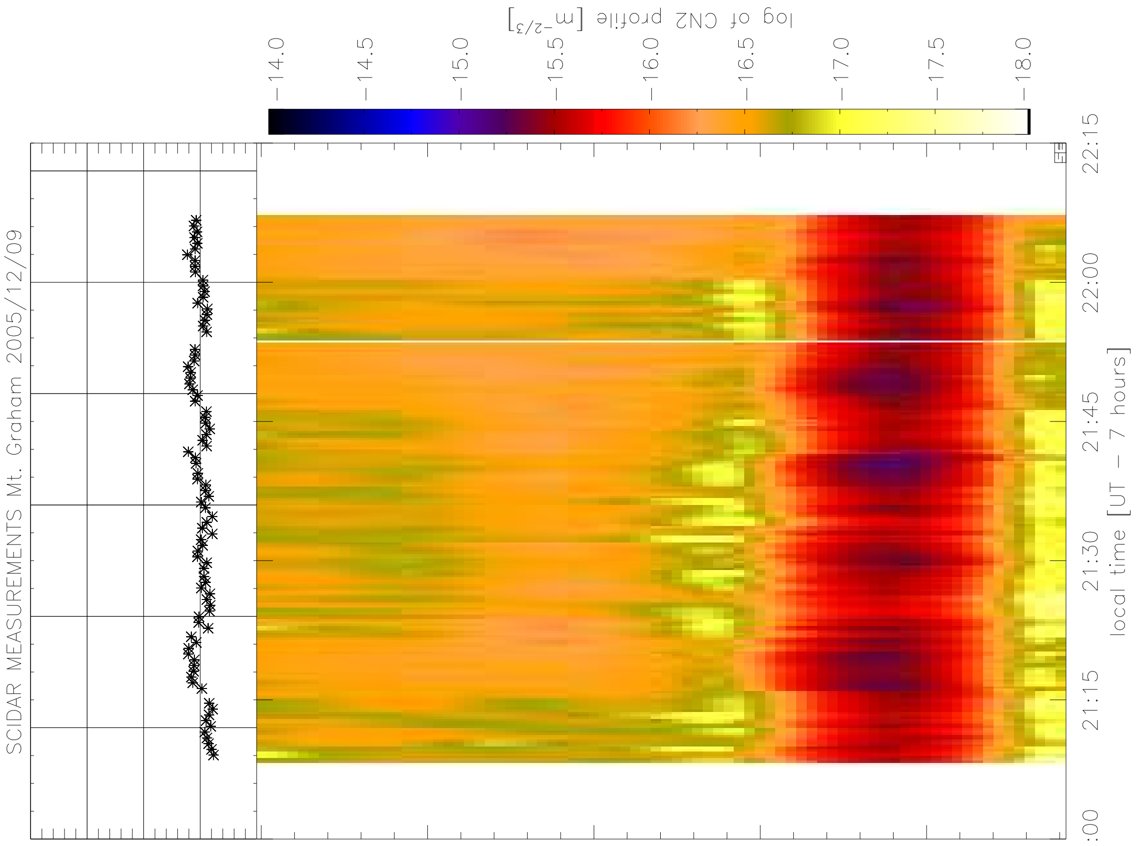
SCIDAR MEASUREMENTS Mt. Graham 2005/12/09
ε[0 – 2km] [arcsec]
0.0
0.5
1.0
1.5
2.0
height above telescope [km]
0.0
0.5
1.0
1.5
2.0
local time [UT – 7 hours]
21:00
21:15
21:30
21:45
22:00
22:15
log of CN2 profile [m^-2/3]
−14.0
−14.5
−15.0
−15.5
−16.0
−16.5
−17.0
−17.5
−18.0

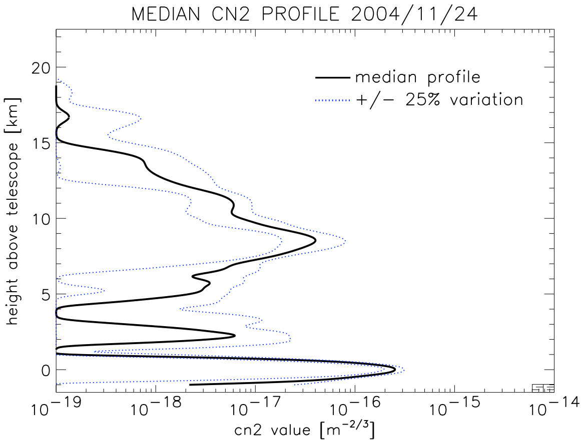
MEDIAN CN2 PROFILE 2004/11/24
median profile
+/− 25% variation
height above telescope [km]
0
5
10
15
20
10^{-19}
10^{-18}
10^{-17}
10^{-16}
10^{-15}
10^{-14}
cn2 value [$m^{-2/3}$]

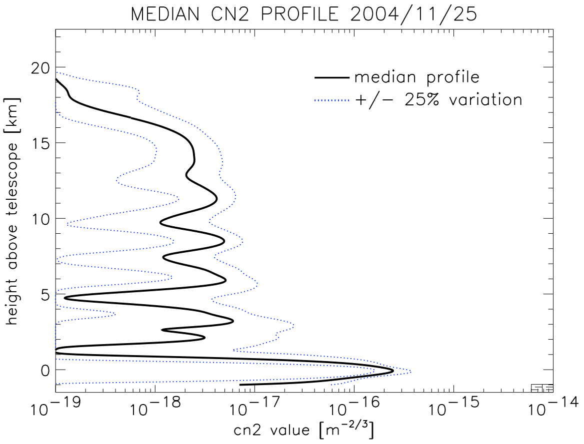
MEDIAN CN2 PROFILE 2004/11/25
median profile
+/− 25% variation
height above telescope [km]
0
5
10
15
20
10^{-19}
10^{-18}
10^{-17}
10^{-16}
10^{-15}
10^{-14}
cn2 value [$m^{-2/3}$]

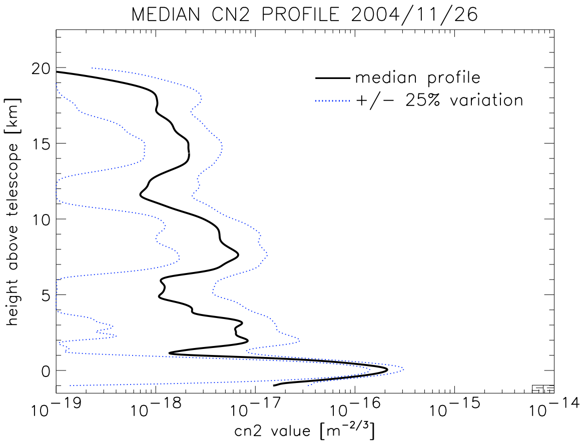
MEDIAN CN2 PROFILE 2004/11/26
median profile
+/− 25% variation
height above telescope [km]
0
5
10
15
20
10^{-19}
10^{-18}
10^{-17}
10^{-16}
10^{-15}
10^{-14}
cn2 value [$m^{-2/3}$]

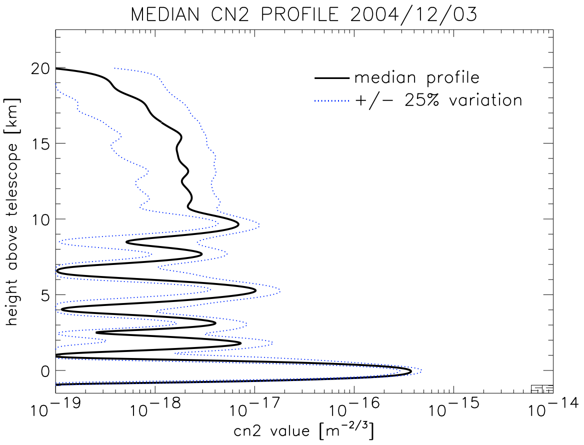
MEDIAN CN2 PROFILE 2004/12/03
median profile
+/− 25% variation
height above telescope [km]
0
5
10
15
20
10^{-19}
10^{-18}
10^{-17}
10^{-16}
10^{-15}
10^{-14}
cn2 value [$m^{-2/3}$]

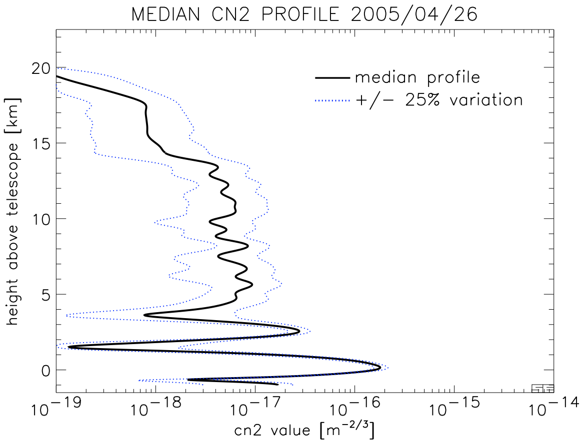
MEDIAN CN2 PROFILE 2005/04/26
median profile
+/− 25% variation
height above telescope [km]
0
5
10
15
20
10^{-19}
10^{-18}
10^{-17}
10^{-16}
10^{-15}
10^{-14}
cn2 value [$m^{-2/3}$]

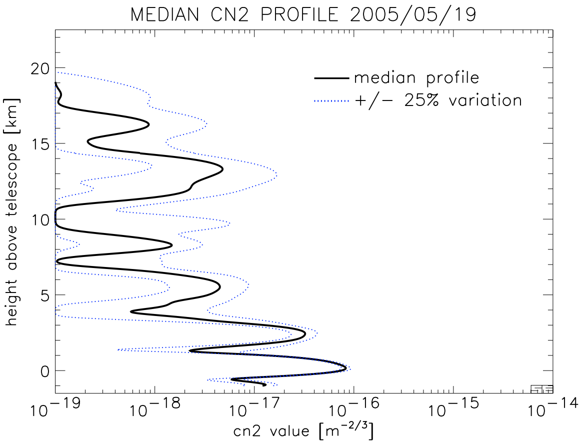
MEDIAN CN2 PROFILE 2005/05/19
median profile
+/− 25% variation
height above telescope [km]
0
5
10
15
20
10^{-19}
10^{-18}
10^{-17}
10^{-16}
10^{-15}
10^{-14}
cn2 value $[m^{-2/3}]$

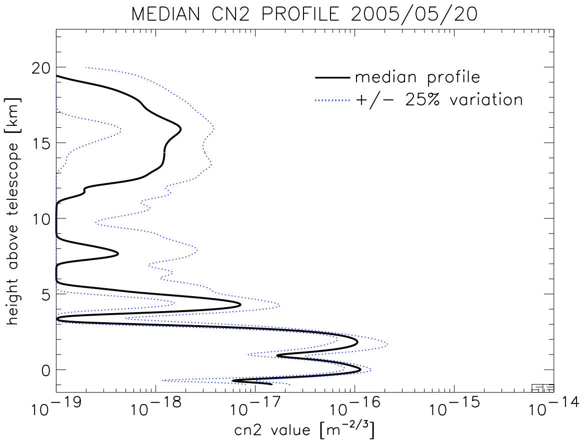
MEDIAN CN2 PROFILE 2005/05/20
median profile
+/− 25% variation
height above telescope [km]
0
5
10
15
20
10^{-19}
10^{-18}
10^{-17}
10^{-16}
10^{-15}
10^{-14}
cn2 value $[m^{-2/3}]$

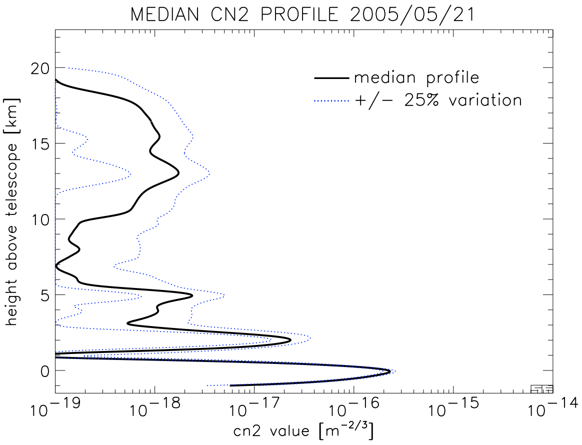
MEDIAN CN2 PROFILE 2005/05/21
median profile
+/− 25% variation
height above telescope [km]
0
5
10
15
20
10^{-19}
10^{-18}
10^{-17}
10^{-16}
10^{-15}
10^{-14}
cn2 value $[m^{-2/3}]$

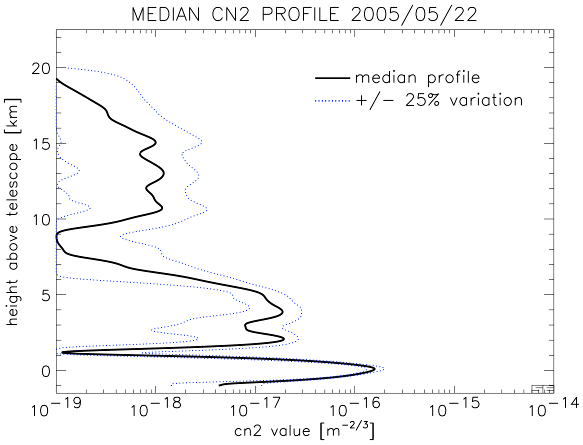
MEDIAN CN2 PROFILE 2005/05/22
median profile
+/− 25% variation
height above telescope [km]
0
5
10
15
20
10^{-19}
10^{-18}
10^{-17}
10^{-16}
10^{-15}
10^{-14}
cn2 value $[m^{-2/3}]$

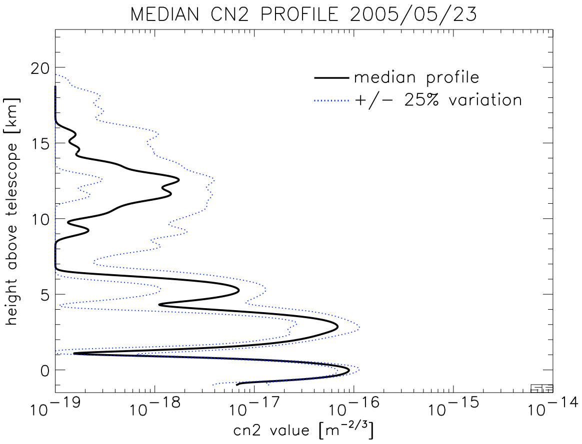
MEDIAN CN2 PROFILE 2005/05/23
median profile
+/− 25% variation
height above telescope [km]
0
5
10
15
20
10^{-19}
10^{-18}
10^{-17}
10^{-16}
10^{-15}
10^{-14}
cn2 value $[m^{-2/3}]$

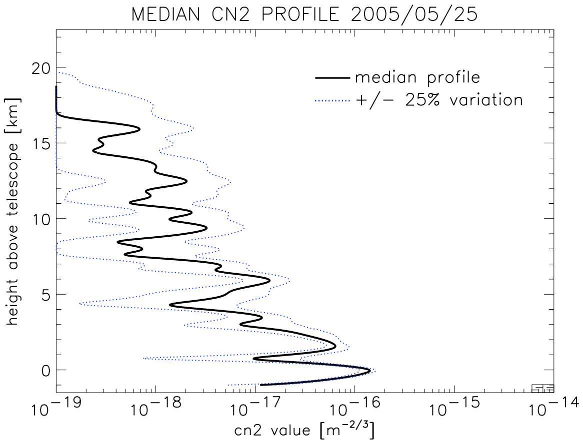
MEDIAN CN2 PROFILE 2005/05/25
median profile
+/− 25% variation
height above telescope [km]
0
5
10
15
20
10^{-19}
10^{-18}
10^{-17}
10^{-16}
10^{-15}
10^{-14}
cn2 value $[m^{-2/3}]$

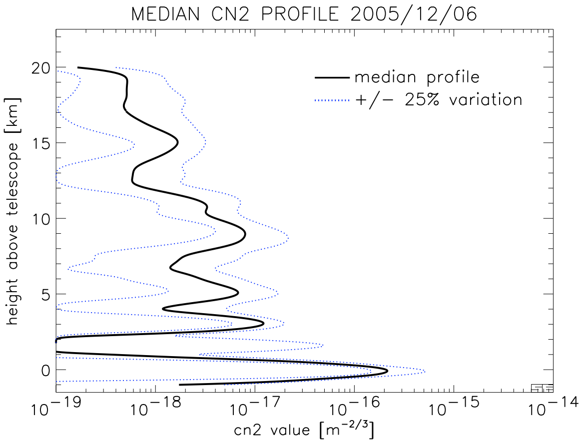

MEDIAN CN2 PROFILE 2005/12/06

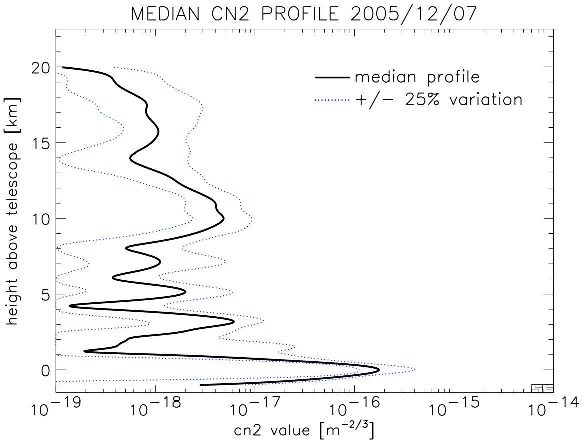

MEDIAN CN2 PROFILE 2005/12/07

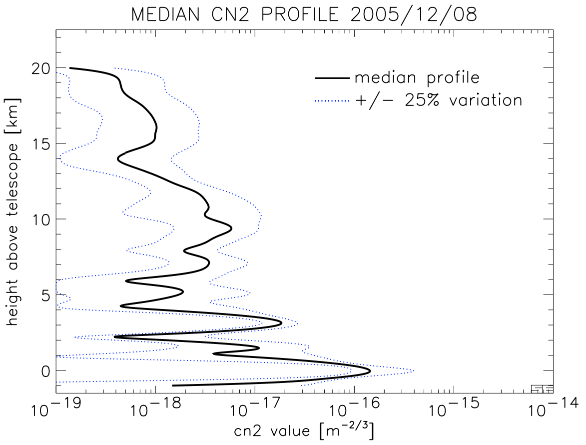

MEDIAN CN2 PROFILE 2005/12/08

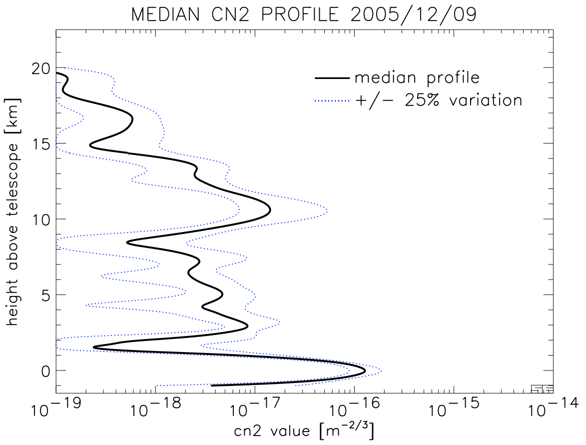

MEDIAN CN2 PROFILE 2005/12/09

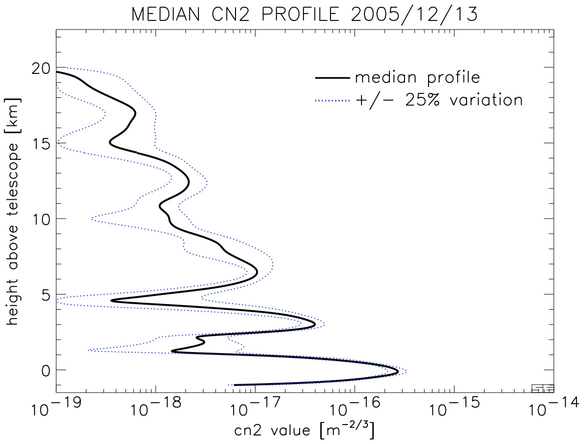

MEDIAN CN2 PROFILE 2005/12/13

APPENDIX B

The Wind-Profiles

> Oh, I like these calm little moments
> before the storm.
>
> *R.M.B., "reality"*

In this appendix the retrieved wind-speed profiles from the measurements by the G-SCIDAR and as extracted from the ECMWF database are shown. As mentioned in section 6.3.1, not for every C_N^2-profile the extraction of the wind-speed profile from the G-SCIDAR measurements is possible. However, the variation of the wind-speed during the observing nights is relatively small. For these reasons, we do not show the temporal evolution, but instead the wind speeds of the detected turbulent layers in all the measurements of a single night are plotted in one figure. Furthermore, the ECMWF provides only one wind-speed profile for each night.

The altitude is given above sea-level and the altitude of Mt. Graham ($\approx$3200 m above sea-level) is indicated by a dashed line.

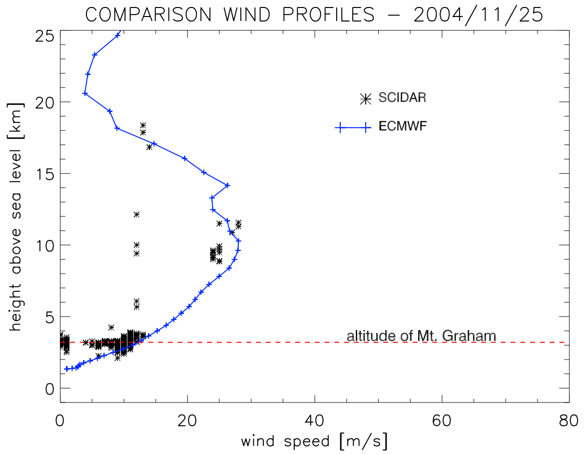
COMPARISON WIND PROFILES – 2004/11/25

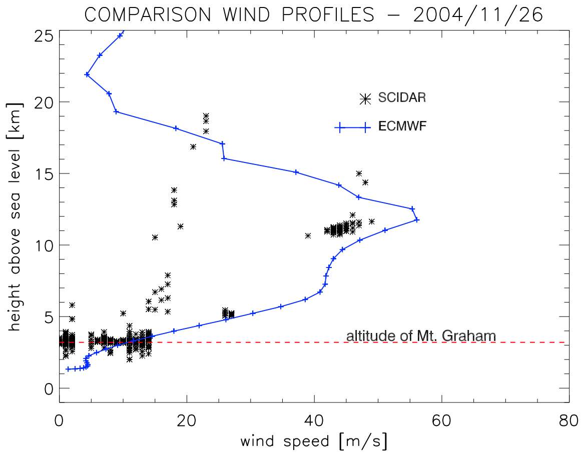
COMPARISON WIND PROFILES – 2004/11/26

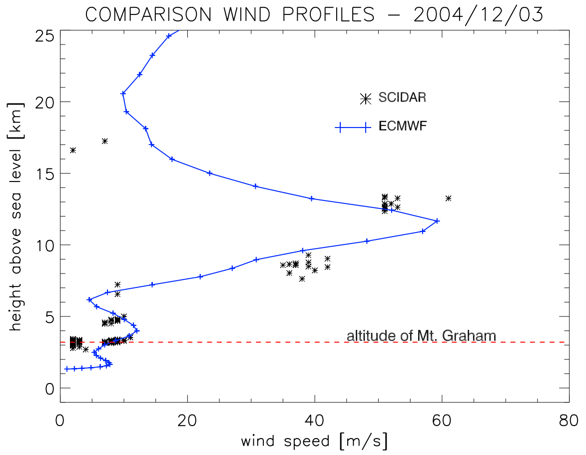
COMPARISON WIND PROFILES – 2004/12/03

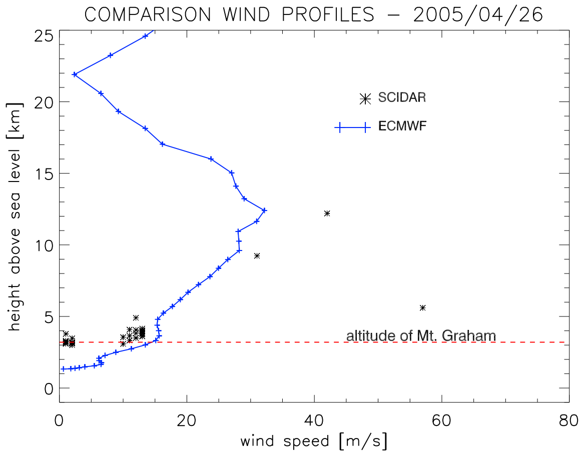
COMPARISON WIND PROFILES – 2005/04/26

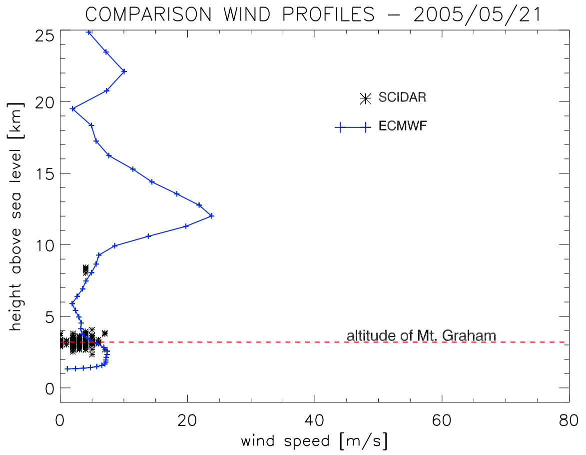
COMPARISON WIND PROFILES – 2005/05/21

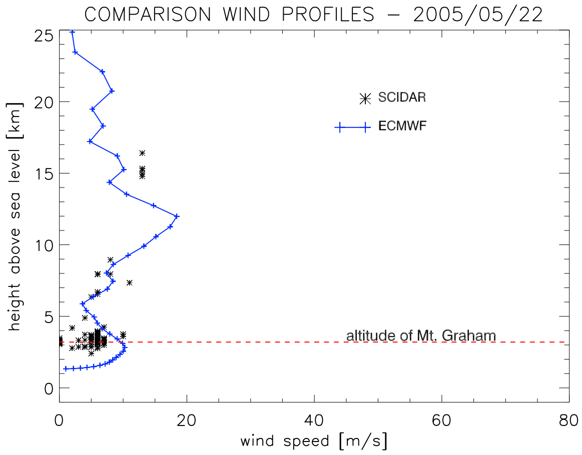
COMPARISON WIND PROFILES – 2005/05/22

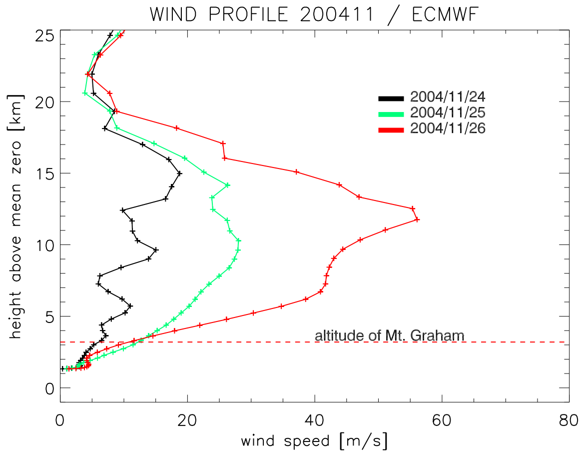
WIND PROFILE 200411 / ECMWF

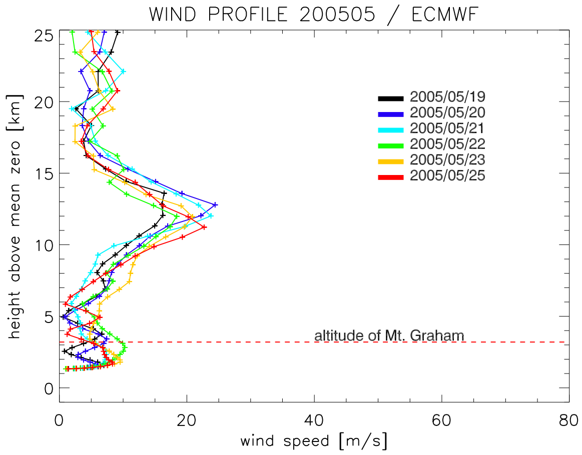
WIND PROFILE 200505 / ECMWF

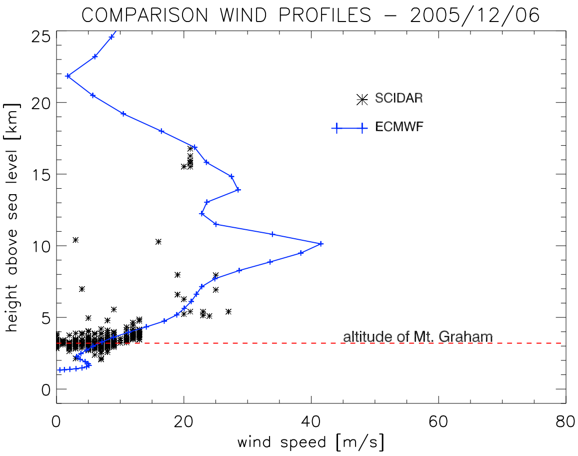
COMPARISON WIND PROFILES – 2005/12/06

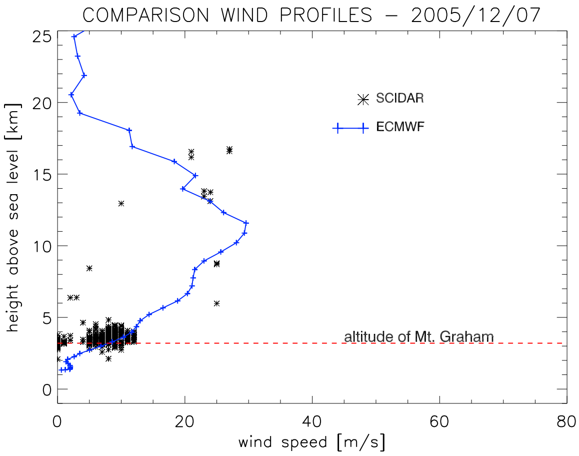
COMPARISON WIND PROFILES – 2005/12/07

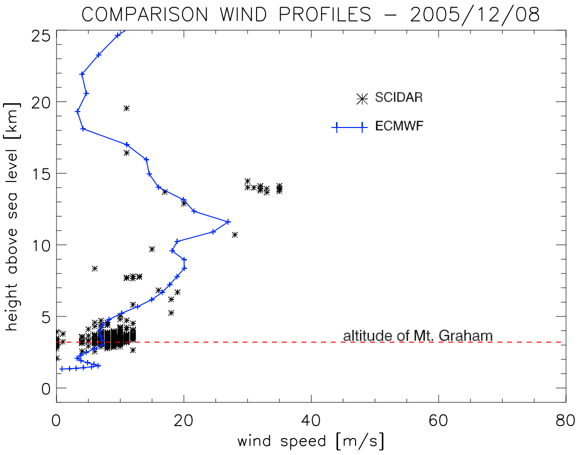
COMPARISON WIND PROFILES – 2005/12/08

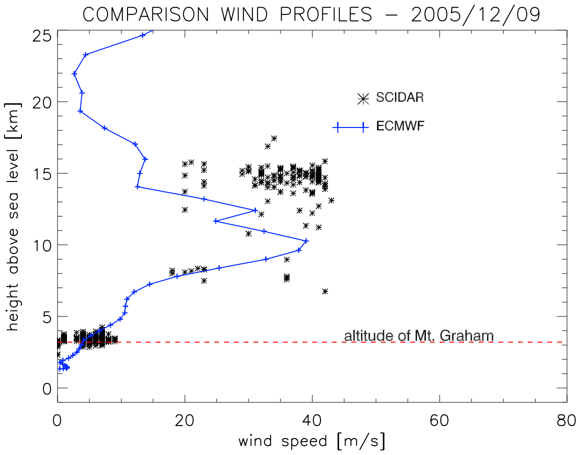
COMPARISON WIND PROFILES – 2005/12/09

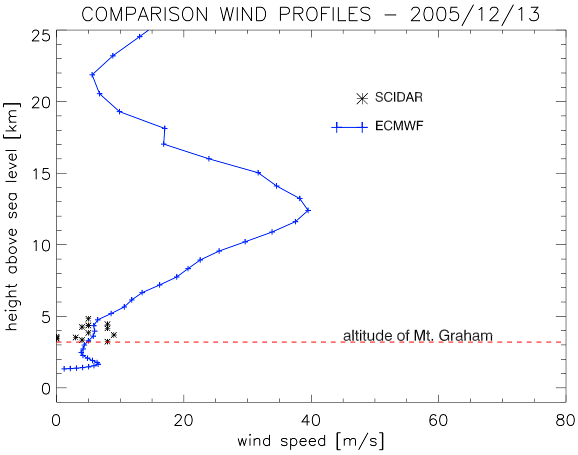
COMPARISON WIND PROFILES – 2005/12/13

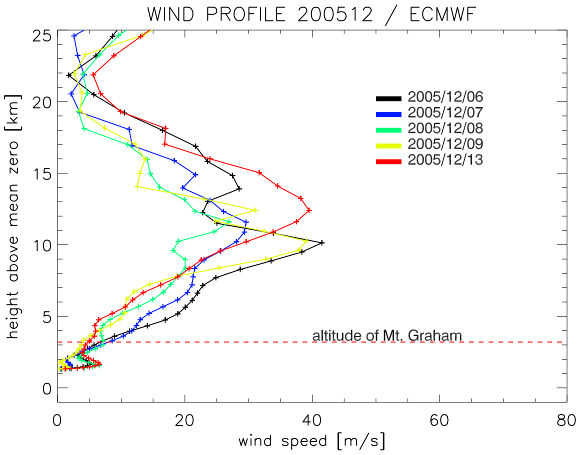
WIND PROFILE 200512 / ECMWF

APPENDIX C

Acronyms

> with the lights out it's less dangerous,
> here we are now, entertain us!
> I feel stupid and contagious
> here we are now, entertain us!
>
> *Nirvana, "Smells like teen spirit"*

AC Auto-Correlation

AO Adaptive Optics

CARMA Control And Reconstruction software for Multi-conjugate Adaptive optics

CC Cross-Correlation

CCD Charged-Coupled-Device

DM Deformable Mirror

ECMWF European Center for Medium Weather Forecast

ELT Extremely Large Telescope

ESO European Southern Observatory

FoV Field-of-View

FWHM Full-Width-Half-Maximum

G-SCIDAR Generalized SCIDAR

GLAO Ground-Layer Adaptive Optics

HVR-GS High Vertical Resolution Generalized SCIDAR

LBT Large Binocular Telescope

LGS Laser Guide-Star

LINC-NIRVANA LBT INterferomertic Camera - Near InfraRed / Visible Adaptive iNterferometer for Astronomy

LO Layer-Oriented

MAD Multi-conjugate-Adaptive-optics Demonstrator

MAPS Multiple Atmospheric Phase screens and Stars

MCAO Multi-Conjugate Adaptive Optics

NGS Natural Guide-Star

OPD Optical Path Difference

OTF Optical-Transfer-Function

PSD Power-Spectral-Density

PSF Point-Spread-Function

RON Read-Out-Noise

SCIDAR SCIntillation Detection And Ranging

SNR Signal-to-Noise Ratio

VATT The Vatican Advanced Technology Telescope

VLT The Very Large Telescope

Appendix D

Bibliography

> Who has the fun, is it always the man with the gun?
> Someone must have told him, if you work too hard, you can sweat.
>
> *The Stranglers, "Always the sun"*

Arcidiacono, C. (2004). *Multi-Conjugate Adaptive Optics for Large Telescopes*. PhD thesis, Universita degli studi di Firenze.

Athey, A., Shectman, S., Phillips, M., and Thomas-Osip, J. (2006). Results from the GMT ground-layer experiment at the Magellan Telescopes. In *SPIE*, 6272.

Athey, A., Shectman, S., Schechter, P., and Lane, B. (2004). The GMT ground-layer AO experiment at the Magellan telescopes. In *SPIE*, 5490, page 960.

Avila, R., Carrasco, E., Ibanez, F., et al. (2006). Generalized SCIDAR Measurements at San Pedro Martir. II. Wind Profile Statistics. *PASP*, 118:503.

Avila, R. and Chun, M. (2004). A method for high-resolution C_N^2 profiling in the first few hundred meters. In *SPIE*, 5490, page 742.

Avila, R., Ibanez, F., Vernin, J., et al. (2003). Optical-Turbulence and Wind Profiles at San Pedro Martir. *RMxAC*, 19:11.

Avila, R., Masciadri, E., Vernin, J., and Sánchez, J. (2004). Generalized SCIDAR Measurements at San Pedro Mártir. I. Turbulence Profile Statistics. *PASP*, 116:682.

Avila, R., Vernin, J., Chun, M., and Sanchez, L. (2000). Turbulence and wind profiling with generalized scidar at Cerro Pachon. In *SPIE*, 4007, page 721.

Avila, R., Vernin, J., and Cuevas, S. (1998). Turbulence Profiles with Generalized SCIDAR at San Pedro Martir Observatory and Isoplanatism Studies. *PASP*, 110:1106.

Avila, R., Vernin, J., and Sanchez, L. (2001). Atmospheric turbulence and wind profiles monitoring with generalized scidar. *A&A*, 369:364.

Babcock, H. W. (1953). The Possibility of Compensating Astronomical Seeing. *PASP*, 65:229.

Baranec, C., Lloyd-Hart, M., Milton, N., et al. (2006). Tomographic reconstruction of stellar wavefronts from multiple laser guide stars. In *SPIE*, 6272.

Beckers, J. (1988). Increasing the Size of the Isoplanatic Patch with Multiconjugate Adaptive Optics. In *Very Large Telescopes and their Instrumentation, ESO Conference and Workshop Proceedings*.

Bello, D., Conan, J.-M., Rousset, G., et al. (2003a). Numerical versus optical layer oriented: a comparison in terms of SNR. In *SPIE*, 4839, page 612.

Bello, D., Verinaud, C., Conan, J.-M., et al. (2003b). Comparison of different 3D wavefront sensing and reconstruction techniques for MCAO. In *SPIE*, 4839, page 554.

Berkefeld, T., Soltau, D., and von der Luehe, O. (2005). Results of the multi-conjugate adaptive optics system at the German solar telescope, Tenerife. In *SPIE*, 5903, page 219.

Bertram, T. (2005). Simulations and estimates of the atmospheric influence on interferometric performance. Technical Report LN-KOELN-FDR-GEN-001, MPIA.

Bertram, T., Andersen, D., Arcidiacono, C., et al. (2004). The LINC-NIRVANA fringe and flexure tracking system: differential piston simulation and detection. In *SPIE*, 5491, page 1454.

Bertram, T., Arcidiacono, C., Straubmeier, C., et al. (2006a). The LINC-NIRVANA Fringe and Flexure Tracker: Image analysis concept and fringe tracking performance estimate. In *SPIE*, 6238.

Bertram, T., Baumeister, H., Laun, W., et al. (2006b). The LINC-NIRVANA Fringe and Flexure Tracker: Cryo-Ambient Mechanical Design. In *SPIE*, 6268.

Bizenberger, P., Diolaiti, E., Egner, S., et al. (2006). LINC-NIRVANA: Optical design of an interferometric imaging camera. In *SPIE*, 6269.

Born, M., Wolf, E., and Bhatia, A. B. (1999). *Principles of Optics*. Cambridge University Press.

Butler, D., Hippler, S., Egner, S., et al. (2004). Broadband, static wavefront generation: Na-Ag ion exchange phase screens and telescope emulation. *Appl. Opt.*, 43:2813.

Carbillet, M., Verinaud, C., Femenia, B., et al. (2004). Modelling astronomical adaptive optics - I. The software package CAOS. *MNRAS*, 356:1263.

Chueca, S., Garcia-Lorenzo, B., Munoz-Tunon, C., and Fuensalida, J. (2004). Statistics and analysis of high-altitude wind above the Canary Islands observatories. *MNRAS*, 349:627.

Conan, J.-M., Rousset, G., and Madec, P.-Y. (1995). Wave-front temporal spectra in high-resolution imaging through turbulence. *JOSA A*, 12:1559.

Conan, R., Avila, R., Sanchez, L., et al. (2002). Wavefront outer scale and seeing measurements at San Pedro Martir Observatory. *A&A*, 396:723.

Costa, J. B. (2005). *Development of a new Infrared Pyramid Wavefront Sensor*. PhD thesis, University of Heidelberg.

Cox, A., editor (2000). *Allen's Astrophysical Quantities*. AIP Press.

Cromwell, R., Haemmerle, V., and Woolf, N. (1988). Seeing on Mt. Graham: Discoveries and Site-to-Site Variations. In *Very Large Telescopes and their Instrumentation, ESO Conference and Workshop Proceedings*.

Dai, G.-M. (1995). Modal compensation of atmospheric turbulence with the use of Zernike polynomials and Karhunen-Loeve functions. *JOSA A*, 12:2182.

Dai, G.-M. (1996). Modal wave-front reconstruction with Zernike polynomials and Karhunen-Loeve functions. *JOSA A*, 13:1218.

Dainty, J., editor (1976). *Laser Speckle and Related Phenomena*. Springer.

Diolaiti, E., Farinato, J., Rohloff, R.-R., and Soci, R. (2005a). Ground Layer Wavefront Sensor Opto-Mechanics. Technical Report LN-INAFA-FDR-AO-002, MPIA.

Diolaiti, E., Farinato, J., and Soci, R. (2005b). Mid-High Wavefront Sensor Optical and Mechanical Design. Technical Report LN-INAFA-FDR-AO-001, MPIA.

Diolaiti, E., Ragazzoni, R., and Tordi, M. (2001). Closed loop performance of a layer-oriented multi-conjugate adaptive optics system. *A&A*, 372:710.

Dravins, D., Lindegren, L., Mezey, E., and Young, A. (1997a). Atmospheric Intensity Scintillation of Stars, I. Statistical Distributions and Temporal Properties. *PASP*, 109:173.

Dravins, D., Lindegren, L., Mezey, E., and Young, A. (1997b). Atmospheric Intensity Scintillation of Stars. II. Dependence on Optical Wavelength. *PASP*, 109:725.

Dravins, D., Lindegren, L., Mezey, E., and Young, A. (1998). Atmospheric Intensity Scintillation of Stars. III. Effects for Different Telescope Apertures. *PASP*, 110:610.

Eaton, F. (2005). Recent developments of optical turbulence measurement techniques. In *SPIE*, 5793, page 68.

Eaton, F. and Nastrom, G. (1998). Preliminary estimates of the inner and outer scales from White Sands Missile Range, NM radar observations. *Radio Sci.*, 33:895.

Eckart, A., Schoedel, R., Straubmeier, C., et al. (2006). Interferometric Observations of the Galactic Center: LBTI and VLTI. In *SPIE*, 6268.

Egner, S. (2004). Damage of the Xinetics Deformable Mirror. Technical Report LN-MPIA-FDR-TN-AIT-006, MPIA.

Egner, S. (2005). Xinetics DM test report. Technical Report LN-MPIA-FDR-TN-AIT-001, MPIA.

Egner, S., Gaessler, W., Herbst, T., et al. (2004). LINC-NIRVANA: the single arm MCAO experiment. In *SPIE*, 5490, page 924.

Egner, S., Gaessler, W., Ragazzoni, R., et al. (2006a). MANU-CHAO: A laboratory Ground-Layer Adaptive Optics Experiment. 6272. SPIE.

Egner, S., Mascidari, E., and etc. (2006b). Beyond conventional G-SCIDAR – the Ground-Layer in high vertical resolution. In *SPIE*, 6272.

Egner, S., Mascidari, E., McKenna, D., et al. (2006c). G-SCIDAR measurements on Mt. Graham: recent results. In *SPIE*, 6272.

Egner, S. E. (2003). Optical turbulence estimation and emulation. Master's thesis, University of Heidelberg.

Ellerbroek, B., Rigaut, F., Bauman, B., et al. (2003). Multiconjugate adaptive optics for Gemini-South. In *SPIE*, 4839, page 55.

Esposito, S., Riccardi, A., and Femenia, B. (2000). Differential piston angular anisoplanatism for astronomical optical interferometers. *AA*, 353:L29.

Esposito, S., Tozzi, A., Puglisi, A., et al. (2004). Integration and test of the first light AO system for LBT. In *SPIE*, 5490, page 228.

Farinato, J., Ragazzoni, R., Arcidiacono, C., et al. (2004a). Layer-Oriented on paper, laboratory, and soon on the sky. In *SPIE*, 5382, page 578.

Farinato, J., Ragazzoni, R., Arcidiacono, C., et al. (2006). The MCAO wavefront sensing system of LINC-NIRVANA: status report. 6272. SPIE.

Farinato, J., Ragazzoni, R., and Diolaiti, E. (2004b). Novel techniques concerning MCAO: trying to overcome fundamental limitations. In *SPIE*, 5490, page 1229.

Feldt, M., Hayano, Y., Takami, H., et al. (2006). SUPY: an infrared pyramid wavefront sensor for Subaru. In *SPIE*, 6272.

Femenia, B. and Devaney, N. (2003). Optimization with numerical simulations of the conjugate altitudes of deformable mirrors in an MCAO system. *A&A*, 403:1165.

Foy, R. and Labeyrie, A. (1985). Feasibility of adaptive telescope with laser probe. *A&A*, 152:L29.

Fried, D. (1965). Statistics of geometric representation of wavefront distortion. *JOSA*, 55:1427.

Fried, D. (1977). Least-squares fitting a wave-front distortion estimate to an array of phase-difference measurements. *JOSA*, 67:370.

Fuchs, A., Tallon, M., and Vernin, J. (1998). Focusing on a Turbulent Layer: Principle of the "Generalized SCIDAR". *PASP*, 110:86.

Fuensalida, J., Chueca, S., Delgado, J., et al. (2004a). Vertical structure of the turbulence above the observatories of the Canary Islands: parameters and statistics for adaptive optics. In *SPIE*, 5490, page 749.

Fuensalida, J., Garcia-Lorenzo, B., Castro, J., et al. (2004b). Statistics of atmospheric parameters for the Observatorio del Roque de los Muchachos. In *SPIE*, 5572, page 1.

Fuensalida, J., Garcia-Lorenzo, B., and Hoegemann, C. (2006). Removal of the Dome-Seeing Contribution in SCIDAR measurements. *MNRAS*, submitted.

Fusco, T., Ageorges, N., Rousset, G., et al. (2004). NAOS performance characterization and turbulence parameters estimation using closed-loop data. In *SPIE*, 5490, page 118.

Fusco, T., Conan, J.-M., Michau, V., et al. (2000). Isoplanatic angle and optimal guide star separation for multiconjugate adaptive optics. In *SPIE*, 4007, page 1044.

Fusco, T., Petit, C., Rousset, G., et al. (2006). Design of the extreme AO system for SPHERE, the planet finder instrument of the VLT. In *SPIE*, 6272.

Gaessler, W., Arcidiacono, C., Egner, S., et al. (2005). LINC-NIRVANA: MCAO toward Extremely Large Telescopes. *Comptes Rendus Physique*, 6:1129.

Gaessler, W., Ragazzoni, R., Herbst, T., et al. (2004). LINC-NIRVANA: how to get a 23-m wavefront nearly flat. 5490, page 527. SPIE.

Garcia-Lorenzo, B. and Fuensalida, J. (2006). Automatic determination of atmospheric turbulence wind profiles using wavelets. In *SPIE*, 6267.

Garcia-Lorenzo, B., Fuensalida, J., Munoz-Tunon, C., and Mendizabal, E. (2005). Astronomical site ranking based on tropospheric wind statistics. *MNRAS*, 356:849.

Geissler, K. (2005). High contrast imaging survey for exoplanets with adaptive optics. Master's thesis, University of Heidelberg.

Geissler, K. and Mascidari, E. (2006). Meteorological Parameter Analysis above Dome C Using Data from the European Centre for Medium-Range Weather Forecasts. *PASP*, 118:1048.

Genzel, R., Ott, T., Eckart, A., Schödel, R., and Alexander, T. (2005). Inward Bound: High Resolution AO Observations of the Galactic Center. In *Science with Adaptive Optics*, page 275. Springer.

Golub, G. and Loan, C. V. (1996). *Matrix Computations*. Johns Hopkins University Press.

Gonzalez, R. and Woods, R. (2003). *Digital Image Processing*. Prentice Hall.

Greenwood, D. P. (1977). Bandwidth specification for adaptive optics systems. *JOSA*, 67:390.

Haering-Neumayer, N., Cappellari, M., Rix, H.-W., et al. (2006). VLT Diffraction-limited Imaging and Spectroscopy in the NIR: Weighing the Black Hole in Centaurus A with NACO. *ApJ*, 643:226.

Hardy, J. W. (1998). *Adaptive Optics for Astronomical Telescopes*. Oxford University Press.

Hartung, M., Herbst, T., Close, L., et al. (2004). A new VLT surface map of Titan at 1.575 microns. *A&A*, 421:L17.

Herrmann, J. (1981). Cross coupling and aliasing in modal wave-front estimation. *JOSA*, 71:989.

Hill, J. and Salinari, P. (2004). The Large Binocular Telescope project. In *SPIE*, 5489, page 603.

Hippler, S., Hormuth, F., Brandner, W., et al. (2006). The MPIA multipurpose laboratory atmospheric turbulence simulator. In *SPIE*, 6272, page 255.

Hubin, N., Louarn, M. L., Conzelmann, R., et al. (2004). Ground layer AO correction for the VLT MUSE project. In *SPIE*, 5490, page 846.

Hunt, B. (1979). Matrix formulation of the reconstruction of phase values from phase differences. *JOSA*, 69:393.

Kasper, M. E. (2000). *Optimization of an adaptive optics system and its application to high-resolution imaging spectroscopy of T Tauri*. PhD thesis, University of Heidelberg.

Keller, C. U. (2005). Adaptive Optics Observations of the Sun. In *Science with Adaptive Optics*, page 119. Springer.

Kellner, S. (2005). *Novel Adaptive Optics Concepts: Wavefront Sensing with Sodium Laser Guide Stars at Extremely Large Telescopes and Simultaneous Differential Imaging*. PhD thesis, University of Heidelberg.

Kenworthy, M. (2005). vibrations in the AO System of the MMT. private communications.

Klückers, V., Wooder, N., Nicholls, T., et al. (1998). Profiling of atmospheric turbulence strenght and velocity using a generalised SCIDAR technique. *A&A Suppl.*, 130:141.

Laun, W., Baumeister, H., and Bizenberger, P. (2006). The LINC-NIRVANA IR cryostat. In *SPIE*, 6269.

Law, N., Mackay, C., and J.E. Baldwin, J. E. (2006). Lucky imaging: high angular resolution imaging in the visible from the ground. *A&A*, 446:739.

Le Roux, B., Conan, J.-M., Kulcsar, C., et al. (2004). Optimal control law for classical and multiconjugate adaptive optics. *JOSA*, 21:1261.

Livingston, P. (1972). Proposed method for inner scale measurements in a turbulent atmosphere. *Appl. Opt.*, 113:684.

Lloyd-Hart, M., Stalcup, T., Baranec, C., et al. (2006). Scientific goals for the MMT's multi-laser-guided adaptive optics. In *SPIE*, 6272.

Louarn, M. L. (2002). Multi-Conjugate Adaptive Optics: a PSF study. In *Beyond Conventional Adaptive Optics, ESO Conference and Workshop Proceedings*, page 271.

Maire, J., Ziad, A., Borgnino, J., et al. (2006). Wavefront outer scale deduced from interferometric dispersed fringes. *A&A*, 448:1225.

Marchetti, E., Brast, R., Delabre, B., et al. (2006). MAD Star Oriented: laboratory results for Ground Layer and Multi-Conjugate Adaptive Optics. In *SPIE*, 6272.

Marchetti, E., Ragazzoni, R., and Diolaiti, E. (2003). Which range of magnitudes for layer oriented MCAO? In *SPIE*, 4839, page 566.

Martin, H., Allen, R., Burge, J., et al. (2003). Fabrication of mirrors for the Magellan Telescopes and the Large Binocular Telescope. In *SPIE*, 4837, page 609.

Martin, H., Cuerden, B., Dettmann, L., and Hill, J. (2004). Active optics and force optimization for the first 8.4-m LBT mirror. In *SPIE*, 5489, page 826.

Masciadri, E. and Egner, S. (2004). First complete seasonal variation study of the 3D optical turbulence above San Pedro Martir Observatory. In *SPIE*, 5490, page 825.

McKenna, D., Avila, R., Hill, J., et al. (2003). LBT facility SCIDAR: recent results. In *SPIE*, 4839, page 825.

Menard, F. (2005). Adaptive Optics and Star Formation. In *Science with Adaptive Optics*, page 163. Springer.

Merrill, K., Favot, G., Forbes, F., et al. (1986). Planning the National New Technology Telescope (NNTT). VII - Site evaluation project observation and analysis procedures. In *SPIE*, 628, page 125.

Morris, S., Gerssen, J., Swinbank, M., and Wilman, R. (2006). Potential science for the OASIS integral field spectrograph with laser guide star adaptive optics. *New Astronomy Reviews*, 49:488.

Morris, T., Berry, P., Butterley, T., et al. (2004). A ground-layer AO system demonstrator for the William Herschel Telescope. In *SPIE*, 5490, page 891.

Morzinski, K., Evans, J., Severson, S., et al. (2006). Characterizating the potential of MEMS deformable mirrors for astronomical adaptive optics. In *SPIE*, 6272.

Munoz-Tunon, C., Vernin, J., and Varela, A. (1997). Night-time image quality at Roque de los Muchachos Observatory. *A&A Suppl.*, 125:183.

Nappo, C. J. (2002). *An Introduction to Atmospheric Gravity Waves*. Academic Press.

Neuhaeuser, R., Guenther, E., Wuchterl, G., et al. (2005). Evidence for a co-moving substellar companion of GQ Lup. *A&A*, 435:L13.

Nicolle, M., Fusco, T., Michau, V., et al. (2004). Ground layer adaptive optics: analysis of the wavefront sensing issue. In *SPIE*, 5490, page 858.

Noll, R. (1976). Zernike polynomials and atmospheric turbulence. *JOSA*, 66:207.

Owner-Petersen, M. and Gontcharov, A. (2002). Multi-conjugate Adaptive Optics for Large Telescopes Analytical Control of the Mirror Shapes. *JOSA*, 19:537.

Petit, C., Conan, J.-M., Kulcsar, C., et al. (2006). First laboratory demonstration of closed-loop Kalman based optimal control for vibration filtering and simplified MCAO. In *SPIE*, 6272.

Petit, C., Quiros-Pacheco, F., Conan, J.-M., et al. (2004). Kalman filter based control for Adaptive Optics. In *SPIE*, 5490, page 1414.

Press, W., Teukolsky, S., Vetterling, W., and Flannery, B. (2002). *Numerical Recipes in C++*. Cambridge University Press.

Quirrenbach, A. (2006). Measurement of the outer scale of turbulence with optical interferometers. In *SPIE*, 6267.

Racine, R. (1996). Temporal Fluctuations of Atmospheric Seeing. *PASP*, 108:372.

Racine, R. and Ellerbroek, B. (1995). Profiles of the nigh-time turbulence above Mauna Kea and isoplanatism extension in adaptive optics. In *SPIE*, 2534, page 248.

Ragazzoni, R. (1996). Pupil plane wavefront sensing with an oscillating prism. *J. Mod. Opt.*, 43:289.

Ragazzoni, R. (2000). Adaptive optics for giant telescopes: NGS vs. LGS. In *Backaskog workshop on Extremely Large Telescopes*, page 175.

Ragazzoni, R., Diolaiti, E., Farinato, J., et al. (2002). Layer-Oriented Wavefront Sensor Prototype Design and Preliminary Test. Technical Report OWL-TRE-INA-60000-0036, INAF Arcetri.

Ragazzoni, R., Diolaiti, E., Vernet, E., et al. (2005). Arbitrarily Small Pupils in Layer-Oriented Multi-Conjugate Adaptive Optics. *PASP*, 117:860.

Ragazzoni, R., Farinato, J., and Marchetti, E. (2000a). Adaptive optics for 100-m-class telescopes: new challenges require new solutions. In *SPIE*, 4007, page 1076.

Ragazzoni, R., Marchetti, E., and Valente, G. (2000b). Adaptive-optics corrections available for the whole sky. 403:54.

Riccardi, A., Brusa, G., Xompero, M., et al. (2004). The adaptive secondary mirrors for the Large Binocular Telescope: a progress report. In *SPIE*, 5490, page 1564.

Rigaut, F. (2002). Ground Conjugate Wide Field Adaptive Optics for the ELTs. In *Beyond Conventional Adaptive Optics, ESO Conference and Workshop Proceedings*, page 11.

Rigaut, F., Ellerbroek, B., and Flicker, R. (2000). Principles, limitations, and performance of multiconjugate adaptive optics. In *SPIE*, 4007, page 1022.

Rimmele, T., Richards, K., Roche, J., et al. (2006). Progress with solar multi-conjugate adaptive optics at NSO. In *SPIE*, 6272.

Rix, H.-W. and Herbst, T. (1998). A Near Infrared Beam Combiner for the LBT. Technical report, Max-Planck-Institute for Astronomy.

Rocca, A., Roddier, F., and Vernin, J. (1974). Detection of atmospheric turbulent layers by spatiotemporal and spatioangular correlation measurements of stellar-light scintillation. *JOSA*, 64:1000.

Roddier, F. (1981). The effects of atmospheric turbulence in optical astronomy. In *Progress in Optics*, 19, page 281.

Roddier, F. (1988). Curvature sensing and compensation: a new concept in adaptive optics. *Appl. Opt.*, 27:1223.

Roddier, F. and Roddier, C. (1991). Wavefront reconstruction using iterative Fourier transforms. *Appl. Opt.*, 330:1325.

Roggemann, M. (1992). Optical performance of fully and partially compensated adaptive optics systems using least-squares and minimum variance phase reconstructors. *Computers Elect. Engng.*, 18:451.

Rohloff, R.-R., Muench, N., Boehm, A., et al. (2006). CFRP structure for the LBT instrument LINC-NIRVANA. In *SPIE*, 6273.

Rutten, R., Blanken, M., McDermid, R., et al. (2006). Prospects for the GLAS Rayleigh laser beacon on the 4.2-m WHT. *New Astronomy Reviews*, 49:632.

Rutten, R., Clark, P., Myers, R., et al. (2003). Facility class Rayleigh beacon AO system for the 4.2m William Herschel telescope. In *SPIE*, 4839, page 360.

Sadibekova, T., Vernin, J., Sarazin, M., and Louarn, M. L. (2006). Generalized SCIDAR measurements at La Silla Observatory. In *SPIE*, 6267.

Sarazin, M. (2006). Astroclimatology of Paranal. Technical report, ESO.

Shack, R. and Platt, B. (1971). Production and Use of a Lenticular Hartmann Screen. *JOSA*, 61:656.

Southwell, W. (1980). Wave-front estimation from wave-front slope measurements. *JOSA*, 70:998.

Storm, J., Seifert, W., Bauer, S.-M., et al. (2004). The acquisition, guiding, and wavefront sensing units for the Large Binocular Telescope. In *SPIE*, 5489, page 374.

Strehl, K. (1902). Über Luftschlieren und Zonenfehler. *Zeitschrift für Intrumentenkunde*, 22:214.

Stuik, R., Hippler, S., Feldt, M., et al. (2004a). Characterization of deformable mirrors for high-order adaptive optics systems. In *SPIE*, 5490, page 1572.

Stuik, R., Louarn, M. L., and Quirrenbach, A. (2004b). Generalized sky coverage for adaptive optics and interferometry. In *SPIE*, 5490, page 331.

Subaru Telescope (2006). Subaru telescope seeing. Technical report, National Astronomical Observatory of Japan.

Tatarski, V. I. (1961). *Wave Propagation in a Turbulent Atmosphere*. Dover, New York.

Taylor, V., Jansen, R., and Windhorst, R. (2004). Observing Conditions at Mount Graham: Vatican Advanced Technology Telescope UBVR Sky Surface Brightness and Seeing Measurements from 1999 through 2003. *PASP*, 116:762.

Tokovinin, A. (2004). Seeing Improvement with Ground-Layer Adaptive Optics. *PASP*, 116:941.

Tokovinin, A., Baumont, S., and Vasquez, J. (2003). Statistics of turbulence profile at Cerro Tololo. *MNRAS*, 340:52.

Tokovinin, A., Louarn, M. L., and Sarazin, M. (2000). Isoplanatism in a multiconjugate adaptive optics system. *JOSA A*, 17:1819.

Tokovinin, A., Thomas, S., Gregory, B., et al. (2004). Design of ground-layer turbulence compensation with a Rayleigh beacon. In *SPIE*, 5490, page 870.

Tokovinin, A. and Travouillon, T. (2006). Model of optical turbulence profile at Cerro Pachon. *MNRAS*, 365:1235.

Tokovinin, A., Vernin, J., Ziad, A., and Chun, M. (2005). Optical Turbulence Profiles at Mauna Kea measured by MASS and SCIDAR. *PASP*, 117:395.

Tubbs, R. (2003). *Lucky Exposures: Diffraction Limited Astronomical Imaging through the Atmosphere*. PhD thesis, St Johns College Cambridge University.

Tyler, G. (1992). In *Adaptive Optics for Large Telescopes, OSA Technical Digest Series 19*, volume 19, page 8.

Ulich, B. and Davison, W. (1985). Seeing measurements on Mount Graham. *PASP*, 97:609.

Velur, V., Flicker, R., Platt, B., et al. (2006). Multiple guide star tomography demonstration at Palomar observatory. In *SPIE*, 6272.

Veran, J.-P., Rigaut, F., Maitre, H., and Rouan, D. (1997). Estimation of the adaptive optics long-exposure point-spread function using control loop data. *JOSA A*, 14:3057.

Vernin, J., Agabi, A., Avila, R., et al. (2000). Gemini site testing campaign. Cerro Pachon and Cerro Tololo. Technical Report RPT-AO-G0094, Gemini.

Vernin, J. and Azouit, M. (1983). Traitment d'image adapte au speckle atmospherique. I. Formation du speckle en atmosphere turbulente. Proprietes statistiques. *J. Optics Paris*, 14.

Vernin, J. and Munoz-Tunon, C. (1998). The temporal behaviour of seeing. *New Astronomy Reviews*, 42:451.

Vernin, J. and Roddier, F. (1973). Experimental determination of two-dimensional spatiotemporal power spectra of stellar light scintillation. Evidence for a multilayer structure of the air turbulence in the upper troposphere. *JOSA*, 63:270.

Wagner, M. (2004). An overview of instrumentation for the Large Binocular Telescope. In *SPIE*, 5492, page 108.

Wang, J. Y. and Markey, J. K. (1978). Modal compensation of atmospheric turbulence phase distortion. *JOSA*, 68:78.

Weiß, R. (2003). *Point Spread Function Reconstruction for the Adaptive Optics System ALFA and its Application to Photometry*. PhD thesis, University of Heidelberg.

Weiss, R., Hippler, S., Kasper, M., et al. (2002a). Simultaneous measurements of the Fried parameter r_0 and the isoplanatic angle ϑ_0 using SCIDAR and adaptive optics - First results. In *Astronomical Site Evaluation in the Visible and Radio Range*, 266, page 86. APS.

Weiss, R., Hippler, S., Kasper, M., and Feldt, M. (2002b). Simultaneous SCIDAR and Adaptive Optics Measurements: Results and Applications. In *SPIE*, 4538.

West, S., Nagel, R., Harvey, D., et al. (1997). Progress at the Vatican Advanced Technolgy Telescope. In *SPIE*, 2871, page 74.

Acknowledgement

it's no secret that a friend
is someone who lets you help

U2, "Mysterious ways"

I would like to thank everyone who greatly contributed to the successful completion of this thesis. Even though there is now just my name written on the title page, this thesis would not have been possible without their dedicated time, prolonged effort and extensive support.

In particular I want to thank:

Hans-Walter Rix for giving me the opportunity to work at the MPIA and being the supervisor of this thesis.

Andreas Quirrenbach for kindly agreeing to referee this thesis. Bernd Jähne and Max Camenzind for being jury members at the defense.

Roberto Ragazzoni for having the idea for this thesis and willing to fund my work.

Tom Herbst for giving me the opportunity to work in the "team Nirvana" and having the courage to let me play with toys worth half a million dollars.

Elena Masciadri for the collaboration and great support on the part of the SCIDAR measurements and site-characterization.

Wolfgang Gaessler for taking care of me and the daily business over the last three years, many fruitful discussions about Adaptive Optics and new ideas of what else could be studied.

Manfred Stickel, Tom Herbst, Wolfgang Gaessler, Elena Masciadri and Stefan Hippler for carefully reading the manuscript and providing me with many helpful comments.

The Alexander von Humboldt Foundation for funding this work through the Wolfgang Pauls-Prize.

Jacopo Farinato, Emiliano Diolaiti, Carmelo Arcidiacono and Elise Vernet-Viard for the development, assembly and initial tests of the MANU-CHAO WFS unit.

Armin Böhm und dem ganzen Team der Werkstatt für die Anfertigung von Halterungen, Montierungen, Adapterplatten, etc. für MAPS und MANU-CHAO immer innerhalb kürzester Zeit.

Brice Le Roux for his support on the implementation of the Kalman filter.

Peter Bizenberger for his support in ZEMAX for the optical design of the telescope simulator for MANU-CHAO and many discussions about optics.

Florian Briegel, Udo Neumann and Frank Kittmann for writing the hardware interface software for the cameras and the deformable mirror of MANU-CHAO.

Lars Mohr and Sam Wagner for their great support during testing and maintenance of the deformable mirror electronics.

Stefan Hippler, Norbert Münch, Ralf-Rainer Rohloff and Felix Hormuth for their efforts in designing and building the MAPS unit.

Dan McKenna for lending us his SCIDAR instrument and many stimulating discussions on atmospheric turbulence.

Richard Boyle, Ned Franz, Randy Swift and Chris Corbally for their support at the VATT.

Peter Garnavich and Brad Tucker for showing me how to operate the VATT.

Many thanks to Sebastian Daemgen for having the patience to spend ten nights with me at the VATT and support me with the SCIDAR observations while learning for his exams.

Betsy & Dale H. Robinson for their support in Tucson and at the MPI-Residence.

Oliver Krause, Christine & Max, Daniel Apai & Ilaria Pascucci for this warm welcome in Tucson.

The computer department at the MPIA, especially Uli Hiller and Frank Richter, who were always glad to help.

Walter Rauh for assigning me to an office at such a prominent place.

My (former) room-mates Stephan Kellner, Fulvio de Bonis, Eva Meyer and Micaela Stumpf for the relaxed atmosphere and all those discussion topics far away from science. . .

美和。写真をどうもありがとう。

Finally, and most importantly, I thank my family for their encouragement and their caring support throughout my thesis.